

**Evaluation of the  $\bar{\text{P}}\text{ANDA}$  Silicon Pixel  
Front-End Electronics  
and  
Investigation of the  $\bar{\Lambda}\Lambda$  Final State**

DISSERTATION

zur  
Erlangung des Grades  
„Doktor der Naturwissenschaften“  
an der Fakultät für Physik und Astronomie  
der Ruhr-Universität Bochum

von  
Simone Esch

aus  
Troisdorf

Bochum 2014

1. Gutachter: Prof. Dr. James Ritman
  2. Gutachter: Prof. Dr. Ulrich Wiedner
- Tag der Disputation: 28. April 2014

# Contents

<b>1. Preface</b>	<b>1</b>
<b>2. Introduction</b>	<b>3</b>
2.1. The Standard Model of Particle Physics . . . . .	3
2.1.1. Fermions . . . . .	3
2.1.2. Bosons . . . . .	4
2.2. The Strong Force . . . . .	4
2.3. Physics Program at $\overline{\text{PANDA}}$ . . . . .	7
2.3.1. Open Charm Spectroscopy . . . . .	7
2.3.2. Charmonium Physics . . . . .	8
2.3.3. Search for Gluonic Excitations and Exotic States . . . . .	9
2.3.4. Baryon Spectroscopy . . . . .	10
2.3.5. Hypernuclear Physics . . . . .	11
<b>3. The <math>\overline{\text{PANDA}}</math> Experiment</b>	<b>15</b>
3.1. The FAIR Facility . . . . .	15
3.2. The HESR Accelerator . . . . .	17
3.3. The $\overline{\text{PANDA}}$ Experiment . . . . .	18
3.3.1. Target . . . . .	18
3.3.2. Tracking System . . . . .	19
3.3.3. Particle Identification . . . . .	22
3.3.4. Calorimeter System . . . . .	24
3.3.5. Event Filter . . . . .	25
3.4. The Micro Vertex Detector . . . . .	25
3.4.1. Physics Motivation . . . . .	25
3.4.2. Requirements to the MVD Design . . . . .	27
3.4.3. Layout . . . . .	28
3.4.4. Silicon Detectors . . . . .	29
3.4.5. Additional Sensors at Small Polar Angles . . . . .	31
<b>4. Jülich Digital Readout System</b>	<b>33</b>
4.1. Overview . . . . .	33
4.2. Basic Concepts . . . . .	34
4.2.1. Digital Readout Board A . . . . .	37
4.2.2. Digital Readout Board B . . . . .	38
4.2.3. Firmware . . . . .	39
4.2.4. MVD Readout Framework . . . . .	40

4.3.	Adaption of the Readout System to the ToPix 3 . . . . .	40
4.4.	GBT Implementation . . . . .	43
4.4.1.	The GBT Project . . . . .	43
4.4.2.	Implementation of the GBT Protocol into the Jülich Digital Read- out System . . . . .	44
<b>5.</b>	<b>The ToPix 3 Front-End ASIC</b>	<b>45</b>
5.1.	The ToPix ASIC . . . . .	45
5.1.1.	ToPix Requirements . . . . .	45
5.1.2.	Analog Readout Chain . . . . .	46
5.1.3.	Digital Readout Chain . . . . .	47
5.1.4.	ToPix 3 Prototype . . . . .	50
5.2.	Testbench . . . . .	52
5.2.1.	Test Setup . . . . .	52
5.2.2.	ToPix Readout Board . . . . .	52
5.2.3.	Calibration Circuit . . . . .	53
5.3.	Measurements with the ToPix 3 . . . . .	55
5.3.1.	Calibration of DAC . . . . .	55
5.3.2.	ToT Linearity . . . . .	56
5.3.3.	Pixel Test . . . . .	58
5.3.4.	Frequency Variation . . . . .	59
5.3.5.	Threshold Determination . . . . .	64
5.3.6.	Threshold Distribution . . . . .	64
5.3.7.	Noise Distribution . . . . .	68
5.3.8.	Calibration of Several Pixel at Once . . . . .	68
5.4.	Test Beam . . . . .	71
5.4.1.	Setup and Environment . . . . .	71
5.4.2.	Number of detected Hits . . . . .	71
5.4.3.	Study of Rate Losses . . . . .	75
5.5.	Conclusion . . . . .	85
<b>6.</b>	<b>Simulation of the <math>\bar{\Lambda}\Lambda</math> Final State</b>	<b>87</b>
6.1.	Simulation Framework . . . . .	87
6.1.1.	Event Generator . . . . .	89
6.1.2.	Propagation . . . . .	89
6.1.3.	Digitization . . . . .	90
6.1.4.	Reconstruction . . . . .	90
6.1.5.	Physics Analysis . . . . .	91
6.2.	Grid . . . . .	91
6.3.	Simulation of the $\bar{\Lambda}\Lambda$ Final State . . . . .	92
6.3.1.	Coordinate System . . . . .	92
6.3.2.	Detector Geometry . . . . .	93
6.3.3.	Simulation . . . . .	94
6.3.4.	Reconstruction . . . . .	97



6.3.5. Particle Identification . . . . .	104
6.3.6. Event Analysis . . . . .	104
6.4. Results . . . . .	106
6.4.1. Counting Rate Studies . . . . .	106
6.4.2. Detection Efficiency . . . . .	108
6.4.3. Production Rate . . . . .	111
6.4.4. Invariant Mass Distributions . . . . .	112
6.4.5. Vertex Resolution . . . . .	112
6.5. Conclusion . . . . .	119
<b>7. Conclusion</b>	<b>121</b>
<b>A. Appendix to <math>\bar{\Lambda}\Lambda</math> Final State</b>	<b>123</b>
A.1. Armenteros-Podolanski-Plot Analysis of the $\bar{\Lambda}\Lambda$ System . . . . .	123
A.2. Counting Statistics . . . . .	128
<b>Bibliography</b>	<b>137</b>
<b>List of Acronyms</b>	<b>145</b>
<b>List of Figures</b>	<b>145</b>
<b>Danksagung</b>	<b>153</b>
<b>Lebenslauf</b>	<b>155</b>



# 1. Preface

---

*There's a chair in my head  
on which I used to sit  
Took a pencil and I wrote  
the following on it*

K's Choice - Virgin State of Mind

---

People have always been interested in the composition of matter. By looking closer and closer into it, scientists found smaller and smaller structures down to the elementary particles, which build up the matter surrounding us. The smallest structures known today are so-called quarks and leptons.

Six different quark and six different lepton types are known. These particles are arranged in three groups each, so-called families. To each of these particles belongs an antiparticle with the same mass and spin, but opposite charge-like quantum numbers.

Although leptons can be observed in isolation, the nature of the strong interaction prevents quarks from being observed in isolation. Instead either quark-antiquark pairs (so-called mesons) or combinations of three quarks (so-called baryons) are observed. The lightest baryons are the proton and neutron. Together with electrons, which are the lightest charged leptons, these three particles build atoms which are the basis for all stable and visible material in the universe.

How quarks and leptons interact and assemble into other particles is described by the Standard Model (SM) of particle physics. The SM was established in the 1960s and developed over the years to a successful model describing quarks and leptons, the weak, the strong and the electromagnetic interaction. But the SM is far from being a complete theory. Many elementary questions are still unsolved, for example how particles like protons and neutrons gain their mass, since the mass of the valence quarks only explains 1-2% of their total mass.

To investigate these and other questions of the SM and the strong interaction in particular, accelerators and detectors are essential, since they can specifically create and investigate particles. To cover many of these open questions, a new accelerator complex is being built in Darmstadt, Germany, with a yet unreached precision. The Facility for Antiproton and Ion Research (FAIR) contains several accelerators, creating high precision particle beams for several experiments.

The Anti**P**roton **A**nnihilation at **D**armstadt ( $\bar{\text{P}}$ ANDA) experiment is one of the large detectors at FAIR.  $\bar{\text{P}}$ ANDAs main physics objectives center around the properties of

## 1. Preface

particles and excited particles made from quarks of the first and second quark family. It is a fixed target experiment within the High Energy Storage Ring (HESR), which delivers an intense, phase-space cooled antiproton beam in the momentum range of 1.5 to 15 GeV/c. With the high precision of the HESR, PANDA will be able to perform precise spectroscopic studies of hadronic states in the charm quark mass range. The luminosity will be up to  $2 \cdot 10^{32} \text{ cm}^{-2}\text{s}^{-1}$ , thus enabling very rare processes to be studied. This high luminosity leads to a high particle flux and a high radiation environment which the sub-detectors must withstand. The most highly affected sub-detector of this high radiation environment is the Micro Vertex Detector (MVD), the innermost detector of PANDA. The main task of the MVD is the detection of the interaction points of events (vertexing). This vertex finding is crucial for the analysis of short living particles like e.g. D-mesons, particles consisting of a c-quark and a light antiquark.

An essential part of the MVD detector is the readout of the semiconductor sensors. The ToPix (Torino Pixel) Application Specific Integrated Circuit (ASIC) is the front-end electronics for the MVD sensor, developed at the Istituto Nazionale di Fisica Nucleare (INFN) in Turin, Italy. It measures the spatial coordinate, the time and the deposited charge of incident charged particles. The most recent prototype of this ASIC is the ToPix 3, a version of reduced size and functionality.

The Jülich Digital Readout System (JDRS) was adopted and extended to be able to readout this prototype, thus enabling specific test measurements of the prototype. In addition, the performance of PANDA for detecting long lived  $\Lambda$  particles was studied, and the possibility of additional sensitive MVD layers to improve the performance was investigated.

This thesis is structured as follows:

- In Chapter 2 a short introduction to the SM of particle physics, the strong force and the physics program of the PANDA experiment is given.
- In Chapter 3 the PANDA detector is described. A special emphasis lies on the MVD detector, the innermost tracking detector in PANDA.
- In Chapter 4 the JDRS is described, a table-top readout system for testing and characterization of front-end ASIC prototypes.
- In Chapter 5 the ToPix 3 is presented, a prototype for the front-end ASIC of the MVD pixel sensors. Measurements using the JDRS are presented.
- In Chapter 6 a simulation and analysis of the reaction  $\bar{p}p \rightarrow \bar{\Lambda}\Lambda \rightarrow \bar{p}\pi^+p\pi^-$  with the PandaRoot software framework is presented. The question is investigated, if additional semiconductor disks further away from the primary interaction point can improve the reconstruction of this channel.
- In Chapter 7 a summary of this thesis is given.

## 2. Introduction

---

*Words like violence  
break the silence  
Come crashing in  
into my little world*

Depech Mode - Enjoy the Silence

---

The Standard Model (SM) of particle physics is the fundamental theory explaining the strong, electromagnetic and weak forces in terms of elementary particles (quarks and leptons) and their interactions. The Quantum Chromodynamics (QCD) is generally accepted to be the correct theory of the strong interaction. It is a quantum field theory of quarks and gluons based on the non-abelian special unitary group of degree 3 (SU(3)) and it is part of the SM. The matter surrounding us is composed of particles (e.g. protons, neutrons) made up of quarks and gluons, which at low temperatures are bound to electrons. The following chapter provides a short description of the SM, the strong force and the physics program at the PANDA experiment.

### 2.1. The Standard Model of Particle Physics

Since the early 1960's the SM has developed into the most complete model, which describes elementary particles and their interactions. In this model the particles are classified in different groups depending on their properties and their constituents. Two basic groups are distinguished:

*Fermions*, particles with half-integer spin, and *bosons*, particles with integer spin.

Both groups contain elementary particles and composite particles. For each particle an antiparticle exists, which has the same mass, spin and lifetime as the particle, but opposite charge-like quantum numbers.

Figure 2.1 shows an overview of the particle classification as provided by the SM. The particles are described below.

#### 2.1.1. Fermions

Fermions can be distinguished into elementary and composite particles. Leptons and quarks are elementary fermions with spin equal to  $1/2$ . Three families of leptons and quarks exist, there are two particles in every family as shown in Figure 2.2.

## 2. Introduction

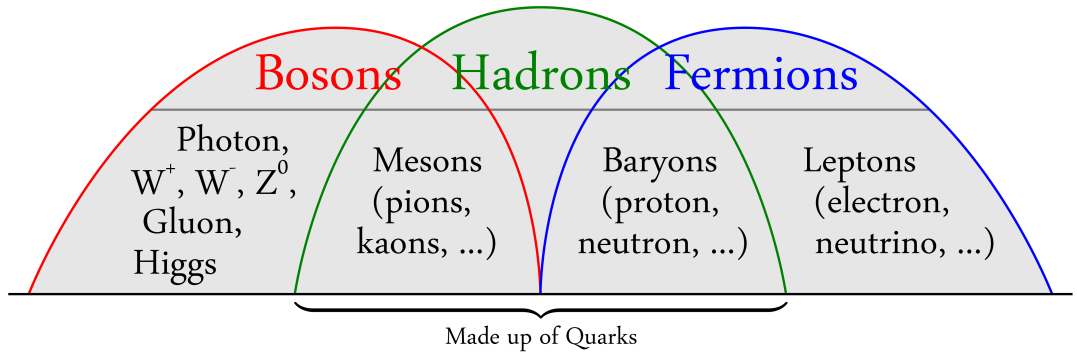


Figure 2.1.: Particle classification in the SM. Picture taken from Ref. [1].

The first family is the lightest and most stable, the third generation is the heaviest. All visible material is made out from particles from the first generation, that combine to protons and neutrons, and electrons.

The leptons are called *electron* ( $e$ ), *muon* ( $\mu$ ) and *tau* ( $\tau$ ) with their neutrino partners *electron-neutrino* ( $\nu_e$ ), *muon-neutrino* ( $\nu_\mu$ ) and *tau-neutrino* ( $\nu_\tau$ ). The quarks are called *up* ( $u$ ), *down* ( $d$ ), *charm* ( $c$ ), *strange* ( $s$ ), *top* ( $t$ ) and *bottom* ( $b$ ).

Composite fermions are combinations of three quarks or three antiquarks, so-called baryons.

### 2.1.2. Bosons

One distinguishes between elementary bosons and composite bosons. The elementary bosons are the *photon* ( $\gamma$ ), *gluon* ( $g$ ),  $W$  and  $Z$ , and *Higgs* boson. The first four are the gauge bosons of the electromagnetic, strong and weak forces, respectively. Photons and gluons are massless, while the  $W$  and  $Z$ , which mediate the weak interaction, are massive. Recently at CERN the Higgs boson was observed [2, 3]. The Higgs boson is an excitation of the Higgs field, which can be measured as a particle. Elementary particles gain their mass through the interaction with the Higgs field.

Composite bosons are called mesons and consists of a valence quark and antiquark.

## 2.2. The Strong Force

The strong force is one of the three interactions covered by the SM. Gluons are bosons which mediate the strong force. All particles which undergo the strong interaction carry a so-called *color charge*. The color charge is an additional degree of freedom needed to explain the existence of particles such as the  $\Delta(u^\uparrow, u^\uparrow, u^\uparrow)$ . The  $\Delta$  baryon consists of three up quarks with parallel aligned spin ( $\uparrow$ ). Without the color charge this state would be forbidden by the Pauli exclusion principle, since all quarks would otherwise have the same quantum numbers. The color charge is defined in analogy to the additive color mixing primary colors and can have the state *red*, *green* or *blue* and the anti-colors

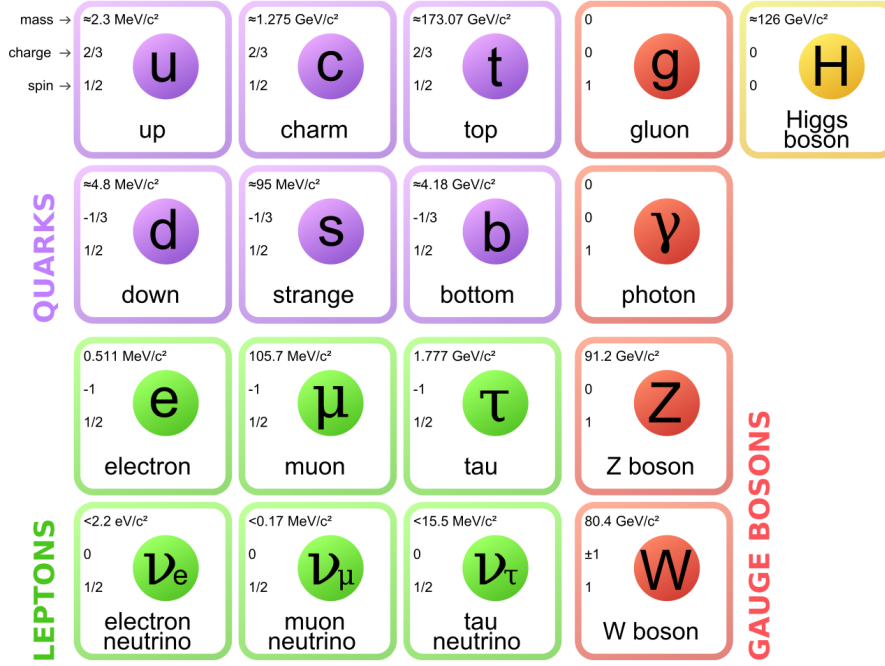


Figure 2.2.: Elementary particles of the SM. The first three columns show the leptons and quarks arranged in three generations. The fourth column shows the gauge bosons and the fifth column displays the Higgs boson. Picture taken from Ref. [4].

*anti-red*, *anti-green* or *anti-blue*. Color neutral states can be produced by combining a quark of a given color and an antiquark with the corresponding anti-color (meson). Alternatively, the combination of all three colors is also neutral (baryons). Up to now no evidence for the existence of objects with non-neutral color charge with length scales over  $\sim 1$  fm have been observed.

Gluons couple to other color-charge carrying particles by the exchange of color-charge. A gluon carries a color and an anti-color charge. The interaction between e.g. a green and a blue quark is mediated by the exchange of a gluon with a blue-antigreen charge. The number of colors and their combination would lead to nine different gluons. Group theory rules of the  $SU(3)$  group sort these nine gluons into two multiplets of states, a singlet state and an octet state. The color-singlet state consists of all three colors and anti-colors, and is thus color neutral. Since gluons are massless, the singlet-state gluon would lead to an unlimited range of the strong interaction. This is not observed, and due to this the singlet state is believed to not exist. The octet state represents eight independent gluons which mediate the strong interaction.

If one takes the three lightest quarks into account the construction of quarks to hadrons is described by a  $SU(3)$  symmetry. The particles are classified according to their angular momentum and their strange quantum number and electrical charge. Figure 2.3 shows the baryon and meson multiplets for the ground state hadrons. The baryons form a

## 2. Introduction

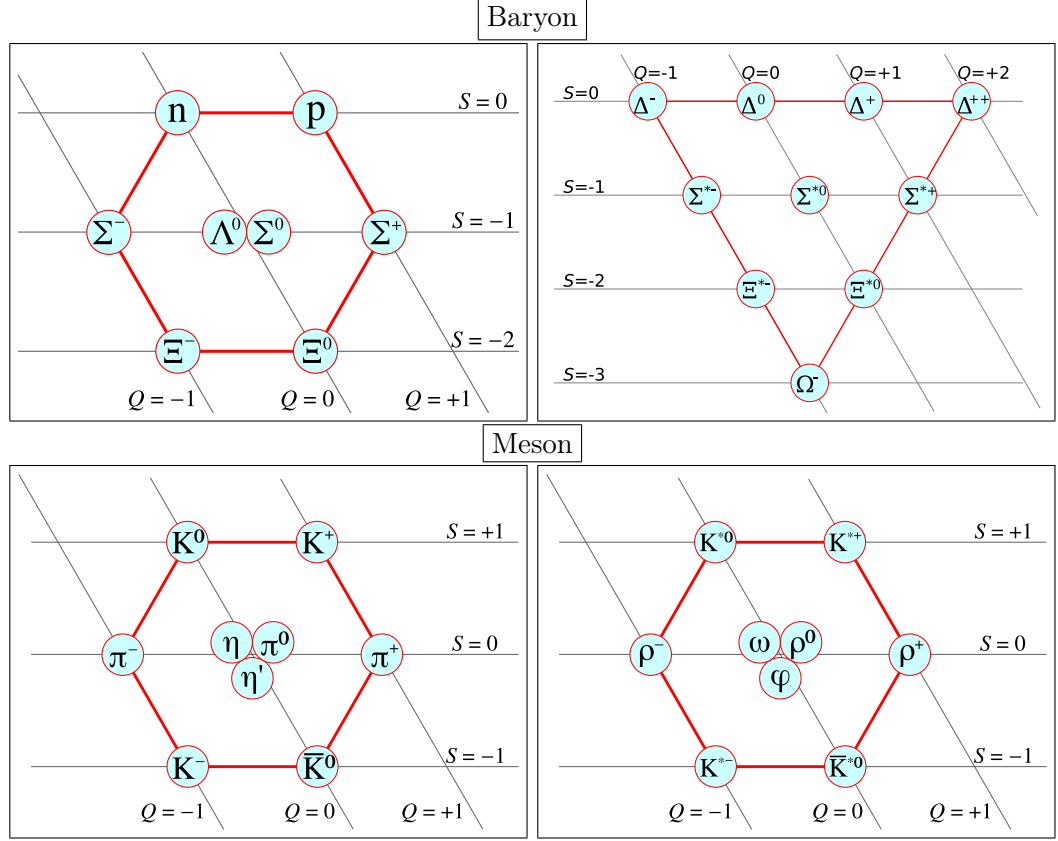


Figure 2.3.: Classification of baryons (upper, left:  $J^P = \frac{1}{2}^+$ , right:  $J^P = \frac{3}{2}^+$ ) and mesons (lower, left:  $J^P = 0^-$ , right:  $J^P = 1^-$ ) built from the lightest quarks up, down and strange. The particles are sorted according to their strangeness (S) and electrical charge (Q). The strangeness is defined by the number of strange antiquarks in the hadron. Pictures taken from Ref. [5, 6, 7, 8].

decuplet of spin  $3/2$  particles and an octet of spin  $1/2$  particles. The mesons form two nonets one for spin 0 and the other for spin 1 particles.

The strength of the force in an interaction is described by the coupling constant. The coupling constant of the strong interaction has some remarkable features (see Figure 2.4). The coupling constant is small for small distances between the quarks or high energies. Quarks interacting with this low coupling constant can be treated as quasi-free particles (asymptotic freedom). In this energy range, perturbative calculations can be used to describe the interaction. With increasing distance or decreasing energy the coupling constant becomes larger. If one tries to separate quarks, the necessary energy increases so much that it is sufficient to create a new quark-antiquark pair, which forms new color neutral particles with the existing quarks (*confinement*) [9].

The mechanisms of confinement are the strong interaction is not completely understood. One of the reasons for confinement is that not only the particles but also the gauge



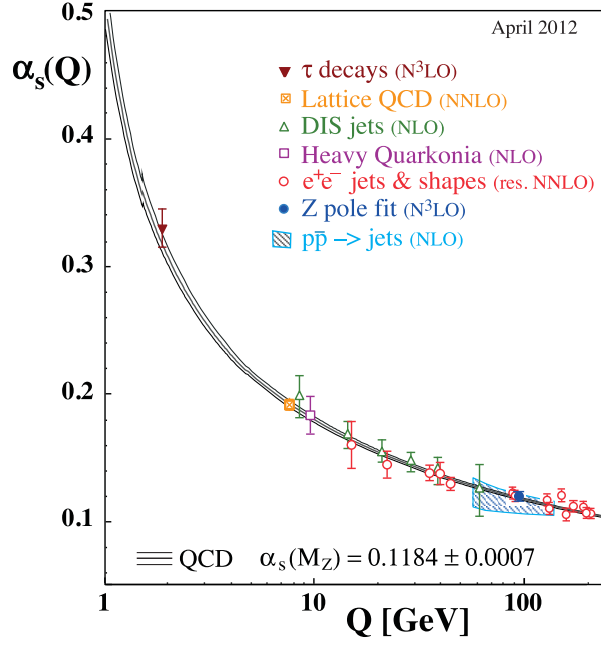


Figure 2.4.: Summary of measurements of the strong coupling constant  $\alpha_s$  as a function of the respective energy scale  $Q$ . Picture taken from [10].

bosons of the strong interaction (*gluons*) carry color charge and consequently interact with each other, in contrast to the gauge bosons of the other forces.

## 2.3. Physics Program at $\overline{\text{PANDA}}$

The aim of the  $\overline{\text{PANDA}}$  experiment is to investigate the strong interaction and the structure of hadrons, which is still not properly understood. The center of mass energy range available to  $\overline{\text{PANDA}}$  was chosen in order to investigate interactions in the transition region between the perturbative and non-perturbative regimes of the strong interaction (see Figure 2.5). The following section gives an overview of the main points of the  $\overline{\text{PANDA}}$  physics program. More information about the physics program at  $\overline{\text{PANDA}}$  can be found in Ref. [11].

### 2.3.1. Open Charm Spectroscopy

D and  $D_s$  mesons consist of a light (anti)quark (u,d,s) and a charm quark (c) and thus have a charm flavor quantum number  $c \neq 0$  (open charm). The combination of a light and heavy quark makes the system comparable to the hydrogen atom. Similar to the investigation of the hydrogen atom, which was instrumental to reach a basic understanding of the electromagnetic force, D-mesons spectroscopy can contribute to the understanding of the strong interaction.

## 2. Introduction

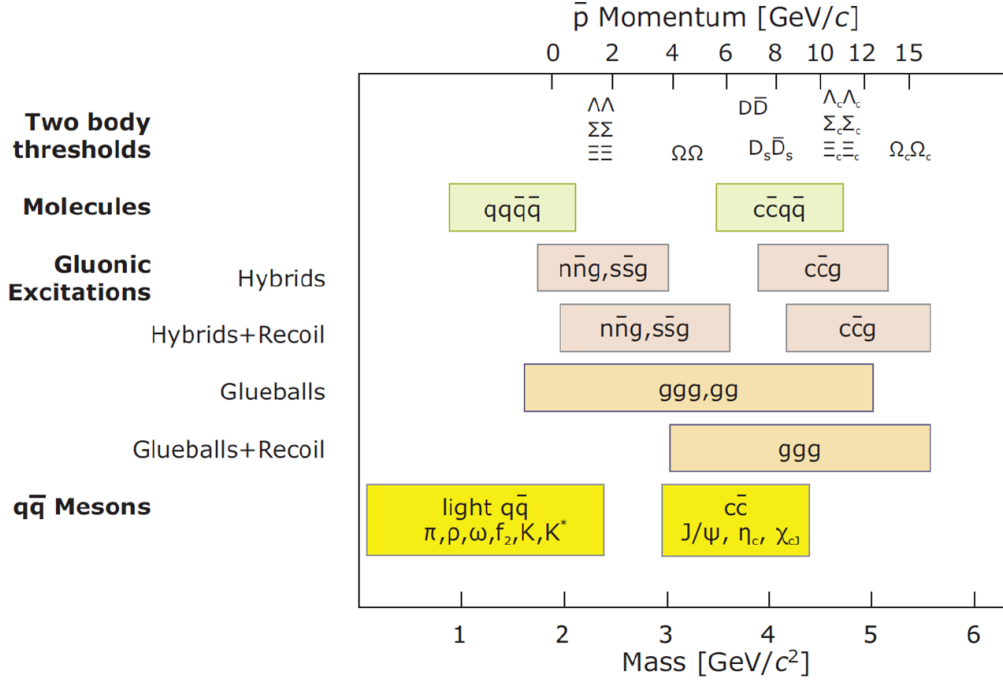


Figure 2.5.: Mass range corresponding systems accessible with the HESR. Picture taken from Ref. [12].

The open charm spectrum was predicted in 1985 [13] and updated in 2001 [14]. However, many recently found states cannot be easily described by quark models (see Figure 2.6). Several theoretical approaches attempt to explain the nature of these states, leading to different predictions for the masses and widths. A precise measurement of the widths and masses of these states, which are currently only roughly known, will help to evaluate the theories. The understanding of the charm spectrum and the unexpected states represents a highlight topic for the PANDA experiment.

### 2.3.2. Charmonium Physics

Charmonium states are mesons which consists of a charm and an anti-charm quark. The electrical charge and the flavor quantum numbers are zero (hidden charm). Charmonium has a similar structure as positronium, which consists of an electron and a positron (see Figure 2.7). The relative differences in the energy states are comparable, despite a scale factor of  $\sim 10^{10}$ . Investigations of positronium brought a huge insight in the electromagnetic force, correspondingly charmonium brings huge insight into the strong interaction.

Charmonium states have been studied intensively at  $e^+e^-$  colliders (see Figure 2.8). Since a virtual photon is created in  $e^+e^-$ , annihilation which has the quantum numbers  $J^{PC} = 1^{--}$ , only charmonium states with these quantum numbers can be formed di-

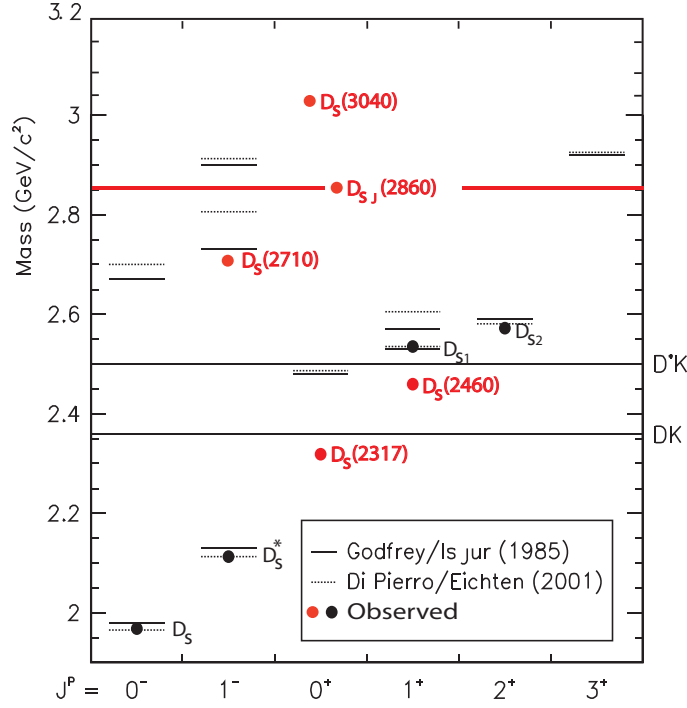


Figure 2.6.:  $D_s$  spectrum predictions (solid/dotted lines) and experimental values (black dots: older, red dots: newer). Picture taken from Ref. [15].

rectly, namely  $J/\psi$ ,  $\psi'$ ,  $\psi(3770)$  and higher vector states. Other states are created via production reactions which leads to higher experimental uncertainties. With  $p\bar{p}$  annihilation it is possible to form all  $c\bar{c}$  states directly, which allows a dramatic improvement in the achievable precision of the mass and width measurements.

Charmonium states below the  $D\bar{D}$  threshold ( $\sqrt{s} = 3739 \text{ GeV}/c$ ) are in good agreement to theoretical calculations. Above the  $D\bar{D}$  threshold many new states have been found since 2003, which do not match with theoretical predictions based on quark potential models [16]. Many different theories attempt to explain these new states mostly as a combination of four quarks. The width of the state in these models is very sensitive to the proposed structure of the state. Precision measurements for these states are often missing which could clarify the nature of these states. One of  $\overline{\text{PANDA}}$  goals is to deliver these precision measurements.

### 2.3.3. Search for Gluonic Excitations and Exotic States

Gluonic excitations are objects, in which the gluons can act as principal components. One representation of a gluonic excitation is a glueball, which is a particle whose valence structure consists only of gluons and sea-quarks. The other representation is a hybrid

## 2. Introduction

POSITRONIUM	CHARMONIUM	RATIO
$5 \times 10^{-6} \text{ MeV}$ $2^1S_0$	$650 \text{ MeV}$ $2^1S_0$	$1.3 \times 10^8$
$4.1 \times 10^{-11} \text{ MeV}$ $\left\{ \begin{array}{l} 1^3P_2 \\ 1^3P_1 \\ 1^3P_0 \end{array} \right.$	$140 \text{ MeV}$ $\left\{ \begin{array}{l} 1^3P_2 \\ 1^3P_1 \\ 1^3P_0 \end{array} \right.$	$3.4 \times 10^{12}$
$8.4 \times 10^{-10} \text{ MeV}$ $1^3S_1$	$115 \text{ MeV}$ $1^3S_1$	$1.4 \times 10^{11}$
$1^1S_0$	$1^1S_0$	
$m_e = 0.5 \text{ MeV}, \alpha_{em} = 1/137$	$m_c = 1500 \text{ MeV}, \alpha_S = 1/3$	
FS, HFS $\alpha_{em}^4 m_e = 1.4 \times 10^{-9}$	$\alpha_S^4 m_c = 18.5$	$1.3 \times 10^{10}$

Figure 2.7.: Comparison between the positronium ( $e^+e^-$ ) and charmonium ( $c\bar{c}$ ) spectra with the ratio of energy scales. Picture taken from Ref. [17].

particle which consists of valence quarks and excited gluons which contribute to the quantum numbers. The gluons lead to additional degrees of freedom, this can cause exotic quantum numbers, which cannot be produced in a fermion-antifermion system. Glueballs are a starting point to understand the mass creation inside hadrons. For a light hadron only a small fraction of the mass is created via the Higgs mechanism, the largest part comes via the strong interaction. Gluons are massless, so the mass of a glueball is created by the strong interaction only.

Figure 2.10 shows the spectrum of glueball masses predicted by Lattice-QCD calculations. Most of the predicted states lie in the accessible energy range of  $\overline{\text{P}}\text{ANDA}$  and could be measured. Lattice-QCD is a non-perturbative theoretical approach to describe the strong interaction especially at low energies.

### 2.3.4. Baryon Spectroscopy

Baryons that contain light and strange quarks have been called hyperons [9]. Strange quarks, due to their mass, are classified as an intermediate case between the light (u,d) and heavy (c,b,t) quarks. Now also baryons containing heavier quarks are classified as hyperons, for which the quark content is indicated by a subscript c or b.

The lightest strange hyperons decay nearly exclusively through the weak interaction and thus have a comparably long life time. The only exception is the  $\Sigma^0$ , which decays electromagnetically. The decay via the weak interaction is not parity conserving. As a result, the daughter particles have an anisotropy relative to the hyperon spin direction [18]. Measuring the angular distribution of the hyperons decay thus provides information about the hyperon spin direction.

The spectrum of hyperon states is not well known (see Figure 2.9). Many excited states need to be investigated further to determine the particle characteristics. The hyperons

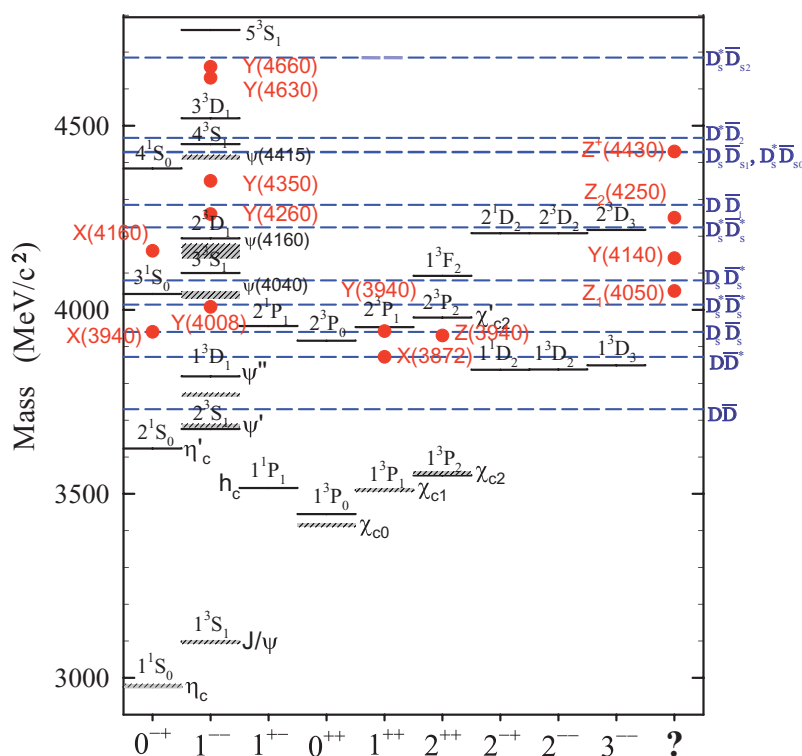


Figure 2.8.: The charmonium spectrum. Solid lines indicate predictions, shaded lines indicate conventional charmonium states. Red dots indicate newly discovered charmonium-like states. Picture taken from Ref. [15].

can help to understand quark-antiquark creation and the formation of hyperons from these created quarks. PANDA will perform spectroscopic measurements of hyperons and compare the results to theoretical models.

### 2.3.5. Hypernuclear Physics

The study of hypernuclei provides information about the nuclear structure and the dynamics of many body hadronic systems. A hypernucleus is a nucleus where one or more nucleons are replaced by hyperons. Due to the presence of the hyperons, the nucleus has a non-zero strangeness quantum number and a new degree of freedom. Since hyperons decay via the weak interaction they live long enough to get bound by the nucleus and can be investigated by spectroscopic methods. Hyperons are very deeply bound in the nucleus because they do not suffer from the Pauli principle due to their strangeness quantum number. Hyperons are distinguishable from the nucleons, which make them a perfect probe for nuclear structure investigations.

## 2. Introduction

In  $\overline{\text{PANDA}}$  it is planned to create double  $\Lambda$  hypernuclei via the capture of the  $\Xi$  hyperon [19]. A two step process with two targets is planned to first create low momentum  $\Xi$  particles which then will be captured by a nucleus and decay there into two  $\Lambda$ s. High purity germanium (HPGe) crystals are employed for  $\gamma$  detectors to measure the de-excitations of the exited nuclei. For the hypernuclear measurements the  $\overline{\text{PANDA}}$  detector will be modified: the Micro Vertex Detector (MVD) will be replaced by the active secondary target and in backward angles a HPGe  $\gamma$  array will be installed.

$J^P$	$(D, L_N^P) S$	Octet members			Singlets
$1/2^+$	$(56, 0_0^+)$	$1/2 N(939)$	$\Lambda(1116)$	$\Sigma(1193)$	$\Xi(1318)$
$1/2^+$	$(56, 0_2^+)$	$1/2 N(1440)$	$\Lambda(1600)$	$\Sigma(1660)$	$\Xi(?)$
$1/2^-$	$(70, 1_1^-)$	$1/2 N(1535)$	$\Lambda(1670)$	$\Sigma(1620)$	$\Xi(?)$ $\Lambda(1405)$
$3/2^-$	$(70, 1_1^-)$	$1/2 N(1520)$	$\Lambda(1690)$	$\Sigma(1670)$	$\Xi(1820)$ $\Lambda(1520)$
$1/2^-$	$(70, 1_1^-)$	$3/2 N(1650)$	$\Lambda(1800)$	$\Sigma(1750)$	$\Xi(?)$
$3/2^-$	$(70, 1_1^-)$	$3/2 N(1700)$	$\Lambda(?)$	$\Sigma(?)$	$\Xi(?)$
$5/2^-$	$(70, 1_1^-)$	$3/2 N(1675)$	$\Lambda(1830)$	$\Sigma(1775)$	$\Xi(?)$
$1/2^+$	$(70, 0_2^+)$	$1/2 N(1710)$	$\Lambda(1810)$	$\Sigma(1880)$	$\Xi(?)$ $\Lambda(?)$
$3/2^+$	$(56, 2_2^+)$	$1/2 N(1720)$	$\Lambda(1890)$	$\Sigma(?)$	$\Xi(?)$
$5/2^+$	$(56, 2_2^+)$	$1/2 N(1680)$	$\Lambda(1820)$	$\Sigma(1915)$	$\Xi(2030)$
$7/2^-$	$(70, 3_3^-)$	$1/2 N(2190)$	$\Lambda(?)$	$\Sigma(?)$	$\Xi(?)$ $\Lambda(2100)$
$9/2^-$	$(70, 3_3^-)$	$3/2 N(2250)$	$\Lambda(?)$	$\Sigma(?)$	$\Xi(?)$
$9/2^+$	$(56, 4_4^+)$	$1/2 N(2220)$	$\Lambda(2350)$	$\Sigma(?)$	$\Xi(?)$
Decuplet members					
$3/2^+$	$(56, 0_0^+)$	$3/2 \Delta(1232)$	$\Sigma(1385)$	$\Xi(1530)$	$\Omega(1672)$
$3/2^+$	$(56, 0_2^+)$	$3/2 \Delta(1600)$	$\Sigma(?)$	$\Xi(?)$	$\Omega(?)$
$1/2^-$	$(70, 1_1^-)$	$1/2 \Delta(1620)$	$\Sigma(?)$	$\Xi(?)$	$\Omega(?)$
$3/2^-$	$(70, 1_1^-)$	$1/2 \Delta(1700)$	$\Sigma(?)$	$\Xi(?)$	$\Omega(?)$
$5/2^+$	$(56, 2_2^+)$	$3/2 \Delta(1905)$	$\Sigma(?)$	$\Xi(?)$	$\Omega(?)$
$7/2^+$	$(56, 2_2^+)$	$3/2 \Delta(1950)$	$\Sigma(2030)$	$\Xi(?)$	$\Omega(?)$
$11/2^+$	$(56, 4_4^+)$	$3/2 \Delta(2420)$	$\Sigma(?)$	$\Xi(?)$	$\Omega(?)$

Figure 2.9.: Spectra of different strange hyperons. The colored boxes indicate states for which little is known about their quantum numbers. These states comprise significant potential for measurements with  $\overline{\text{PANDA}}$  (status Nov. 2011). Figure based on Ref. [10].

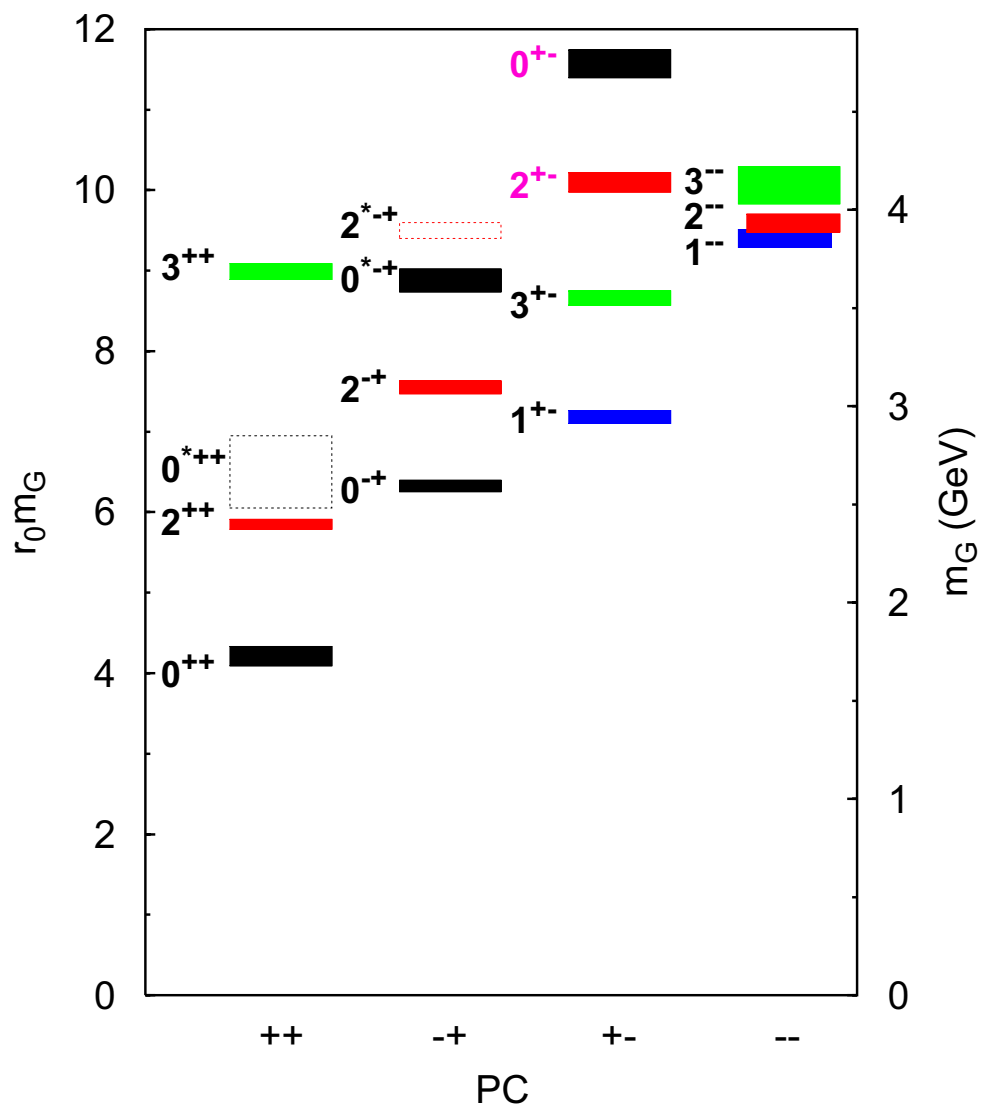


Figure 2.10.: Spectrum of glueball masses predicted by Lattice-QCD calculations. Picture taken from Ref. [20].





## 3. The $\bar{\text{P}}\text{ANDA}$ Experiment

---

*And I miss you  
Like the deserts miss the rain*

Everything but the Girl - Missing

---

The  $\bar{\text{P}}\text{ANDA}$  (Anti**P**roton **A**nnihilation at **D**armstadt) experiment will be one of the large detectors at the Facility for Antiproton and Ion Research (FAIR) which is being built in Darmstadt, Germany. It is an internal experiment at the High Energy Storage Ring (HESR) which delivers an intense, phase space cooled antiproton beam in the momentum range of 1.5 GeV/c to 15 GeV/c [12].

This Chapter gives an overview of the FAIR facility, briefly describes the  $\bar{\text{P}}\text{ANDA}$  detector and introduces the Micro Vertex Detector (MVD), the innermost tracking detector of the  $\bar{\text{P}}\text{ANDA}$  experiment in more detail.

### 3.1. The FAIR Facility

The FAIR facility is being built adjacent to the research center Gesellschaft für Schwerionenforschung (GSI) in Darmstadt. A schematic overview of the combined GSI and FAIR complex is shown in Figure 3.1. Existing accelerators at GSI will be integrated into the FAIR complex and will serve as pre-accelerators for protons and heavy ions for the FAIR synchrotrons. The accelerators at GSI include the Universal Linear Accelerator (UNILAC), the Experimental Storage Ring (ESR) and the Schwerionen Synchrotron (SIS18), a heavy ion synchrotron with a maximum rigidity of 18 T·m.

The FAIR complex will start its operation in a modularized start version, containing the main experiments and accelerators [21]. This start version will be extended over the years with additional accelerators upgrades and specialized experiments.

Part of the modularized start version is the linear accelerator (p-LINAC). The p-LINAC will pre-accelerate protons and inject them into the SIS18. Protons in SIS18 will be accelerated to a momentum of 2 GeV/c before being transferred to the main synchrotron SIS100 or the later extension SIS300. FAIR experiments like CBM and several atom and plasma physics experiments will be served with particles directly from SIS100/SIS300 [22].

For the physics of  $\bar{\text{P}}\text{ANDA}$ , a cooled antiproton beam is necessary which is created in a multi-staged process. In the first stage, protons are accelerated in SIS100 to a momentum of 29 GeV/c. Roughly  $4 \cdot 10^{13}$  protons will be shot in a bunch of 25 ns duration on an

### 3. The $\bar{\text{P}}\text{ANDA}$ Experiment

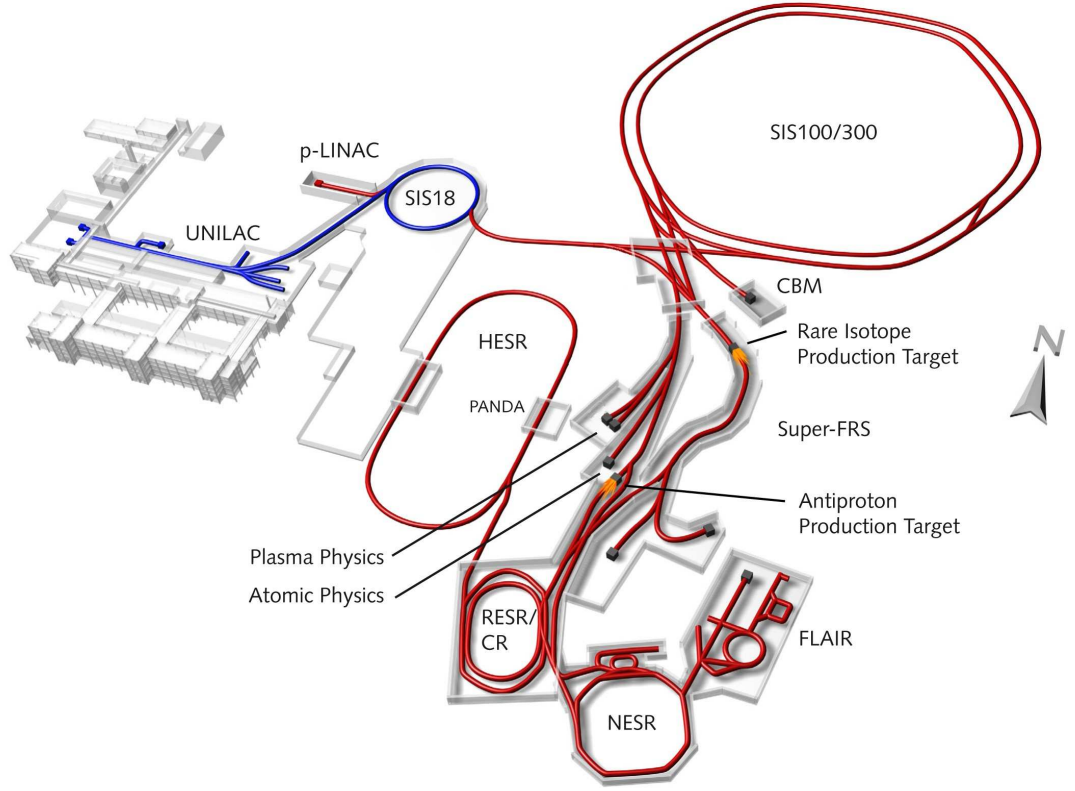


Figure 3.1.: Overview of the full FAIR facility. The existing accelerators of the GSI are displayed in blue, displayed in red are the new systems which belong to the FAIR facility. Picture taken from Ref. [23].

iridium target, creating  $2 \cdot 10^8$  antiprotons within the phase space acceptance via the reaction:

$$p + p \rightarrow p + p + p + \bar{p} \quad (3.1)$$

The created antiprotons will be separated from the protons and collected in the Collector Ring (CR). In this stage, a first stochastic cooling of the antiprotons is performed. The antiprotons will be delivered every 10 s at 3 GeV from the CR into the HESR until the final filling amount of  $1 \cdot 10^{10}$  antiprotons is reached. In a later stage a second ring, the Recycled Experimental Storage Ring (RESR), will collect a complete HESR filling of antiprotons during operation of HESR [22]. In this way, a continuous operation of the HESR will be possible without spending time for collecting the antiprotons. As a result the RESR will allow both a higher duty cycle and a higher number of stored antiprotons ( $10^{11}$ ) in the HESR

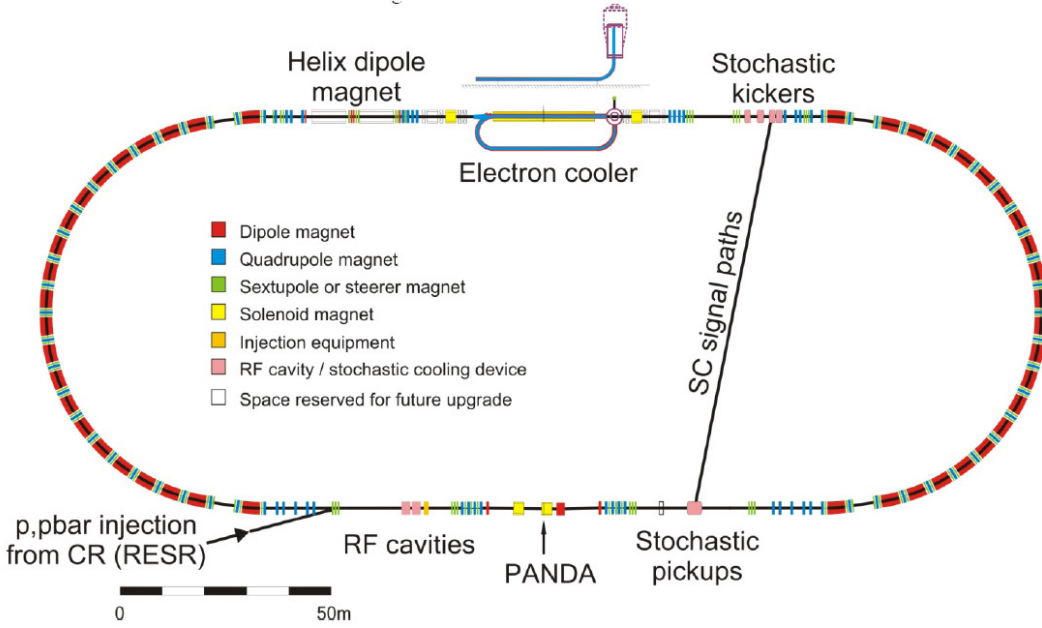


Figure 3.2.: Schematic drawing of the HESR. The  $\bar{\text{PANDA}}$  experiment will be located in the lower straight part. The electron cooling will be located in the upper straight section. Picture taken from Ref. [24].

### 3.2. The HESR Accelerator

The HESR is a synchrotron and a storage ring, dedicated to supply the  $\bar{\text{PANDA}}$  detector with a high intensity and high quality antiproton beam. A schematic drawing of the HESR can be seen in Figure 3.2. The storage ring consists of two arc sections with a radius of 42 m and two straight sections of 155 m length. The total circumference of the ring is 575 m. The  $\bar{\text{PANDA}}$  detector will be located in one straight section.

Two beam cooling methods, electron cooling and stochastic cooling, are used in the HESR to achieve the small momentum spread and size of the antiproton beam required by  $\bar{\text{PANDA}}$ .

For electron cooling, electrons are accelerated to the same average velocity as the antiproton beam and injected to overlap the beam. These electrons undergo Coulomb scattering with the antiprotons. Thus, the antiprotons loose transversal momentum and longitudinal momentum that differs from the antiproton momentum corresponding to the mean velocity of the cooling electrons. After several meters these electrons are removed from the beam via a magnet. Electron cooling is a powerful way of cooling a beam without removing particles and is most effective for lower beam momenta. The cooling method was first tested in 1974 at the NAP-M storage ring at INP, Novosibirsk, and is now a widely used method for cooling of ion beams, e.g. at the Cooler Synchrotron (COSY) accelerator in Jülich. The electron accelerator (electron cooler) necessary for the electron cooling is installed in the opposite straight section of the  $\bar{\text{PANDA}}$  experiment. Electron

### 3. The $\overline{\text{PANDA}}$ Experiment

cooling is typically good to cool the core of the beam (particles with small deviations from the nominal value).

The stochastic cooling mechanism scans the antiproton beam at a certain position (pick-up) and measures the phase space position of particles in the beam. The measured displacement of the beam is used to generate a correction signal which is transmitted on a direct way to an electromagnetic field generator (kicker) while the beam goes in the beam pipe along the arc section. The kicker corrects strongly deflected particle bunches towards the middle of the beam. Stochastic cooling is possible for all beam momenta and is most effective to correct particles with a large deviation from the desired momentum. In the full FAIR version, the HESR will be able to operate in two different modes to match individual requirements of different measurements. In the high resolution mode (HR), the HESR offers a  $\bar{p}$  beam with an excellent momentum resolution of  $\sigma_p/p \leq 4 \cdot 10^{-5}$  with a peak luminosity of  $2 \cdot 10^{31} \text{ cm}^{-2}\text{s}^{-1}$  in the beam momentum range between 1.5 GeV/c and 9 GeV/c. To reach this momentum resolution, the ring is filled with a lower number of antiprotons of  $10^{10}$ . In the high luminosity mode (HL), the HESR offers a beam with a ten times higher luminosity of  $2 \cdot 10^{32} \text{ cm}^{-2}\text{s}^{-1}$  and a relative momentum resolution of  $\sigma_p/p \leq 1 \cdot 10^{-4}$  in the beam momentum range between 1.5 GeV/c and 15 GeV/c. In this mode the HESR is filled with  $10^{11}$  antiprotons [25].

## 3.3. The $\overline{\text{PANDA}}$ Experiment

The  $\overline{\text{PANDA}}$  detector will be one of the large experiments at FAIR. It is planned to be an internal experiment at the HESR synchrotron.

$\overline{\text{PANDA}}$  is a fixed target experiment, which means that accelerated antiprotons which circulate inside HESR collide with protons or heavier nuclei that are at rest in the lab reference frame. The particles produced in these collisions are then measured by two spectrometers, the Target Spectrometer (TS) surrounding the interaction region (see Figure 3.3) and the Forward Spectrometer (FS) measuring the forward boosted particles with shallow polar angles (see Figure 3.4).

To measure the momentum and the sign of the charge of charged particles, a homogeneous solenoid field of 2 T strength along the beam axis is used in the TS. In the FS, a dipole magnet with a field strength of 2 T·m perpendicular to the beam is used. The different sub-detectors of the target spectrometer are assembled in a shell-like structure around the Interaction Point (IP). The FS has a downstream layer ordering of the sub-detectors. The following sections describe the individual parts of the experiment.

### 3.3.1. Target

The target system provides the reaction partners for the circulating antiproton beam within HESR. Different target materials are foreseen to answer different physical questions. To reach the desired luminosity, the target has to be of a certain thickness. On the other hand, if the target is too thick it attenuates the antiproton beam too quickly and causes multiple scattering as well as secondary interactions of the particles in the target

material. Thus, the maximum useful target thickness is  $4.5 \times 10^{15}$  atoms/cm<sup>2</sup> [26]. Hydrogen, deuterium and heavier nuclei are planned as target materials. Deuterium, which is an isotope of hydrogen, has a special role. It consists of one proton and one neutron and will serve as an effective neutron target. To study antiproton nucleus reactions, heavier target materials such as <sup>4</sup>He, N<sub>2</sub>, Ne, Ar, Xe, Kr are foreseen.

Currently, two different target systems are developed for the measurements at the  $\bar{\text{PANDA}}$  detector. Both targets have complementary techniques but fulfill the basic requirements for the target thickness.

One target option is the so-called cluster-jet target. Pressurized cooled gas is injected through a nozzle into vacuum. The gas condenses and forms clusters with a size of about  $10^3$ - $10^5$  atoms per cluster. These clusters align in a supersonic jet with a target thickness of  $2 \times 10^{15}$  atoms/cm<sup>2</sup> which flies through skimmers and into the antiproton beam. Cluster-jet targets are operating in different experiments throughout the world. Due to the uniform distribution of the clusters, the cluster-jet target produces no time structure in the antiproton-proton reaction rate at  $\bar{\text{PANDA}}$ .

The other target option is a pellet target. It uses a piezo crystal to form small frozen droplets out of a stream of liquid hydrogen, so-called pellets. The pellets have a size of about 25-30  $\mu\text{m}$  and a mean target thickness of  $2$ - $4 \times 10^{15}$  atoms/cm<sup>2</sup>. Due to the high target density, a continuous series of interactions takes place on a single pellet. A vertexing of the pellet path can be performed and the interaction vertex improved. The instantaneous luminosity depends directly on the number of pellets crossing the beam. Therefore, a constant number of pellets is necessary to avoid strong fluctuations in the instantaneous luminosity which could be a problem for the detector systems. A successfully running pellet target was developed at Uppsala University for the usage at the CELSIUS accelerator and is now running in the WASA-at-COSY experiment at the Forschungszentrum Jülich.

For further information about the target system please consult the Technical Design Report for the Target [26].

#### 3.3.2. Tracking System

The tracking detectors belong to the first detectors around the IP where the reaction takes place. Its main task is to determine the momentum and the origin of the particles. It consists of four sub-detectors, the MVD, the Straw Tube Tracker (STT), the Gas Electron Multiplier (GEM) stations and the Forward Tracking System (FTS). The MVD, the innermost tracking detector in  $\bar{\text{PANDA}}$  is explained in detail in Section 3.4. The other three tracking detectors are described below.

**Straw Tube Tracker** The STT belongs to the central tracking detectors at  $\bar{\text{PANDA}}$ . The task of the STT is to determine the momentum of charged particle tracks and supply particle identification information via specific energy deposit measurements. The detector consists of 4636 straw tubes of 1.5 m length, arranged in a cylindrical volume around the MVD and the IP, achieving a spatial resolution of 150  $\mu\text{m}$  in radial direction. Each tube consists of an anode wire within a tube of 30  $\mu\text{m}$  thick aluminized mylar foil of

### 3. The $\bar{P}$ ANDA Experiment

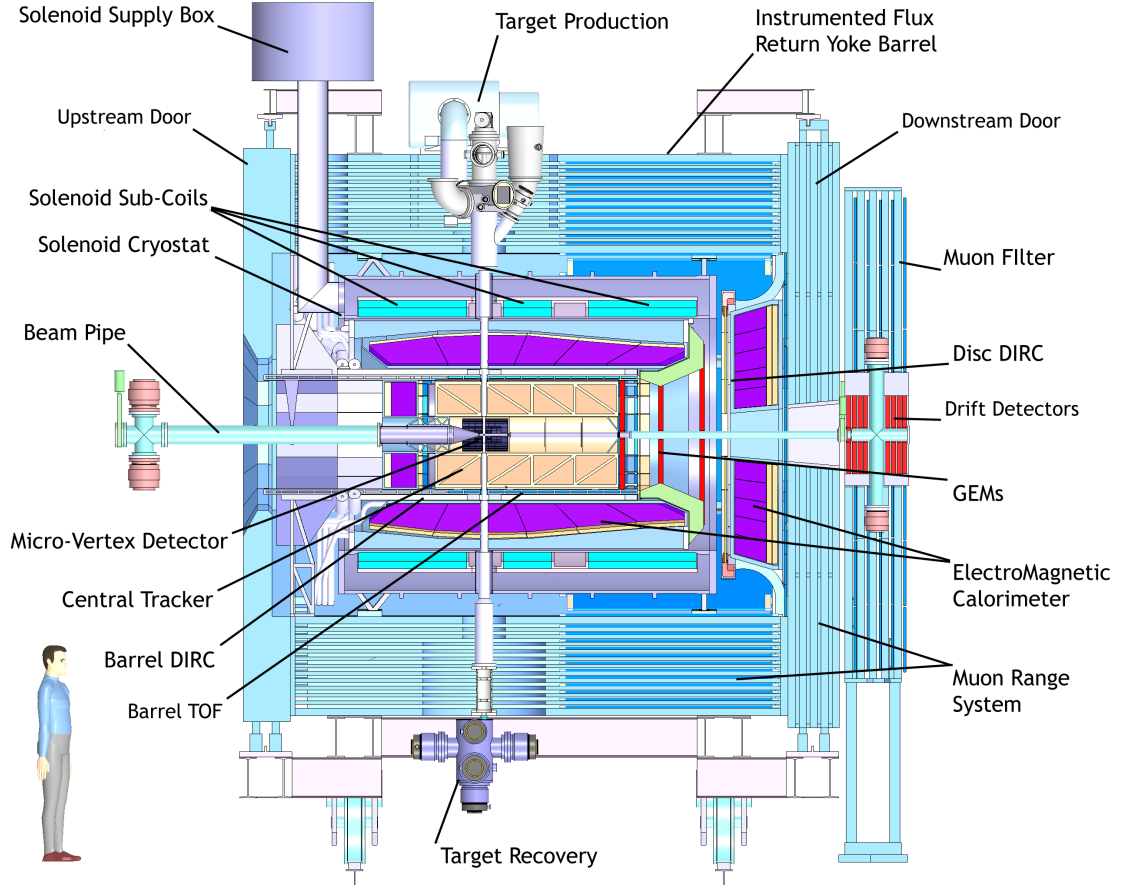


Figure 3.3.: Side view of the  $\bar{P}$ ANDA target spectrometer with all sub-detectors. The antiproton beam approaches from the left. Picture taken from Ref. [27].

10 mm inner diameter. The inner side of the tube is conductive to function as a cathode. A voltage of a few kV is applied between the anode wire and the cathode wall. The tube is filled with a gas mixture of argon and  $\text{CO}_2$  at 1 bar overpressure, making it stiff and self-supporting, reducing the needed support structure to a minimum.

If a charged particle passes a tube, it ionizes the gas. Due to the voltage difference between the foil and the wire, the electrons are accelerated towards the wire. Close to the wire, the acceleration of the electrons is high enough to create an electron avalanche amplifying the signal. The signal is then readout via the anode wire at one side of the tube. Due to the limited space in the forward direction, the straw signal is readout only at the upstream side of the straw. Therefore, a single straw only provides spatial information perpendicular to the wire and not along the wire.

Measuring the drift time of the electrons in the straw significantly improves the spatial resolution of the track path. In this way, information about the minimal particle track distance from the wire, the so-called isochrone radius is obtained. All points on the

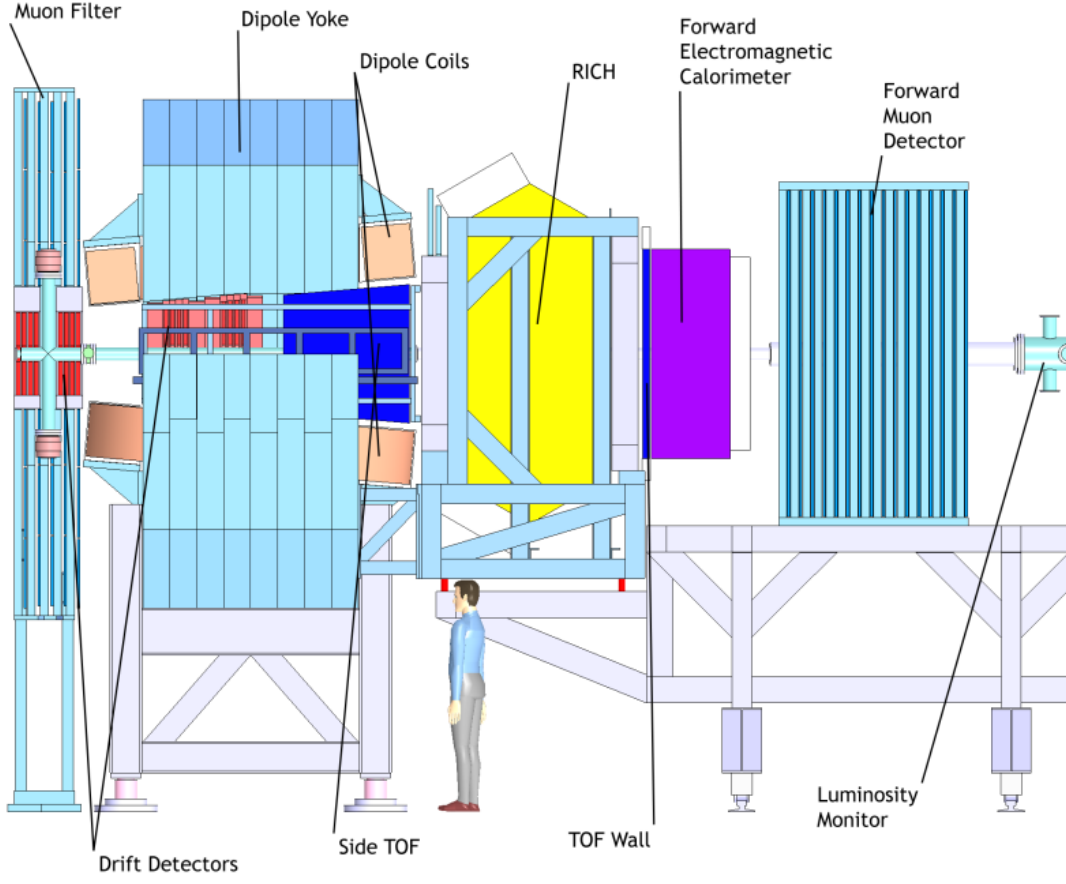


Figure 3.4.: Side view of the  $\bar{\text{PANDA}}$  forward spectrometer with its sub-detectors. The antiproton beam approaches from the left. Picture taken from Ref. [27].

isochrone radius have the same drift time.

The straw tube tracker is subdivided in two halves, each half consists of three sectors. The tubes inside the sectors are arranged in layers. In the inside and the outside of the STT the tubes are parallel to the beam axis. In the middle there are four double-layers of STT tubes tilted alternating by  $\pm 3^\circ$  w.r.t. the beam axis. By combining the information of the different skewed layers the z-position of the particle tracks is determined. The STT has a very small contribution to the material budget, with a radiation length of about  $1.2\% X/X_0$ , since the detector consists mainly of gas and low Z materials.

For further information please consult the Technical Design Report of the Straw Tube Tracker [24].

**GEM Stations** The GEM stations are located directly after the STT in the beam direction at distances of 1.2 m, 1.5 m and 1.9 m from the interaction point. The GEM



### 3. The $\bar{P}$ ANDA Experiment

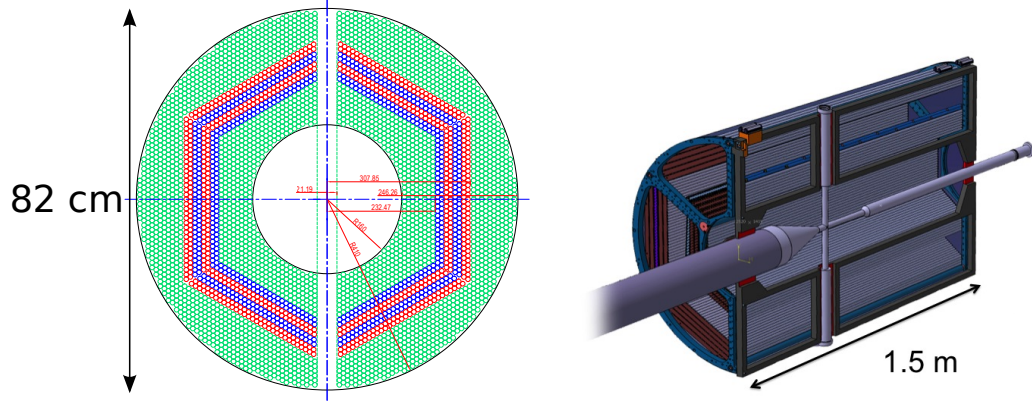


Figure 3.5.: Technical drawings of the STT: Left: Front view along the beam axis. Green indicate straw tubes oriented parallel to the beam axis, blue and red indicate straw tubes skewed by an angle of  $\pm 3^\circ$  with respect to the beam axis [24]. Right: STT with beam and target pipe [28]. The antiproton beam enters from the left.

stations track particles emitted at a polar angle lower than  $22^\circ$ . Each station is a double-layered plane with two projections per plane, one giving cartesian coordinates and the other polar coordinates.

The stations consist of a drift volume and gaseous micro-pattern detectors, based on GEM foils as amplification stages. GEM foils are made of a thin Kapton foil (50-70  $\mu\text{m}$ ) covered on both sides with copper. Small holes with a diameter in the range of several tens of  $\mu\text{m}$  are etched through the foil. A voltage difference is applied to the copper layers, creating a high electrical field around and inside the holes capable of creating electron avalanches.

Electrons, created in the gas of the drift volume, travel towards the GEM foils due to an applied electric field. These electrons are amplified in the GEM holes and detected as particle hits.

**Forward Tracking System** The FTS measures the deflection of charged particles in the magnetic field of the dipole magnet in the FS. Six tracking stations are planned, two before, two within and two behind the dipole magnet. Each station consist of four double layers of straw tubes aligned perpendicular to the beam axis. Two double layers have a vertical orientation, two double layers are inclined by  $\pm 5^\circ$  with respect to the vertical layers. The straw tubes have a diameter of 10 mm and are filled with a gas mixture of argon and  $\text{CO}_2$  at 1 bar overpressure [29].

#### 3.3.3. Particle Identification

In addition to the momentum of a particle also the velocity or the mass of the particle is needed for a full description of a particle. The tracking detectors give the momentum



and the sign of the charge of the particle due to the direction of curvature of the track in the applied magnetic field. So called Particle Identification (PID) detectors provide information on the actual particle type usually by measuring the velocity directly or indirectly. Several detectors within  $\bar{\text{PANDA}}$  are dedicated to the particle identification task, sensitive in different energy ranges and specialized to distinguish between special particle types. Also other detectors such as the tracking detectors deliver PID information like the specific energy loss of a particle in the STT or MVD.

**Cherenkov Detector Systems** One of the main particle identification detectors is the Detection of Internally Reflected Cherenkov Light (DIRC) detector. This detector uses the Cherenkov effect for separation of particle types. The Cherenkov effect describes the emission of light from a charged particle, which is moving faster than the speed of light in a material with the refractive index  $n$ . The light is emitted in a cone of opening angle  $\Theta_C$ , which is related to the speed of the particle ( $\beta$ ) as follows:

$$\cos \Theta_C = \frac{1}{n\beta}$$

$\bar{\text{PANDA}}$  will have two DIRC detectors: The barrel DIRC, which is located between the STT tracker and the Electromagnetic Calorimeter (EMC) covering a polar angle range of  $22^\circ$  to  $144^\circ$ . The forward DIRC part has a disk-like construction and covers a polar angle of  $5^\circ$  to  $22^\circ$ . The Cherenkov light is created and transported by internal reflection in fused silica slabs to focusing elements which project the light on photon detectors. For both DIRC detectors Micro-Channel Plate Photomultipliers (MCT-PMTs) are foreseen. From the measured pattern of the PMT the opening angle and with this the velocity of the particle can be reconstructed.

A further Cherenkov detector is planned in the FS as a later upgrade option. The detector will be a dual radiator Ring Imaging Cherenkov Detector (RICH) similar to the RICH detector used at HERMES [30]. The RICH enables the  $K/\pi$  and  $K/p$  separation. This detector measures directly the Cherenkov angle without internal reflection to get the velocity of the particle.

**Time-of-Flight Detector** For slow particles below  $\approx 800$  MeV/c, a Time-of-Flight (TOF) detector will be installed right outside the barrel DIRC to provide velocity information. Since there will be no start detector, the TOF detector gives relative track timing only. The TOF detector consists of 5,760 Scintillator Tiles (SciTil) with a size of  $28.5 \times 28.5$  mm<sup>2</sup>. One SciTil is readout by two silicon photomultipliers. The TOF can be enhanced with additional 1,000 tiles in the forward direction right before the disk-DIRC. The time resolution of the TOF detector system will be about 100 ps.

In the FS it is planned to build a wall of slabs of plastic scintillators, located 7 m away from the interaction point right behind the forward RICH detector and in front of the forward EMC. These plastic scintillators will be readout on both sides with fast phototubes. The expected time resolution is about 50 ps [27].

### 3. The $\bar{P}$ ANDA Experiment

**Muon Detector** The muon detectors surround the EMC and are integrated in the flux-return yoke of the solenoid magnet. The magnet return yoke is segmented to provide space for the muon detectors and acts to filter out all particles except muons. Due to this, muon signals can be clearly determined, which is important for certain physics channels. The sensitive detector layers are arranged alternating with iron layers, consisting of Mini Drift Tubes (MDT). In total, more than 3,000 MDT will be installed.

#### 3.3.4. Calorimeter System

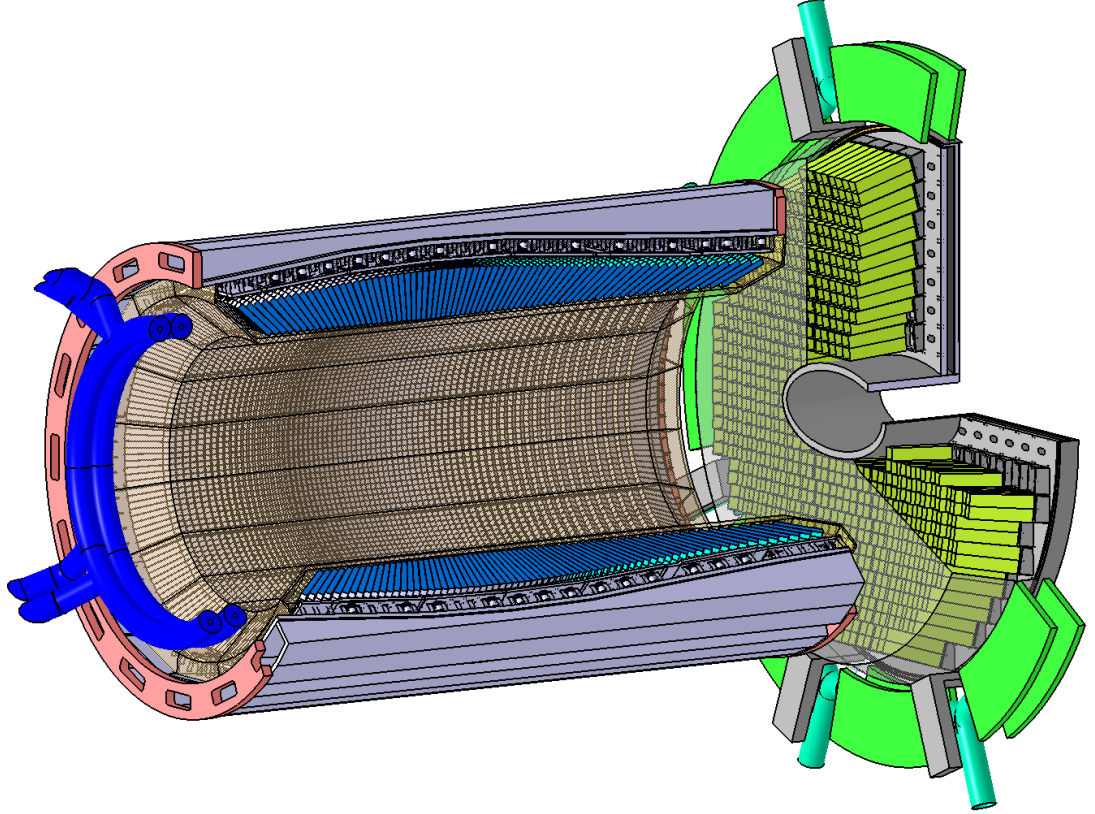


Figure 3.6.: Schematic drawing of the barrel and forward end-cap EMC with support and cooling structures. Picture taken from Ref. [31].

The energy of charged and neutral particles will be measured by an Electromagnetic Calorimeter (EMC). The calorimeter covers a wide range of photon energies with a high resolution. Lead tungstate ( $\text{PbWO}_4$ , short: PWO) was chosen as the scintillating material due to its reasonably high light output, good energy resolution, high radiation hardness, fast response time and high density leading to a compact setup of the EMC. The barrel part of the EMC consists of 11,360 crystals with a length of 200 mm ( $\approx 22$  radiation lengths) each, oriented to point close to the interaction point. Large Area

Avalanche Photo-Diodes (LAAPDs) are planned for the readout of the crystals. The operating temperature of the EMC is  $-25^{\circ}\text{C}$  to increase the light output of the crystals. Almost the full solid angle will be covered by upstream and downstream end-caps. The upstream end-cap will be made of 592 crystals in a planar arrangement and readout by LAAPDs. In the forward direction, the end-cap consists of 3,856 crystals. Due to the higher particle flux in the forward region, the inner 20% of the forward crystals will be readout with Vacuum Photo-Tetrodes (VPTT), the outer 80% will be readout with LAAPDs [32]. The tetrodes have a high radiation tolerance and are thus capable to withstand the higher flux in the region near to the beam axis.

In the FS of  $\bar{\text{PANDA}}$ , a shashlik-type sampling calorimeter will be installed. Shashlik calorimeters consist of alternating layers of absorber (high Z material, e.g. lead) and scintillator material. Light guide material penetrates the different layers perpendicular to the layers (like a shashlik spit). The light guides will be readout with Photomultiplier Tubes (PMT) modules. The calorimeter will consist of 1404 modules with surface areas of  $55 \times 55 \text{ mm}^2$ , covering a total area of  $2.97 \times 1.43 \text{ m}^2$ , and a total length of 68.4 cm [33].

Further information on the EMC can be found in the EMC Technical Design Report [31].

#### 3.3.5. Event Filter

The signature of physical interesting events in  $\bar{\text{PANDA}}$  is very similar to the huge background of events. Therefore, simple selection criteria are not possible. This distinguishes  $\bar{\text{PANDA}}$  from most other particle physics experiments in which just a few fast detectors are readout and analyzed to decide if a physically interesting event has happened. In that case, a trigger signal is sent to the remaining detectors to record their data of this event for further analysis. In contrast  $\bar{\text{PANDA}}$  follows a trigger-less readout concept: data from all detectors is readout in a continuous stream. All hits get a precise time-stamp and are transported to compute nodes. The compute nodes calculate tracks using the continuous stream of hits and combines them to event candidates. After this *event building*, the physical interesting events are selected and saved for further analysis.

## 3.4. The Micro Vertex Detector

The MVD is the innermost detector of the  $\bar{\text{PANDA}}$  experiment and has thus the smallest distance to the IP. It is made completely out of semiconductor sensors, readout by specialized Application Specific Integrated Circuits (ASICs).

The following section presents a description of the MVD. For further detailed information please consult the MVD Technical Design Report [27].

### 3.4.1. Physics Motivation

The main task of the MVD is the precise tracking of charged particles to determine the point (vertex) where they were produced. This information is primarily used to identify (tag) particles which travel a short distance from the primary interaction point before

### 3. The $\overline{\text{PANDA}}$ Experiment

Particle	Lifetime	decay length $c\tau$	main decay channels (fraction)
$K_S^0$	89.53(5) ps	2.6842 cm	$\pi^+\pi^- ((69.20 \pm 0.05)\%)$
$D^\pm$	1.040(7) ps	311.8 $\mu\text{m}$	$e^+$ semileptonic + c.c. $((16.07 \pm 0.30)\%)$ $K^-$ anything + c.c. $((25.7 \pm 1.4)\%)$ $K^+$ anything + c.c. $((5.9 \pm 0.8)\%)$ $\overline{K}^0$ anything + $K^0$ anything $((61 \pm 5)\%)$ e.g. $K^-\pi^+\pi^+$ + c.c. $((9.4 \pm 0.4)\%)$ $\overline{K}^0\pi^+\pi^+\pi^+$ + c.c. $((6.8 \pm 0.29)\%)$
$D^0$	410.1(15) fs	122.9 $\mu\text{m}$	$e^+$ anything + c.c. $((6.49 \pm 0.11)\%)$ $\mu^+$ anything + c.c. $((6.7 \pm 0.6)\%)$ $K^-$ anything + c.c. $((54.7 \pm 2.8)\%)$ $K^+$ anything + c.c. $((3.4 \pm 0.4)\%)$ $\overline{K}^0$ anything + $K^0$ anything $((47 \pm 4)\%)$ e.g. $K_S^0K^+K^- ((4.65 \pm 0.3)\%)$ $K^-\pi^+\pi^+\pi^-$ + c.c. $((8.09^{+0.21}_{-0.18}\%))$ $K_S^0\pi^+\pi^-\pi^0$ + c.c. $((5.4 \pm 0.6)\%)$
$D_s^\pm$	500(7) fs	149.9 $\mu\text{m}$	$e^+$ semileptonic/c.c. $((6.5 \pm 0.4)\%)$ $K^-$ anything + c.c. $((18.7 \pm 0.5)\%)$ $K^+$ anything + c.c. $((28.8 \pm 0.7)\%)$ e.g. $K^+K^-\pi^+$ + c.c. $((5.50 \pm 0.27)\%)$
$\Lambda$	263.1(20) ps	7.89 cm	$p\pi^- ((63.9 \pm 0.5)\%)$
$\Sigma^+$	80.18(26) ps	2.404 cm	$p\pi^0 ((51.57 \pm 0.30)\%)$ $n\pi^+ ((48.31 \pm 0.30)\%)$
$\Sigma$	147.9(11) ps	4.434 cm	$n\pi^- ((99.848 \pm 0.005)\%)$
$\Xi^-$	163.9(15) ps	4.91 cm	$\Lambda\pi^- ((99.887 \pm 0.035)\%)$
$\Omega^-$	82.1(11) ps	2.461 cm	$\Lambda K^- ((67.8 \pm 0.7)\%)$ $\Xi^0\pi^- ((23.6 \pm 0.7)\%)$ $\Xi^-\pi^0 ((8.6 \pm 0.4)\%)$

Table 3.1.: Strange and charmed particles that can be identified in  $\overline{\text{PANDA}}$  by their delayed decay. Table taken from Ref. [27]. The abbreviation "c.c." stands for charge conjugated.

they decay into secondary particles. The most challenging particles to identify with this method inside  $\overline{\text{PANDA}}$  are D mesons with a decay length  $c\tau$  of 123  $\mu\text{m}$  ( $D^0$ ) and 312  $\mu\text{m}$  ( $D^\pm$ ). This identification is essential for a wide range of physics studies at  $\overline{\text{PANDA}}$ , like the search for and precise measurement of open and hidden charm states. Furthermore, various strange particles (like  $\Lambda$ ) can be identified by the MVD if they decay in the volume enclosed in the MVD. A corresponding list of particles can be found in Table 3.1 together with their decay information. In addition, the momentum resolution of the central tracker system is significantly improved by the precise track points generated by the MVD.

#### 3.4.2. Requirements to the MVD Design

The  $\overline{\text{PANDA}}$  collaboration has developed a wide and ambitious physics program (see Chapter 2.3). For this the following requirements to the design of the MVD can be summarized.

**Spatial Resolution** The main task of the MVD is tracking of charged particle tracks and the determination of the decay point (vertex) of long lived particles. The vertex resolution shall be better than 100  $\mu\text{m}$  to resolve displaced decay vertices of open-charm states such as  $D_0$  ( $c\tau=123 \mu\text{m}$ ) or  $D^\pm$  ( $c\tau=312 \mu\text{m}$ ), considering their mean lab velocity of  $\beta\gamma \approx 2$

**Time Resolution** Due to the trigger-less readout concept of  $\overline{\text{PANDA}}$ , all hits in the detector have to be tagged with a timestamp value. This time information is necessary in the reconstruction stage to combine the informations of all sub-detectors into physics events. The MVD has a special role in this context as it is the innermost detector and can deliver a time information for the slower STT. The goal is to achieve a time resolution better than 10 ns.

**Material Budget** The MVD is the innermost detector, any effects by the MVD on the particle trajectories will reduce the resolution of the other detectors. Due to this, the material budget has to stay as low as possible to minimize unwanted effects like multiple scattering and photon conversion.

The total material budget of the whole MVD shall stay below 10% of a radiation length. Therefore, thinned sensors are developed and low Z materials are used for support structures, cables, and the cooling pipes.

**Radiation Hardness** The MVD has to withstand a high radiation environment due to its proximity to the interaction point and the high event rates, especially in the forward region. The expected radiation dose has been calculated to be  $10^{14} \text{ n}_{1\text{MeV eq}}\text{cm}^{-2}$ , given in terms of 1 MeV neutron equivalent particles per square centimeter [34], which is the expected fluence for the first 10 years of  $\overline{\text{PANDA}}$  operation.

### 3. The $\bar{P}$ ANDA Experiment

#### 3.4.3. Layout

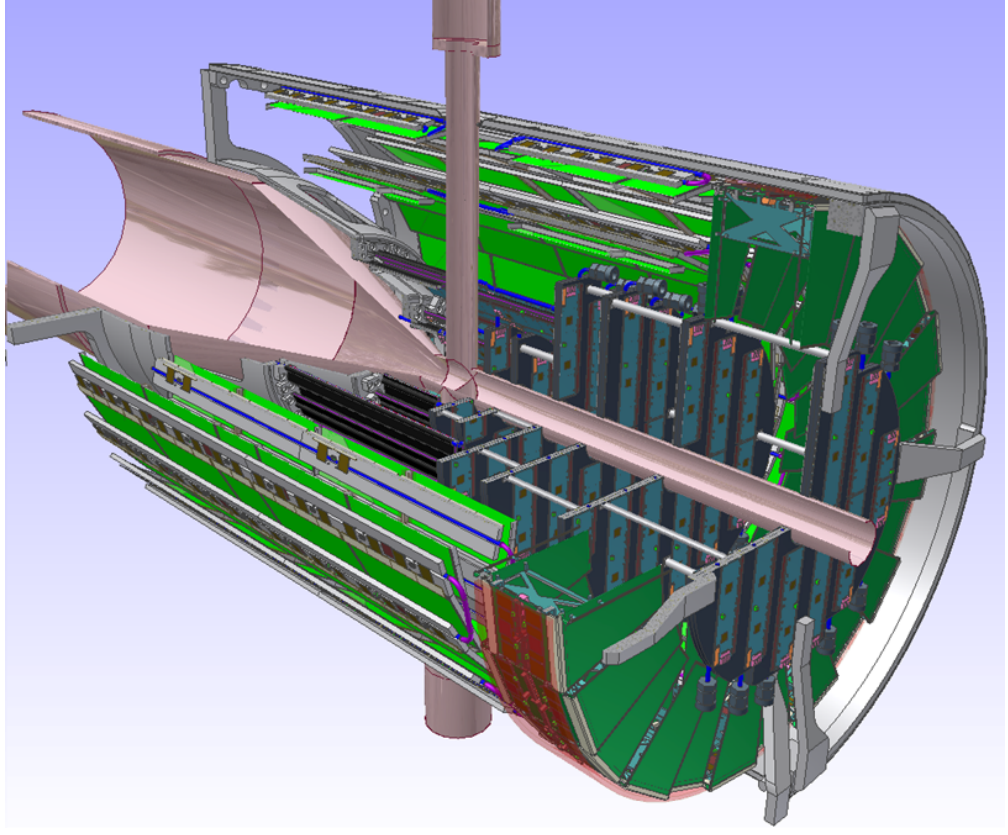


Figure 3.7.: Technical drawing of the MVD with support structure, cooling, and beam pipe. The antiproton beam enters from the left. Picture taken from Ref. [27].

The MVD was designed to perform stand-alone tracking. Tracking algorithms need at least four hit points for tracking. Due to this, the detector consists of four barrel layers and six disk layers, which provides a sufficient number of hits for particles created inside the MVD. The barrel layers cover a polar angle range of  $40^\circ$  to  $150^\circ$ , while the disks cover a polar angle range from  $3^\circ$  to  $40^\circ$ . The MVD has a maximum radius of 15 cm. The innermost barrel layer is located at a radius of 2.5 cm. To achieve the required vertex resolution, it is important to have sensitive detector layers as close as possible to the decay point. A technical drawing of the MVD, together with beam pipe, support structure and cooling can be seen in Figure 3.7. The total length of the active components of the MVD is 46 cm.

The innermost two barrel layers consist of semiconductor pixel detectors. Close to the interaction point pixel detectors are used since they can withstand the high radiation environment and can handle high densities of particle tracks. Pixel detectors deliver



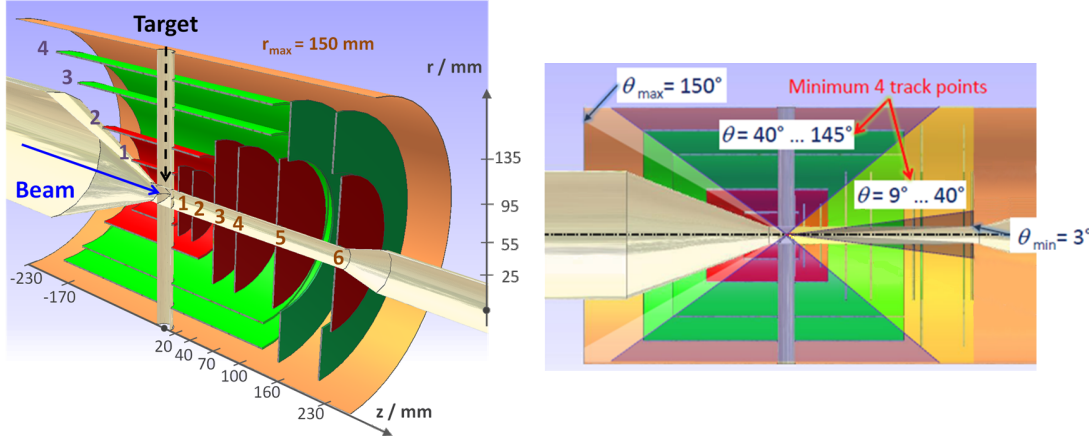


Figure 3.8.: Schematic overview of the MVD detector. Red structures indicate pixel detectors, green structures indicate strip detectors. Yellow is the outer boundary of the MVD. Picture taken from Ref. [27].

a two-dimensional spatial coordinate, a precise time stamp and information about the deposited energy. The outer two barrel layers consist of semiconductor strip detectors. Strip detectors deliver a good spatial resolution with fewer readout channels and less material compared to pixel detectors. But due to the double sided setup of the strips, ghost hits are created which have to be removed. The first four disks consist of pixel detectors, the last two disks have pixel sensors in the center and strip sensor in the outer part. Summed up, there are more than 10 million pixel channels and 200,000 strip channels to be readout in the MVD.

The MVD will operate at a temperature of about 30 °C at atmospheric pressure. The pixel sensor modules have a rectangular shape with four different lengths. They can house two to six front-end ASICs in a row (see Figure 3.9, top left). The strip sensor modules have two different shapes, rectangular and wedge-like. The rectangular sensors come in two sizes, readout by  $2 \times 2$  or  $2 \times 4$  readout chips and will be used in the barrel part. The wedge sensor will be readout by eight front-end chips each and will be used in the forward disks.

#### 3.4.4. Silicon Detectors

Semiconductor sensors are a well tested and frequently used technology to detect charged particles. To create an electron-hole pair in silicon, an average energy of 3.6 eV is necessary. This value is quite low, compared to other detectors like gaseous detectors, where energies between 20-30 eV are needed. This leads to comparably high signals even with thin silicon layers. The MVD will be equipped with hybrid pixel sensors and double-sided strip sensors, as described below:

### 3. The $\bar{\text{PANDA}}$ Experiment

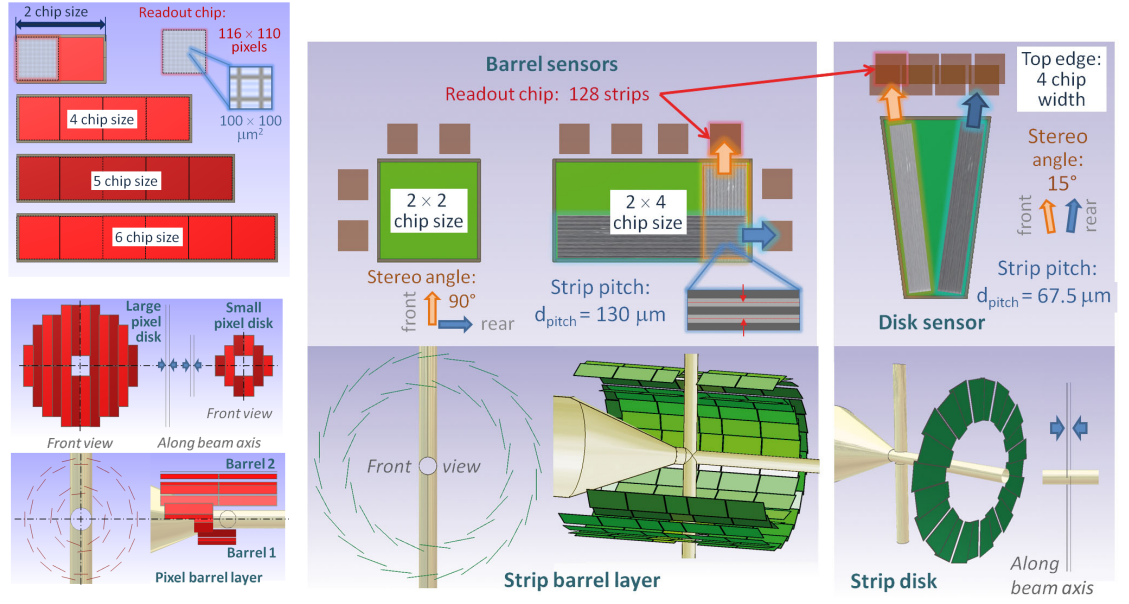


Figure 3.9.: Schematic overview of the sensor module sizes of the MVD. Left: Pixel modules. Center and right: Strip modules [27].

#### Hybrid Pixel Detectors

Hybrid pixel sensors are widely used in particle physics experiments, e.g. for all experiments at the Large Hadron Collider (LHC). Figure 3.10 shows a profile of a pixel sensor with readout electronic, support structure, and cooling. The sensors are segmented in two dimensions and are connected via small metal balls (“bump bonds”) to the readout electronics. The readout electronics is attached to the support structure which is connected to the cooling of the MVD.

Epitaxial sensors are under investigation as a sensor technique. Epitaxy describes a special method of crystal growing, where the silicon crystals grow on a Czochralski substrate. The epitaxial layer can have different thicknesses. For  $\bar{\text{PANDA}}$ , a thickness of 100 μm has been chosen. After growing, the Czochralski substrate is thinned down to about 20 μm. Epitaxial sensors have good radiation hardness and show no type inversion after irradiation. The front-end readout ASIC of the pixel part (ToPix) will be explained in detail in Chapter 5.

#### Double-Sided Strip Detectors

The strip part of the detector will consist of Double-sided Silicon Strip Detectors (DSSD). In contrast to pixel sensors, strip sensors are segmented in just one dimension. To reconstruct a two dimensional hit point, it is necessary to combine the information of two different measurements with different orientations. For a double-sided strip sensor, this is achieved by a segmentation of the top and the bottom side of the sensor with a



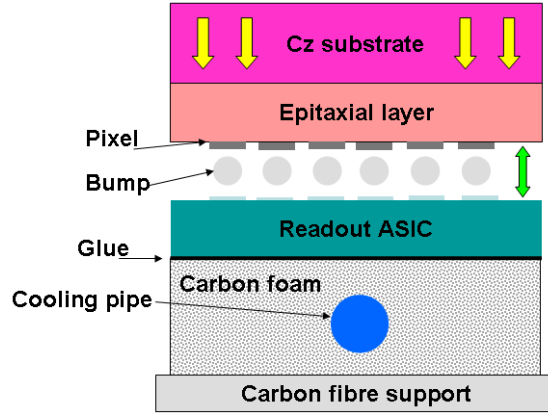


Figure 3.10.: Schematic profile of a hybrid pixel sensor with readout, support structure and cooling. Picture taken from Ref. [27].

tilt angle between the two orientations (stereo angle). For the barrel strip sensors, the stereo angle is  $90^\circ$ , for the wedge-shape sensors, the stereo angle is  $15^\circ$ .

For the readout of the strip sensors a new ASIC is under development. The  $\bar{\text{P}}\text{ANDA}$  Strip ASIC (PASTA) is a free running and low power ASIC which uses the Time-over-Threshold (ToT) method for charge determination. The ASIC is based on Time-of-Flight Positron Emission Tomography (TOFPET) ASIC, a readout ASIC for silicon photomultipliers for the Endoscopic TOFPET & Ultrasound (EndoTOFPED-US) experiment [35]. The first PASTA prototype is expected to be ready for submission in 2014.

Due to the much lower number of strip channels, the material budget is smaller. But due to the net like structure, ghost hits occur. If two particles hit a strip module at the same time, two x and two y strips will fire. These four firing strips create four intersections, which will lead to four possible hit points, two real ones and two ghost hits. By comparing the measured energy in the strip hits on the top with the ones from the bottom and by taking hit points from other detector layers into account the ambiguities in the strip assignment can be resolved at the hit densities expected at  $\bar{\text{P}}\text{ANDA}$ .

### 3.4.5. Additional Sensors at Small Polar Angles

The MVD is optimized to measure D mesons which typically decay much closer than 1 mm from the point where they are produced. However, for long lived particles like hyperons, the length of the MVD is not optimal. The decay length of hyperons in the lab frame is typically several to tens of centimeters (see Table 3.1). Therefore, they often decay in an outer part or even outside the MVD with few or no hits detected in the MVD.

To improve the reconstruction ability and track quality of these event types, plans are explored to install additional silicon sensor disks in the empty space between the last MVD disk and the GEM stations. Two disks are foreseen (so-called  $\Lambda$ -disks) at distances of about 40 cm and 60 cm with respect to the interaction point. An optimization of the

### *3. The $\overline{P}$ ANDA Experiment*

disk position is shown in Chapter 6. The disks should consist completely of double sided silicon strip sensors.

In addition these disks would increase the angular coverage of the MVD for particles at low polar angles.

## 4. Jülich Digital Readout System

---

*PLZ, UPS und DPD*  
*BMZ, BPM und XTC*  
*EMI, CBS und BMG*  
*ADAC, DLRG - ojemine*  
Die Fantastischen Vier - MFG (Mit freundlichen Grüßen)

---

*Note: Section 4.1 and 4.2 have already been published as an appendix in the MVD Technical Design Report [27].*

### 4.1. Overview

The evaluation of prototypes and detector components is very important for the development of the Micro Vertex Detector (MVD). Different prototypes of the pixel front-end chip Torino Pixel (ToPix) must be tested and characterized under similar conditions to improve the development.

A suitable readout system is necessary to control these Devices under Test (DUT) and to save the collected data. To have similar conditions for different prototypes and development stages, a modular concept of a readout system is required, which can be adapted in a simple way to the specific interfaces of different types of electronics. At the same time the system must provide a high performance to allow the evaluation of single front-end chips as well as fully assembled modules. The possibility to implement routines for online data processing is also desirable.

The Jülich Digital Readout System (JDRS) has been developed to meet all these requirements for the development of the MVD.

The JDRS is a compact and powerful tabletop setup which allows new detector components to be quickly tested. The setup consists of (see Figure 4.1):

- Digital readout board
- Field Programmable Gate Array (FPGA) Firmware
- MVD Readout Framework (MRF) Software with Graphical User Interface (GUI)
- Readout PC
- DUT

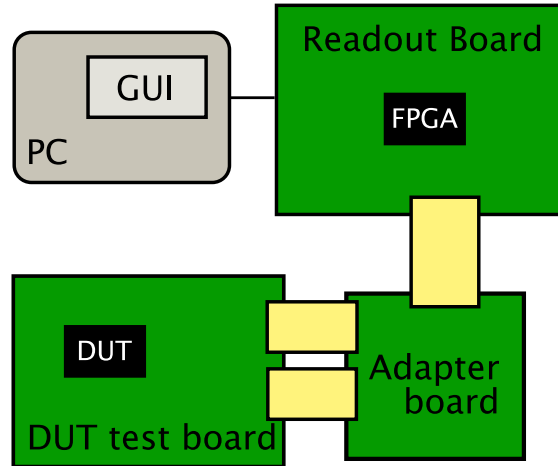


Figure 4.1.: Schematic drawing of the JDRS.

- Adapter board for the Printed Circuit Board (PCB)

The central component is the FPGA based readout board, which is connected to the readout PC via an optical connection and receives commands from the user and sends data to the PC for further processing. The corresponding software infrastructure is implemented within the MRF. The prototype is controlled by the user with a GUI. On the other side the readout board is connected to the DUT on its test board. If necessary an intermediate adapter board converts the DUT signal interface to the interface of the readout board.

## 4.2. Basic Concepts

In the following the basic concept of the JDRS is outlined and the individual components comprising the modular design is introduced.

**Modularity** Complex procedures are broken down into simpler subtasks which are each handled by individual modules. To add or change functionality it is only necessary to add a new module or to change an existing one limiting required changes to individual modules which significantly improves stability and simplifies debugging. The modules can also easily be reused when already implemented subtasks reappear in a different context. This modular concept makes the readout system very flexible and easy to maintain.

**Communication Layers** In addition to the modular setup the MRF follows the principle of different abstraction layers based on the Open Systems Interconnection (OSI) model. Following this principle, the MRF defines four communication layers (see Figure 4.2). Every hardware component of the readout system corresponds to a specific communication layer and has a representation in software or firmware. Each layer uses the

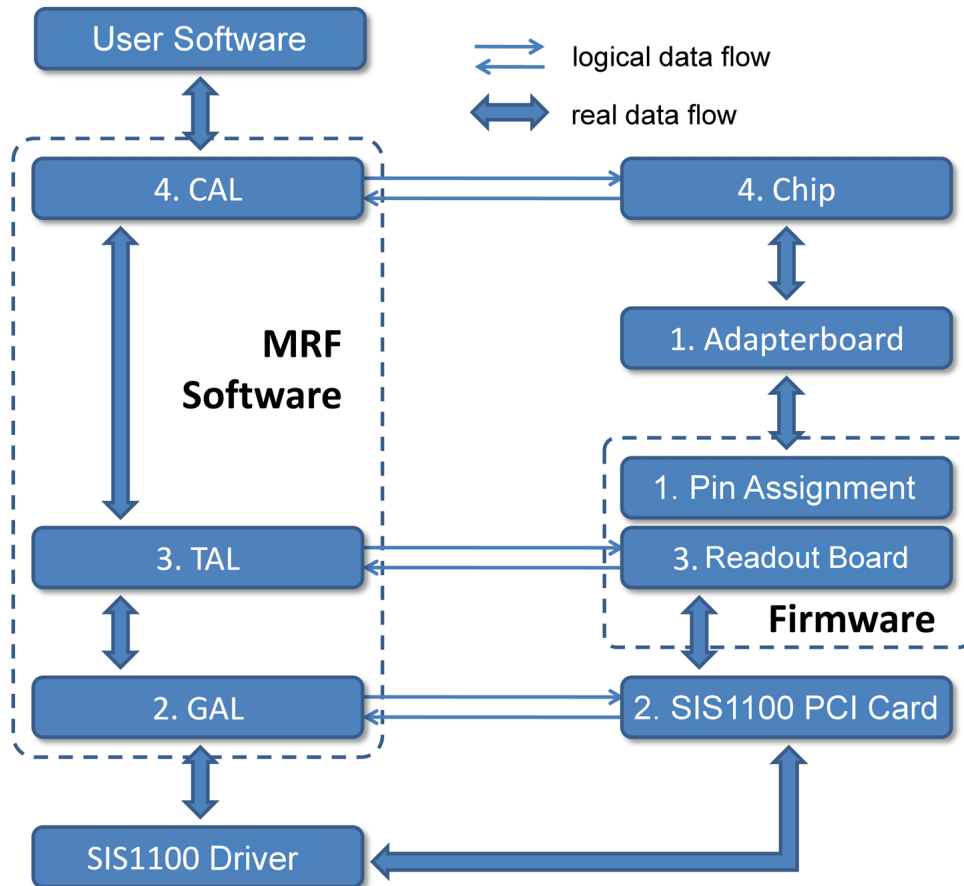


Figure 4.2.: Schematic overview of the JDRS. Every hardware component of the system corresponds to one of the four defined communication layers and has a representation in software or firmware. Figure adapted from Ref. [36].

#### 4. Jülich Digital Readout System

functionality of the layer directly below, without knowledge of the exact implementation, and provides a well-defined set of functions to the layer above. Due to this approach layers can be replaced without changes to the other layers. The MRF defines the following layers:

- Layer 1 - Physical Layer: Establishing of signal connections
- Layer 2 - Generic Access Layer (GAL): Communication with readout board via SIS1100 optical connection.
- Layer 3 - Transport Access Layer (TAL): Access to functionality of the readout board
- Layer 4 - Chip Access Layer (CAL): Communication with DUT

In the following, the most important components of the readout system are listed and it is indicated to which communication layer they belong.

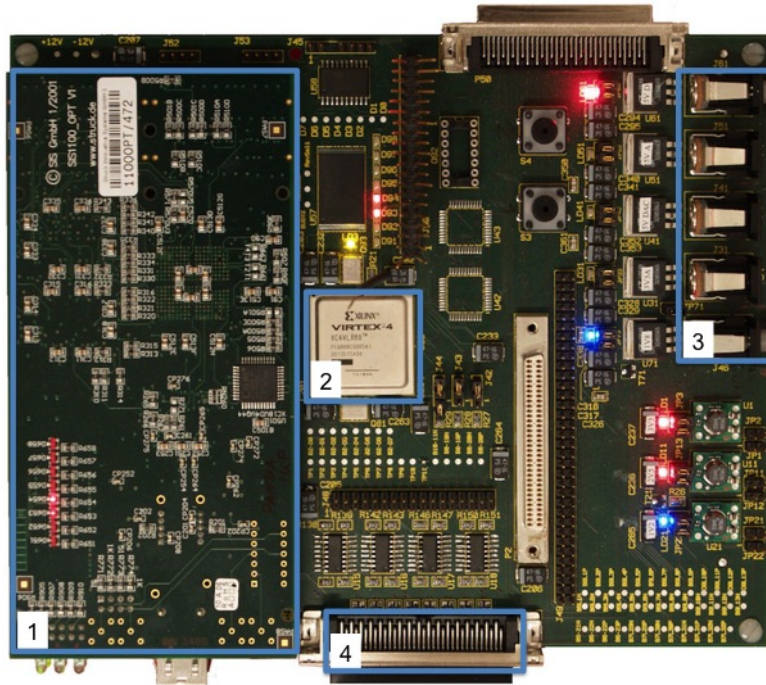


Figure 4.3.: The digital readout board A of the readout system: 1) SIS1100 CMC 2) Xilinx Virtex-4 FPGA 3) power connectors 4) 68-pin connector to adapter board. Picture taken from Ref. [36].

**Adapter Board, Layer 1** The adapter board establishes the signal connection between the readout board and the DUT. Since the interface of the DUT testboard is usually non-standard, a specific adapter board needs to be developed for each type of DUT.

**Digital Readout Board with Firmware, Layer 1 and 3** The FPGA based digital readout board is the main hardware component of the system. The Very High Speed Integrated Circuit Hardware Description Language (VHDL) based firmware configures the FPGA with the implemented functionality (layer 3) and the pin assignment (layer 1) of the DUT interface.

**Optical connection to readout board, Layer 2** The data transport from the digital readout board to the PC is done via a 1 Gbit/s optical connection (SIS1100, [37]). On the PC side a SIS1100 PCI card is installed. The SIS1100 interface of the digital readout board is implemented as a SIS1100 Common Mezzanine Card (CMC) (Board A) or as a combination of a SIS1100 FPGA core and an Small Form Factor Pluggable (SFP) optical gigabit transceiver (Board B).

**MRF Readout Software, Layer 2, 3, 4** The MRF is the main software component of the readout system. Here the communication layers 2, 3 and 4 are defined (See Chapter 4.2.4). These layers establish connections to the DUT and the firmware of the digital readout board.

**MRF-Control: Graphic User Interface** A GUI has been developed in C++ based on the Qt framework [38] for easy control by the user. Full configuration and readout routines are available. Measured data can be easily saved to disk. The settings of the DUT and the setup can be saved and reload in special configuration files.

#### 4.2.1. Digital Readout Board A

The first digital readout board (see Figure 4.3) is a custom development and production of the Zentralinstitut für Engineering, Elektronik und Analytik (ZEA-2) of the Forschungszentrum Jülich [39]. A Xilinx Virtex-4 FPGA, configured with the firmware, takes control of the DUT communication and of the data buffering. The readout board is connected to the PC via a 1 Gbit/s optical link. An optical fiber has the advantage of galvanic separation of the PC from the readout board. The SIS1100 protocol is used to transfer the data from the buffer to the PC. A CMC with SIS1100 functionality is connected to the readout board to implement the SIS1100 protocol. The adapter board is connected by a 68-pin flat band cable.

The main features and external interfaces of the digital readout board are:

- Xilinx Virtex-4 XC4VLX60 FPGA
- 32 MB Xilinx Platform Flash for firmware storage
- 64 free configurable FPGA input/output pads
- 16 Low Voltage Differential Signal (LVDS) inputs
- 16 LVDS outputs

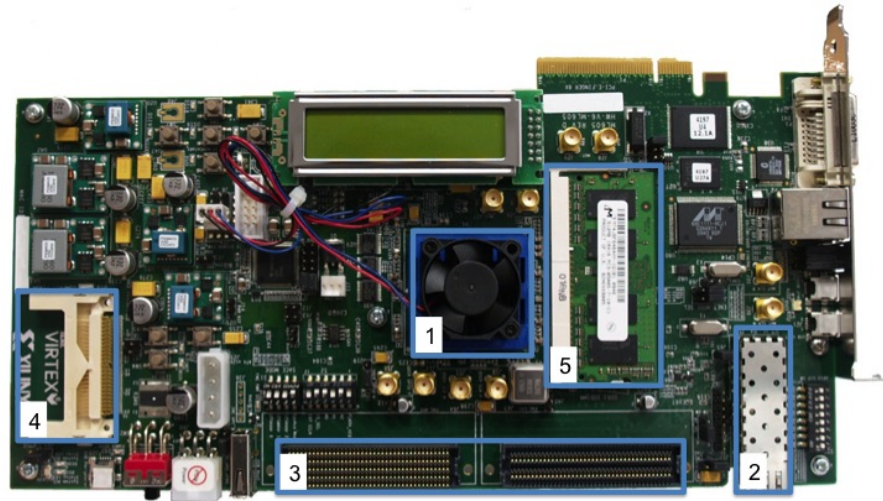


Figure 4.4.: The digital readout board B ML605 from Xilinx: 1) Virtex-6 2) SFP port 3) FMC connectors to adapter board 4) Compact flash slot 5) DDR3 RAM.

- SIS1100 based optical connection to PC with 1 Gbit/s
- 50 MHz single ended clock

##### 4.2.2. Digital Readout Board B

To meet the requirements of an upcoming full size ToPix prototype and online analysis an upgrade of the digital readout board was developed. The ML605 evaluation board is a commercial product by Xilinx and is comparatively cheap and an off-the-shelf product. It contains a DDR3 RAM slot for data storage and a Virtex-6 FPGA (see Figure 4.4). The connection to the PC is established via a SFP gigabit transceiver. The SIS1100 protocol is implemented as an IP core into the firmware.

Specification of the ML605 are:

- Xilinx Virtex-6 XC6VLX240T FPGA
- DDR3 SODIMM memory (expandable)
- SFP Module connector
- FMC connectors for Standard Mezzanine Cards
- LC-Display
- Compact Flash Card for firmware storage
- 66 MHz single ended and 200 MHz differential clock



### 4.2.3. Firmware

The FPGA on the digital readout board is configured with a firmware which implements the desired functionality and configures the external interfaces.

The firmware for both readout boards is written in VHDL, a hardware description language, and then synthesized with the Xilinx development tools, i.e. translated to a format which is understandable by the FPGA.

The firmware is divided into modules which handle different subtasks concerning the DUT, the board functionality or the communication. All modules are connected to the register manager which is itself connected to the SIS1100 interface (see Figure 4.5). Data which arrive via the SIS1100 are formatted in address-data pairs. The register manager will distribute the data depending on the address to the concerning modules. If data should be read from the board, the register manager will take the data from the module indicated by its address.

This modular design makes it easy to adapt the firmware to a different readout board or a different DUT respectively.

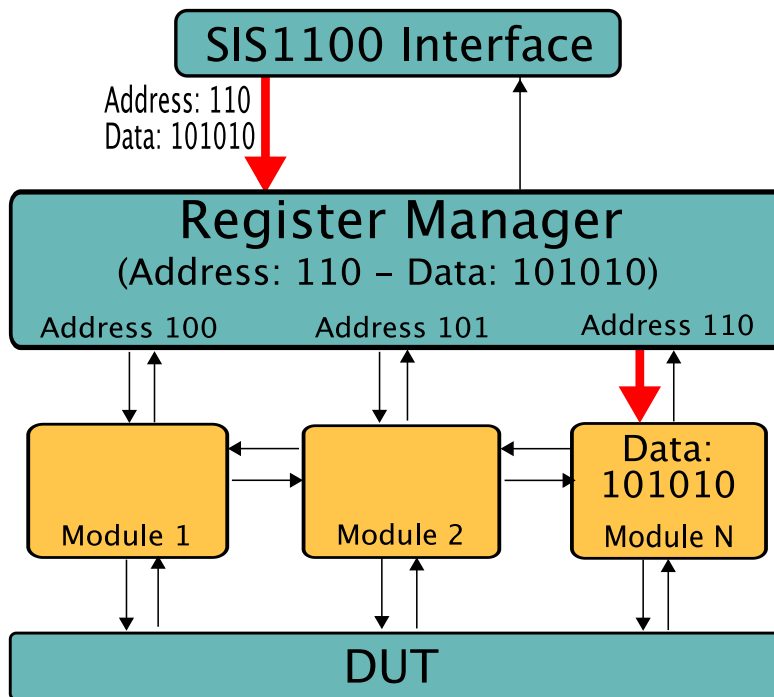


Figure 4.5.: Schematic firmware setup. Data delivered via SIS1100 will be distributed to the modules indicated by the address. The red arrows indicate the path the data packet will take for the example given.

### 4.2.4. MVD Readout Framework

The MRF software framework implements the upper three levels of the communication model. The MRF is written in C++ and has no external dependencies except the Standard Template Library (STL) to avoid conflicts with other libraries. This makes the MRF software a decoupled package which can be used in any environment.

For every communication layer a basic set of commands is implemented to provide the data transport between the layers. In addition, specific commands are implemented for the hardware used.

**GAL: Generic Access Layer** The generic access layer provides the basic functionality for communication with the digital readout board. The *read* and *write* commands provide a basic reading and writing to registers over an open connection.

All more complex commands of the upper layers are implemented using these basic functions.

More powerful functionality is implemented by including the SIS1100 driver into the GAL. The SIS1100 driver provides Direct Memory Access (DMA) transfer. Data from a buffer on the readout board can be send directly to a data container structure in the MRF software. In addition the readout board is able to send interrupt signals to the PC to indicate certain conditions such as data from the DUT being available. A transfer to the PC can then be triggered automatically.

**TAL: Transport Access Layer** The transport access layer provides access to the functionality of the firmware. Certain basic functionality is available for both versions of the digital readout board such as the online configuration of the clock generator and the controlling of status LEDs.

**CAL: Chip Access Layer** The Chip Access Layer implements the functionality of the DUT and needs to be adapted to the specific hardware e.g. configuration of the chip or the readout sequence. Different versions have been made for the control of the ATLAS FE-I3 [40], the ToPix 2 and the ToPix 3. The complete readout and all testing procedures are available for both chips.

## 4.3. Adaption of the Readout System to the ToPix 3

The JDRS has been used to readout the ToPix 3. Software and firmware have been adapted and extended to match to the ToPix 3 interface. The CAL layer classes of the ToPix 2 could not be reused due to modifications of the ToPix 3 readout interface and different components in the ASIC test board.

**Connector** The ToPix readout board now has a Low Pin Count FPGA Mezzanine Card (LPC-FMC) connector which matches directly to a connector on the ML605. An

### 4.3. Adaption of the Readout System to the ToPix 3

intermediate adapter board is no longer necessary. The signal standard of the ToPix Test Board interface is LVDS, which is directly supported by the ML605.

**Transport Access Layer** Instead of one 8-channel Digital to Analog Converter (DAC) there are two 4-channel DACs implemented on the ToPix 3 test board. The chips are in a daisy chain configuration, which means that the shift register output of the first DAC (DAC 1) is connected with the shift register input of the second DAC (DAC 2).

A shift register has a serial input. The data word is pushed consecutively into the shift register. If more bits are pushed into the register than its length, the first bit is pushed out to the shift register output. Via the daisy chain configuration it is possible to configure both DACs via one configuration line. The data classes to handle this special configuration have been implemented into the MRF Software.

**Chip Access Layer** The end-of-column logic of the ToPix 3 has been expanded, which simplifies the communication with the chip. Basically there are two de-serializer used for the configuration and the data readout, respectively.

The first deserializer is responsible for the readout of the ToPix 3 data. In the data taking mode of the ToPix 3 the 32-bit wide hit data are automatically send out off the chip. The data transmission is indicated by the ToPix 3 by activating the data enable signal. The readout module is activated by this signal, deserializes the transmitted word and fills it into the output First In First Out (FIFO) buffer.

The configuration module is a combination of serializer and deserializer to send and receive configuration data to and from the ToPix 3. The configuration module is connected to a shift register of the ToPix 3. The received configuration information is loaded by the ToPix 3 from its shift register into internal registers for processing, the requested configuration data is put into its shift register by the ToPix 3. The data can then be readout by pushing new data into the ToPix 3 shift register. The configuration module takes care of sending the serialized data and simultaneous receiving and deserialization of the data read back.

To enable a continuous readout of hits from all four double columns of the ToPix 3, a module takes care of the right column changing procedure. The automatic sending of hit data by the ToPix 3 has to be stopped by raising the `DATA_WAIT` signal. This state has to hold for at least 3 clock cycles, to ensure the signal has been processed by the ToPix 3. The system waits to finish ongoing data transmission. After the data transmission has finished, the system checks if a new data transmission starts, which has been registered for transmission before `DATA_WAIT` was processed. After this procedure the column can be safely changed.

**Data Container** For the configuration and the readout of the ToPix 3 new data containers have been implemented, to represent the bit allocation specific for the ToPix 3. Tables 4.1, 4.2 and 4.3 show bit allocation for the Chip Configuration Register (CCR) and 4.4 show the bit allocation for the Pixel Configuration Local Register (PCLR) within the data stream.

#### 4. Jülich Digital Readout System

Bit	Description
11:9	Freeze stop (3 Most Significant Bits (MSBs) of the time stamp current)
8:5	SLVS current control
4	Activate driver pre-emphasis
3	Readout cycle half speed
2	Counter enable
1	Counter Mode
0	Read leading edge only

Table 4.1.: Bit definition of CCR0 [41].

Bit	Description
11:6	Not used
5	Analog timeout enable
4	lleak_ctrl2
3	lleak_ctrl1
2	select_pol
1	leak_P
0	leak_N

Table 4.2.: Bit definition of CCR1 [41].

Bit	Description
11:0	Counter stop value

Table 4.3.: Bit definition of CCR2 [41].

Bit	Description
7	Threshold DAC sign
6:3	Threshold DAC
2	Pixel comparator test out enable
1	Pixel test pulse enable
0	Pixel Mask

Table 4.4.: Bit definition of the PCLR [41].

## 4.4. GBT Implementation

In parallel to the tests of the ASIC prototypes, tests of the readout scheme of the final ToPix within  $\overline{\text{PANDA}}$  are ongoing. The GigaBit Transceiver (GBT) project is under development at CERN to transmit digital data with high data rates in a high radiative environment. The following section describes the GBT project and the test of it with the ML605.

### 4.4.1. The GBT Project

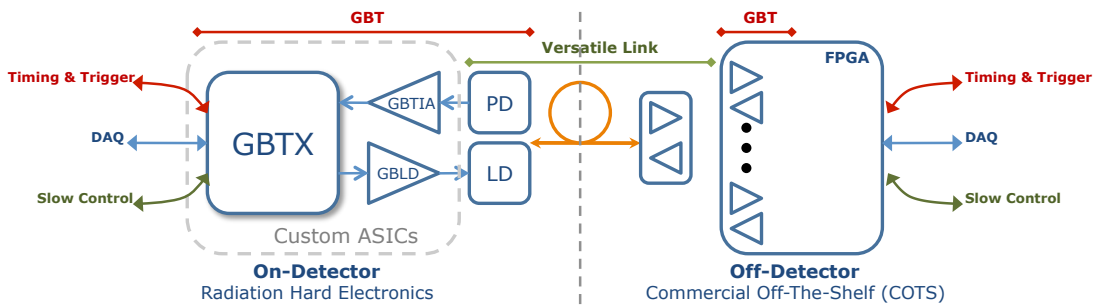


Figure 4.6.: Schematic overview of the GBT and Versatile Link project [42].

The data which is produced in the front-end ASICs in the sub-detectors need to be transmitted to the off-detector processing devices for further processing and permanent storage. To cope with the increasing data rates produced in modern particle detectors an early conversion from electrical to optical signals as close as possible to the front-end electronics is necessary. Therefore, the electronics and data transmission protocols used have to be optimized for operation in a high radiation environment, which prohibits the usage of standard optical components.

To address this problem, the GBT [42] and the Versatile Link [43] project have been started at CERN. These projects are now under investigation for the readout of the MVD front-end ASICs.

The GBT project takes care of the development of radiation tolerant protocols and hardware for the coding and decoding of detector data. The Versatile Link group develops radiation tolerant hardware for the optical transmission of the data.

On the detector site the GBT-X ASICs communicates with the front-ends electrically via the e-link protocol and converts the data received into the GBT line code. This data is then optically transmitted to the counting room where it is decoded by a GBT-FPGA instance running on a commercial FPGA [44]. In addition, timing, trigger and slow control data can be transmitted via the GBT connection.

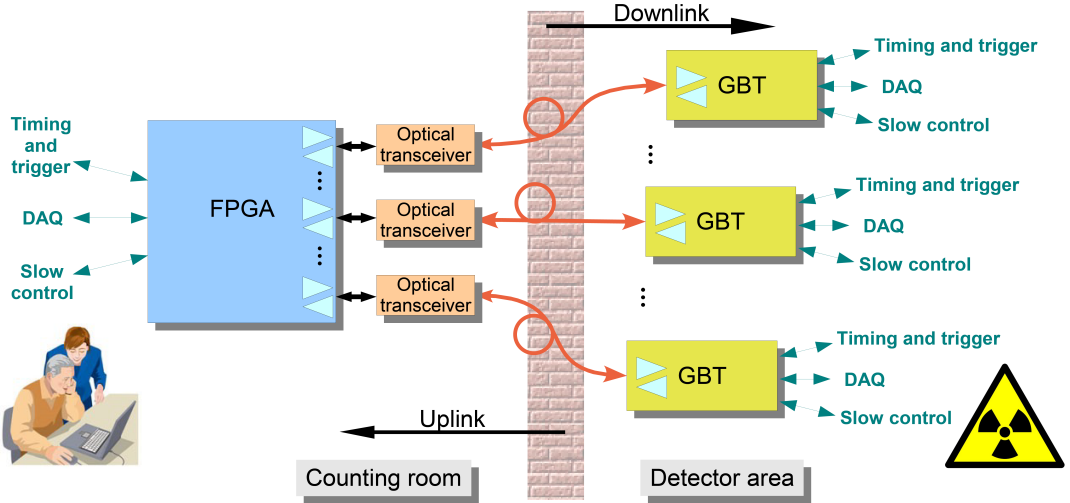


Figure 4.7.: Schematic usage of the GBT-FPGA core within the GBT project [44].

#### 4.4.2. Implementation of the GBT Protocol into the Jülich Digital Readout System

As a first step to implement the GBT data transmission for the readout of the ToPix ASIC the GBT-FPGA module from the GBT-starter kit was adopted to run with the Virtex-6 FPGA of the JDRS. The starter kit contains all necessary modules for GBT coding/decoding and FPGA specific modules for the Virtex-5 for gigabit transmission. The gigabit transceiver module has to be replaced by Virtex-6 specific modules.

The implementation was tested with two ML605 boards, one generating dummy data transmitted via the GBT protocol over coaxial cable to a second ML605 board where it was decoded and compared. The dummy data words are 84-bit wide and consist of four 21-bit counters. A test over 48 hours showed no errors on the transmission. An optical transmission was not possible because the available SFP optical transceiver have a maximum data rate of 4.25 Gbit/s while GBT has a data rate of 4.8 Gbit/s. Due to the clock restrictions on the ML605, the data rate of 5 Gbit/s was even higher. To run the MVD via optical cable on a ML605, Enhanced Small Form Factor Pluggable (SFP+) modules are necessary, which have a maximum data rate of 8 Gbit/s via optical fiber channel. The ML605 is not able to handle SFP+ modules directly. Additional FPGA Mezzanine Card (FMC) daughter cards can extend the ML605 functionality and provide space for SFP+ modules.

The future ToPix 4 prototype will be equipped with the e-link protocol so that a readout via the JDRS or a GBT-X ASIC will be possible.

## 5. The ToPix 3 Front-End ASIC

---

*When the lights turned down, they don't know what they heard  
Strike the match, play it loud, giving love to the world  
Cause we got the fire, fire, fire,  
And we gonna let it burn burn burn burn*

Ellie Goulding - Burn

---

Semiconductor detectors have been used in many particle physics experiments in the last decades.

**Picture Element** (Pixel) detectors are often used if a three dimensional coordinate of charged particles tracks within a high radiation and high rate environment is necessary. Since detectors become more and more specialized to physical questions and experimental setups, thus Application Specific Integrated Circuits (ASICs) are necessary. The following chapter describes the ToPix 3 (Torino Pixel), a reduced size prototype for the Micro Vertex Detector (MVD) pixel front-end electronics and presents measurements characterizing this ASIC.

### 5.1. The ToPix ASIC

#### 5.1.1. ToPix Requirements

ToPix is a custom developed ASIC for the pixel part of the  $\overline{\text{P}}$ ANDA MVD, developed at the Istituto Nazionale di Fisica Nucleare (INFN) in Turin. The ToPix ASIC is a mixed-signal hybrid chip. Mixed-signal means that analog and digital signals are processed on the same chip. Each pixel contains an analog part, where the charge from the sensor is amplified and measured, and a digital part, where the measured charge is digitized, serialized and send out to the Data Acquisition (DAQ) system. Mixed-signal systems have the advantage that the hit information is send digitally, which makes the data transport more robust. Hybrid detector consists of two parts, sensor and readout ASIC, which are connected via small metal balls, so-called bump bonds. Due to the bump bonding technique the readout cell has to match the area of the sensor cell it is connected to.

---

*To ensure the right interpretation of numbers with different bases the following prefix convention is used: binary numbers (base 2) - 0b, decimal numbers (base 10) - 0d, octal numbers (base 8) - 0o , hexagonal numbers (base 16) - 0x.*

*Gray encoded binary values are marked with the subscript 'Gray'.*

## 5. The ToPix 3 Front-End ASIC

Hybrid sensors have the advantage that the sensors and electronics can be separately produced and optimized.

The full size ToPix will have  $116 \times 110$  pixel readout cells with a size of  $(100 \times 100)$   $\mu\text{m}$  each, covering a total active area of  $(11.6 \times 11)$   $\text{mm}^2$ . The operating frequency of the ToPix will be 155.52 MHz. This leads to a time resolution of  $\sim 6.4$  ns.

The ToPix has to work in a high radiation environment. The “hottest” ASIC, meaning the one with the highest radiation has to withstand a Total Ionizing Dose (TID) of 10 Mrad ( $= 100$  kGy) and a non-ionizing radiation damage of  $10^{14}$   $\text{n}_{1\text{MeV eq}}\text{cm}^{-2}$ , given in terms of 1 MeV neutron equivalent particles per square centimeter [34], in 10 years of operation. Pixel cells in this area have to withstand a hit rate of  $\sim 10^3$  hits/second. In this high radiation environment the sensor will also be damaged. Due to this damage, the leakage current of the sensor will increase with time. Leakage current results from electrons which are spontaneously created in the depletion zone and are readout like signal electrons. The ToPix ASIC is designed to compensate a leakage current up to 50 nA per pixel cell.

A Minimum Ionizing Particle (MIP) is expected to leave an ionizing charge of  $\sim 1.3$  fC in a 100  $\mu\text{m}$  silicon epitaxial sensor. The highest amount of ionizing charge is expected from slow protons with a momentum down to  $\sim 200$  MeV/c. These particles can deposit up to 50 fC, which defines the dynamic range of the ToPix. The Equivalent Noise Charge (ENC) of a pixel should be in the order of 200  $\text{e}^-$  or 32 aC. The cooling of the front-end ASICs will be done with a liquid cooling system. In order to stay in the limits of the cooling system the power consumption per analog cell must stay below 20  $\mu\text{W}$ .

The requirements for the ToPix ASIC are summarized in Table 5.1.

Pixel Size	100 $\mu\text{m}$ x 100 $\mu\text{m}$
Noise Level	200 $\text{e}^-$ rms
Linear dynamic range	Up to 50 fC
Power consumption	$< 20$ $\mu\text{W}$
Leakage compensation	Up to 50 nA

Table 5.1.: Pixel cell requirements for the ToPix. Table taken from Ref. [45].

### 5.1.2. Analog Readout Chain

Each pixel cell contains analog electronics for amplification and charge measurement. A sketch of the analog readout chain is displayed in Figure 5.1. An electron pulse which is created in the sensor is received by a Charge Sensitive Amplifier (CSA) circuit. The signal pulse is integrated by collecting the signal electrons on the feedback capacitance  $C_f$  of the CSA. A constant current source is connected in parallel to the CSA. It discharges the feedback capacitance  $C_f$  with a constant current as soon as charge is applied to it. The output of the CSA is connected to a comparator circuit where the voltage is compared with a constant preset voltage ( $V_{th}$ , the threshold of the pixel). The threshold voltage is common to all pixels, but can be adjusted pixel-wise by a local 5-bit Pixel DAC (PDAC)



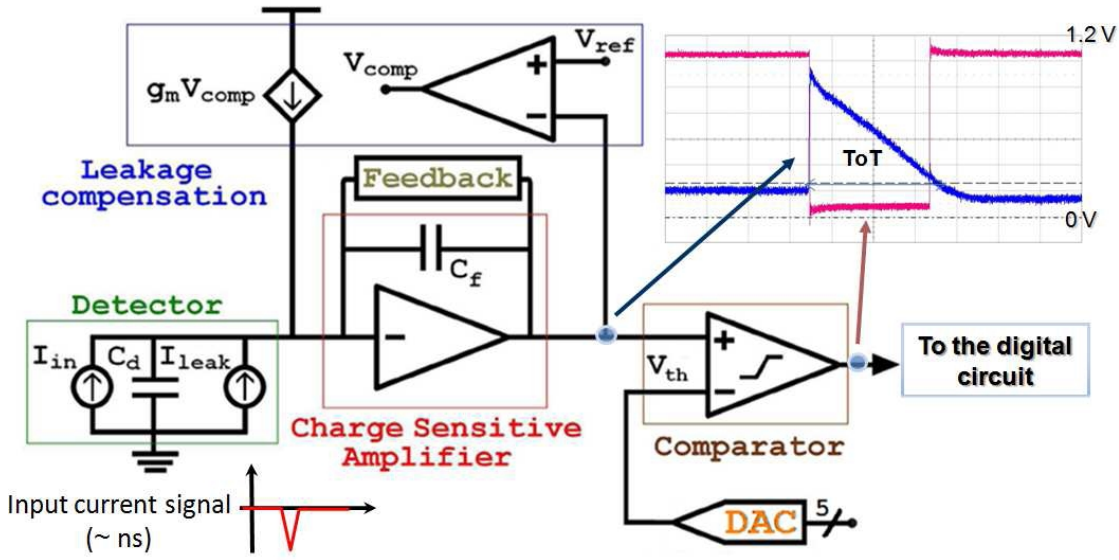


Figure 5.1.: ToPix 3 analog part of a pixel cell. Figure from Ref. [45].

value. If the CSA output crosses the preset threshold voltage, the comparator output changes its state. A rectangular pulse is created whose length represents the time the CSA output was higher than the threshold voltage. This time is proportional to the total amount of charge that was created in the sensor. This method to measure the deposited charge is called Time-over-Threshold (ToT).

The sensor creates not just the signal electrons. Leakage current, created by spontaneous created free charge carriers, flows into the CSA and causes a shift of the baseline. To compensate the constant flow of leakage current from the sensor, a baseline restorer is implemented. A comparator senses the output of the CSA by comparing it to a reference value. If the output deviates from this reference, a current is applied to the CSA input to compensate the leakage current. The baseline restorer can compensate a leakage current of up to 50 nA per pixel cell.

### 5.1.3. Digital Readout Chain

The digital part of the readout chain controls the timestamp determination, the configuration and the readout of the pixel cell. A schematic drawing of the pixel control logic is displayed in Figure 5.2. A global 12-bit time information (clock) is distributed to each pixel cell. The digitized signal from the analog comparator (**pixel\_in**) is processed by determining and saving the value of the global clock (timestamp) for the leading (**le\_reg**) and the trailing edge (**te\_reg**) of the rectangular signal to the corresponding registers. The filling of the trailing edge register activates the busy signal, which indicates that hit data is ready for readout. A third register in the pixel saves the pixel configuration (**cfg\_reg**). Via the pixel configuration the local pixel threshold can be finely adjusted. This tuning is necessary to overcome production related dispersion of the pixel thresholds.

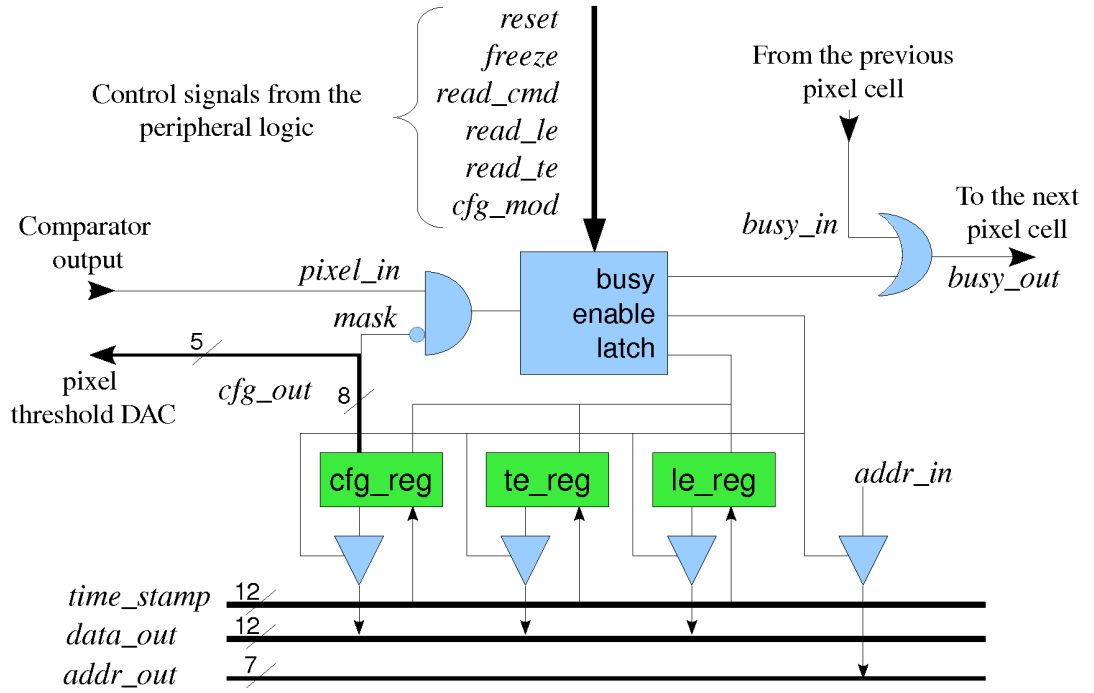


Figure 5.2.: Pixel Control Logic for a single pixel. Figure taken from Ref. [45].

Each pixel can be masked, i.e. deactivated. This is necessary if a pixel is broken or noisy. To analyze the comparator output without digitization one is able to put the comparator output of a pixel to a dedicated output which can be accessed with an oscilloscope. The configuration register enables the injection of a test pulse created by a calibration circuit into the pixel cell. With this test pulse one is able to test the functionality of the pixel cell without a sensor. A description of the calibration circuit is given in Section 5.2.3.

The pixels of a double column are steered by a group of signals which are set in the Column Readout Control Unit (CRCU). Basically two operation modes are available, readout of data and configuration of pixel cells.

The busy lines of all pixels in one column are connected in a logical OR chain in the way that the **busy\_in** of the higher pixel is connected via an OR with the **busy\_out** of the current pixel. If one or more pixels detect a hit, the busy signal goes to one and triggers the readout process. The **read\_cmd** signal is then applied to all pixels and requests the active pixel to apply its address and then the leading and trailing edge registers to the output lines **addr\_out** and **data\_out**, respectively. The active pixel is defined as the pixel with the highest address in which the **busy\_in** signal is low and the **busy\_out** signal is high. All pixels with an active busy signal before the **read\_cmd** was applied are readout. The activation of the busy signal by pixels which detect a hit while the **read\_cmd** is active is blocked by an active freeze signal. This is done to prevent the blocking of the readout of low priority pixels by noisy high priority pixels, which would frequently re-enter the

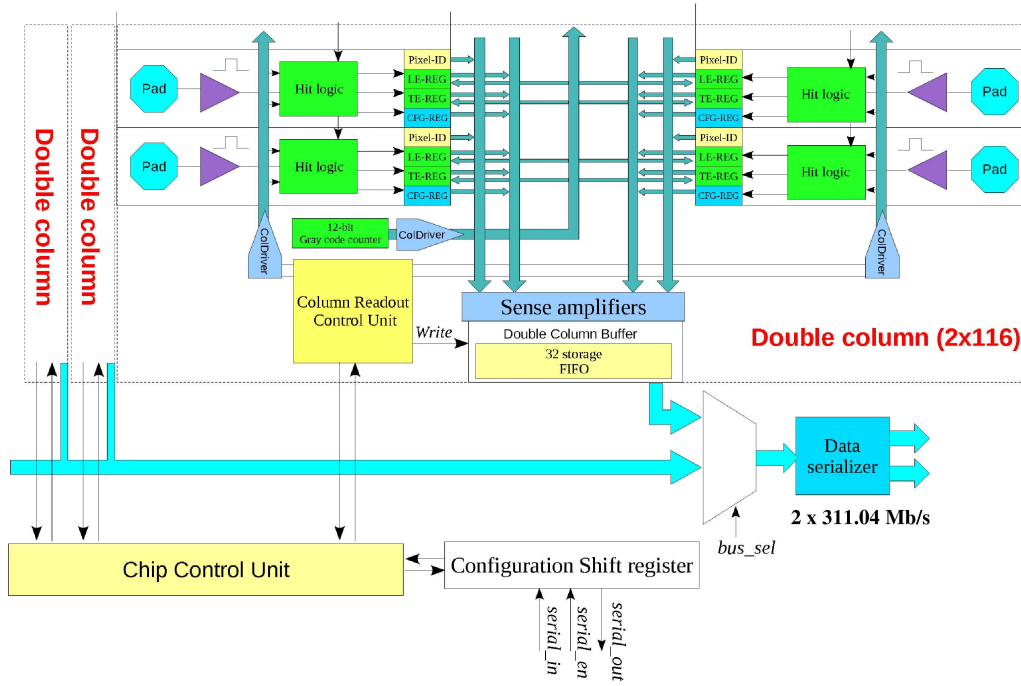


Figure 5.3.: Double column readout logic of the final production version of the ToPix ASIC. Picture taken from Ref. [45].

readout process before the low priority pixels are readout out.

The configuration of the pixel is initialized with activating the `config_mode` signal. The commands and registers from the readout mode now have a different meaning. If the `config_mode` signal is asserted, then all pixels set their busy signal to high. The pixel with the highest priority receives the pixel configuration via the `data_out` lines and saves it in its configuration register. After that, the busy signal of that pixel is deactivated and then the configuration is loaded for the pixel with the next highest priority. The configuration is loaded. This process is repeated until all pixel cells are configured.

The pixel cells are arranged and readout in a double column structure. The ToPix will have 55 double columns with  $2 \times 116$  pixels each. Hit data from the active double column is readout and saved in the double column buffer (see Figure 5.3), which consists of a 32 entries deep First In First Out (FIFO) storage. A data serializer takes the data from the different double columns and sends it further in the readout chain.

The configuration of the pixel cells and the chip itself are done via three serial link signals, `SERIAL_IN`, `SERIAL_EN` and `SERIAL_OUT`. If the `SERIAL_EN` is drawn low by the user, the chip expects configuration data at `SERIAL_IN`, which is connected to the 17-bit Configuration Shift Register (CSR). To read back the configuration from the ToPix, a read command has to be applied via the `SERIAL_IN`. After processing the command the ToPix puts the requested data into the shift register. A dummy word has to be send to

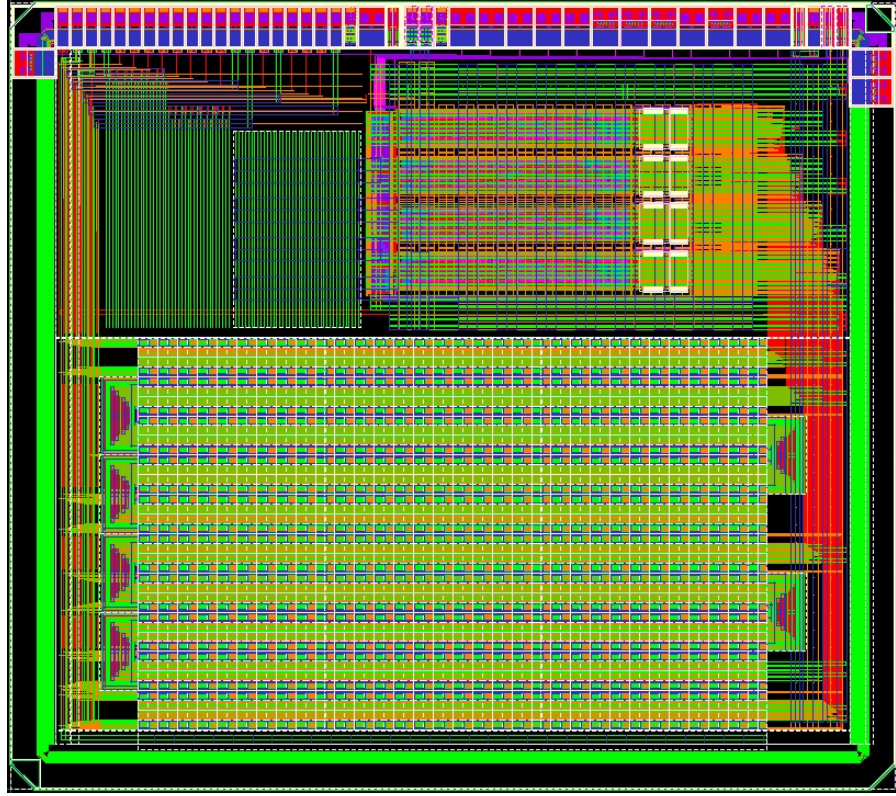


Figure 5.4.: Layout scheme of the ToPix 3. In the lower part are the pixels in double columns located. Figure taken from Ref. [45].

`SERIAL_IN` to shift the configuration through the shift register out to `SERIAL_OUT` where it can be detected.

#### 5.1.4. ToPix 3 Prototype

ToPix 3 is a reduced size prototype, 640 pixels are arranged in 4 double columns, 2 short columns ( $2 \times 32$  pixel cells per double column) and 2 long columns ( $2 \times 128$  pixel cells per double column) covering an active area of  $(2 \times 3.2) \text{ mm}^2$ . The long double columns have a meander-like structure on the ASIC (see Figure 5.5).

The ToPix 3 ASIC is produced in a Complementary Metal Oxide Semiconductor (CMOS) 130 nm technology [46]. This technology is used by industry and has a good radiation hardness even without Hardness-By-Design solutions [47].

The freeze signal of the ToPix 3 is set by the overflow of the 12-bit timestamp counter and not activated by a pixel busy signal. The freeze signal lasts until the three Most Significant Bits (MSBs) of the time stamp are identical to a preset pattern which can be set in the chip configuration (**Freeze Stop**, CCR0, see Table 4.1). The default value is 0b101, which means that the freeze signal is released if the time stamp reaches the

Pin name	Type	Description
vdd_pre	Shield	Input triple well bias
gnd_pre	Ground	Preamplifier ground
vdd_ilc	Power	Offset compensation circuit power
vdd_a	Power	Analogue power
VcasP1	Ibias	Preamplifier cascode load bias (pMOS, vdd_a)
VcasP2	Ibias	Preamplifier direct cascode bias (pMOS, vdd_a)
Isf	Ibias	Source follower bias (pMOS, nMOS)
Ilc_cas_bias	Ibias	Loop filter bias (nMOS, gnd_a)
Ilc_cas_in	Vbias	Loop filter cascode bias (nMOS, gnd_a)
Ifb_bias	Ibias	Feedback stage bias ( $\times 10$ ) (pMOS, vdd_a)
Ifb_cas	Vbias	Feedback stage cascode bias (pMOS, vdd_a)
Vref	Vbias	Analogue baseline reference voltage
gnd_a	Ground	Analogue ground
vdd_d	Power	Digital power (analogue section)
dac_bias_2	Ibias	DAC bias (pMOS, vdd_d)
Ibias_d	Ibias	Comparator bias ( $\times 10$ ) (nMOS, gnd_d)
Vref_d	Vbias	Comparator reference voltage (nMOS, gnd_d)
Vcas_d	Vbias	Comparator cascode bias (pMOS, vdd_d)
cal_level	Vref	Calibration voltage for test pulse ( $C_{REF} = 36$ fF)
gnd_d	Ground	Digital ground, analog section

Table 5.2.: ToPix 3 analog pad list. Table taken from Ref. [45].

value  $(0b101000000000)_{Gray} = 0d3072$ , which is  $3/4$  of the 12-bit counter time (12 bit =  $0d4095$ ). After the release of the freeze signal, the readout of the hits starts at this time.

The ToPix 3 has a reduced end-of-column logic to readout the double columns. Instead of a data serializer which collects the data from all double columns one has to choose a double column manually. Each double column has a 32 entries deep FIFO to buffer hits. The data of the active double column is automatically sent out of the ASIC via a serial link (`DATA_OUT` and `DATA_VALID`). The `DATA_VALID` signal is raised by the ToPix to indicates the transmission is starting. A double column is selected by setting the 2-bit signal `SEL[1:0]`. To switch to another double column for readout it is necessary to stop this automatic readout of hit data by setting the `DATA_WAIT` signal to high. After applying the `DATA_WAIT` signal, one has to wait until the ToPix has processed the signal and the ongoing data transmission is finished. After that one can change to another double column, otherwise data can be lost.

Some configuration voltages still have to be applied from the outside, they will be implemented into the chip later. A complete list of the analog pads of the ToPix 3 is displayed in Table 5.2, a list of the adjustable voltages with the used settings is displayed in Tables 5.4 and 5.5.

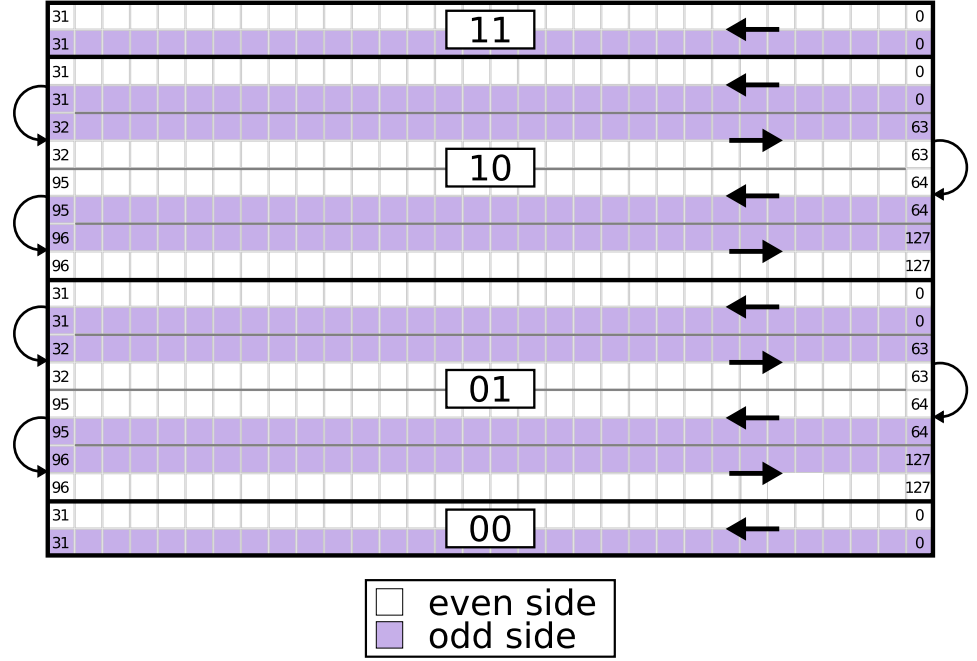


Figure 5.5.: Numbering scheme of the pixel cells on the ToPix 3. Four double columns with an even and an odd side. The two short columns (0b00 and 0b11) are at the top and the bottom of the matrix, the two folded long double columns (0b01 and 0b10) are located in the middle. Arrows indicate the direction of rising pixel addresses.

## 5.2. Testbench

### 5.2.1. Test Setup

The ToPix 3 prototype is readout with the Jülich Digital Readout System (JDERS), described in Chapter 4. Figure 5.6 shows a picture of the setup. The setup consists of the ML605, the Field Programmable Gate Array (FPGA) board of the readout system, the ToPix Readout Board, which can be attached directly to the ML605 and three external power supplies to power the ToPix readout board. A readout PC, that controls the system and saves the data is connected via optical fibers to the ML605.

### 5.2.2. ToPix Readout Board

Testing the ToPix 3 ASIC, a ToPix Readout Board was designed at the INFN in Turin. Figure 5.7 shows the ToPix Readout Board equipped with a ToPix 3.

The ToPix Readout Board is the interface between the ToPix 3 ASIC and the readout system. Table 5.3 shows the necessary voltages to power the test board and the current consumption for a standard configured ToPix with a clock frequency of 50 MHz. It generates the necessary supply voltages of the ToPix 3 (1.55 V analog, 1.55 V digital)



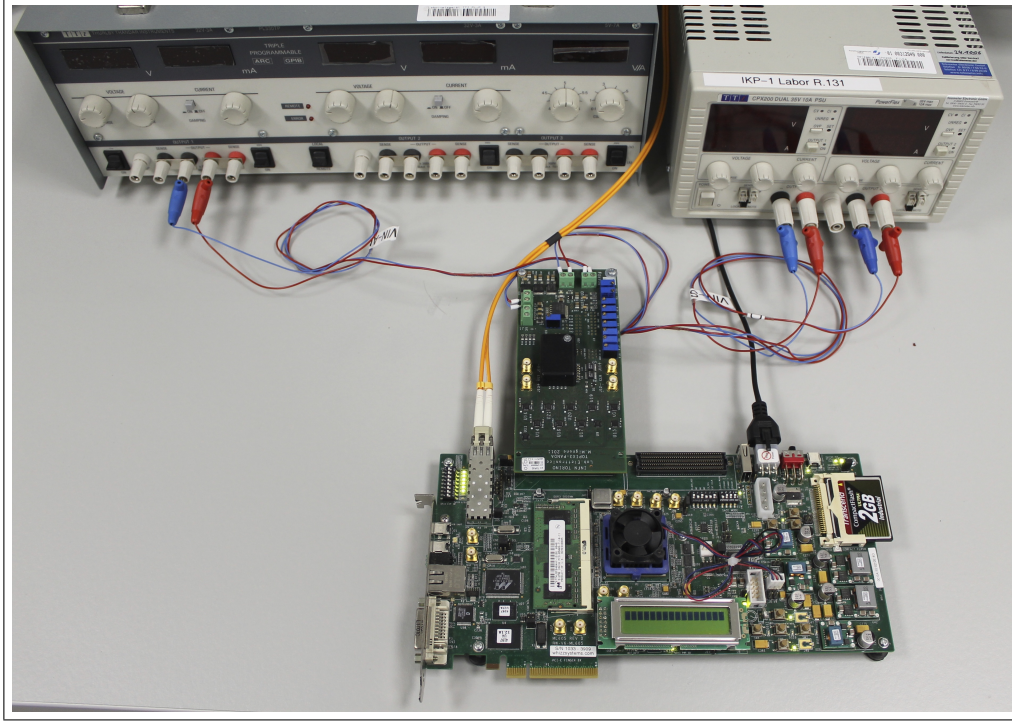


Figure 5.6.: Photograph of the ToPix 3 test setup.

Name	Voltage [V]	Current consumption [A]
$V_{in}$ Service	5.00	0.176
$V_{in}$ Digital	5.00	0.082
$V_{in}$ Analog	5.00	0.010

Table 5.3.: Test board supply voltages and current consumption for standard CCR configuration and 50 MHz ASIC frequency.

and converts the Scalable Low Voltage Signal (SLVS) signals of the ToPix 3 into Low Voltage Differential Signal (LVDS) signals needed by the readout system and vice versa. Eight potentiometers give the possibility to adjust bias voltages for the ToPix 3 to change settings (see Table 5.5). The connection to the JDRS is done via a FPGA Mezzanine Card (FMC) connector. In addition, the readout board is equipped with two 4-channel 16 bit Digital to Analog Converter (DAC) (LTC2604, [48]) which generate the 6 voltages (see Table 5.4).

### 5.2.3. Calibration Circuit

An internal calibration circuit is integrated into the ToPix ASIC to test the functionality of the chip with and without an attached sensor and to calibrate the ASIC. It generates

## 5. The ToPix 3 Front-End ASIC

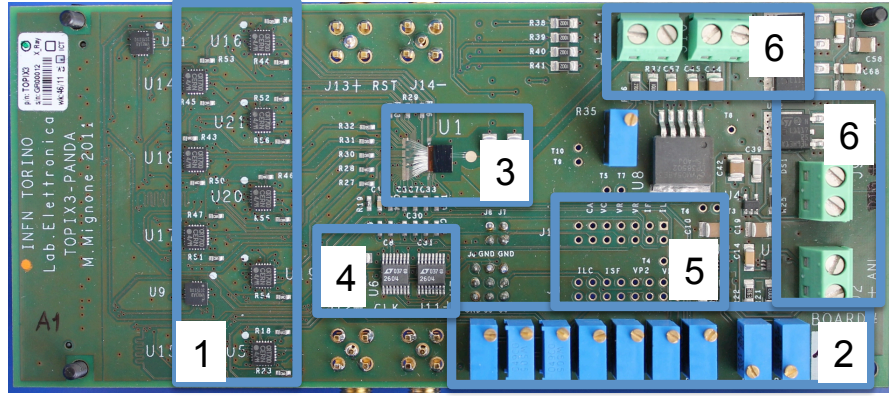


Figure 5.7.: ToPix Readout Board: 1) LVDS↔SLVS level converter 2) Potentiometer 3) ToPix 3 4) DAC 5) Measurement jumper 6) Power connectors.

Name	Ch. Name	Control Point	Voltage [V]
ILC_CAS_IN	LTC1-A	J18-2	0.850
IFB_CAS	LTC1-B	J18-4	0.750
VREF	LTC1-C	J18-6	0.700
VREF_D	LTC1-D	J18-8	variable
VCAS_D	LTC2-A	J18-10	0.720
CAL_LEVEL_DAC	LTC2-B	J18-12	variable

Table 5.4.: List of DAC channels with used settings and control point (Jumper).

a test charge via an adjustable voltage step and a calibration capacitance which is connected to the input of the CSA. The height of the injected charge depends on the height of the applied voltage step.

The total value of the injected charge is:

$$Q_{cal} = \int_{t_0}^{t_1} i(t)dt = C_{Cal} \int_0^{cal\_level} dV_c = C_{Cal} \cdot cal\_level \quad (5.1)$$

[45]. The injection capacitance has a nominal value of  $C_{Cal} = 36$  fF.

The pixel for injection is selected by the pixel configuration local register (bit 1, `TESTP_EN`, see Table 4.4).

The level of the calibration signal is defined by the `cal_level` voltage, which is set by the test board DAC (see Table 5.4) and commonly applied to all pixel. To inject charge into the CSA, the `TESTP` signal which is directly connected to the injection circuit, has to change its state. A positive `TESTP` step injects a positive charge into the input node and a negative step injects a negative charge.

The value of this capacitor can vary by up to 10% due to variations in the wafer processing, which limits the precision of the injected charge. The DAC delivers a maximum



Name	Control Point	Voltage [V]
VCASP1_MON	J3	0.180
VCASP2_MON	J3	0.094
ISF_MON	J3	0.075
ILC_CAS_BIAS_MON	J3	0.040
IFB_BIAS_MON	J3	0.196
DAC_BIAS_2_MON	J3	0.245
IBIAS_D_MON	J3	0.075

Table 5.5.: List of bias voltages adjustable with potentiometers, used settings and control point (Jumper).

voltage of 1.2 V, which limits the injectable charge to 43.2 fC. This injectable charge covers almost the entire dynamic range of the ASIC of 50 fC.

If a rectangular TESTP signal is applied to the injection circuit, two charges are injected into the preamplifier, a positive charge on the rising edge and a negative charge on the falling edge. Therefore, the time between changing the state of TESTP has to be long enough not to influence the measurement. The necessary time between the two injections was determined by the following measurement.

Figure 5.8 shows the measured ToT value for the maximum injectable charge of 43.2 fC with varying lengths of the TESTP signal. One can see that the measured ToT value depends on the length of the TESTP signal up to 8  $\mu$ s. After that value, the ToT stays constant as it should. Therefore, the TESTP length was set to 10  $\mu$ s for all subsequent measurements.

## 5.3. Measurements with the ToPix 3

### 5.3.1. Calibration of DAC

The height of the pixel test pulse is defined by the `cal_level` voltage delivered by one of the DAC chips on the testboard. To know the exact voltage a calibration curve has been recorded. The result of this calibration curve can be seen in Figure 5.9. The measurement was done with a Keithley 2400 source meter at jumper J18-P12. The curve was fitted with a quadratic fit function:

$$f(x) = ax^2 + bx + c \quad (5.2)$$

To obtain the transfer function:

$$\text{cal\_level} = -4.233 \cdot 10^{-13} \cdot \text{DAC}^2 + 1.871 \cdot 10^{-5} \cdot \text{DAC} - 0.001414 \quad [\text{V}] \quad (5.3)$$

The absolute deviation from the measurement to the fit is below 0.1 mV. This error is small in comparison to the error of 10% on the injection capacitance, and therefore is neglected.

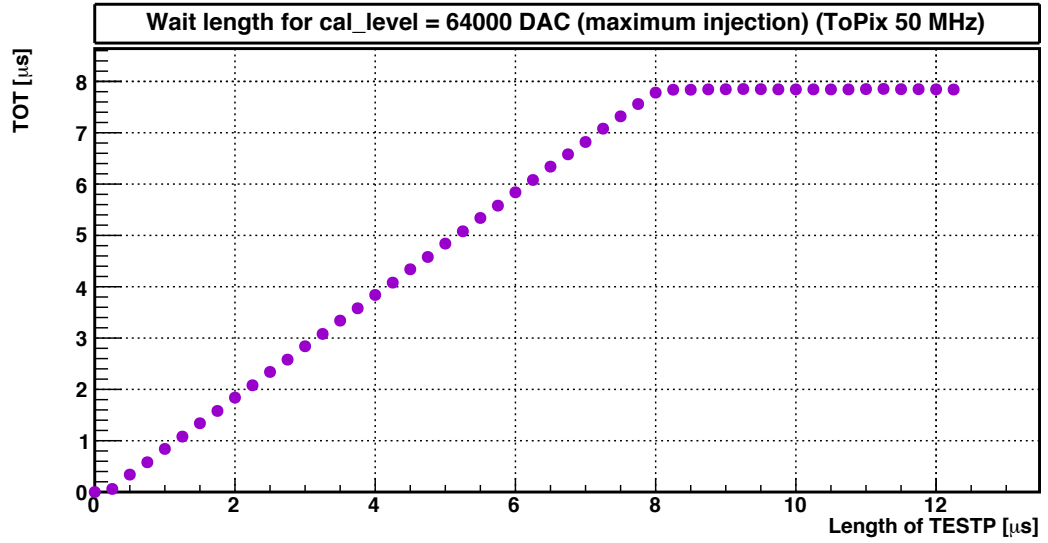


Figure 5.8.: Time difference between the switching of TESTP versus the detected charge of the pixel. The TESTP has to keep the polarity for at least 8  $\mu\text{s}$  to ensure the complete processing of the testpulse for all injectable charges.

To obtain a mean translation between the DAC value and the corresponding voltage, a linear fit was applied to the data, leading to the relation:

$$\text{cal\_level} = 1.869 \cdot 10^{-5} \cdot \text{DAC} \quad [\text{V}] \quad (5.4)$$

### 5.3.2. ToT Linearity

The deposited energy in the sensor is measured via the Time-over-Threshold (ToT) method. The ToT value is expected to rise linearly with the deposited energy. This linear dependence is measured for a pixel cell in each prototype to ensure the behavior and to determine a calibration function to convert ToT values into deposited energy.

Figure 5.10 shows the result of this measurement for a single pixel as an example. The upper frame shows the ToT value depending on the injected number of electrons.

The number of electrons was calculated with the expected injection capacitance of 36 fF. The measurement is approximated by a linear fit. The fit parameters are determined to be

$$\text{ToT} = 3.064 \cdot 10^{-2} \frac{\text{ns}}{e^-} Q_{in} + 9.633 \text{ ns} \quad [\text{ns}] \quad (5.5)$$

The lower frame shows the deviation from the linear fit at the low edge of the distribution, i.e. at small injected charges. Figure 5.11 shows a zoom of the low injected charge region of Figure 5.10. The steps in the deviation from the linear fit are effects of the charge digitization. The non-linear behavior for low injected charge is expected, since the tip of the triangular ToT behavior is round (see Figure 5.12). This rounding is an effect of

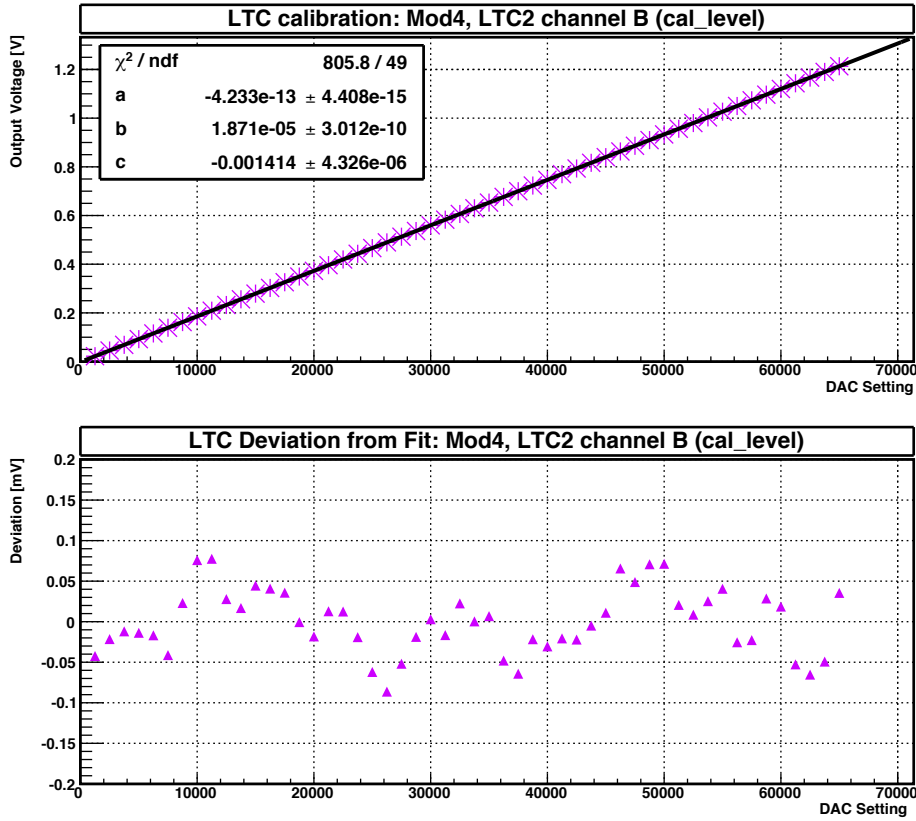


Figure 5.9.: Calibration measurement of the DAC channel for the internal injection circuit for Module 4. Upper frame: Calibration curve with quadratic fit function. Lower frame: Deviation of the data points from the quadratic fit.

the analog readout. The discharging of the feedback capacitor starts before the injected charge is fully integrated on the integration capacitor. This behavior is typical for this type of preamplifiers.

The inverse slope gives the discharging current of the constant current source:

$$32,637 \frac{e^-}{\mu s} = 5.229 \frac{fC}{\mu s} = 5.229 \text{ nA} \quad (5.6)$$

The discharging current can be adjusted with a potentiometer located on the test board. Via the IFB\_BIAS\_MON tab one is able to measure the voltage drop over a fixed resistor ( $R_{12}=510 \text{ k}\Omega$ ) which can be compared with the discharging current determined via the slope measurement shown before. The current which flows through this resistor is 80 times larger than the discharging current [41]. With a voltage IFB\_BIAS\_MON=0.196 V the discharging current is calculated to be 4.8 nA. The two values agree, taking into account the  $\sim 10\%$  error of the injection capacitance.

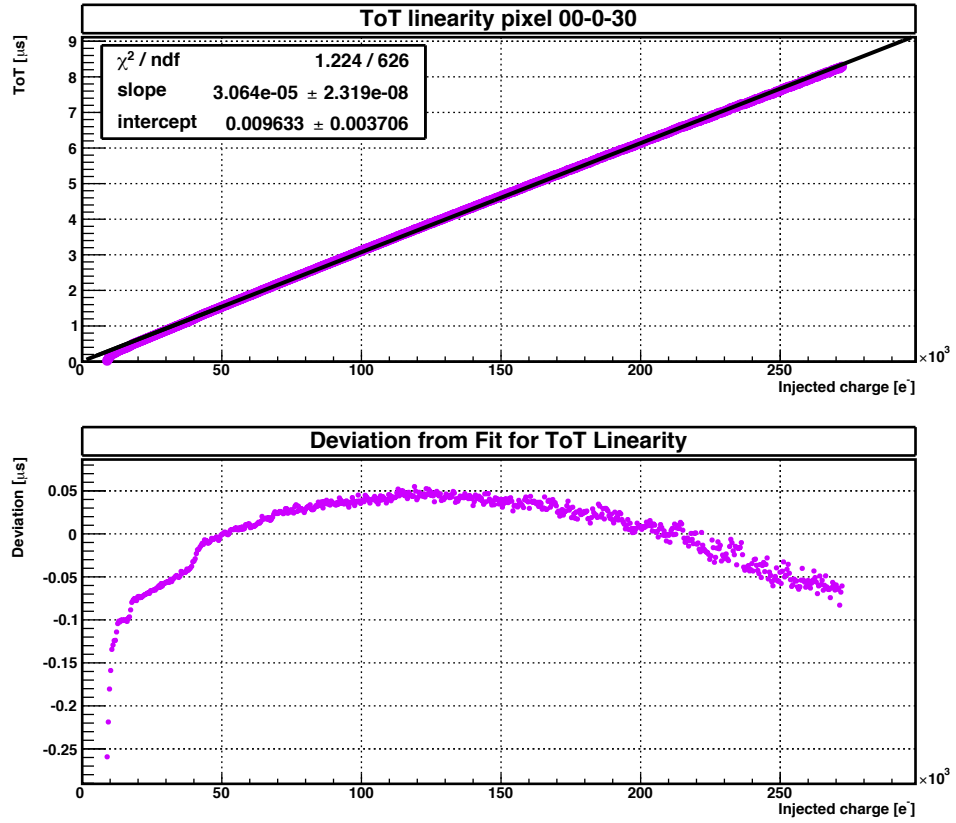


Figure 5.10.: Test of ToT linearity for the full charge range. Upper frame: ToT as a function of the injected charge. Lower frame: Deviation of the ToT data from the linear fit.

### 5.3.3. Pixel Test

A first analog test for a ToPix ASIC is the injection of a high charge  $n$ -times (in our case  $n=10$ ) into each pixel cell and to measure the number of recorded hits. A comparison between the pixel cell address of the injected pixel cell and the data address is not done at this stage, only the number of hits is counted. The result of this test can be seen in Figure 5.13. All pixels respond to the injections and all except three show the number of expected hits. The three pixels at the end of the double column have twice the entries compared to the number of injections. The reason for this is that these pixels create two hit words with each injection. The first word is the expected data word, the second word always contains the pixel number 127 and the leading and trailing edge value 2730. In binary format and Gray coded these values correspond to:

$$0b1010\ 1010\ 1010 = (0b1111\ 1111\ 1111)_{Gray} \quad (5.7)$$

The transmitted data in this faulty event corresponds to all bits being 1 in Gray code.

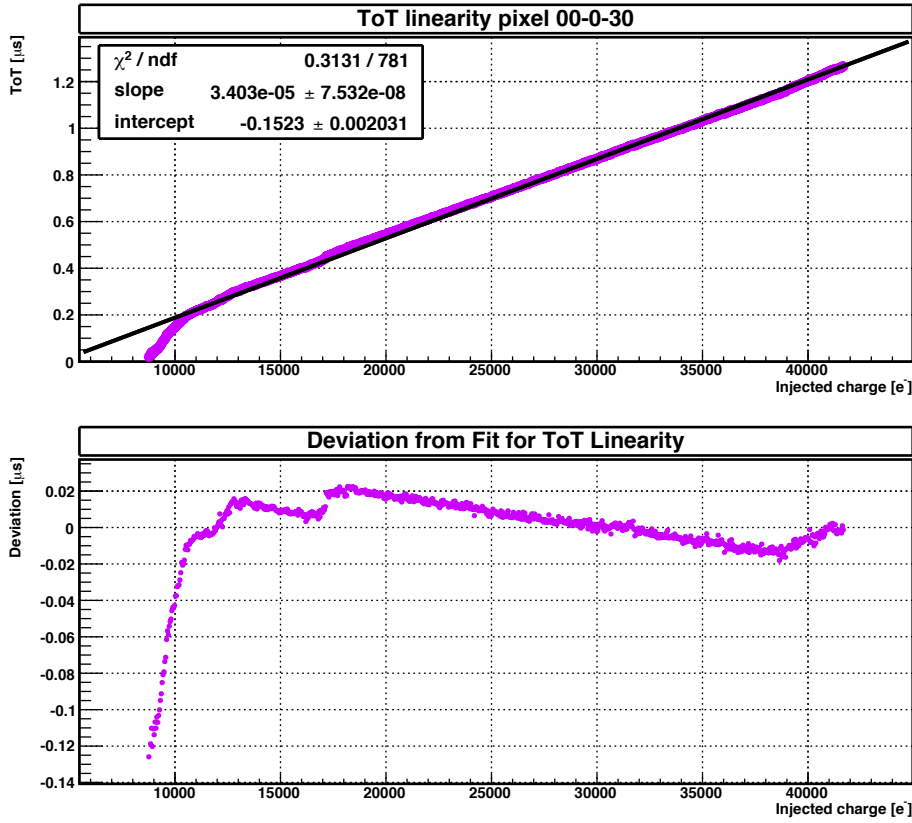


Figure 5.11.: Test of ToT linearity for low injected charges. Upper frame: ToT as a function of the injected charge. Lower frame: Deviation of the ToT data from the linear fit.

The error is caused by a readout problem of the ToPix 3. The capacitive load on the readout lines is higher than expected due to the meander-like structure of the pixel cells in one double column [41]. Therefore, the readout driver is too weak causing timing problems in the readout of the pixel columns. This problem gets more obvious when the clock frequency of the ToPix 3 is increased above 50 MHz. This is shown in Section 5.3.4.

#### 5.3.4. Frequency Variation

The target operational frequency of the ToPix is 155.52 MHz. Due to an error in the column drivers it is not possible to operate the ToPix 3 at this frequency since the pixel cells cannot be readout properly. A stable operation of the ToPix 3 is possible up to 50 MHz.

To show the behavior of the ToPix at higher frequencies the pixel check was repeated for different frequencies: 50 MHz, 60 MHz, 70 MHz, 80 MHz, 90 MHz, 100 MHz, 110 MHz, 120 MHz, 130 MHz, 140 MHz, 150 MHz and 155 MHz. The results of this measurement

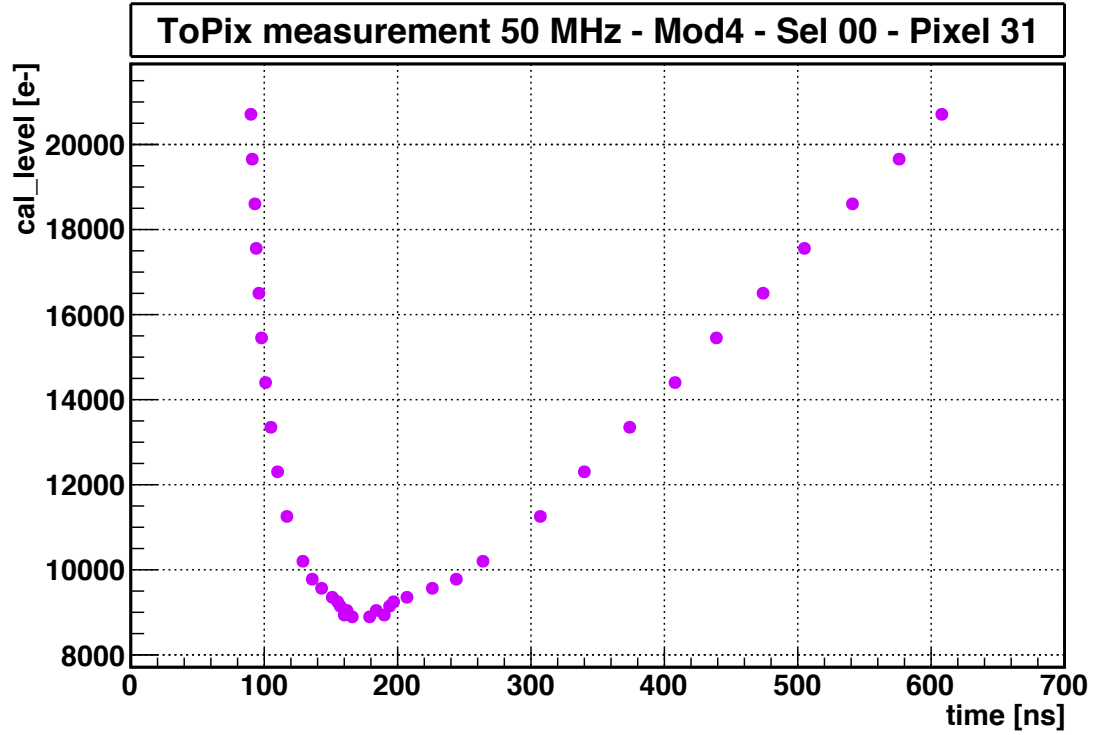


Figure 5.12.: Measurement of the signal shape for the ToPix 3. Displayed are the leading edge (left side of the peak) and trailing edge (right side of the peak) time stamps for hits with different injected charges.

are displayed in Figures 5.14, 5.15 and 5.16. All measurements show the pixel check measurement on the left, the average leading edge value over the 10 measurements in DAC units in the middle and the average trailing edge value over the 10 measurements in DAC units on the right. At 50 MHz the chip is nearly completely functional. The long columns show for some higher priority pixels too high leading edge values. This effect is not limited to specific pixels, different measurements show the too high leading edge values at different pixels. This behavior is not seen for other tested ToPix 3 ASICs.

With higher frequencies one can see that the readout of the pixel cells at the end of a column is not working properly anymore. The pixels returns twice many responses as data injections have been done. The leading and trailing edge values are nearly all of the value 0d2730, which indicates an all high data word (see Section 5.3.3). Also the addresses of these pixels is incorrect, the value is always 0d127 which is an all high pixel address. With rising frequency the number of pixels sending out too many hit words increases. The effect rolls down from the high end of the double column to the low end. At the design frequency only the low index pixels of the short double columns are working properly. This error will be corrected in the next version of the ToPix.

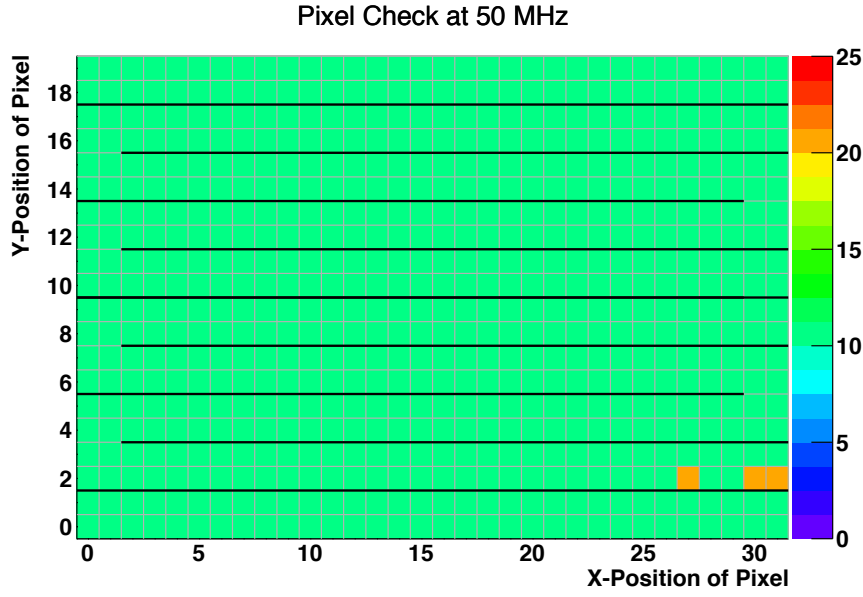


Figure 5.13.: Pixel check measurement at 50 MHz without address filtering. 10 injections/Pixel.

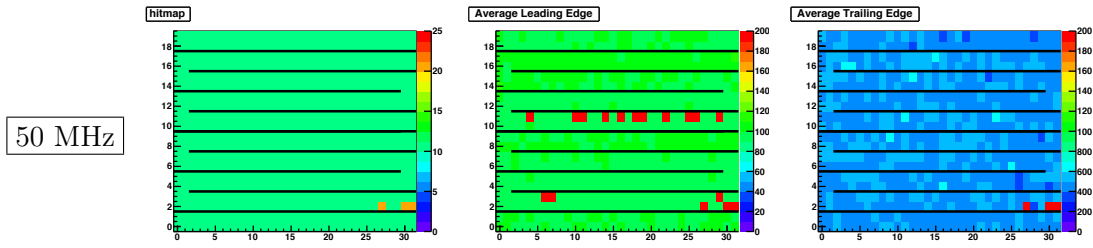


Figure 5.14.: Frequency variation measurement of a ToPix 3 prototype at 50 MHz clock frequency. Left frame: number of detected hits for 10 injections. Middle frame: Average leading edge. Right frame: Average trailing edge.

## 5. The ToPix 3 Front-End ASIC

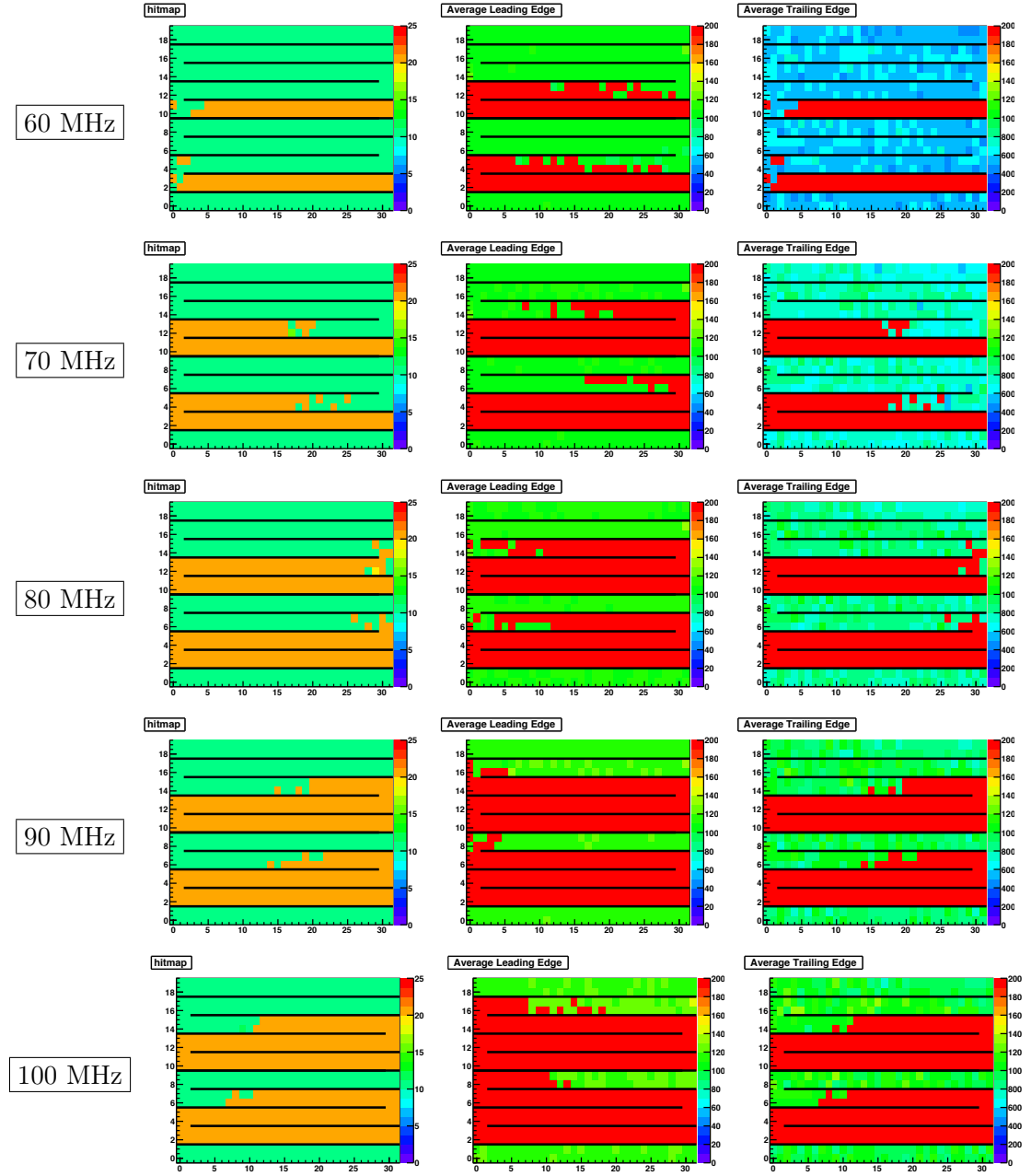


Figure 5.15.: Frequency variation measurement of a ToPix 3 prototype. Left frames: number of detected hits. Middle frames: Average leading edge. Right frames: Average trailing edge. From top to bottom at 60 MHz, 70 MHz, 80 MHz, 90 MHz and 100 MHz clock frequency.



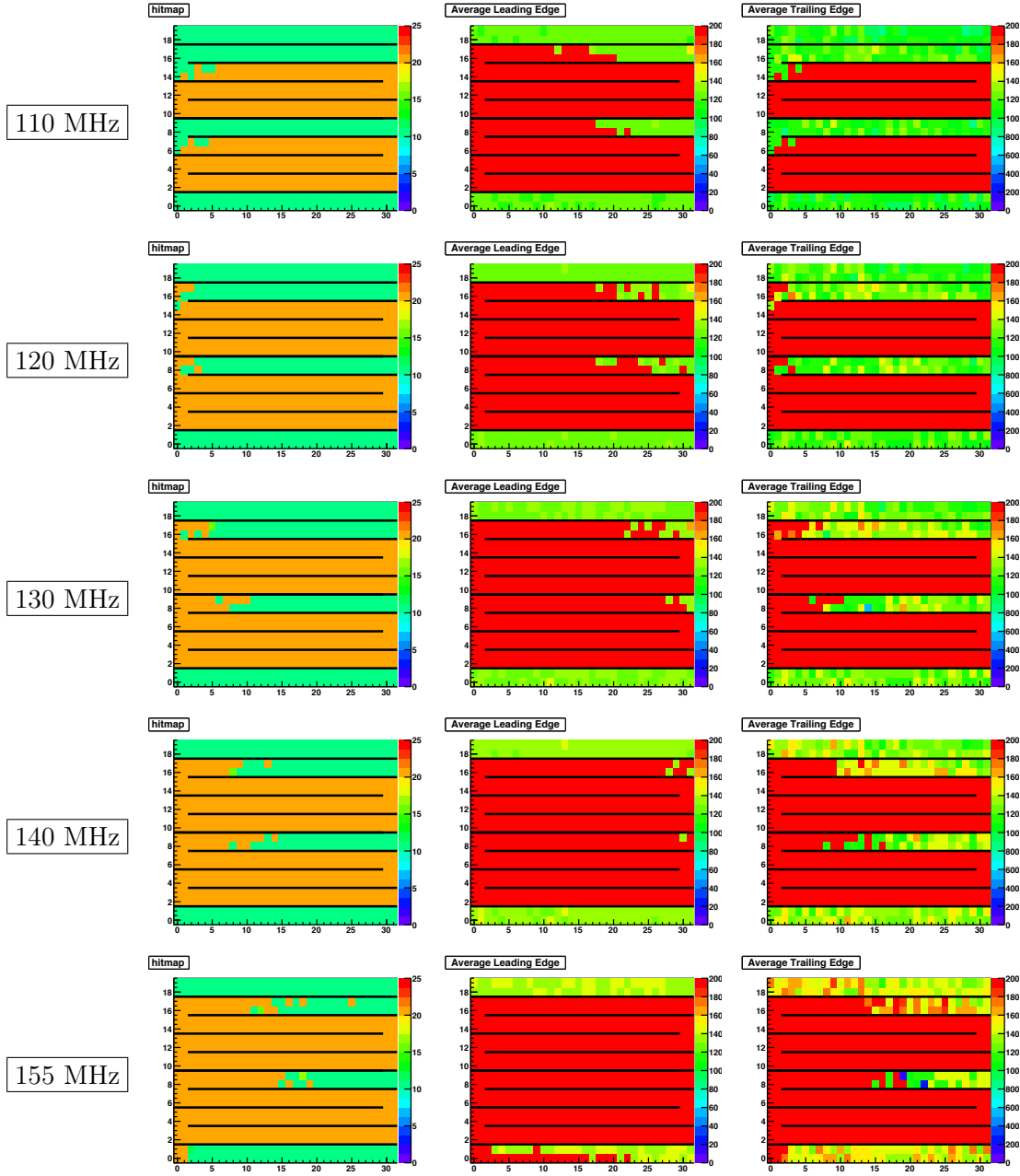


Figure 5.16.: Frequency variation measurement of a ToPix 3 prototype. Left frames: number of detected hits. Middle frames: Average leading edge. Right frames: Average trailing edge. From top to bottom at 110 MHz, 120 MHz, 130 MHz, 140 MHz and 155 MHz clock frequency.

### 5.3.5. Threshold Determination

This section describes the determination of the threshold of a pixel. The threshold of a pixel is an important characteristic which influences the energy and spatial resolution of the detector. If the deposited charge is distributed on several pixels the spatial resolution of the hit can be improved by interpolation between the fired pixels taking the charge per pixel into account. With an increasing threshold, the ratio of multiply fired pixels to single fired pixels drops, thereby decreasing the spatial resolution of the MVD. On the other hand, a too low threshold causes noise hits which are not connected with a particle track with negative effects on the tracking performance and the needed data transmission bandwidth. Above a certain level of noise hits they could even block the readout of real hits.

In an ideal case all charges below the threshold are not detected while all charges above the threshold are detected like a step-function. But due to the electronic noise the ideal step-function is smeared by the Gaussian noise of the system. The threshold is then defined as the charge at which 50% of the hits are detected.

With a threshold scan it is possible to determine the response of the pixel around the threshold. The measurement is done in the following way: A certain amount of charge is injected  $n$  times into the pixel. The number of responses is determined. The amount of injected charge is then varied, and the measurement is repeated. The collection of measurements gives the behavior of the pixel around the threshold. Due to the shape of the response function (see Figure 5.17) this measurement is also called the s-curve measurement. The s-curve can be measured with the internal injection circuit of the ToPix 3 ASIC. The measurement is then fitted with a convolution of a step-function with a Gauss error function [36]:

$$R(q) = \frac{n}{2} \cdot \left( 1 + \operatorname{erf} \left( \frac{q - \mu}{\sqrt{2} \cdot \sigma} \right) \right) \quad (5.8)$$

where the Gauss error function is:

$$\operatorname{erf}(x) = \frac{2}{\sqrt{\pi}} \int_0^x e^{-t^2} dt \quad (5.9)$$

and  $n$  the number of injections,  $\mu$  the center of the function (threshold) and  $\sigma$  the width of the noise distribution.

### 5.3.6. Threshold Distribution

A global threshold value is applied to all pixel in the ASIC for a coarse threshold setting. The wider this dispersion is, the higher the global threshold has to be, to avoid noise hits in the pixel cells with the lowest threshold. This leads to a worse energy resolution, especially for these pixels which have a higher threshold.

The distribution of pixel thresholds without individual threshold tuning for one module was measured with the previously described s-curve method. The results of this measurement are displayed in Figure 5.18.

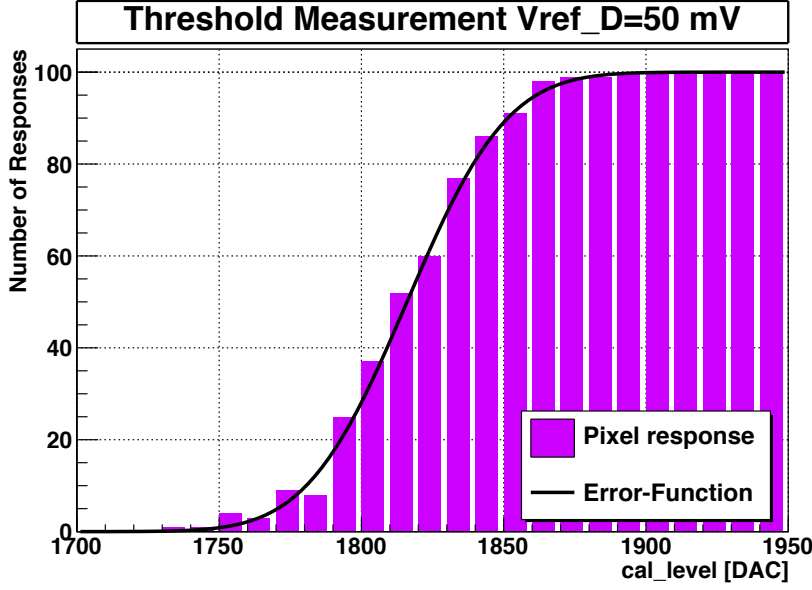


Figure 5.17.: S-curve measurement of a pixel cell. The number of detected hits for a constant number of injections is displayed as a function of the injected charge. The black line indicates the fitted error-function.

The width of the distribution is given by the Gaussian fit as

$$\sigma = (128.8 \pm 4.8) \text{ DAC} = (2.39 \pm 0.09) \text{ mV} \approx (539 \pm 58) e^- \quad (5.10)$$

The error on the injection capacitance was assumed to be 10% and dominates the final error on the dispersion.

Figure 5.19 shows the two dimensional distribution of the pixel cell thresholds. Four pixel cells have a disproportionally high threshold compared to the other pixel cells. For the remaining pixel cells the thresholds are equally distributed.

To correct the threshold dispersion, every pixel is equipped with a 5-bit PDAC to individually vary the threshold and to narrow the threshold distribution. With a calibration scan one is able to find the right PDAC setting to narrow this distribution. The calibration scan varies the PDAC setting and repeats the s-curve scan to see if the varied threshold is closer to the predefined threshold. The result of this measurement is displayed in Figure 5.20. Figure 5.21 shows the two dimensional distribution of tuned threshold. The distribution is more equal compared to the untuned distribution. The four pixel cells with the high threshold are still visible due to a slightly higher threshold. In this case was the PDAC range not sufficient to lower the threshold to the average value.

After tuning the width of the threshold distribution shrinks to

$$\sigma = (15.3 \pm 0.4) \text{ DAC} = (0.29 \pm 0.0075) \text{ mV} \approx (64 \pm 7) e^- \quad (5.11)$$

Which is almost a factor 10 smaller than before and well below the required dispersion width of  $200 e^-$ .

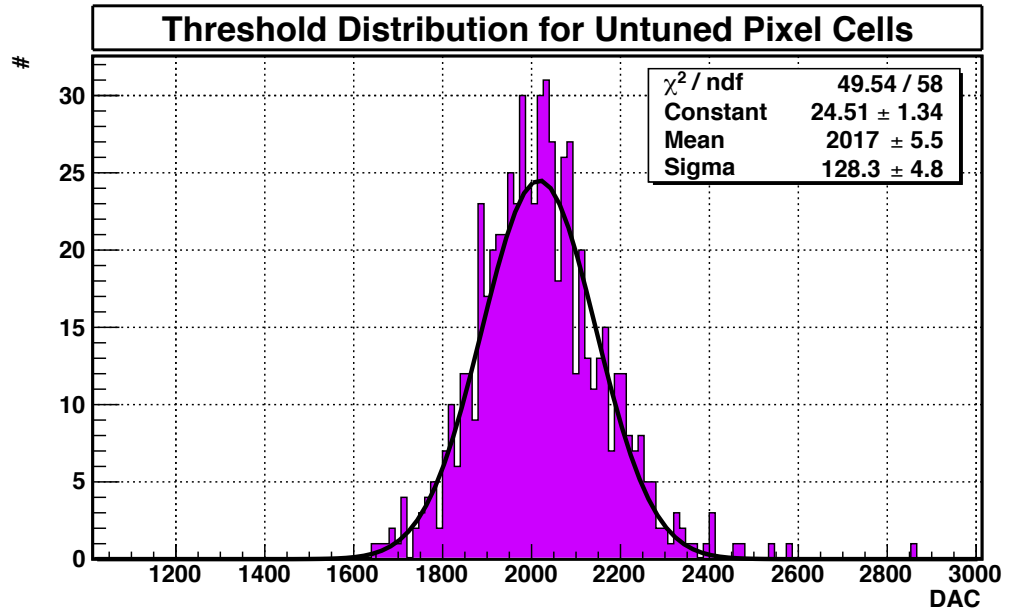


Figure 5.18.: Threshold distribution for untuned pixel cells.

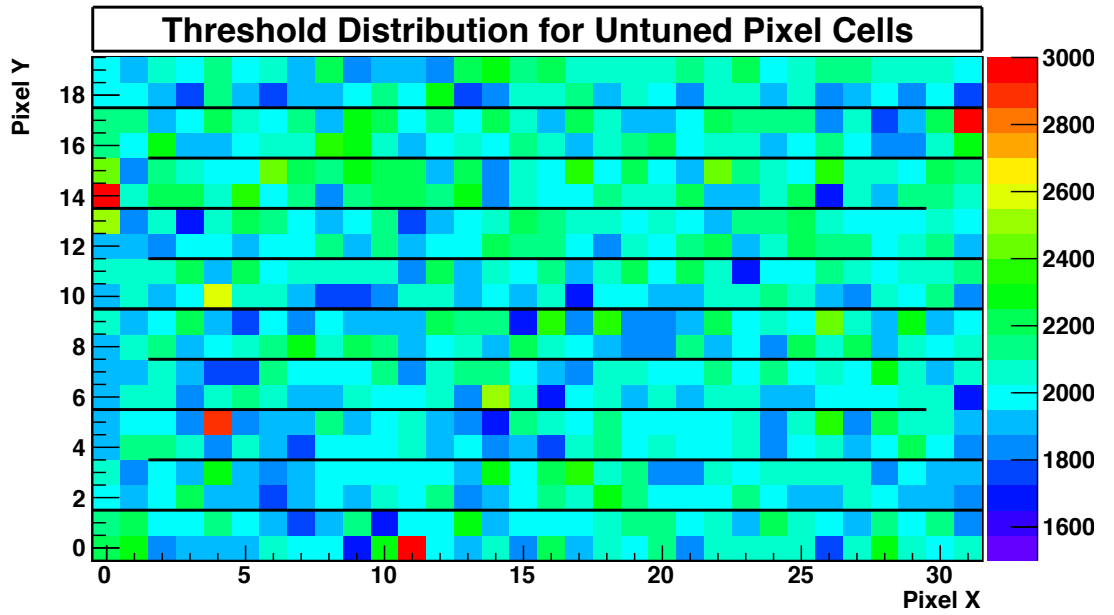


Figure 5.19.: 2D threshold distribution for untuned pixel cells. The black line indicates a gaussian fit.

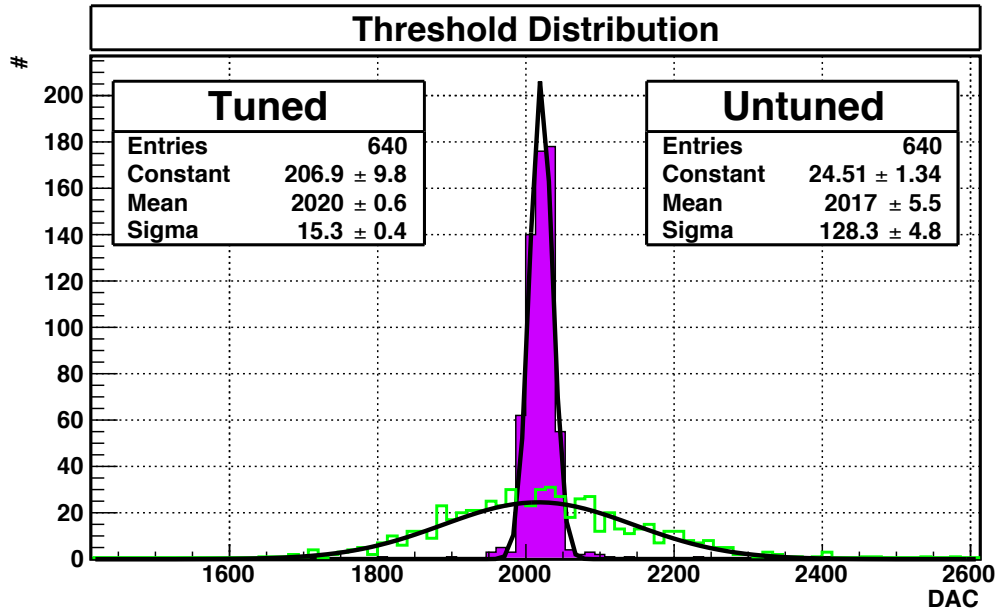


Figure 5.20.: Pixel cells threshold distributions. Green: Untuned threshold distribution. Violet: Tuned threshold distribution. The black lines indicates gaussian fits.

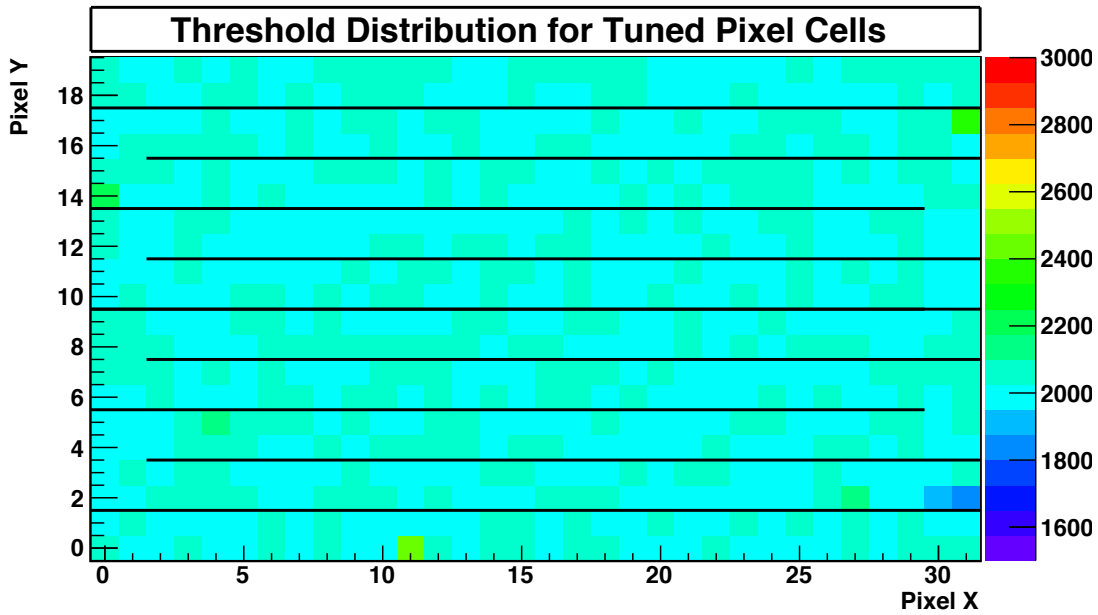


Figure 5.21.: 2D threshold distribution for tuned pixel cells.

## 5. The ToPix 3 Front-End ASIC

This value is comparable with earlier ToPix 2 versions ( $100 e^-$  including the JDRS Rev. A [49, Cha. 9.4.3.]), indicating that the calibration works.

### 5.3.7. Noise Distribution

The distribution of the noise of all pixels is displayed in Figure 5.22. The distribution follows a Gaussian distribution. The mean noise has a value of  $(29.3 \pm 0.1)$  DAC values and does not change for tuned pixel cells. Using the injection capacitance of 36 fF this corresponds to a noise level of  $\sim 126 e^-$ . This value is comparable with earlier ToPix 2 versions ( $129 e^-$  using the JDRS Rev. A [49, Cha. 9.4.3.]) and is well below the required noise level of  $200 e^-$ . This noise level will increase however after the sensor is connected to the front-end chip.

Figure 5.23 shows the two dimensional distribution of the noise value in the untuned case. Pixels with a high noise value of 50 DAC or more also had a high threshold in the untuned case (compare to Figure 5.19).

### 5.3.8. Calibration of Several Pixel at Once

To reduce the time needed to calibrate a complete ToPix front-end with more than 10,000 pixels it is necessary to calibrate more than one pixel at a time.

A first test was performed with two pixel scans at the same time with both pixels from the same double column. Due to the missing buffer readout stage in the current ToPix 3 prototype it is not advisable to inject pixels from different double columns due to the time needed to switch the buffer readout to different double columns.

Figure 5.24 shows a calibration measurement of two pixels from the same side of a double column. If the threshold of the pixels are far apart of each other, both s-curve measurements work as expected. If the thresholds of the pixels are too close to each other the s-curve measurement gets corrupted. For many cases one of the s-curve measurements loses data. For other injected pixel combinations the s-curve scan looks reasonable but the threshold values are shifted compared to the single injection. The data loss always occurs, when pixel with the higher threshold initiate the response.

Discussions with the designer led to the conclusion that this is also an effect of the not appropriate column driver which will be enhanced in the next version of the ToPix [41]. The data is lost due to a conflict on the data bus, triggered by two pixel cells accessing the bus (nearly) at the same time. While the data of the first pixel writing to the bus is still ok the second data gets corrupted. If the thresholds are different the time between the two write out processes gets larger and the possibility of data corruption of the second pixel is reduced.

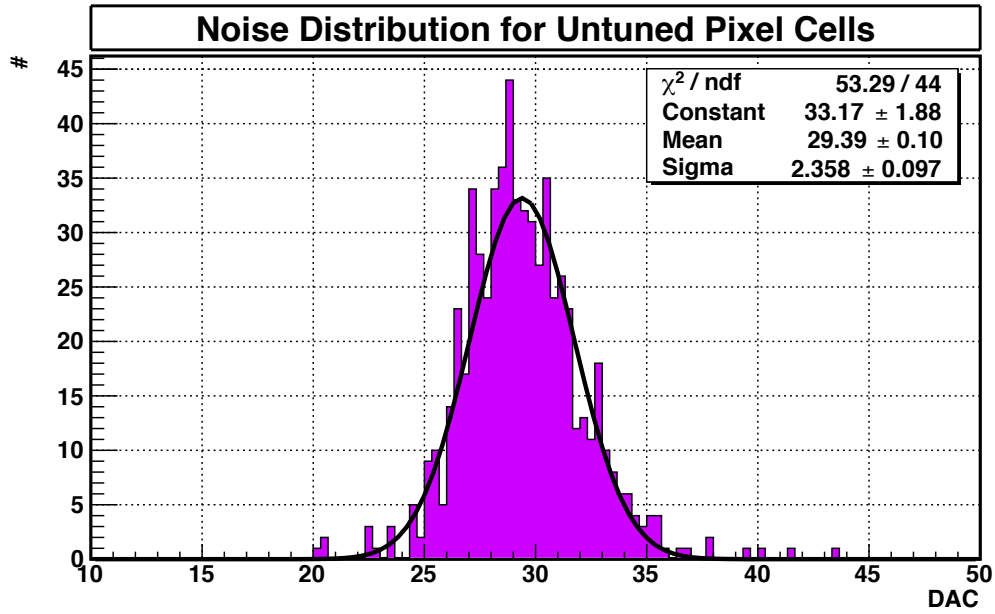


Figure 5.22.: Noise distribution of all pixel cells. The black line indicates a gaussian fit.

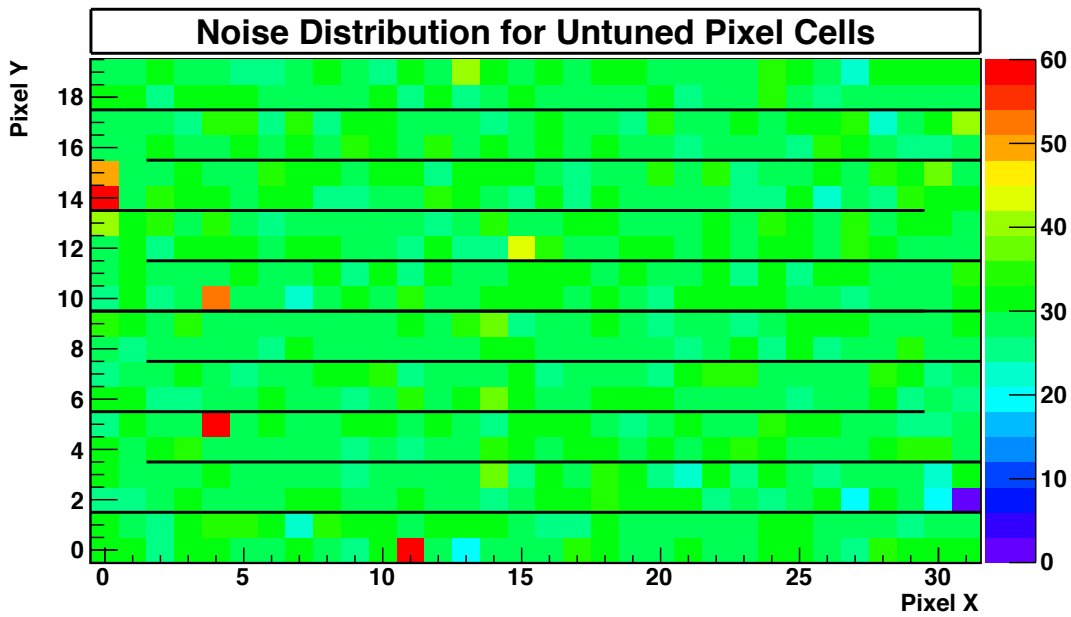


Figure 5.23.: 2D noise distribution of all pixel cells.

## 5. The ToPix 3 Front-End ASIC

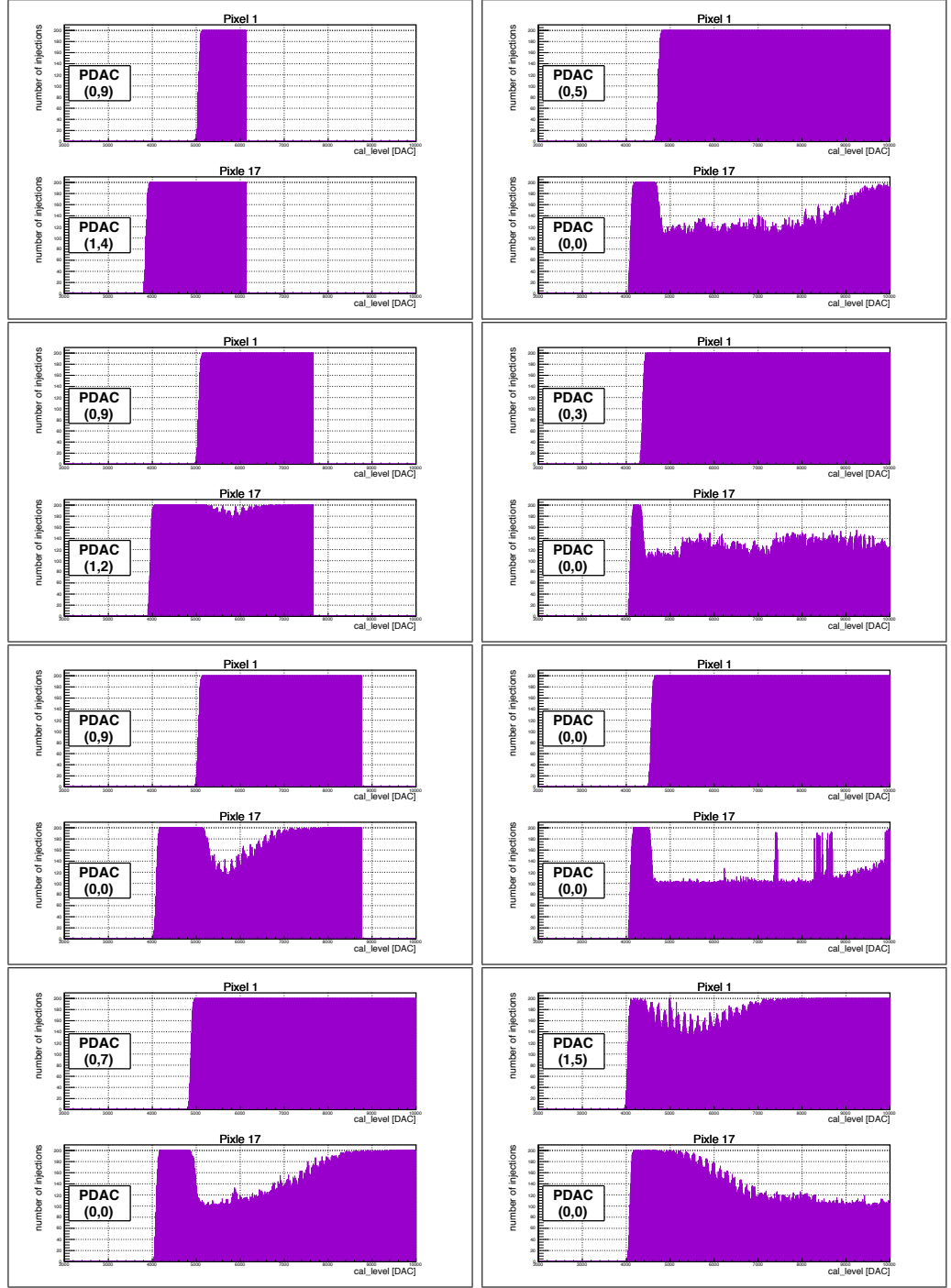


Figure 5.24.: S-curve determination of two pixel cells (1 and 17) of the same side of a double column (col 0, side 0). Each measurement was done with a different PDAC setting. If the pixel threshold are close to each other, the s-curve measurements show a drop of efficiency.



## 5.4. Test Beam

For a complete characterization and test of detector systems, measurements with real particle beams are essential. Those *test beams* offer the possibility to test the detectors under conditions which are very similar to the actual experiment. A test beam has been performed to investigate in the performance of the ToPix 3 and the JDRS at high particle rates, which is described in the following.

### 5.4.1. Setup and Environment

The test beam has been performed with the ToPix 3 ASIC and the JDRS, which has been described in Chapter 4.

The detector test was done at the external beam line of the former Jessica experiment at the Cooler Synchrotron (COSY) accelerator complex at the Forschungszentrum Jülich (see Figure 5.25). COSY is an accelerator for (polarized) protons and deuterons in a momentum range from 0.3 GeV/c up to 3.7 GeV/c. The particles are created in an ion source and pre-accelerated in the Jülich Light Ion Cyclotron (JULIC) before injection into the COSY ring.

For this test a proton beam with momentum of 2.95 GeV/c was available which is above the minimum value for MIPs. With the change of the Micropulse (MP) it is possible to vary the intensity of the COSY accelerator which was used in this test beam.

A MP of 1 means that all protons from the cyclotron are injected into the COSY accelerator, a value smaller than 1 means a reduced amount of particles. The actual amount of particles on the COSY accelerator can be roughly estimated by measuring the beam current. The protons in COSY are extracted continuously over 90 s, the extraction is followed by a pause of 20 s where the accelerator is refilled. The whole procedure is called a *spill*.

The ToPix 3 frequency was set to 50 MHz, to be able to readout all pixels (see Section 5.3.3). The sensor applied to the ToPix is a 100  $\mu\text{m}$  epitaxial sensor.

### 5.4.2. Number of detected Hits

The number of detected hits seen by the ToPix 3 is measured as a function of the MP and the number of protons accelerated in COSY.

Table 5.6 and Figure 5.26 show the hits per spill for the readout of the complete ToPix 3. The hit rate is expected to increase with the higher amount of protons, which is the case. The raise should be linear with the raise of the number of protons, meaning that the fraction of hits per proton should remain constant. But the fraction of hits per proton is decreasing with higher beam intensities, meaning that the ToPix is not able to process all of the hits which appear.

This reduction in efficiency may be connected to the readout scheme of the double columns. Since the end-of-column logic is not finalized for the ToPix 3, the double columns have to be changed by the readout system (see Section 5.1.4). Each double column has a 32 entries deep FIFO to buffer data until the next readout. This changing

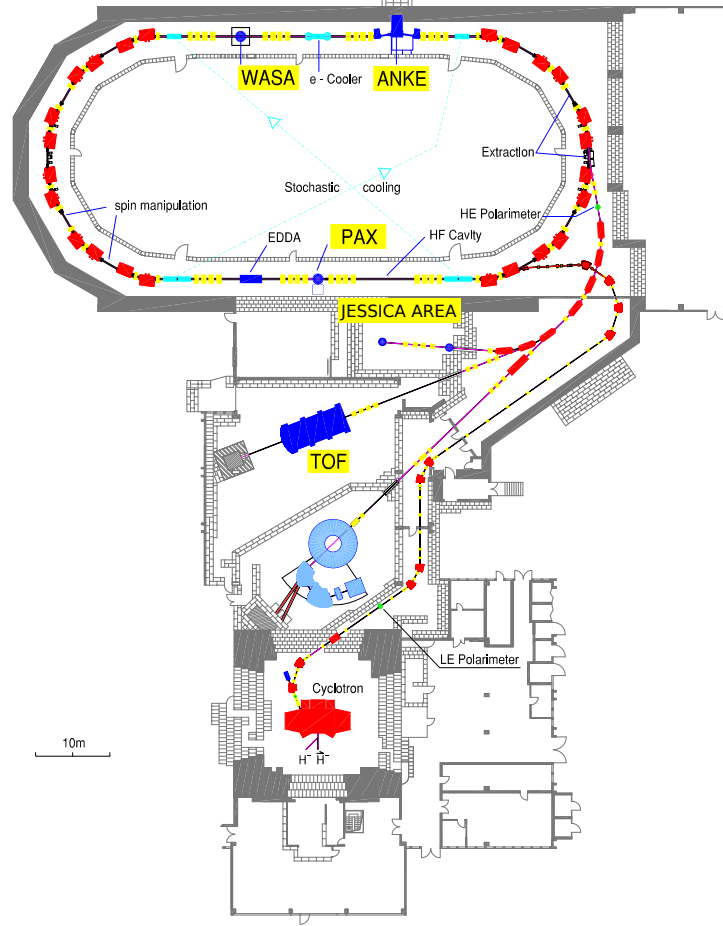


Figure 5.25.: Overview of the COSY accelerator complex at the Forschungszentrum Jülich. At the bottom of the picture is the JULIC cyclotron with the proton and deuteron ion source. The pre-accelerated particles from the cyclotron are injected into to COSY ring at the top of the picture. After the acceleration and cooling to the desired beam momentum the particles are delivered to the different experiments and experimental places marked in yellow in the middle of the picture. Picture taken from Ref. [50].

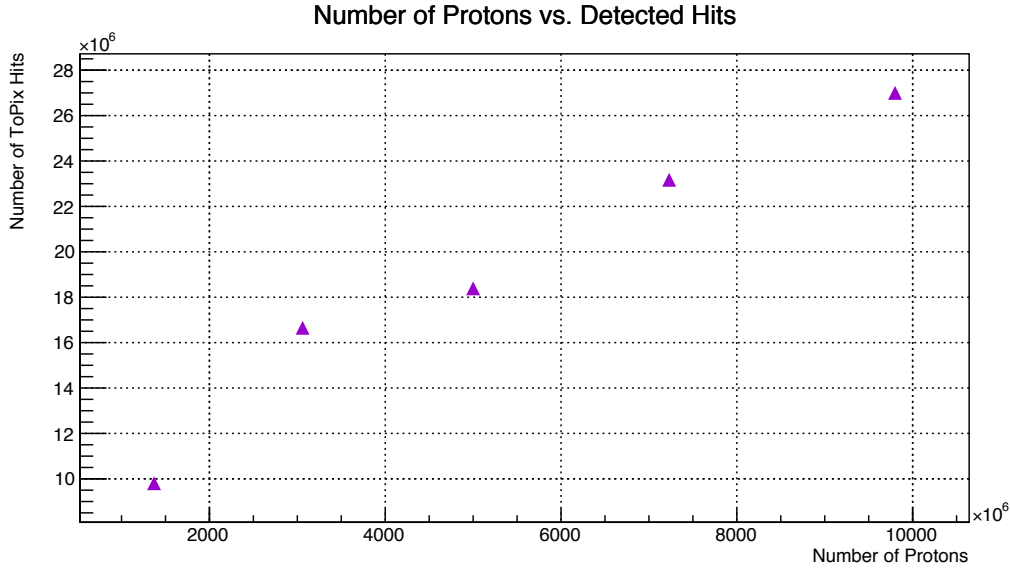


Figure 5.26.: Number of protons in the COSY accelerator versus the number of detected hits per spill for the complete ToPix 3 ASIC.

takes time and reduces the bandwidth. For high data rates the buffer can be too small to save all data until the next readout. If a buffer overflow happens the readout of data is stopped. Hits remain in the pixel cells until the buffer has again free entries. If these pixels are hit a second time while the previous hit is not readout, this hit then gets lost. To test the effect of the external changing of the columns, just the data of one double column was studied (double column 0) in two different readout modes:

a full readout of all double columns (marked as *with column loop*) and the readout of one single double column (marked as *without column loop*).

Figure 5.27 shows the hits per spill of double column 0 with and without the column loop.

MP	# Protons/spill	# ToPix Hits	Hits/(s pixel cell)	Hits/Proton
0.1	$1.37 \times 10^9$	9,804,980	170	0.0072
0.3	$3.06 \times 10^9$	16,653,950	289	0.0054
0.5	$5.00 \times 10^9$	18,390,654	319	0.0037
0.7	$7.23 \times 10^9$	23,173,283	402	0.0032
0.9	$9.80 \times 10^9$	27,001,017	469	0.0027

Table 5.6.: Number of hits per spill seen by the ToPix 3 for different beam intensities with column loop for all double columns. Shown is the setting of the MP, the number of protons per spill, the total number of hits, the mean number of hits per pixel cell and the number of average hits per proton.

## 5. The ToPix 3 Front-End ASIC

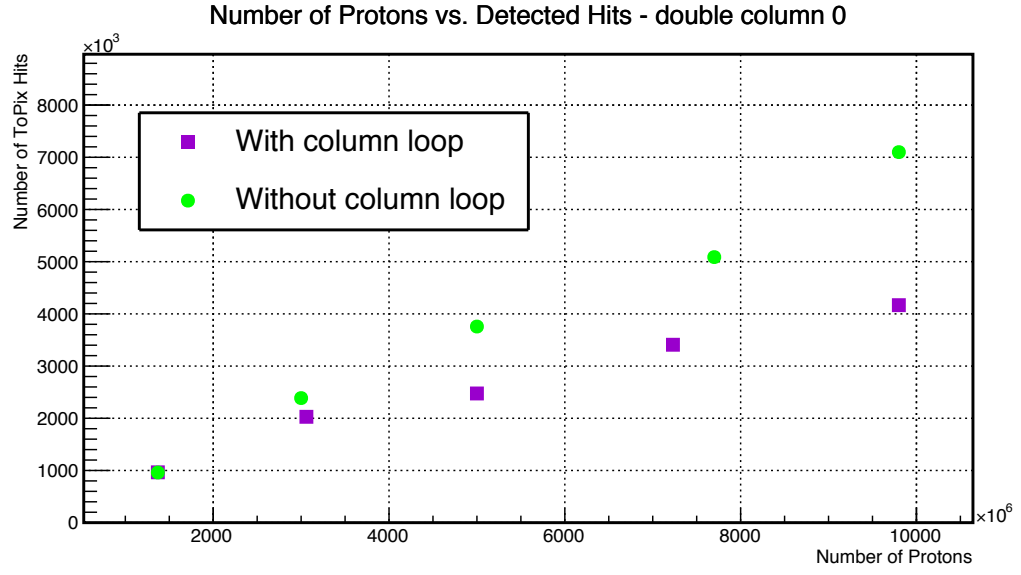


Figure 5.27.: Number of protons in the COSY accelerator versus the number of detected hits in double column 0. Comparison of the settings with and without the column loop.

MP	# P	# hits total	Hits/Proton	# hits even	%	# hits odd	%
0.1	$1.37 \times 10^9$	961,228	0.000702	519,675	54.1	441,553	45.9
0.3	$3.00 \times 10^9$	2,386,947	0.000796	1,287,331	53.9	1,099,616	46.1
0.5	$5.00 \times 10^9$	3,757,421	0.000751	2,028,185	54.0	1,729,236	46.0
0.7	$7.70 \times 10^9$	5,087,548	0.000660	2,752,040	54.2	2,335,508	46.0
0.9	$9.80 \times 10^9$	7,098,837	0.000724	3,845,344	54.2	3,253,493	45.8

Table 5.7.: Number of detected hits per spill for double column 0 without the column loop.

MP	# P	# hits total	Hits/Proton	# hits even	%	# hits odd	%
0.1	$1.37 \times 10^9$	964,579	0.000704	520,529	54.0	444,050	46.0
0.3	$3.06 \times 10^9$	2,028,204	0.000663	1,103,171	54.4	925,033	45.6
0.5	$5.00 \times 10^9$	2,475,145	0.000495	1,392,336	56.3	1,082,809	43.7
0.7	$7.23 \times 10^9$	3,408,532	0.000471	1,988,371	58.3	1,420,161	41.7
0.9	$9.80 \times 10^9$	4,166,857	0.000425	2,485,147	59.6	1,681,710	40.4

Table 5.8.: Number of detected hits for double column 0 with the column loop.

For the lowest intensity the number of hits are nearly identical. The higher the beam intensity gets, the bigger gets the difference between the different readout modes. This is a strong indication of event loss due to buffer overflow while the readout of the whole ToPix 3 ASIC.

In addition of the total hit rate also the hit rate of the odd and even side of the double column was investigated. Both sides of a double column should have the same probability to be readout, reflected in the same amount of hits. Tables 5.7 and 5.8 show the hits split by their column side affiliation.

In both measurements a disbalance between both sides of the double column is visible. The column loop mode shows a growing disbalance between the double column sides with growing beam intensity. Starting at an even-odd relation of 54%-46% at the lowest beam intensity to a relation of 59.6%-40.4% for the highest beam intensity. The increasing disbalance between the odd and even side is not seen in the readout of column 0 without the column loop. This measurement shows, that in a case of buffer overflow the odd and even side are not treated in the same way, preferring the even side. A possible explanation of this behavior is the internal readout behavior of the ToPix 3.

For the non-column loop mode readout it is expected, that no buffer overflow happens. Due to this both sides of the double column should see the same amount of hits. But this is not the case. One sees a constant even-odd disbalance of hits of approximately 54%-46%. The reason for this disbalance is still under investigation.

### 5.4.3. Study of Rate Losses

To study in more detail the reason for the losses of hits an extensive investigation of the leading and trailing edge information was performed.

#### Trailing Edge Distributions

The hit information consist of a leading edge time stamp and a trailing edge time stamp. The particle beam has no time structure within the extraction time of 90 s, due to this the distribution of leading and trailing edges should be homogeneously distributed over all possible timestamp values. Figures 5.28 and 5.29 show the total and the even/odd side trailing edge distribution for the double column 0 (short) and the double column 1 (long). On the abscissa the trailing edge values are displayed (12 bit counter leads to 0d4094 timestamp values). In one spill of 90 s roughly  $10^6$  timestamp overflows occure. So the displayed picture is a overlay of occurred trailing edges (= readout hits) within these  $10^6$  timestamp cycles.

For the lowest beam intensity the trailing edge distribution follows the expected flat distribution. The distribution shows an oscillating behavior around time stamp values of 3100-3400. With higher beam intensities a pattern appears which gets stronger with beam intensity. The distributions show a falling slope in the first 2/3 of the time stamp range until a time stamp value of around 3100. From  $\sim 3100$  to  $\sim 3450$  the distribution follows an oscillating count rate, followed by a rising slope.

A comparison of the even and odd sides of the double column shows again the disbalance

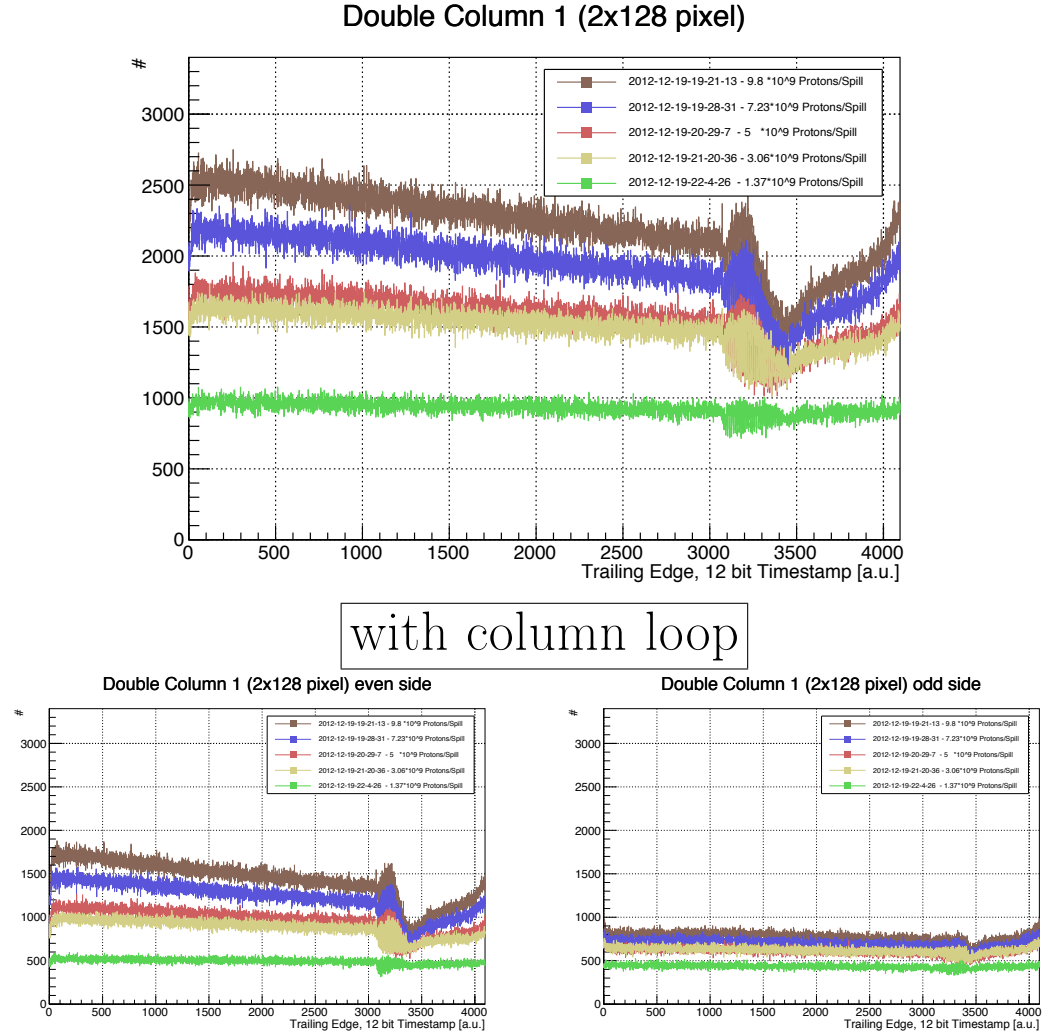


Figure 5.28.: Trailing edge distribution for five different beam intensities with column loop. Upper frame: Both sides. Lower left: even side. Lower right: odd side.

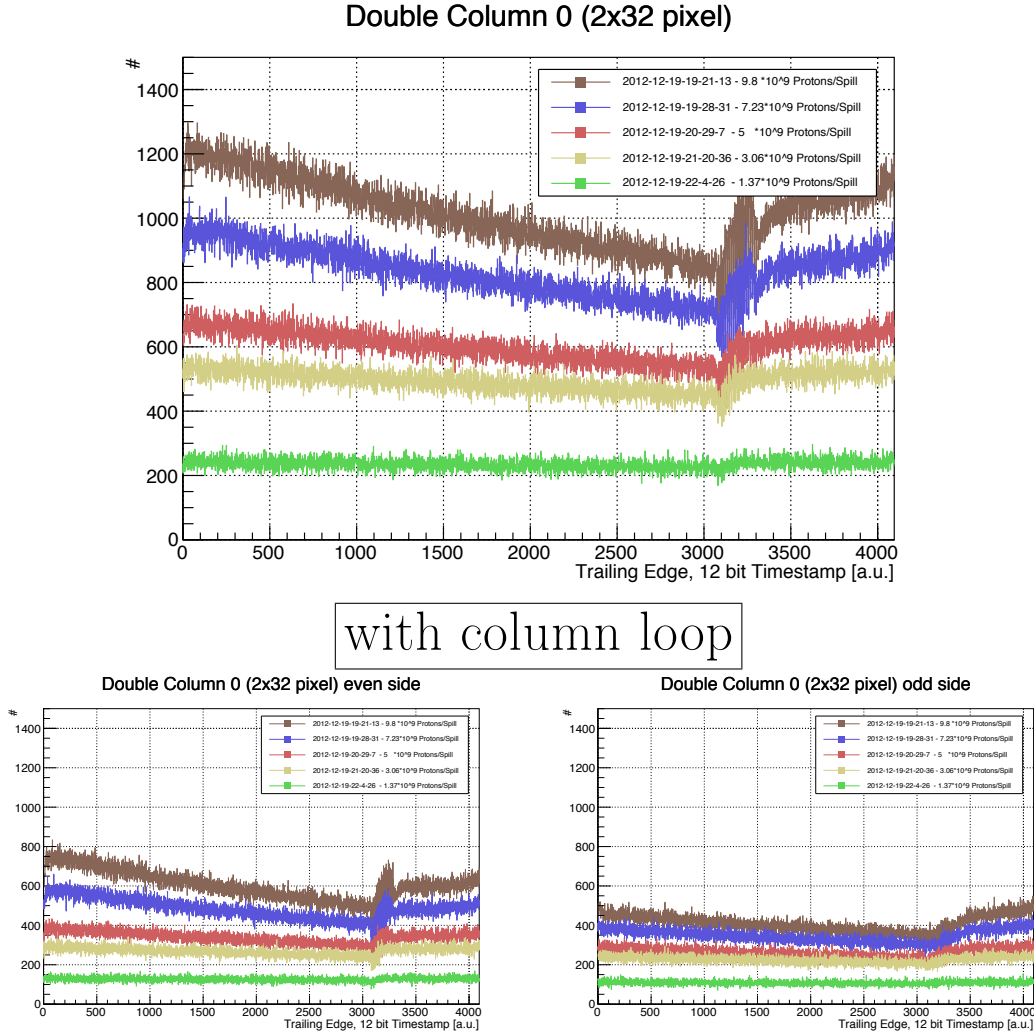


Figure 5.29.: Trailing edge distribution for five different beam intensities with column loop. Upper frame: Both sides. Lower left: even side. Lower right: odd side.

## 5. The ToPix 3 Front-End ASIC

in the number of hits for both sides. The odd side of the double column has a stagnation in number of hits for higher beam intensities compared to the even side. The oscillating part, where the amplitude seems to be correlated with beam intensity, is less pronounced on the odd side compared to the even part.

Figure 5.30 shows the trailing edge distribution of double column 0 (short) without the column loop setting. The distribution shows in general the same pattern compared to the measurement with the column loop. The disbalance of the odd and even sides is less pronounced compared to the previous setting. The total amount of detected hits is higher for all beam intensities. The column loop leads to a loss of hits in the end-of-column buffer, since the loop is not fast enough. The higher the beam intensity is the stronger the effect, as expected since a higher intensity leads to more hits which are lost.

The comparison between the odd and even side of the double column shows the disbalance between the number of hits on both sides.

The trailing edge distribution changes behavior for all histograms at the same trailing edge value close to 3100. This value correlates with the release of the internal freeze signal at 0d3072 (see Section 5.1.4). The release of the freeze signal starts the readout of the hit data from the pixel cells.

The freeze signal is on from clock values 0 until 0d3072. In this time all incoming hits are stored in the internal buffers of the pixel and old hits are readout. After 0d3072 the freeze signal goes down and all stored hits in the pixel cells are marked for readout. New hits can come into the readout process until the overflow of the internal clock happens. After that the cycle starts again.

However, this measurements indicate that this readout scheme is not fast enough for the rates in  $\bar{\text{P}}\text{ANDA}$  and needs to be optimized.

The falling slope at the first 3/4 of the trailing edge values could be related to double hits in the pixel cells. If a particle hit is processed and stored in a pixel cell ready for readout and a second particle hits the pixel cell, the second hit is lost.



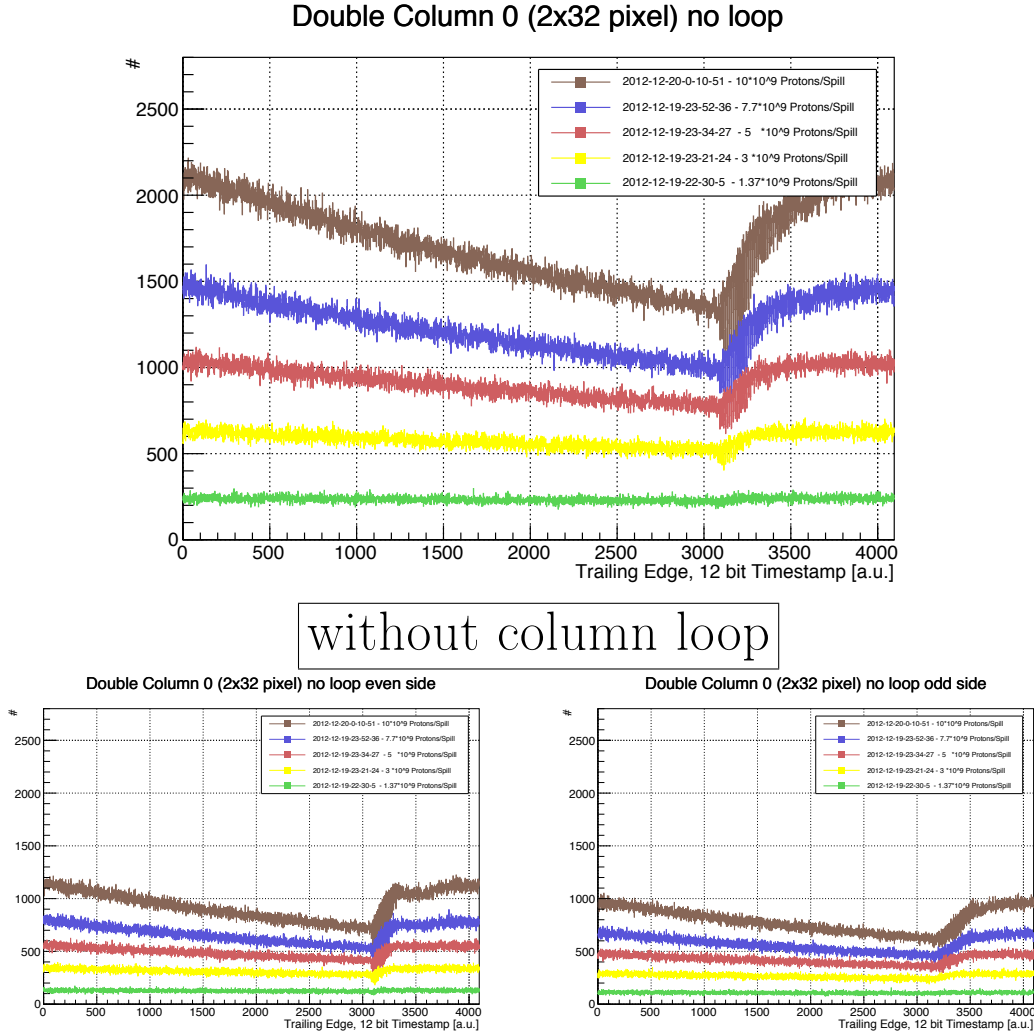


Figure 5.30.: Trailing edge distribution for double column 0 for five different beam intensities without column loop. Upper frame: Both sides. Lower left: even side. Lower right: odd side.

## 5. The ToPix 3 Front-End ASIC

### Leading Edge Distribution

The leading edge distribution should show a homogeneous behavior as expected for the trailing edge distribution. Figures 5.31 and 5.32 show the leading edge distribution for double column 0 and double column 1, respectively.

The measurement of the leading edge distribution varies strongly from the expected homogeneous distribution. The behavior looks similar to the distribution of the trailing edge shown before and the correlation between leading edge and trailing edge is studied in more detail in the following part.

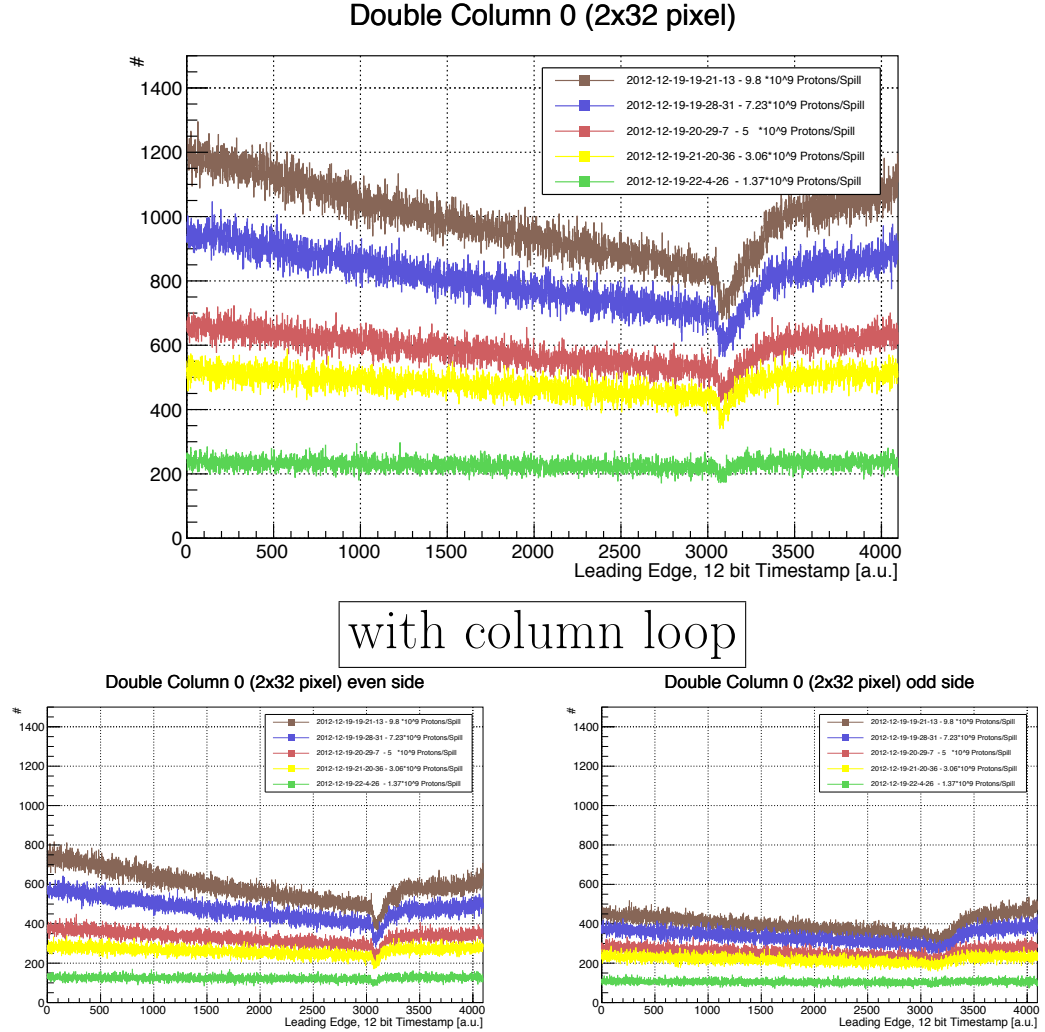


Figure 5.31.: Leading edge distribution for five different beam intensities for double column 0 (short) with column loop. Upper frame: Both sides. Lower left: even side. Lower right: odd side.

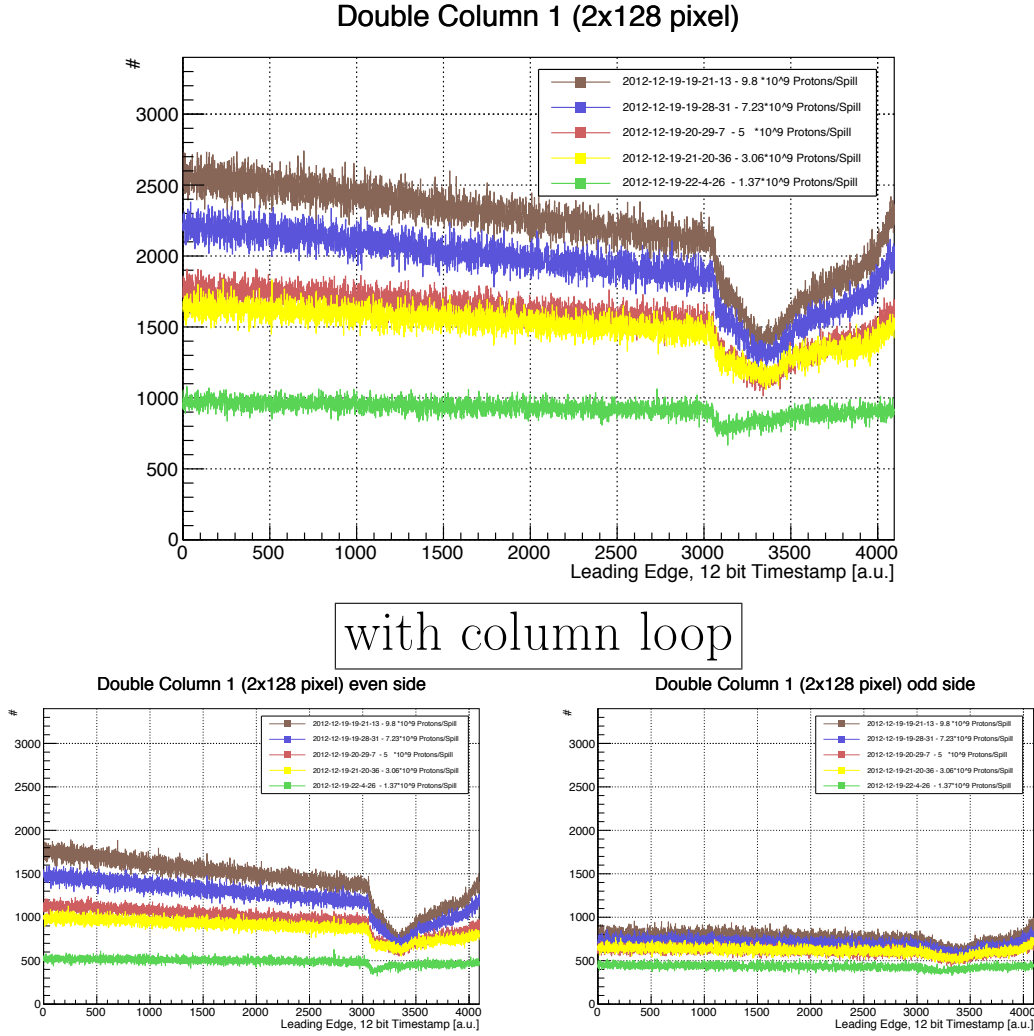


Figure 5.32.: Leading edge distributions for five different beam intensities for double column 1 (long) with column loop. Upper frame: Both sides. Lower left: even side. Lower right: odd side.

### **Leading Edge - Trailing Edge Correlation**

Figures 5.33 and 5.34 show the trailing edge of a hit as a function of the leading edge. The difference between trailing edge and leading edge is proportional to the deposited charge. Therefore the trailing edge is correlated with the leading edge via the Landau distribution. Thus one would expect an intense diagonal line coming from the most probable value of the Landau distribution, a small band with lower trailing edge values and a wide distribution of large trailing edge values coming from the long tail of the Landau distribution. This general behavior can be seen in Figures 5.33 and 5.34 if one takes into account that timestamp values are not corrected for timestamp overflows.

In addition to the expected behavior one sees a horizontal band in the histogram. In the horizontal band the entries have a trailing edge value between 3100 and 3400 and leading edge values between 0 and 3400. For most of the entries the ToT (trailing edge minus leading edge) is too high to be explained by a real hit.

The values in this band have most probably a correct trailing edge value, but a wrong leading edge value. The leading edge distribution shows a dip at the area between 3100 and 3400, meaning that entries are missing. These entries are equally distributed on the other leading edge values.

With increasing beam intensity the horizontal band becomes more populated. For the highest beam intensity the area above the band is also more populated than it should be.

The effect exists for the long double columns as well as for the short double columns. For the short double columns the horizontal lines are less populated compared to the long double columns.

The reason for the horizontal band is still under investigation. It is probably a corruption of the data words during readout of the pixel cells. This would explain the non-physical ToT values and would match to the problems seen in the lab measurements for injecting two pixels in the same double column at the same time (see Section 5.3.8).

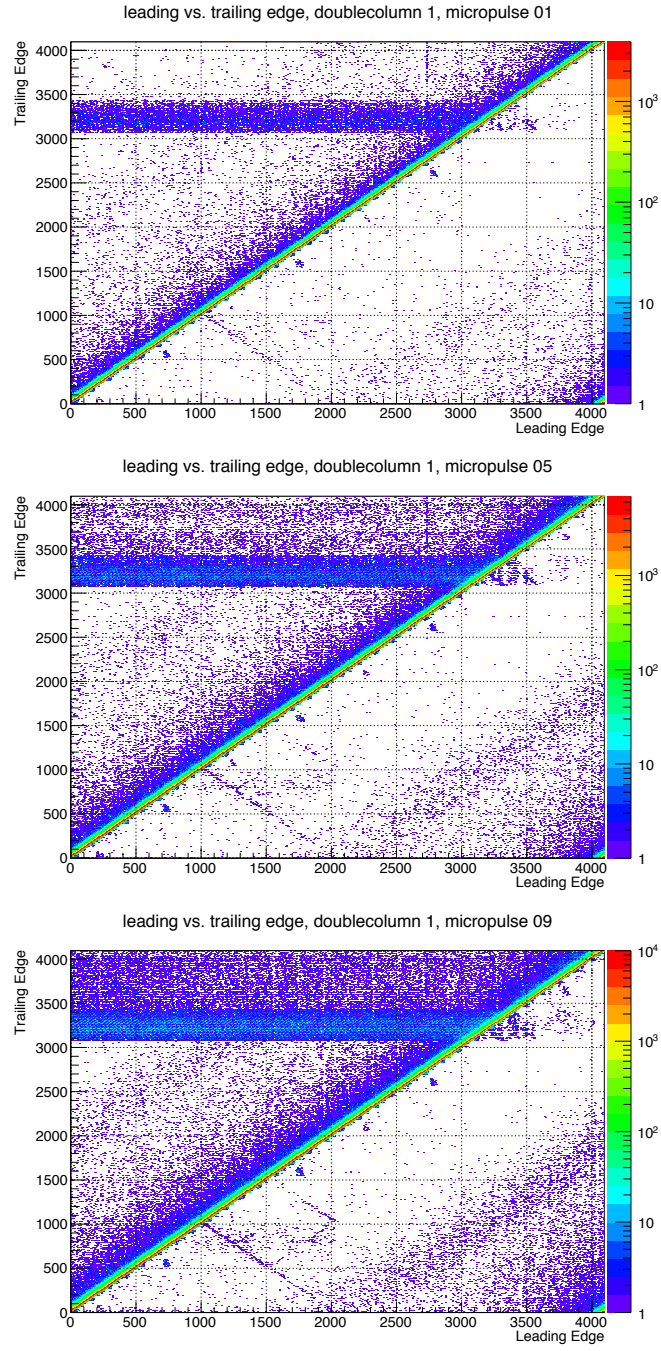


Figure 5.33.: Leading edge vs. trailing edge distribution for different beam intensity of the long double column 1. Upper: MP 0.1. Middle: MP 0.5. Lower: MP 0.9.

## 5. The ToPix 3 Front-End ASIC

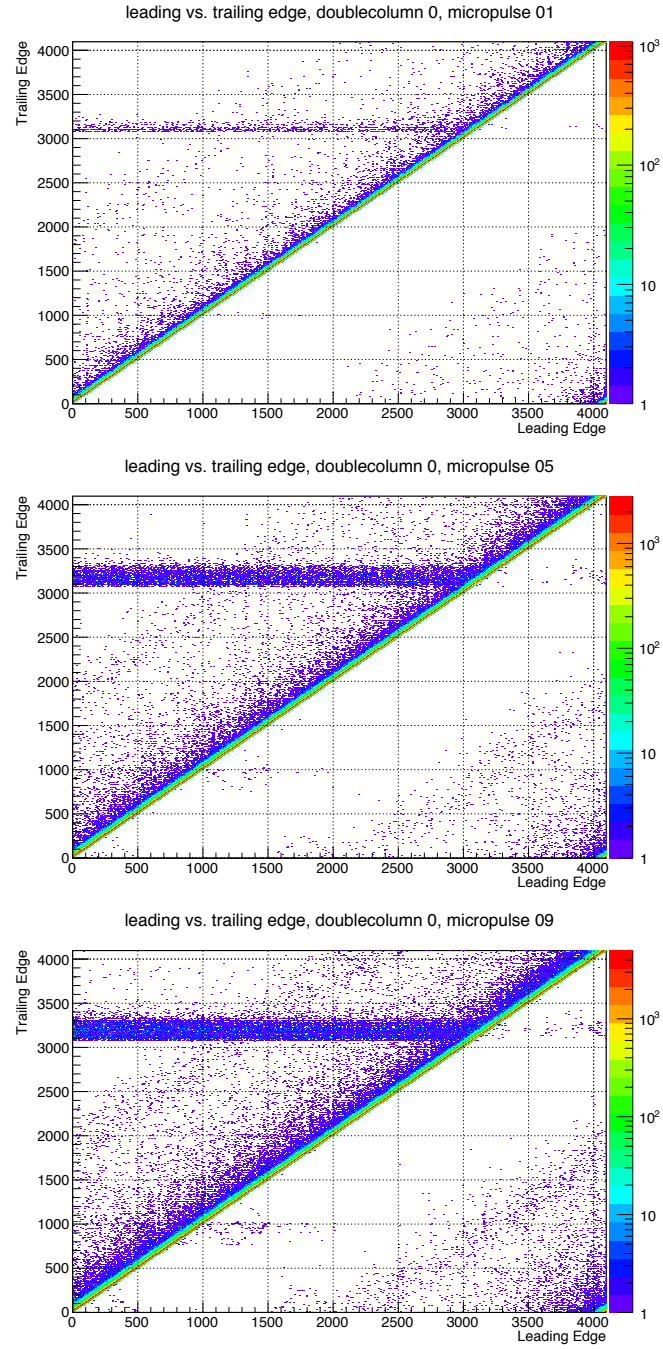


Figure 5.34.: Leading edge vs. trailing edge distribution for different beam intensity of the short double column 0. Upper: MP 0.1. Middle: MP 0.5. Lower: MP 0.9.

## 5.5. Conclusion

The ToPix 3 is a reduced size prototype of the MVD pixel front-end electronics. Characterizing measurements of the ToPix 3 have been done using the JDRS in lab and test beam measurements.

The ToT charge measurement has been demonstrated to be linear within 1 %. The gain of the CSA has been measured to be 5.23 nA, which agrees with the preset gain of 4.8 nA within the errors. The untuned threshold distribution has been measured to have a dispersion of  $\sigma=539\text{ e}^-$ . A tuning procedure has been applied to calibrate the individual PDAC settings of the pixel cells. The width of the threshold distribution could be reduced down to  $\sigma=64\text{ e}^-$ , which is below the design requirement of  $200\text{ e}^-$ . The mean noise level has been measured to be  $\sim 126\text{ e}^-$ , which is below the design requirements of  $200\text{ e}^-$ .

Measurements have been done in the range from 50 MHz to 155 MHz. It has been confirmed that the column driver the clock frequency of the ToPix 3 has to be set to 50 MHz to have all pixel cells working this is because the column driver has been dimensioned too small. With higher clock frequencies the pixel cells at the end of the long double column stop working. The higher the clock frequency the more pixel cells are effected.

To reduce the time necessary to configure all pixel cells, a test have been made to configure more than one pixel cell at the same time. The test showed that data loss can occur at identical threshold positions of two pixel cells. This problem is most probably an effect of the column driver.

For the first time a high rate test beam has been performed with the ToPix 3. The test beam showed an unexpected data loss at higher event rates for certain trailing edge time stamps. The structure of the event loss is correlated with a ToPix 3 configuration setting which steers the readout scheme.

The test beam showed furthermore an asymmetry in the event rates for the odd and the even side of a double column. The odd-even event rate has a ratio of 54%-46% for the lowest beam intensity. With higher beam intensities the asymmetry rises up to a ratio of  $\sim 60\%-40\%$ . This measurement shows that the readout scheme has a preference for the odd side of a double column, which depends on the hit rate of the detector.

In another analysis the readout of the ToPix 3 was limited to a single short double column to achieve highest readout speed. The odd-even asymmetry was 54%-46% and stayed constant for all beam intensities. This measurement indicates that at least part of the asymmetry is coming from the readout of the hit data into the end-of-column buffer when buffer overflows happen. These effects will be fixed in the next prototype version of the ToPix ASIC.





## 6. Simulation of the $\bar{\Lambda}\Lambda$ Final State

---

*Deep in the bosom of the gentle night  
Is when I search for the light  
Pick up my pen and start to write  
I struggle, fight dark forces  
In the clear moon light  
Without fear... insomnia*

Faithless - Insomnia

---

The  $\Lambda$  particle is the lightest of the strange hyperons, it occurs in many decay trees of heavier hyperon particles.  $\Lambda$  hyperons decay weakly and thus parity is not conserved. This opens the possibility to investigate spin correlations and the polarization of the hyperon. With the  $\Lambda$  the creation of quark-antiquark pairs (in particular of the strange quarks), can be investigated, and the formation of these quarks with other quarks to hadrons.

To investigate these topics, precise simulations of the whole detector setup and the particle interactions are necessary. With these simulations, an analysis of the decay can be done to prove the reconstruction ability of the detector and the analysis framework. In this chapter, the reaction  $\bar{p}p \rightarrow \bar{\Lambda}\Lambda \rightarrow \bar{p}\pi^+p\pi^-$  is investigated using the PandaRoot simulation and analysis framework. The analysis will show the reconstruction efficiency of the detector and the analysis framework. In addition, the question is investigated how much two additional semiconductor layers, the so-called  $\Lambda$ -disks, can contribute to the reconstruction efficiency of hyperons.

### 6.1. Simulation Framework

Powerful software tools are essential for the simulation and analysis of the performance of the  $\bar{P}$ ANDA detector. Decay studies must be done prior to building the experiment in order to determine the hardware specifications and to optimize the detector layout as well as to develop the event reconstruction and analysis algorithms. In addition, Monte Carlo (MC) simulations of the full detector are necessary to interpret the data that will be measured later with the detector. The framework contains a geometry model of the  $\bar{P}$ ANDA detector. The detector response to particles traversing the sensitive layers is realistically simulated. Particle tracks are reconstructed and analyzed to extract the track information of the charged decay products. With this information one is able

## 6. Simulation of the $\bar{\Lambda}\Lambda$ Final State

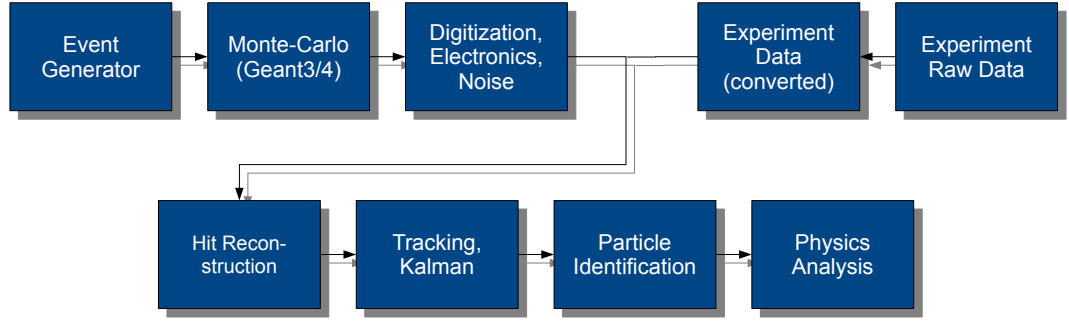


Figure 6.1.: Schematic workflow of data processing with the PandaRoot framework. The reconstruction and analysis part can use either simulated or real data as input. Figure taken from Ref. [51].

to reconstruct events and investigate the processes that happened within the primary interaction. The analysis part can be fed with simulated data or real experimental data, this has the benefit of developing and cross-checking the reconstruction and analysis algorithms before the experiment starts and allows to use the same framework later while data taking (see Fig. 6.1).

PandaRoot consists of mainly three parts which are described in the following:

**FairRoot** To avoid that all experiments at the FAIR facility develop their own simulation and analysis software, a common structure of functionality which is identical for the experiments was created. The so-called FairRoot classes manage the parameter database, data streams, file handling, as well as the interface to third-party software from external packages.

**PandaRoot** The PandaRoot [52] classes inherit from general FairRoot detector classes and implement the  $\bar{\text{P}}\text{ANDA}$  detector specific characteristics. They implement the detector geometry, the digitization for the individual detector parts and detector specific track finding and fitting, Particle Identification (PID) and analysis.

**External Packages** The external packages form a collection of third-party software which are included in FairRoot. It provides functionality used for simulation or analysis. The packages contain programs for event generation (Pluto [53], Pythia [54], DPM-Gen [55, 56], UrQMD [57, 58, 59], EvtGen [60]), particle propagation through material (GEANT3 [61] & Geant4 [62]), ROOT [63] and Virtual Monte Carlo (VMC). VMC allows the usage of different MC engines without changing the code, this makes the comparison very easy. ROOT covers an immense amount of functionality for high energy physics experiments like data presentation, graphical interface, mathematical calculation, file management etc.

In the following the single simulation steps are explained using the tracking detectors as an example.

### 6.1.1. Event Generator

The first step of the simulations is the generation of the physics process of interest. Event generators simulate the physical processes in the primary interaction of the beam with the target material. The output of an event generator is a list of position and 4-momenta vectors of particles created in the primary interaction. Different kinds of event generators exist to simulate specific physical channels, background reactions or so-called particle guns, which just create one given type of particle with a user defined range of momentum and direction. Different event generators can be used within the PandaRoot framework for the particle decay of interest. The most important event generators are:

- **EvtGen/EvtGenDirect** allows the simulation of a single decay channel. This channel can be user-defined or chosen from a database of existing decay trees. Not only branching ratios but also decay models can be chosen. It is also possible to include user-defined decay-models for special decays.
- **DPMGen** generates elastic and inelastic  $\bar{p}p$  reactions with the dual parton model. It is used as the main event generator for background reactions in  $\bar{P}$ ANDA.
- **UrQMD** Antiproton-nucleus ( $\bar{p}$  A) reactions are simulated with the UltraRelativistic Quantum Molecular Dynamics (UrQMD) model.
- **Box Generator** The Box Generator, also called the “particle gun”, shoots one or more particles per event randomly into the detector. The user can set the numbers of particles per event, momentum range and the direction range of the particles being shot.

### 6.1.2. Propagation

After the production of particles by one of the event generators mentioned above, the particles are propagated through the detector and interact with the detector material. This task is executed by a propagation software. This software calculates the tracks of the particles through the magnetic field and the material of the detector. The effect of active and passive material on the energy and direction of the particle are taken into consideration. Possible effects are e.g. scattering, nuclear reactions, bremsstrahlung or ionization. The effects are randomly applied to the particle taking into account the expectation value and variations of the probability of these effects. In addition the decay of the primary particle and the creation of secondary particles is calculated. A **MCTrack** object is created for each particle containing the creation point of the particle, its four momentum vector and a link to the mother particle it originates from.

A particle passing through active detector material creates a so-called **MCPPoint**. This point saves the entering and exiting coordinate of the particle in the material, the time when it happens and the deposited energy.

## 6. Simulation of the $\bar{\Lambda}\Lambda$ Final State

In PandaRoot, the propagation is done mainly with GEANT3/Geant4 (**G**eometry **a**nd **T**racking). It uses MC methods and is developed at CERN. PandaRoot takes advantage of VMC which is included in ROOT, giving the opportunity to exchange both Geant versions through a common, unified interface using the same geometry description for both propagators. This is a very convenient way to compare the propagation results of GEANT3 with Geant4. VMC is a development by the ALICE software project [64].

### 6.1.3. Digitization

After the creation of particles and their transport through the detector, the response of the active detector material is emulated. This step is called digitization.

The digitization task takes the created `MCPoints` and calculates the deposited energy according to entry and exit points of the sensitive element of the corresponding detector. Physical effects like electron drift and noise are simulated. The behavior of the electronic readout is implemented e.g. thresholds for the signals. The output of the digitization stage is a `Digi` which should be as similar as possible to the real experimental data. Using these tools, the reconstruction and analysis software can be developed before the experimental data is available.

### 6.1.4. Reconstruction

#### Local Reconstruction/ Hit Reconstruction

The aim of the local reconstruction is the translation from measured, digitized quantities into global physical quantities. For tracking detectors this is for example the calculation of hit coordinates in the global coordinate system of the detector from fired front-end and pixel numbers. It includes also clusterization of neighboring channels and improvement of hit coordinates by correlation of the deposited charge in these channels.

The output of this stage is for tracking detectors a `RecoHit`, containing the space coordinates, a timestamp, the deposited energy and the corresponding errors.

#### Track Finding and Fitting

In the track finding step, reconstructed hits from different detectors and detector layers are combined to possible tracks from particles. Different algorithms are available to find particle tracks like the Riemann track finder [65] or conformal mapping [66] and Hough transformation [67, 68].

These track finding algorithms provide in addition a pre-fit of the track parameters. These pre-fit data is used as input into a Kalman based track fitter which calculates the track parameters taking the complete detector geometry and the measured magnetic fields into account. Within PandaRoot the track fitting is done with the GenFit package (Rev. 400) [69]. GenFit is a general track fitting framework developed in C++ not limited to any specific experiment. It uses Kalman Filter [70, 71] and Deterministic Annealing Filter algorithms.

## Particle Identification

The next important step for the reconstruction of the event is the identification of particles which leave a track in the detector. There are almost always five particle types which live long enough to generate signals in the sensitive layers of the detector:  $e$ ,  $\mu$ ,  $\pi$ ,  $K$  and  $p$ . In addition to dedicated PID detectors, nearly all detectors can in principle contribute to the process of particle identification. Each detector has the capability to calculate from e.g. the energy loss of a particle in the active material a Probability Density Function (PDF) for each of the above mentioned particle types. This function reflects the probability of a given particle being of a certain kind. In a global particle identification these individual PDFs are combined to an overall particle PDF.

### 6.1.5. Physics Analysis

After all particle tracks are reconstructed and identified the reconstruction of events takes place. The reconstructed particle tracks are combined to mother particle candidates. These candidates are further fitted with the particle candidate constraints to test the hypothesis.

The combination and handling of the particle candidates is done with the Rho package [51, 72] integrated in the PandaRoot framework. The Rho package contains selected parts from the BETA [73] analysis package of the BaBar experimental framework.

Rho takes care of particle candidate lists. It offers a convenient way to combine reconstructed tracks to candidates and takes care of combinatorial issues like double counting and overlapping. Cut criteria can be applied such like mass or PID cuts. MC truth information are provided for cross-checks. Different fitters are available and can be applied to single particle candidates such as whole decay trees. Fitted candidates are saved in addition to the original tracks for a convenient comparison.

## 6.2. Grid

To reduce the statistical errors of the simulation a large number of signal events and an even larger number of background events are necessary. Even the newest single user computers are not powerful enough to simulate and analyze a sufficient number of events in a reasonable time. For the simulation of millions of signal and background events a *Grid* (PANDA Grid) was set up which allows the simulation of a high number of events in a short time. A Grid is a collection of computer resources at different locations which are combined to work on a single task, in this case the simulation and analyzation of PandaRoot events.

The PANDA Grid uses the Grid software from the ALICE experiment, Alice Environment (AliEn) [74]. AliEn is a lightweight Open Source Grid Framework. Clients (the user) can send so-called *jobs* to the Grid. These jobs are described in a Job Description Language (JDL) file which defines the simulation parameters. In the central services the jobs are split and distributed to different working sites all over the world. These jobs can be

## 6. Simulation of the $\bar{\Lambda}\Lambda$ Final State

controlled by the AliEn monitoring software called Monitoring Agents using a Large Integrated Services Architecture (MonALISA) [75].

### 6.3. Simulation of the $\bar{\Lambda}\Lambda$ Final State

#### 6.3.1. Coordinate System

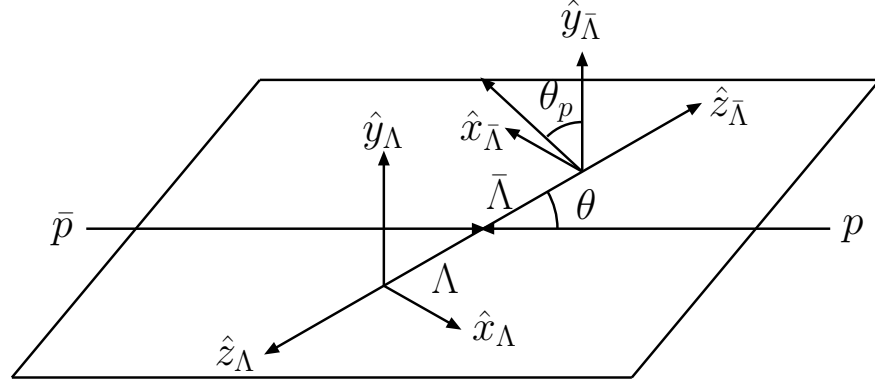


Figure 6.2.: The center-of-mass frame for the  $\bar{p}p \rightarrow \bar{\Lambda}\Lambda$  system. Drawn in this sketch is the coordinate system for the CMS frame of the  $\Lambda$  or  $\bar{\Lambda}$ . Figure taken from Ref. [76].

Figure 6.2 shows the Center-of-Mass System (CMS) for the interaction  $\bar{p}p \rightarrow \bar{\Lambda}\Lambda$ . To analyze the decay of the hyperons into the final state particles it is convenient to define a coordinate system in the rest frame of the hyperon/anti-hyperon. The scattering plane of the decay is defined by the incoming antiproton momentum vector and the outgoing hyperon momentum vectors. The vector product of these two vectors defines the normal vector to the scattering plane. These vectors are the basis for the rest frame. The hyperon momentum vector sets the z-axis of the coordinate system [77].

$$\hat{z} = \vec{p}_i, \quad i = \Lambda, \bar{\Lambda} \quad (6.1)$$

The normal vector to the scattering plane defines the y-axis.

$$\hat{y} = \hat{z} \times \vec{p}_{\bar{p}} \quad (6.2)$$

The x-axis is defined in that way, that the coordinate system is right-handed.

$$\hat{x} = \hat{y} \times \hat{z} \quad (6.3)$$

After determining the reference frame and coordinate system, detector efficiency studies can be performed as a function of the kinematic variables.

## 6.3.2. Detector Geometry

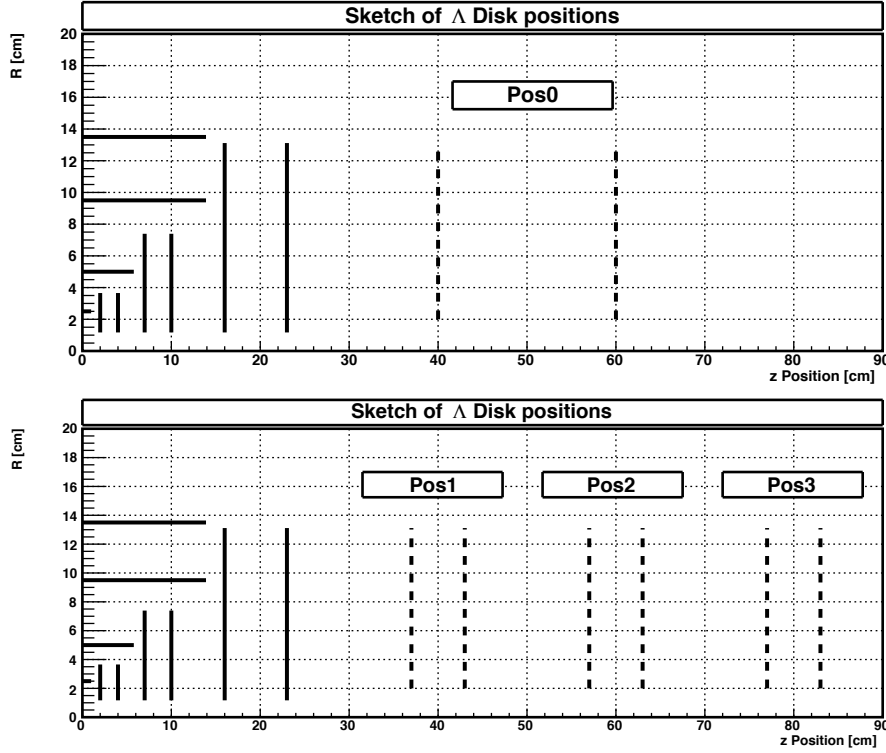


Figure 6.3.: Sketch of the MVD and the different  $\Lambda$ -disk positions. Solid lines indicate the MVD, dashed lines the  $\Lambda$ -disks. The point of origin is identical with the interaction point. The upper sketch displays the proposed disk position at 40 cm and 60 cm, the lower picture displays three disk positions with the proposed double disk at around 40 cm, 60 cm and 80 cm.

Due to their weak decay, strange hyperons have a comparably long lifetime and a typical flight distance of several to tens of centimeters. This leads to a decay of the hyperons in an outer part or even outside of the MVD. Hits within the MVD are important for the resolution of the tracking system since the MVD delivers high precision 3D points. To improve the track quality for hyperons it is proposed to add two additional semiconductor detector layers in the empty space between the MVD and the GEM stations. These disks consists of silicon strip sensors similar to those in the MVD disks 5 and 6. In the following these additional disks are called  $\Lambda$ -disks.

In this thesis it is investigated how much the  $\Lambda$ -disks contribute to the reconstruction capability of  $\bar{\text{PANDA}}$  for  $\Lambda$  hyperons. Four different configurations of the  $\Lambda$ -disks are investigated and compared to the setup without the  $\Lambda$ -disks (see Figure 6.3, Table 6.1). The first design configuration foresees two independent semiconductor disks located at 40 cm and 60 cm. In the following this configuration is called Pos0. For the following

## 6. Simulation of the $\bar{\Lambda}\Lambda$ Final State

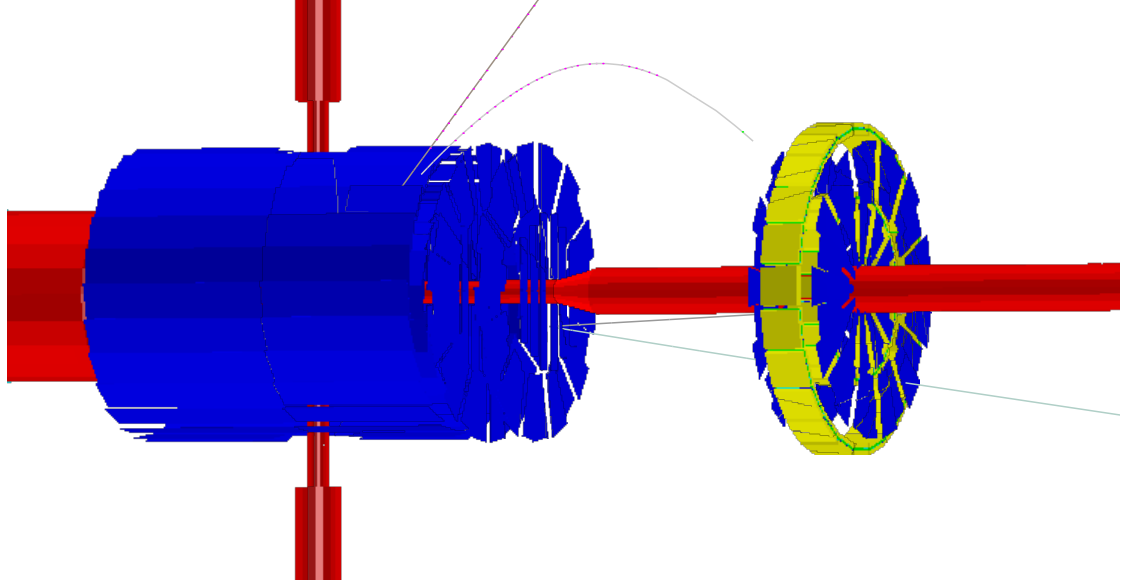


Figure 6.4.:  $\bar{\Lambda}\Lambda$  geometry of the beampipe (red), MVD sensors (blue, left) and  $\Lambda$  double disk (blue and yellow). Blue indicates active sensor material, yellow indicated front-end electronics and support. Just the front-end electronics and support for the  $\Lambda$  double-disk (Pos2) are displayed.

three positions the disks are closer together and form a unit with a separation of 6 cm between the disks. This reduces the material budget since parts of the readout and holding structures can be shared between the two disks (see Figure 6.4). This double disk is then positioned around 40 cm (Pos1), 60 cm (Pos2) or 80 cm (Pos3) with respect to the interaction point. All these positions are compared to simulations without  $\Lambda$ -disks (Pos-1).

Figure 6.5 shows a single  $\Lambda$ -disk. Green indicates the 300  $\mu\text{m}$  thick silicon sensors. The blue and grey blocks represent the readout, cooling and support structure for the disk. The blocks consists (from inside to outside) of 8 mm of aluminum, 0.4 mm of silicon, 0.4 mm of carbon fibers and 2 mm of carbon foam.

### 6.3.3. Simulation

The EvtGenDirect event generator is used for the simulation of the  $\bar{\Lambda}\Lambda$  final state. EvtGen provides three different decay models for the  $\bar{\Lambda}\Lambda$  final state: *LambdaLambdaBar*, *LambdaLambdaBarPol* and *LambdaLambdaBarHE* (see Figure 6.6).

*LambdaLambdaBarPol* is based on the measured  $\bar{\Lambda}\Lambda$  angular distribution from the PS185 experiment [78]. The experiment measured the angular distribution for 1.642 GeV/c and 1.918 GeV/c. Due to that, the model *LambdaLambdaBarPol* is limited to beam momentum  $< 2.5$  GeV/c, above this momenta the same distribution is just scaled with the beam momentum.



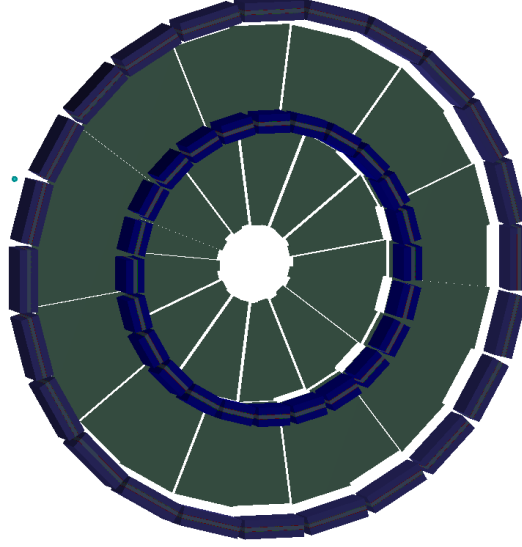


Figure 6.5.: Geometry of a single  $\Lambda$ -disk. Green indicates semiconductor material. Blue/grey blocks represent the readout, cooling and support structure.

Position Name	Location disk one	Location disk two
Pos-1	-	-
Pos0	40 cm	60 cm
Pos1	37 cm	43 cm
Pos2	57 cm	63 cm
Pos3	77 cm	83 cm

Table 6.1.: Positions of the  $\Lambda$ -disks for the different options.

In addition to the data from the PS185 experiment the model *LambdaLambdaBar* includes a parametrization of a wire chamber experiment at the CERN PS which was performed at 6 GeV/c [79].

The measured differential cross section distribution of the PS185 experiment is displayed in Figure 6.7 in comparison with the simulated MC angular distribution.

The distribution for *LambdaLambdaBarPol* and *LambdaLambdaBar* at 1.642 GeV/c and 1.918 GeV/c are identical, since they have the same parametrization. The overall tendency of the simulated distribution matches with the experimental data, the  $\bar{\Lambda}$  is strongly boosted in the forward direction. The forward boost of the  $\bar{\Lambda}$  is visible in Figure 6.8, which shows the decay points of  $\Lambda$  and  $\bar{\Lambda}$  for the lowest and the highest beam momentum. Minor differences exist between the simulated and real distribution. In forward directions the medium energy distribution is shallower than measured. In the backward region, around  $\cos(\Theta_{\bar{\Lambda}}) = -0.7$ , the bump of the medium energy distribution is not as pronounced as in the experimental data. The low energy distribution describes a small positive bump in backward direction rather than remaining flat as in the experimental

## 6. Simulation of the $\bar{\Lambda}\Lambda$ Final State

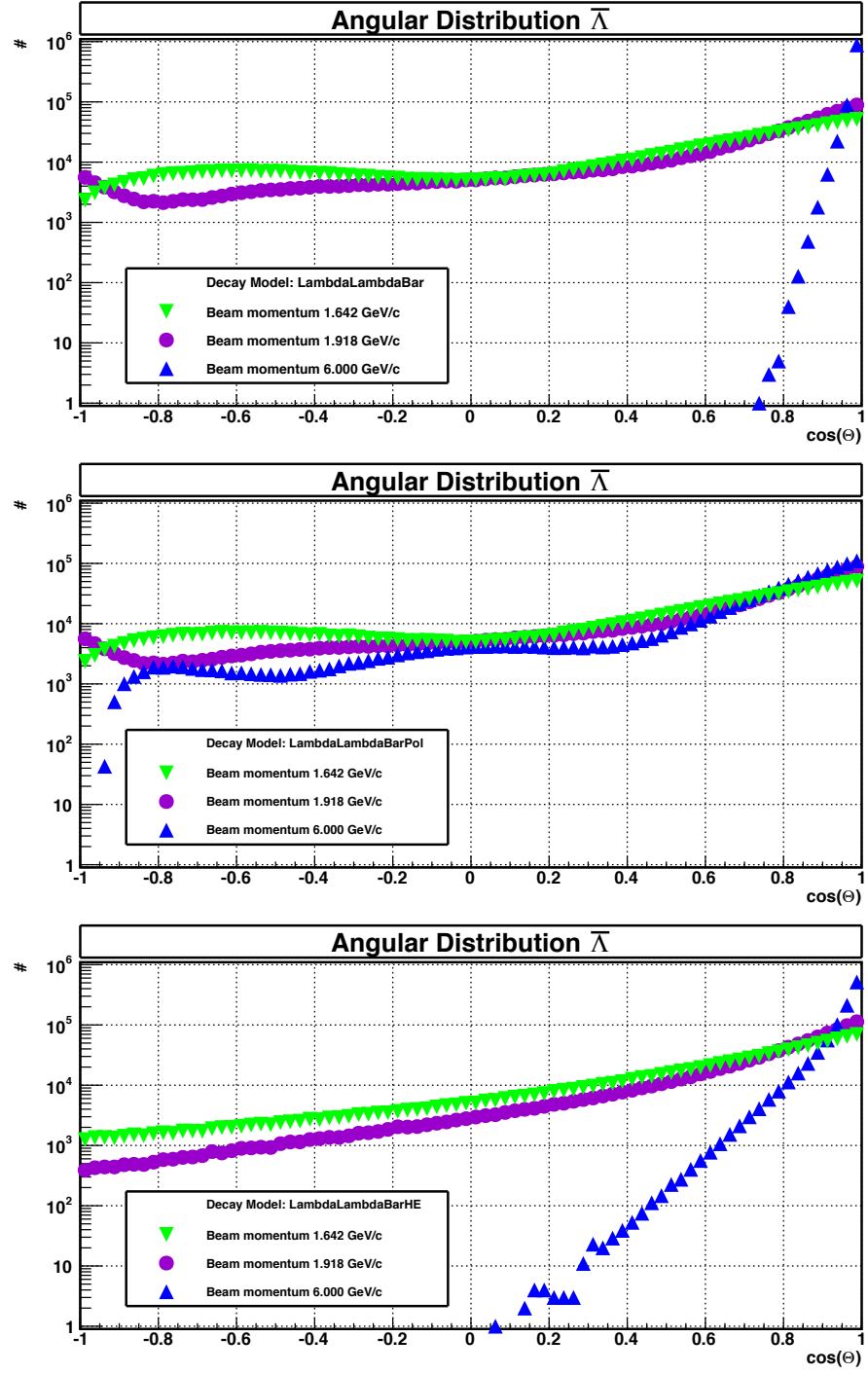


Figure 6.6.: Simulated angular distribution of the  $\bar{\Lambda}$  for three different event generator models. Green/Triangle down: 1.642 GeV/c. Violet/Circle: 1.918 GeV/c. Blue/Triangle up: 6.000 GeV/c. Upper:  $\Lambda\bar{\Lambda}Bar$ , Center:  $\Lambda\bar{\Lambda}BarPol$ , Lower:  $\Lambda\bar{\Lambda}BarHE$ .

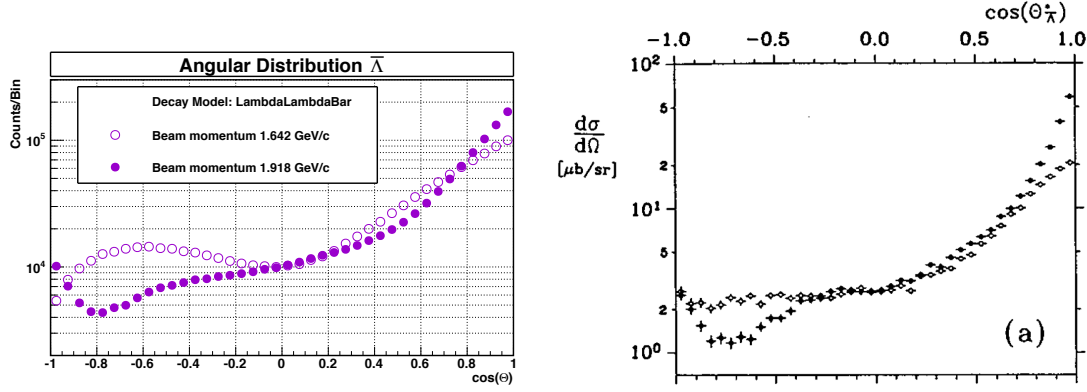


Figure 6.7.: Angular distribution of the  $\bar{\Lambda}$ . Left: Simulated angular distributions. Right: Measured differential cross section from the PS185 experiment, Figure taken from Ref. [78].

data. Despite these differences, the *LambdaLambdaBar* class is the best distribution compared to the experimental data and therefore is used in this simulation.

$\Lambda$  ( $\bar{\Lambda}$ ) hyperons decay mainly into two final states,  $p\pi^-$  ( $\bar{p}\pi^+$ ) with a probability of  $(63.9 \pm 0.5)\%$  and  $n\pi^0$  ( $\bar{n}\pi^0$ ) with a probability of  $(35.8 \pm 0.5)\%$  [10]. For this analysis the neutral particles branch was neglected because they do not leave hit points in the detectors to be studied. For the following analysis  $10^6$  events have been created for each beam momentum and disk position with the *LambdaLambdaBar* decay model.

The proper time distribution generated by the MC simulation was analysed to cross-check the generator. The results are shown in Figure 6.9. Within errors, the simulated decay length matches the Particle Data Group (PDG) value of  $c\tau = 7.89$  cm [10].

#### 6.3.4. Reconstruction

The track finders within the PandaRoot framework are under active development. At the moment, no track finder is capable of finding secondary vertices which are further away from the interaction point more than  $\sim 1$  cm. Therefore, an ideal track finder has been used to find tracks from  $\bar{\Lambda}\Lambda$  events. The ideal track finder uses MC information to combine reconstructed hits to track candidates with starting parameters needed for the track fitting. Afterwards the finder stores all tracks which leave at least three reconstructed hits in the tracking detectors. This is not a very realistic setup, since track finding with just three points is very difficult. To represent a more realistic track finding algorithm a loose cut has been applied to cut away all tracks which are very unlikely to be found by more realistic track finding algorithms. The selection criteria has been set according to the following rule:

$$\begin{aligned}
 &(\# \text{ Hits(MVD)} > 3 \text{ and } \# \text{ Hits(STT+GEM+FTS)} > 1) \\
 &\quad \text{or} \\
 &(\# \text{ Hits(MVD+STT+GEM+FTS)} > 9)
 \end{aligned}$$

## 6. Simulation of the $\bar{\Lambda}\Lambda$ Final State

This number of hits is expected to be found by future track finding algorithms.

An overview of the reduction of events at each reconstruction step is displayed in Table 6.3. After the track selection by the ideal track finder the efficiency was found to be roughly 55% for the individual  $\Lambda$  and the  $\bar{\Lambda}$  particles. The fraction of events where both particles is found is 32%.

The fraction for individually found  $\Lambda$  particles gets smaller at higher beam momenta (48.3% at 1.918 GeV/c and 8.2% at 6.00 GeV/c) since the particles are emitted at backward angles in the CMS and thus have smaller lab momenta. In contrast,  $\bar{\Lambda}$  particles have a relatively constant fraction of found particles (58.9% at 1.918 GeV/c and 52.8% at 6.00 GeV/c). Due to the drop of found  $\Lambda$  particles, the fraction of found  $\bar{\Lambda}\Lambda$  events drops with increasing beam momentum (7.4% at 1.918 GeV/c and 1.3% at 6.00 GeV/c). A more detailed statistical analysis of the remaining tracks at the different beam momenta can be seen in Figure 6.10. The figures show the number of final state tracks which fulfilled the cut criterium. For the incomplete events, the missing particles are indicated on the ordinate. The higher the beam momentum gets, the lower the fraction of events is where all four final state tracks are found. If an event is not completely found at 1.642 GeV/c or 1.918 GeV/c, it is mainly the  $\pi^+$  or the  $\pi^-$  which is missing. At 6 GeV/c it is mainly the proton which is missing.

The track fitting is performed after track finding.

The used Kalman fitter GenFit returns an indication if the performed fit was successful or not. If one excludes tracks with a bad track flag one gets the results shown in Figure 6.11. For the two lower beam momenta the pion tracks are slightly stronger excluded due to the bad track flag than the proton tracks. For the highest beam momentum the  $\pi^-$  tracks are much more strongly excluded by the bad track flag than the other particle tracks (see Figure 6.12).

The track fitting and the removing of bad tracks reduces the fraction of found events at the two lower beam momenta by  $\sim 20$  percentage points (single particle and full event) and for the highest beam momenta by 2.5 - 5.5 percentage points.

All marked tracks are defined as bad by a wrong conversion from the GenFit track data class, `GenFitTrack` to the PandaRoot track data class, `PndTrack` or zero degrees of freedom (NDF=0). A new version of GenFit was developed and currently is under implementation into the PandaRoot framework. This new revision should fix the error mentioned above.

### 6.3. Simulation of the $\bar{\Lambda}\Lambda$ Final State

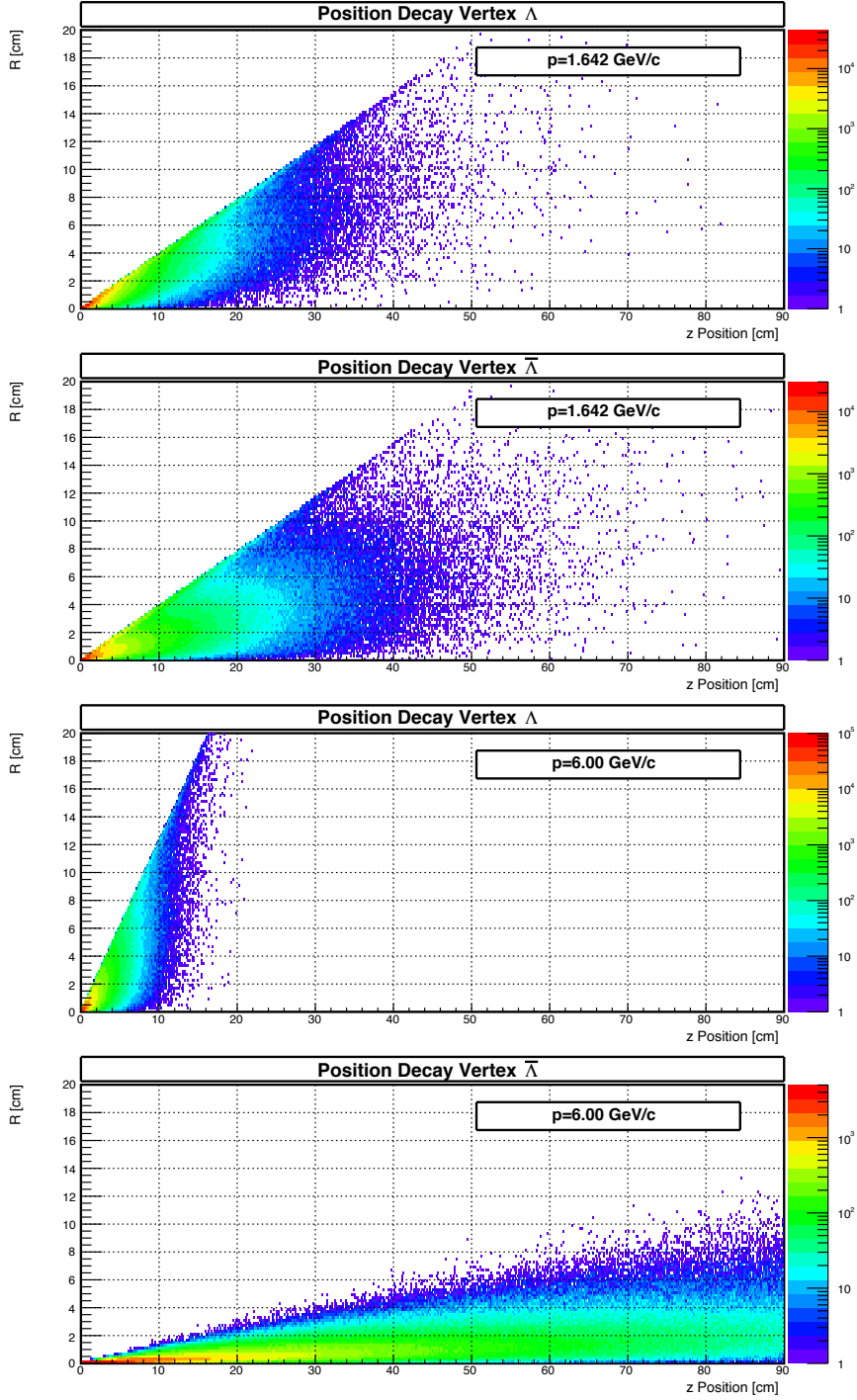


Figure 6.8.: Simulated radial vs. longitudinal decay position of the  $\Lambda$  (first and third frame) and  $\bar{\Lambda}$  (second and fourth frame) hyperon in the lab reference frame for beam momenta of 1.642 GeV/c (first and second frame) and 6.00 GeV/c (third and fourth frame).

## 6. Simulation of the $\bar{\Lambda}\Lambda$ Final State

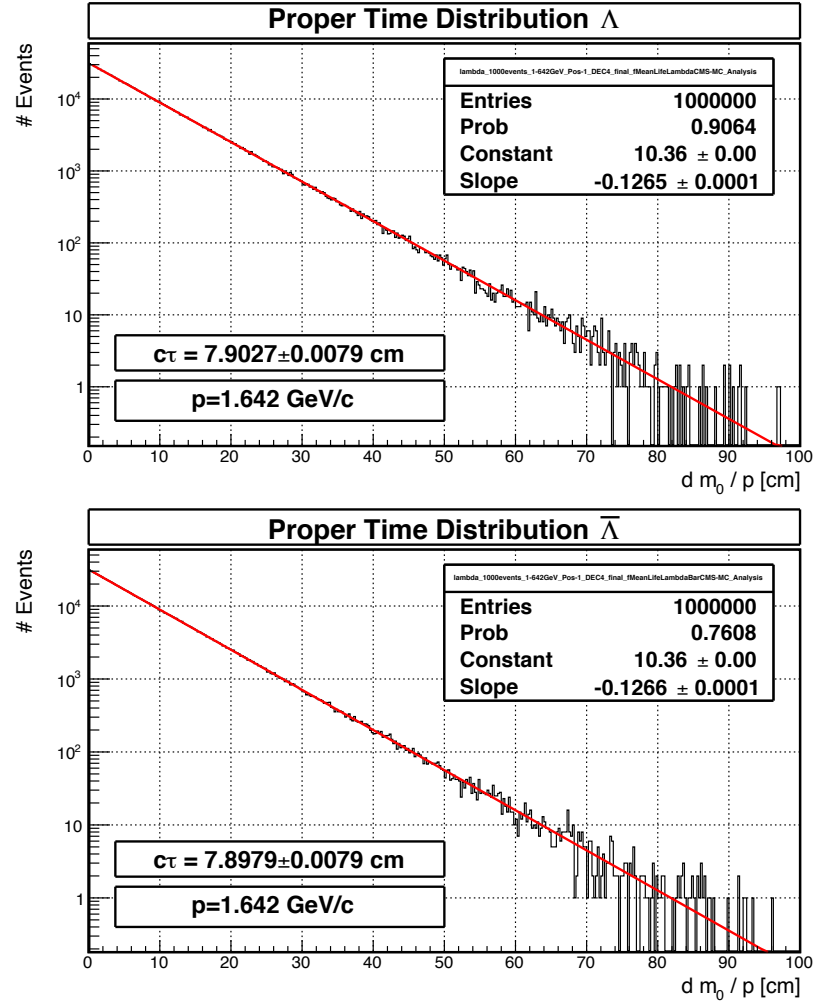


Figure 6.9.: Simulated proper time distribution of the  $\Lambda$  (left) and  $\bar{\Lambda}$  (right).

### 6.3. Simulation of the $\bar{\Lambda}\Lambda$ Final State

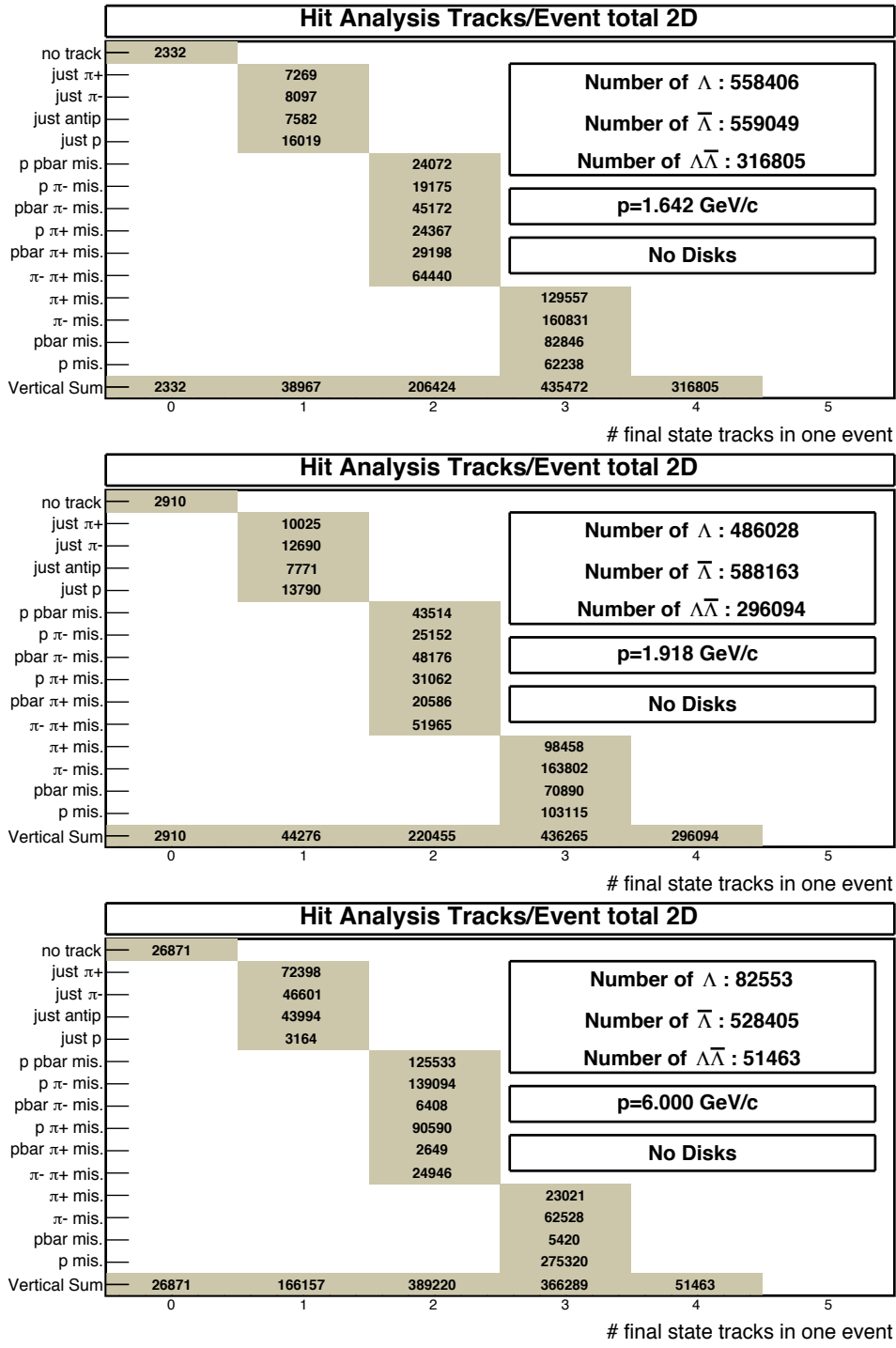


Figure 6.10.: Analysis of simulated final state tracks per event which fulfill the selection criterion. Upper: 1.642 GeV/c. Center: 1.918 GeV/c. Lower: 6.000 GeV/c.

## 6. Simulation of the $\bar{\Lambda}\Lambda$ Final State

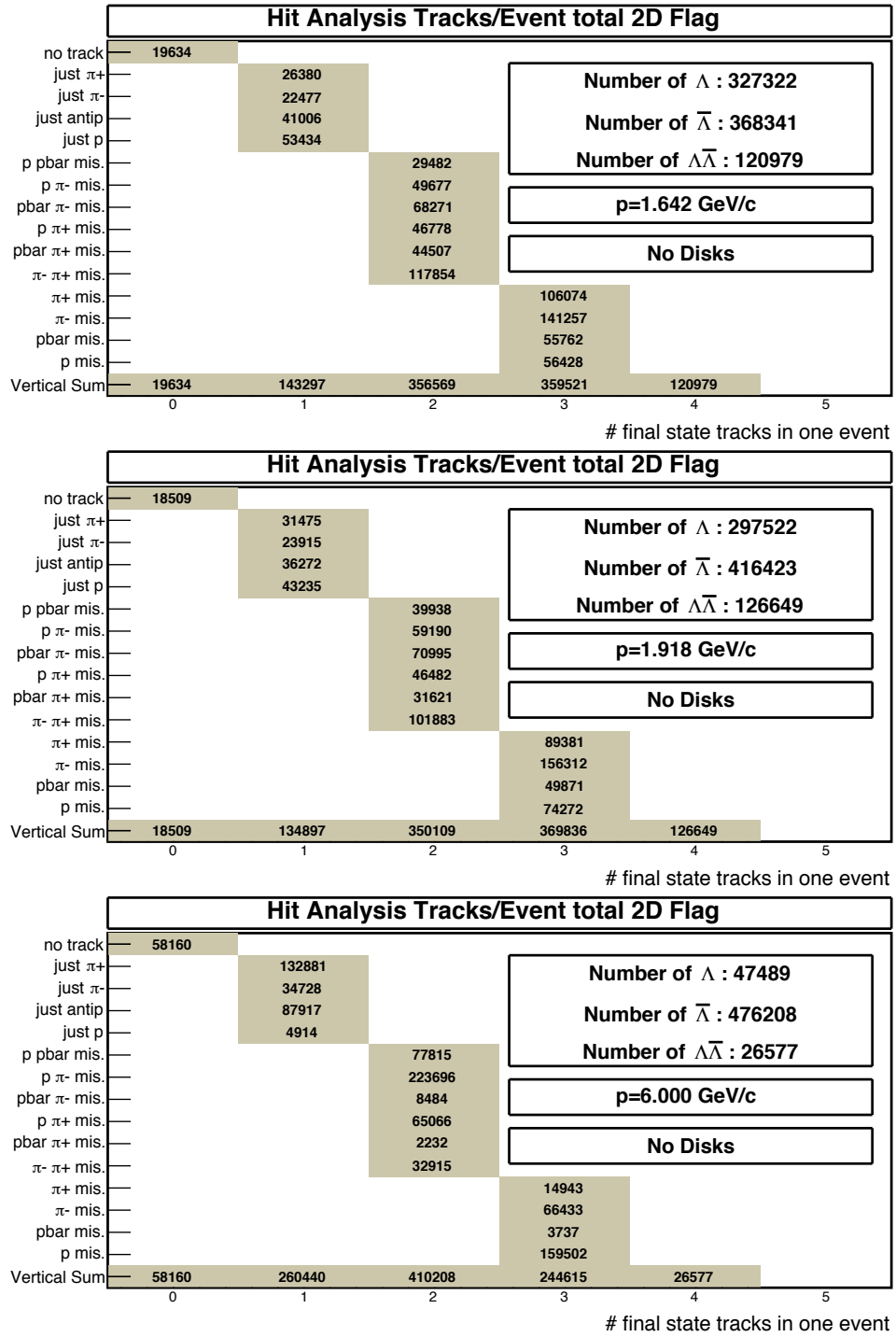


Figure 6.11.: Analysis of simulated final state tracks per event which fulfill the selection criterion after track fitter filtering. Upper: 1.642 GeV/c. Center: 1.918 GeV/c. Lower: 6.000 GeV/c.



### 6.3. Simulation of the $\bar{\Lambda}\Lambda$ Final State

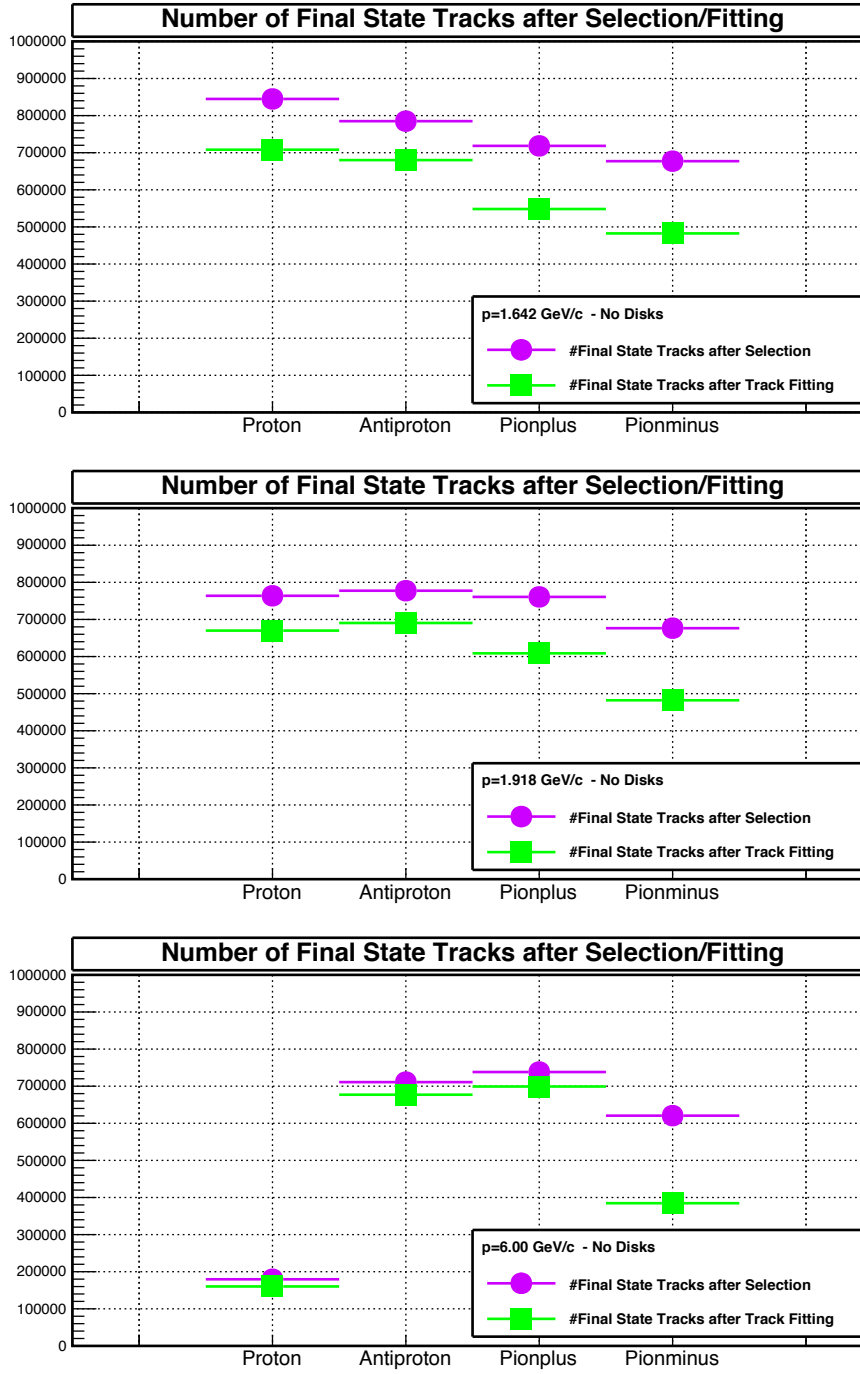


Figure 6.12.: Track fitter bad-flag reduction per final state particle type for three beam momenta. Upper: 1.642 GeV/c. Center: 1.918 GeV/c. Lower: 6.000 GeV/c.

## 6. Simulation of the $\bar{\Lambda}\Lambda$ Final State

### 6.3.5. Particle Identification

Because PID algorithms within PandaRoot are still under development, ideal PID has been used. The ideal PID sets the particle probability by the MC truth value. In this case the charge of the particle is still determined by the track's direction of curvature after track fitting.

### 6.3.6. Event Analysis

After the reconstruction of the particle tracks and the identification of the particles types, the  $\bar{\Lambda}\Lambda$  events have to be reconstructed. This is done in the following way:

- All  $\pi^-$  ( $\pi^+$ ) and p ( $\bar{p}$ ) particles per event are combined
- The `PndVtxPRGFitter` vertex-fitter is applied to find a common vertex for both particle tracks
- An event is removed if the  $\chi^2$ -probability of the fit is below 0.01. The  $\chi^2$ -probability distributions are displayed in Figure 6.13.

The cut on the probability distribution reduced the background of wrong combinations of particles. The combinatorial background is larger for  $\Lambda$  than for  $\bar{\Lambda}$ , due to the large number of secondary particles created in the reaction of the final state antiprotons with detector material. These reactions create many particles mostly pions, protons and neutrons, which are combined to  $\Lambda$  candidates. Table 6.2 shows the number of p and  $\pi$  combinations and the true number of  $\Lambda$  before and after the probability cut.

Table 6.3 gives an overview of the event reduction for the different reconstruction and analysis steps.

$P_{\text{Beam}}=1.642 \text{ GeV}/c$	p $\pi^-$	real $\Lambda$	background	$\bar{p} \pi^+$	real $\bar{\Lambda}$	background
before cut	572,431	326,228	246,203	402,032	367,387	34,645
after cut	303,740	247,029	56,711	297,476	293,708	3,768
$P_{\text{Beam}}=1.918 \text{ GeV}/c$	p $\pi^-$	real $\Lambda$	background	$\bar{p} \pi^+$	real $\bar{\Lambda}$	background
before cut	524,067	296,569	227,498	455,755	415,489	40,266
after cut	261,828	212,038	49,790	337,680	331,445	6,235
$P_{\text{Beam}}=6.000 \text{ GeV}/c$	p $\pi^-$	real $\Lambda$	background	$\bar{p} \pi^+$	real $\bar{\Lambda}$	background
before cut	347,968	47,354	300,614	577,721	476,015	101,706
after cut	144,227	30,508	113,719	442,293	401,474	40,819

Table 6.2.: Number of  $\Lambda$  candidates and true  $\Lambda$  before and after the probability cut.

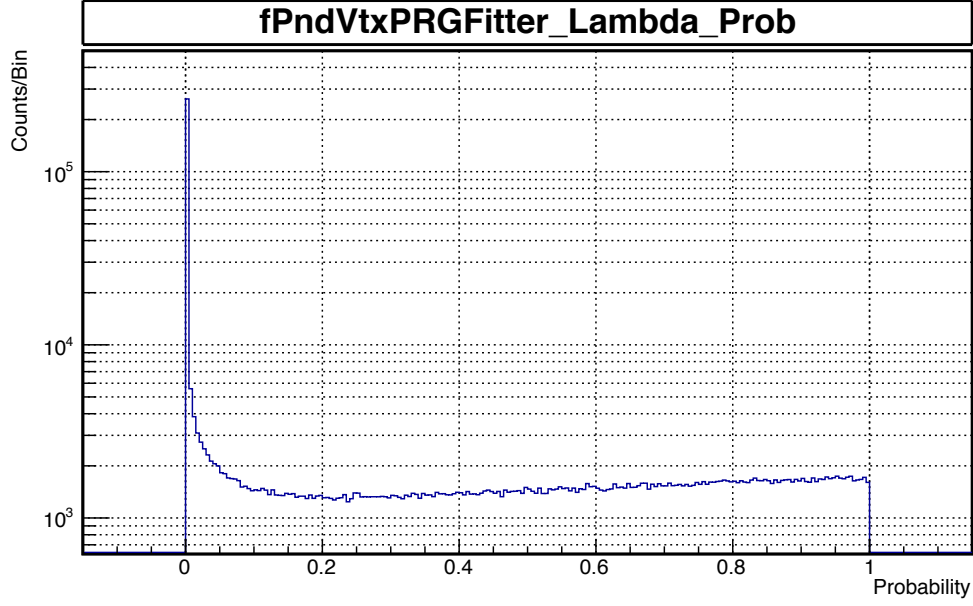


Figure 6.13.:  $\chi^2$ -probability distribution of **PndVtxPRGFitter** vertex fitter. All events with a  $\chi^2$ -probability  $< 0.01$  have been removed.

$P_{\text{Beam}}=1.642 \text{ GeV}/c$		$\Lambda$		$\bar{\Lambda}$		$\Lambda\bar{\Lambda}$	
Production	1,000,000	100.0%	1,000,000	100.0%	1,000,000	100.0%	100.0%
Track Selection	558,406	55.84%	559,049	55.90%	316,805	31.68%	31.68%
Track Fitting	327,322	32.73%	368,341	36.83%	120,979	12.10%	12.10%
Vertex Fit Prob Cut	247,029	24.70%	293,708	29.37%	76,500	7.650%	7.650%
$P_{\text{Beam}}=1.918 \text{ GeV}/c$		$\Lambda$		$\bar{\Lambda}$		$\Lambda\bar{\Lambda}$	
Production	1,000,000	100.0%	1,000,000	100.0%	1,000,000	100.0%	100.0%
Track Selection	486,028	48.60%	588,163	58.82%	296,094	29.61%	29.61%
Track Fitting	297,522	29.75%	416,423	41.64%	126,649	12.66%	12.66%
Vertex Fit Prob Cut	212,038	21.20%	331,445	33.14%	73,784	7.38%	7.38%
$P_{\text{Beam}}=6.00 \text{ GeV}/c$		$\Lambda$		$\bar{\Lambda}$		$\Lambda\bar{\Lambda}$	
Production	1,000,000	100.0%	1,000,000	100.0%	1,000,000	100.0%	100.0%
Track Selection	82,553	8.26%	528,405	52.84%	51,463	5.15%	5.15%
Track Fitting	47,489	4.75%	476,208	47.62%	26,577	2.57%	2.57%
Vertex Fit Prob Cut	30,508	3.05%	401,474	40.15%	12,829	1.28%	1.28%

Table 6.3.: Number of true events after reconstruction and analysis steps for **Pos-1**. All percentage values are with respect to the initial number of events.

## 6.4. Results

### 6.4.1. Counting Rate Studies

The  $\Lambda$ -disks should bring additional points for particle tracks to improve the reconstruction capability and the track quality in particular for hyperons. However, more material raises the risk of unwanted interactions with the particles and negative influence on the particle tracks. This is in particular dangerous for particles with low momentum, like a  $\pi$  in the  $\bar{\Lambda}\Lambda$  decay.

To investigate purely the effect of the  $\Lambda$ -disks on the number of events a counting rate study has been done prior to the track fitting stage. This study shows how many additional events could be detected and which disk setting has the most advantage. Table 6.4 shows the results of the counting rate study.

The  $\bar{\Lambda}$  particle has the most benefit at all beam momenta. Due to the strong boost in the forward direction the  $\bar{\Lambda}$  decays closer to the  $\Lambda$ -disks. The detected number of particles rises by about 5.7 percentage points for 1.642 GeV/c and 6.4 percentage points for 1.918 GeV/c for all disk positions. For 6.00 GeV/c the gain is lower, 1.6 percentage points on average, since many  $\bar{\Lambda}$  particles decay behind the  $\Lambda$ -disks.

The  $\Lambda$  particle gains less in comparison. For low beam momentum an average gain of 1.2 percentage points and for the medium beam momentum an average gain of just 0.3 percentage points was obtained. For the high beam momentum fewer events are detected compared to the simulation without the  $\Lambda$ -disks (`Pos2`), however the difference is statistically not significant. For the other  $\Lambda$ -disk positions one sees a gain which is positive but very small.

At the highest simulated energy the  $\Lambda$  particles are emitted backwards in the CMS. Due to the boost in forward directions the  $\Lambda$  particles are very slow and fly nearly perpendicular to the beam axis into the detector. Due to this it is very unlikely that the proton and pion hit the  $\Lambda$ -disks. Even if a final state particle of the  $\Lambda$  hits the  $\Lambda$ -disks, it is very possible that it is scattered or stopped due to its low momentum.

The detection possibility of the whole  $\Lambda\bar{\Lambda}$  final state rises on average by 3.5, 2.5 and 0.4 percentage points for the three beam momenta studies.

None of the different positions of the  $\Lambda$ -disks has a clear advantage against the others. At 1.642 GeV/c `Pos2` shows the highest gain rate for the individual particles and the whole decay. For 1.918 GeV/c different positions have the highest rates for the individual particles and both particles, the same is true for 6.00 GeV/c.

$P_{\text{Beam}}$	Position	$\Lambda$		$\bar{\Lambda}$		$\Lambda\bar{\Lambda}$	
1.642 GeV/c	-1	558,406	55.84%	559,049	55.90%	316,805	31.68%
	0	568,960	56.96% (+1.06%)	616,943	61.69% (+5.85%)	351,177	35.12% (+2.98%)
	1	563,177	56.38% (+0.48%)	616,211	61.62% (+5.72%)	346,641	34.66% (+2.98%)
	2	574,745	57.47% (+1.63%)	619,385	61.94% (+6.03%)	355,922	35.59% (+3.91%)
	3	574,631	57.46% (+1.62%)	610,495	61.05% (+5.14%)	351,831	35.18% (+3.50%)
1.918 GeV/c	-1	486,028	48.60%	588,163	58.82%	296,094	29.61%
	0	486,455	48.65% (+0.04%)	655,103	65.51% (+6.69%)	320,525	32.05% (+2.44%)
	1	484,731	48.47% (-0.13%)	655,277	65.53% (+6.71%)	319,541	31.95% (+2.34%)
	2	491,134	49.13% (+0.53%)	654,822	65.48% (+6.67%)	324,089	32.41% (+2.80%)
	3	493,848	49.35% (+0.75%)	643,847	64.38% (+5.57%)	321,430	32.14% (+2.53%)
6.00 GeV/c	-1	82,553	8.26%	528,405	52.84%	51,463	5.15%
	0	82,792	8.28% (+0.02%)	546,517	54.65% (+1.81%)	55,524	5.55% (+0.41%)
	1	82,659	8.27% (+0.01%)	547,958	54.80% (+1.96%)	55,518	5.55% (+0.41%)
	2	80,866	8.09% (-0.17%)	538,148	53.81% (+0.97%)	54,699	5.47% (+0.32%)
	3	83,044	8.30% (+0.05%)	545,290	54.53% (+1.69%)	54,623	5.46% (+0.32%)

Table 6.4.: Counting statistics for different  $\Lambda$ -disk settings. All percentage values are with respect to the Pos-1 setup.

### 6.4.2. Detection Efficiency

For the benchmark of the detector and the reconstruction we define the *detection efficiency* as the overall ratio of reconstructed events to simulated events. This is the product of the geometrical efficiency, which is the probability for a particle to be incident on the sensors, times the reconstruction efficiency, which is the efficiency to reconstruct a particle from the measured hits in the detector.

#### Detection Efficiency as a Function of the Hyperon Production Angle

Figure 6.14 shows the detection efficiency as a function of the CMS angle for the three beam momenta studied and for the different disk positions.

One can see that the efficiency drops in the backward direction for all disk positions at the lower beam momenta. Particles which are emitted backwards in the CMS have a lower lab momentum. Due to this lower momentum they have a lower detection efficiency and many events are lost.

In the forward direction one can see the effect of the  $\Lambda$ -disks. Without the disks the detection efficiency drops close to  $\cos(\Theta)=1$ . With the disks the efficiency is higher. The different disk positions are equally in the effect on the detection efficiency, due to this no  $\Lambda$ -disk position is preferred.

#### Detection Efficiency as a Function of the Final State Antiproton Production Angle

Figure 6.15 shows the detection efficiency of the final state antiproton as a function of the angle  $\Theta_p$  (see Figure 6.2) between the antiproton and the normal vector  $\hat{y}$  in the  $\bar{\Lambda}$  reference frame for the three beam momenta and for all  $\Lambda$ -disk positions. These histograms are necessary for the investigation of spin correlations. Since the simulation model used does not include polarization, the  $\Lambda$  distributions should be uniform [76]. Instead, the Figures show a minimum of detected antiprotons symmetric around  $\cos(\Theta_y)=0$  for the lower two beam momenta. For the highest beam momentum the distribution is nearly flat. Values of  $\cos(\Theta_y)$  around zero indicates that the antiproton goes either in positive or in negative  $z$ -direction. If it goes in the positive direction, the corresponding  $\pi^+$  goes against the boost direction and is slowed down, and consequently lost.

The  $\Lambda$ -disks lead to a small increase of the detection efficiency, which decreases with increasing beam momentum. Apart from a small region of the production angle  $\Theta$ , this is only a general increase of efficiency, without newly accessible regions of phase space. Furthermore, the effect is independent of the position of the  $\Lambda$ -disks studied.

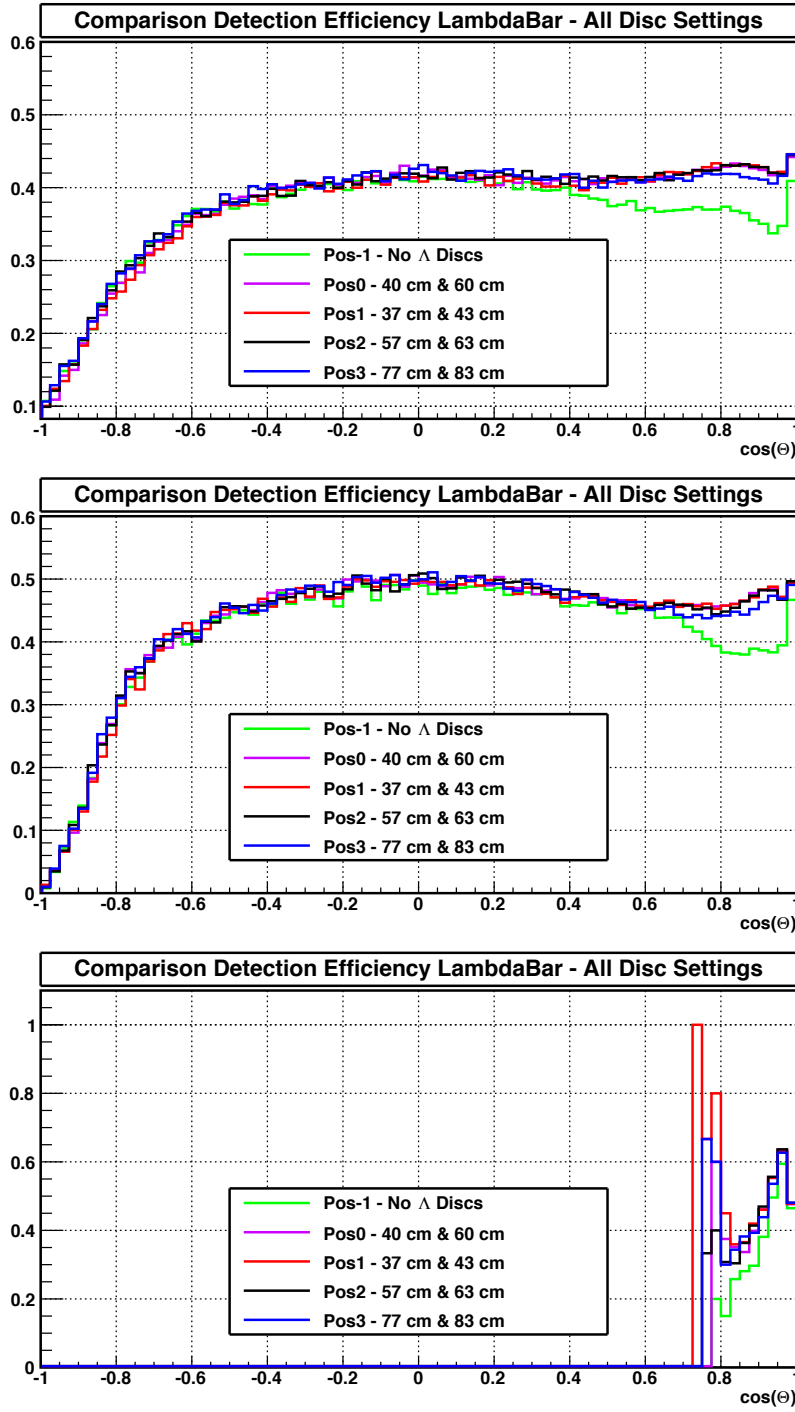


Figure 6.14.: The detection efficiency as a function of the CMS production angle of the  $\bar{\Lambda}$  for all three beam momentum and all disk positions. Upper: 1.642 GeV/c. Center: 1.918 GeV/c Lower: 6.00 GeV/c.

## 6. Simulation of the $\bar{\Lambda}\Lambda$ Final State

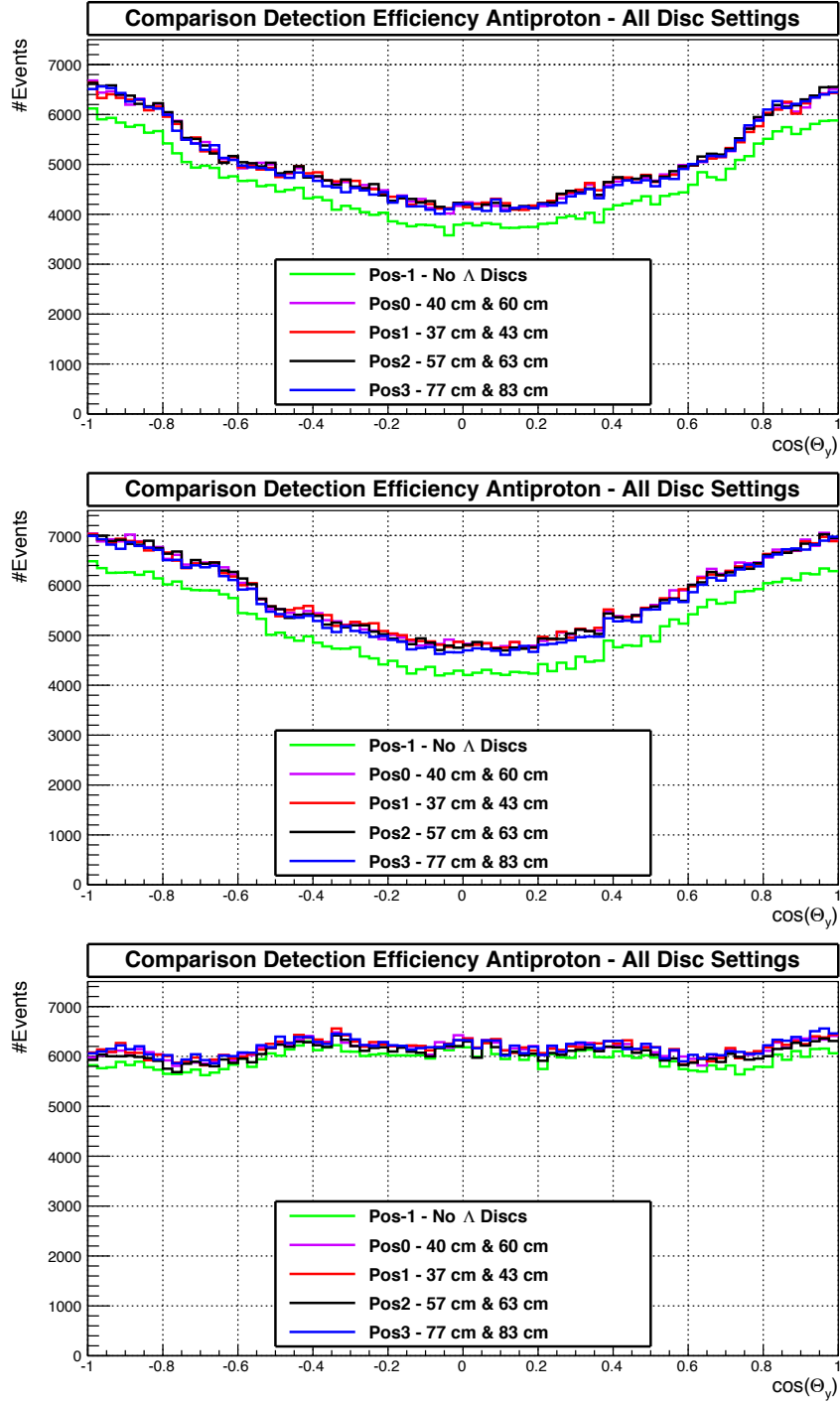


Figure 6.15.: Detection efficiency of the antiproton as a function of the angle  $\Theta_p$  between the antiproton and the normal vector  $\hat{y}$  in the  $\bar{\Lambda}$  reference frame. Upper: 1.642 GeV/c. Center: 1.918 GeV/c Lower: 6.00 GeV/c.



### 6.4.3. Production Rate

To get an estimation of the expected  $\bar{\Lambda}\Lambda$  production rate at the  $\bar{\text{P}}\text{ANDA}$  experiment, several variables are necessary.

The decay  $\bar{\Lambda}\Lambda \rightarrow \bar{p}\pi^+p\pi^-$  has been reconstructed and analysed at three different beam momenta with  $10^6$  generated events each. Table 6.5 shows the reconstruction efficiencies for the different beam momenta.

The selected decay of  $\Lambda$  ( $\bar{\Lambda}$ ) into  $p\pi^-$  ( $\bar{p}\pi^+$ ) has a branching ratio of 63.9%. Since both particles decay into the charged final state this branching ratio appears twice.

The expected luminosity in the full FAIR version is  $\mathcal{L}=2\cdot 10^{32} \text{ cm}^{-2}\text{s}^{-1}$ . The experimental cross section for the  $\bar{\Lambda}\Lambda$  production at the different beam momenta is taken from References [78, 79].

The number of expected reconstructable events is then calculated with:

$$\epsilon \cdot \mathcal{L} \sigma \text{BR}(\Lambda \rightarrow p\pi)^2 \quad (6.4)$$

	1.642 GeV/c	1.918 GeV/c	6.00 GeV/c
Reconstruction Efficiency $\epsilon$	7.6%	7.4%	1.3%
Experimental cross section $\sigma$	$(64.1 \pm 0.4 \pm 1.6) \text{ } \mu\text{b}$	$(88.0 \pm 0.7 \pm 1.9) \text{ } \mu\text{b}$	$(40.5 \pm 4.1) \text{ } \mu\text{b}$
Events/s	397	531	42

Table 6.5.: Reconstruction efficiency, experimental cross section and event rate for three beam momenta.

	1.642 GeV/c	1.918 GeV/c	6.00 GeV/c
Pos-1	7.6%	7.4%	1.3%
Pos0	8.3%	7.8%	1.4%
Pos1	8.2%	7.9%	1.4%
Pos2	8.5%	7.8%	1.3%
Pos3	8.0%	7.8%	1.3%

Table 6.6.: Reconstruction efficiency for the different  $\Lambda$ -disk positions and the beam momenta studied.

The simulated number of events ( $10^6$ ) corresponds to 42 minutes (1.642 GeV/c), 31 minutes (1.918 GeV/c) and 397 minutes (6.00 GeV/c) of data taking. Table 6.6 shows the reconstruction efficiency for the different  $\Lambda$  disk positions. One can see that with the  $\Lambda$ -disk a slight increase on average of 0.7, 0.4 and 0.1 percentage points for 1.642 GeV/c, 1.918 GeV/c and 6.00 GeV/c, respectively. None of the positions have a clear advantage compared to the others.

Despite the small reconstruction efficiency it is possible to collect a large number of events on a short time scale.

#### 6.4.4. Invariant Mass Distributions

The reconstructed invariant mass distributions of  $\bar{\Lambda} \rightarrow \bar{p}\pi^+$  for the three beam momenta are shown in Figure 6.16. A Gaussian function has been fit to the distributions, the results are displayed in Table 6.7. The functions have widths of around 2-3 MeV/c<sup>2</sup> for  $\bar{\Lambda}$  and  $\Lambda$  particles at all beam momenta studied. The mean invariant mass is slightly higher than the PDG value:  $M_{\Lambda, \text{PDG}} = (1115.683 \pm 0.006) \text{ MeV}/c^2$

The errors on the mean invariant masses are on the same order as for the PDG value. Figure 6.17 shows the invariant mass distributions for different  $\Lambda$ -disk positions at  $p_{\text{beam}}=1.642 \text{ GeV}/c$ . The disks have no significant influence on the invariant mass resolution.

$P_{\text{Beam}} [\text{GeV}/c]$	Particle	Mean $[\text{MeV}/c^2]$	$\sigma [\text{MeV}/c^2]$
1.642	$\Lambda$	$1116.02 \pm 0.005$	$2.50 \pm 0.006$
	$\bar{\Lambda}$	$1115.96 \pm 0.005$	$2.34 \pm 0.005$
1.918	$\Lambda$	$1116.02 \pm 0.006$	$2.49 \pm 0.006$
	$\bar{\Lambda}$	$1116.00 \pm 0.004$	$2.21 \pm 0.004$
6.000	$\Lambda$	$1116.41 \pm 0.018$	$3.14 \pm 0.027$
	$\bar{\Lambda}$	$1115.91 \pm 0.005$	$3.05 \pm 0.006$

Table 6.7.: List of mean invariant mass and resolution of the  $\Lambda \rightarrow p\pi^-$  and  $\bar{\Lambda} \rightarrow \bar{p}\pi^+$  for three beam momenta. All values for **Pos-1**.

#### 6.4.5. Vertex Resolution

A vertex fitter finds a crossing-point of two or more tracks (vertex) taking the measured covariance matrices of the tracks into account and under the assumption that they have the same origin.

For the analyzed dataset the **PndVtxPRGFitter** has been used to find the vertex of the proton and pion tracks. More information about the fit algorithm are available in Reference [51].

Figures 6.18, 6.19 and 6.20 show the difference between the generated and reconstructed vertex location for the three beam momenta. Displayed is the reconstructed value minus the MC truth value for the three cartesian coordinates. The distributions have been fitted with a Lorentz function:

$$f(x) = \frac{1}{2\pi} \frac{\Gamma}{(x - \mu)^2 + \Gamma^2/4}. \quad (6.5)$$

Here  $\Gamma$  indicated the Full-Width at Half Maximum (FWHM) and  $\mu$  indicates the position of the peak. Since the vertex distribution is not always well described by the Lorentz function, also the FWHM has been determined.

In general the resolution in the  $z$ -direction is two to three times worse compared to the  $x$ - and  $y$ -directions. This is expected since the detectors do not have the same resolution

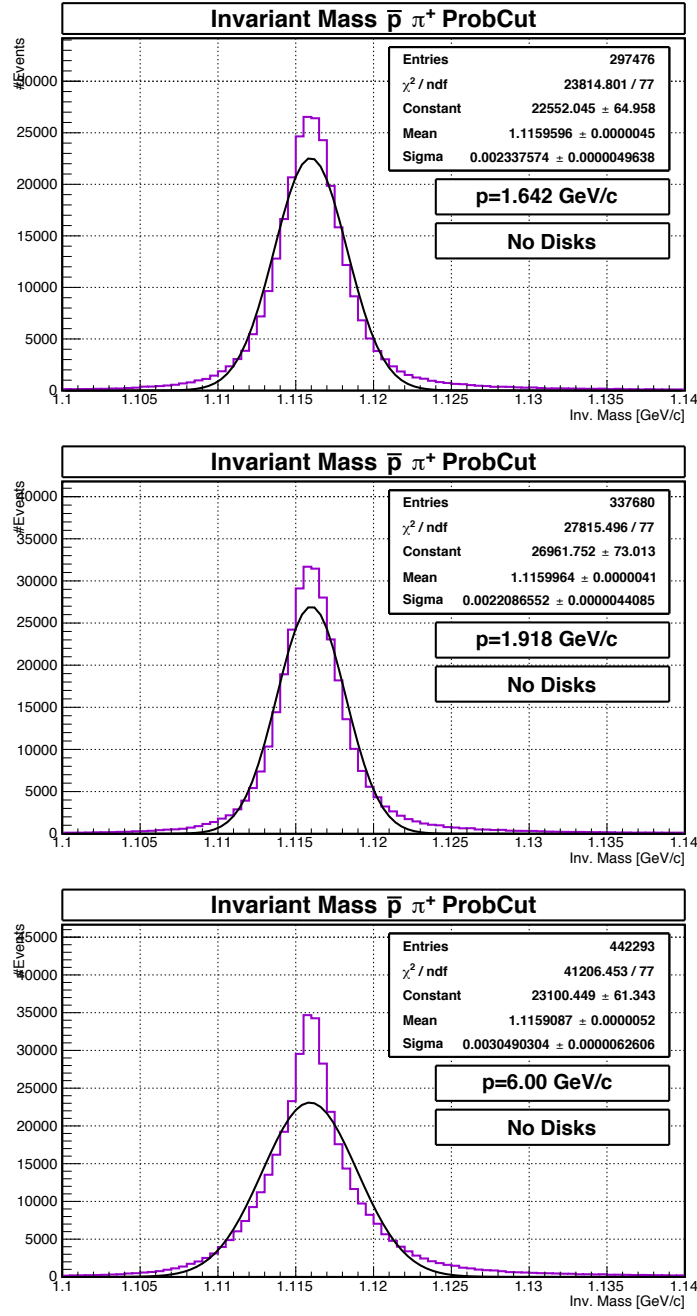


Figure 6.16.:  $\bar{p}\pi^+$  invariant mass distribution for beam momenta of 1.642 GeV/c (upper), 1.918 GeV/c (middle) and 6.00 GeV/c (lower) beam momentum for Pos-1 (no disks).

## 6. Simulation of the $\bar{\Lambda}\Lambda$ Final State

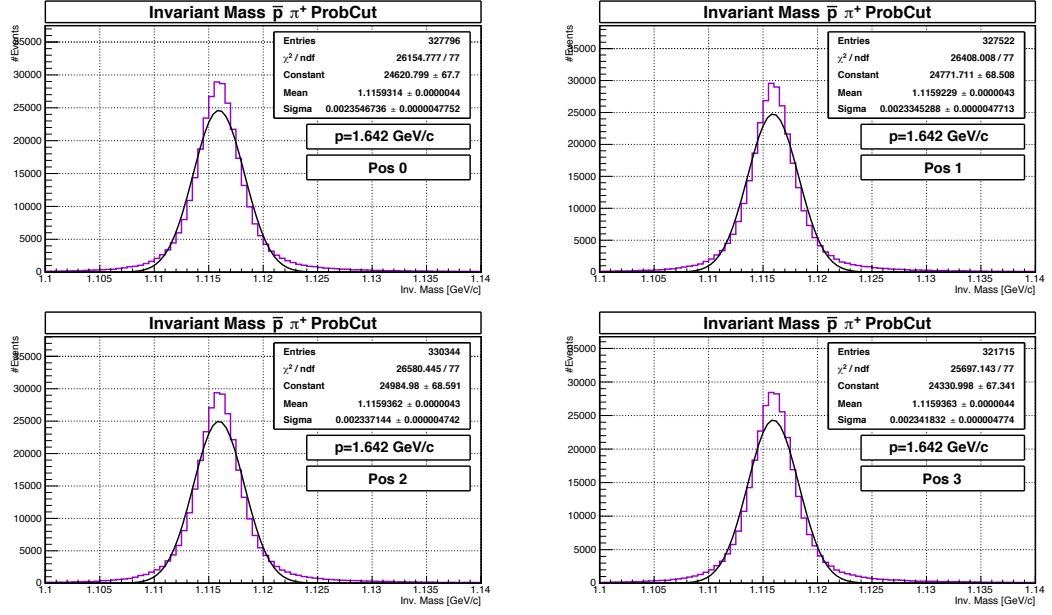


Figure 6.17.:  $\bar{p}\pi^+$  invariant mass distributions for the 1.642 GeV/c at the different  $\Lambda$ -disk positions.

in all directions. The Straw Tube Tracker (STT) has a spatial resolution of  $\sim 150$   $\mu\text{m}$  in  $r$  and  $\phi$ , but  $\sim 3$  mm in the  $z$ -direction due to the tube orientation. The GEM stations have a good spatial resolution, but are too far away to contribute to the vertex resolution. The MVD has a good resolution in  $z$ , but not all hyperon events have MVD hits. Table 6.8 shows the FWHM of the vertex distributions for all beam momenta and disk positions studied.

The resolutions at  $p_{\text{beam}}=1.642$  GeV/c and 1.918 GeV/c are comparable to each other. The FWHM in  $x$ - and  $y$ -direction is between 550  $\mu\text{m}$  and 700  $\mu\text{m}$ . The value of  $\Gamma$  is bigger, between 887  $\mu\text{m}$  and 1016  $\mu\text{m}$  because the distribution is not well described by the Lorentz function.

The FWHM of the vertex distributions are slightly worse by 50-100  $\mu\text{m}$  for the different disk positions, compared to the setting without disks.

Only the  $\bar{\Lambda}$  resolution at 6.00 GeV/c improved by adding the  $\Lambda$ -disks. The  $\bar{\Lambda}$  which is forward boosted gains from the additional MVD points.

$P_{\text{Beam}}$ [GeV/c]	Disk setting	Particle	$x$ (FWHM)	$y$ (FWHM)	$z$ (FWHM)
1.642	Pos-1	$\Lambda$	700 $\mu\text{m}$	650 $\mu\text{m}$	1500 $\mu\text{m}$
	Pos-1	$\bar{\Lambda}$	650 $\mu\text{m}$	650 $\mu\text{m}$	2150 $\mu\text{m}$
1.918	Pos-1	$\Lambda$	650 $\mu\text{m}$	550 $\mu\text{m}$	1350 $\mu\text{m}$
	Pos-1	$\bar{\Lambda}$	550 $\mu\text{m}$	550 $\mu\text{m}$	2250 $\mu\text{m}$
6.000	Pos-1	$\Lambda$	1700 $\mu\text{m}$	1400 $\mu\text{m}$	2450 $\mu\text{m}$
	Pos-1	$\bar{\Lambda}$	1800 $\mu\text{m}$	1600 $\mu\text{m}$	9950 $\mu\text{m}$
1.642	Pos0	$\Lambda$	750 $\mu\text{m}$	750 $\mu\text{m}$	2100 $\mu\text{m}$
	Pos0	$\bar{\Lambda}$	650 $\mu\text{m}$	650 $\mu\text{m}$	2250 $\mu\text{m}$
1.918	Pos0	$\Lambda$	650 $\mu\text{m}$	600 $\mu\text{m}$	1700 $\mu\text{m}$
	Pos0	$\bar{\Lambda}$	550 $\mu\text{m}$	550 $\mu\text{m}$	2250 $\mu\text{m}$
6.000	Pos0	$\Lambda$	1950 $\mu\text{m}$	1550 $\mu\text{m}$	2350 $\mu\text{m}$
	Pos0	$\bar{\Lambda}$	1300 $\mu\text{m}$	1250 $\mu\text{m}$	9950 $\mu\text{m}$
1.642	Pos1	$\Lambda$	750 $\mu\text{m}$	750 $\mu\text{m}$	2000 $\mu\text{m}$
	Pos1	$\bar{\Lambda}$	650 $\mu\text{m}$	650 $\mu\text{m}$	2300 $\mu\text{m}$
1.918	Pos1	$\Lambda$	650 $\mu\text{m}$	600 $\mu\text{m}$	1600 $\mu\text{m}$
	Pos1	$\bar{\Lambda}$	550 $\mu\text{m}$	550 $\mu\text{m}$	2300 $\mu\text{m}$
6.000	Pos1	$\Lambda$	1950 $\mu\text{m}$	1550 $\mu\text{m}$	2450 $\mu\text{m}$
	Pos1	$\bar{\Lambda}$	1300 $\mu\text{m}$	1350 $\mu\text{m}$	9950 $\mu\text{m}$
1.642	Pos2	$\Lambda$	750 $\mu\text{m}$	750 $\mu\text{m}$	2000 $\mu\text{m}$
	Pos2	$\bar{\Lambda}$	650 $\mu\text{m}$	650 $\mu\text{m}$	2250 $\mu\text{m}$
1.918	Pos2	$\Lambda$	650 $\mu\text{m}$	550 $\mu\text{m}$	1700 $\mu\text{m}$
	Pos2	$\bar{\Lambda}$	550 $\mu\text{m}$	550 $\mu\text{m}$	2400 $\mu\text{m}$
6.000	Pos2	$\Lambda$	1800 $\mu\text{m}$	1550 $\mu\text{m}$	2350 $\mu\text{m}$
	Pos2	$\bar{\Lambda}$	1300 $\mu\text{m}$	1250 $\mu\text{m}$	9950 $\mu\text{m}$
1.642	Pos3	$\Lambda$	750 $\mu\text{m}$	500 $\mu\text{m}$	2100 $\mu\text{m}$
	Pos3	$\bar{\Lambda}$	650 $\mu\text{m}$	650 $\mu\text{m}$	2300 $\mu\text{m}$
1.918	Pos3	$\Lambda$	650 $\mu\text{m}$	600 $\mu\text{m}$	1800 $\mu\text{m}$
	Pos3	$\bar{\Lambda}$	550 $\mu\text{m}$	550 $\mu\text{m}$	2250 $\mu\text{m}$
6.000	Pos3	$\Lambda$	1900 $\mu\text{m}$	1600 $\mu\text{m}$	2700 $\mu\text{m}$
	Pos3	$\bar{\Lambda}$	1350 $\mu\text{m}$	1350 $\mu\text{m}$	9950 $\mu\text{m}$

Table 6.8.: FWHM for the vertex distributions for  $\Lambda$  and  $\bar{\Lambda}$  for all disk positions and beam momenta.

## 6. Simulation of the $\bar{\Lambda}\Lambda$ Final State

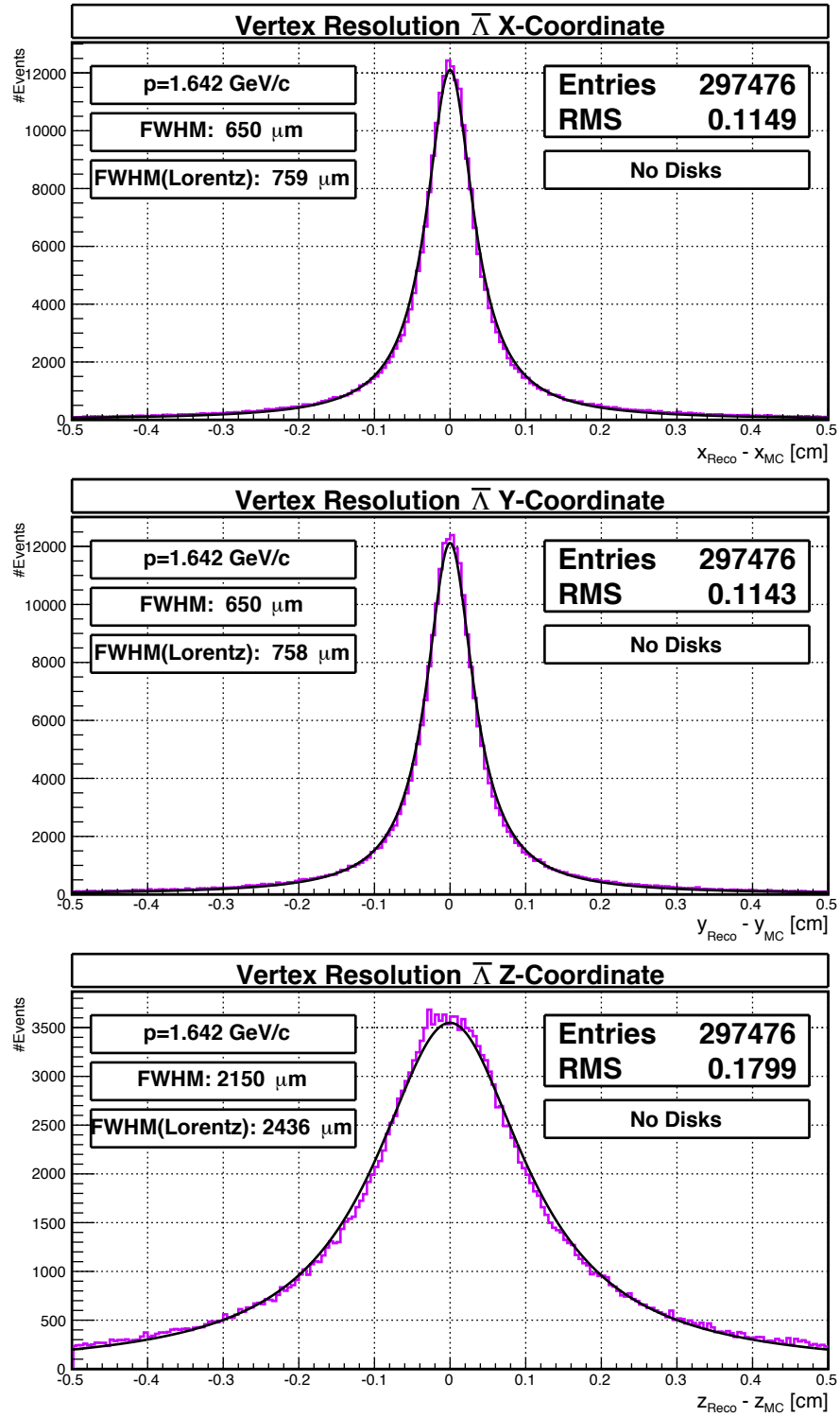


Figure 6.18.: Vertex Resolution when using PndVtxPRGFitter for  $p_{\text{beam}}=1.642$  GeV/c for Pos-1. Upper: x-coordinate. Center: y-coordinate. Lower: z-coordinate.

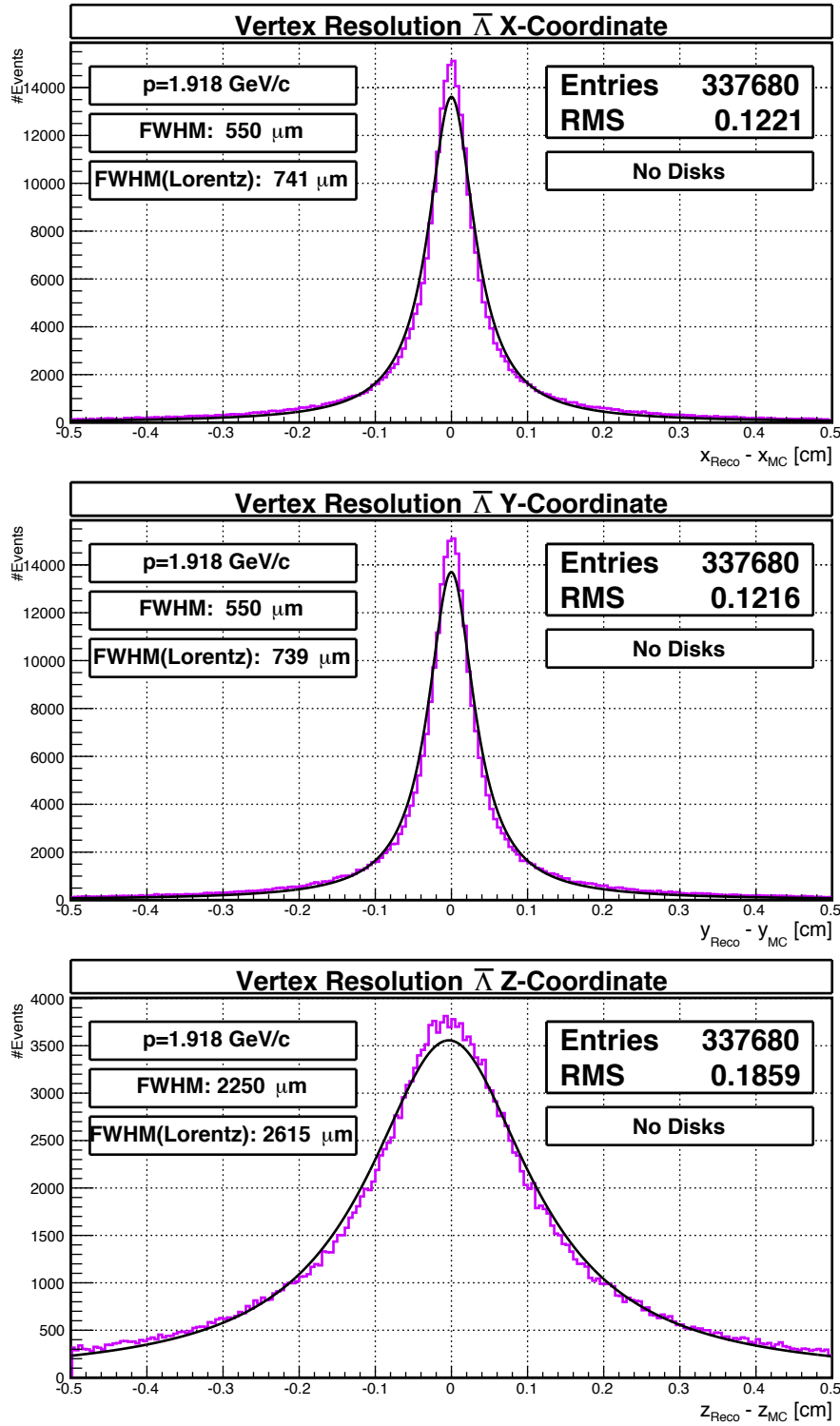


Figure 6.19.: Vertex Resolution when using PndVtxPRGFitter for  $p_{\text{beam}}=1.942$  GeV/c for Pos-1. Upper: x-coordinate. Center: y-coordinate. Lower: z-coordinate.

## 6. Simulation of the $\bar{\Lambda}\Lambda$ Final State

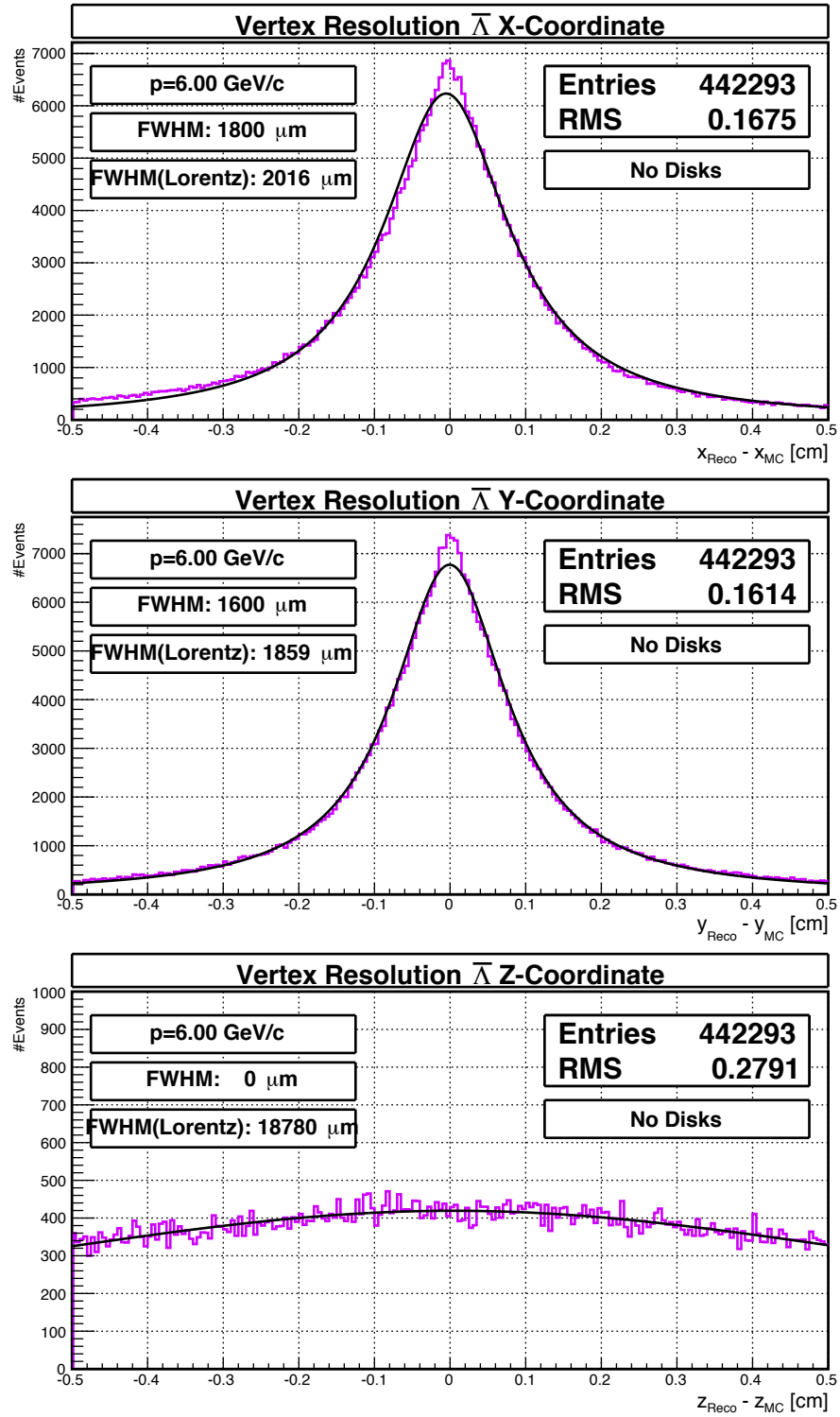


Figure 6.20.: Vertex Resolution when using PndVtxPRGFitter for  $p_{\text{beam}}=6.00$  GeV/c for Pos-1. Upper: x-coordinate. Center: y-coordinate. Lower: z-coordinate.



## 6.5. Conclusion

A full reconstruction chain of the  $\bar{\Lambda}\Lambda$  decay with the PandaRoot framework has been performed. Since the framework is under development, MC information are still necessary at selected stages to do a complete simulation and analysis chain.

The number of found events before the analysis stage rises on average by 3.5, 2.5 and 0.4 percent points for the different beam momenta.

The vertices of the  $\Lambda$  and  $\bar{\Lambda}$  particles has been fit with the `PndVtxPRGFitter`. For the lower two beam momenta the FWHM of the obtained resolutions are in the order of (550-700)  $\mu\text{m}$  for  $x$ - and  $y$ -direction (perpendicular to the beam axis) and around 1.35-1.5 mm ( $\Lambda$ ) and 2.15-2.25 mm ( $\bar{\Lambda}$ ) for  $z$ -direction (parallel to the beam axis). The vertex resolution for 6.00 GeV/c is worse and on the order of 1.4-1.8 mm for the  $x$ - and  $y$ -direction and up to 9 mm for the  $z$ -direction. The vertex resolutions is slightly worse with the  $\Lambda$ -disks. Only the  $\bar{\Lambda}$  at the highest beam momentum gains in resolution from the additional  $\Lambda$ -disk points.

The invariant mass resolution has been determined to be on the order of 2-3 MeV/c for the different beam momenta. The  $\Lambda$ -disk have no significant influence on the invariant mass resolution.

The overall reconstruction efficiency for the  $\bar{\Lambda}\Lambda$  final state is 7.6%, 7.4% and 1.3% for 1.642 GeV/c, 1.918 GeV/c and 6.00 GeV/c respectively. The reconstruction efficiency rises with the  $\Lambda$ -disks on average by 0.7, 0.4 and 0.1 percentage points for 1.642 GeV/c, 1.918 GeV/c and 6.00 GeV/c, respectively. The low efficiency is partly caused by a bug in the track fitting algorithm, which should be fixed with the next version of the software which is being implemented.

Despite the small quantitative improvements, the  $\Lambda$ -disk lead to no qualitative improvements of the measurements. Thus, no clear proposal can be given for a best position of the  $\Lambda$ -disk.



## 7. Conclusion

**Upgrade of the Jülich Digital Readout System** The JDRS is a universal tabletop readout system developed in Jülich for ASIC prototypes. The JDRS has been enhanced in this work with new hardware and software components.

An upgrade of the digital readout board was developed to meet the requirements of an upcoming full size ToPix prototype, including full detector setups and online analysis of measurement data. The ML605, a commercial FPGA test system, replaces the custom made FPGA board. The existing firmware has been adapted to the new hardware component and specifications.

The JDRS has been adapted to the new interface of the ToPix 3 and the ToPix testboard. The firmware now includes configuration and readout routines for the ToPix 3 and other electrical components on the test board which are necessary for operation.

A new GUI, data classes and test routines have been implemented in the MRF control software to enable the operation and measurements of the ToPix. Subroutines have been implemented in software and firmware to enable a continuous readout mode of the ToPix necessary for test beam measurements.

To be prepared for future detector testing the GBT protocol has been ported and successfully tested to the ML605. The GBT protocol is under development at CERN to transmit digital data with high data rates in a high radiative environment. This implementation enabled the JDRS to readout future prototypes of the ToPix whose interface bases on a protocol of this project.

**Characterizing Measurements of the ToPix** The ToPix 3 is the recent front-end prototype for the readout of the pixel part of the MVD. A characterization of the ToPix 3 was done using the upgraded JDRS in lab and test beam measurements. In detailed lab measurements the digital functionality of the front-end ASIC was tested as well as the threshold, noise and threshold tuning capabilities of the chip. It could be shown that the performance of the ToPix 3 meets the given requirements for these points. The behavior of the ToPix 3 in the frequency range between 50 MHz and 155 MHz has been studied in detail. With these measurements it could be confirmed that the readout speed of the ToPix 3 needs to be reduced from the design frequency of 155.52 MHz to 50 MHz to have the full functionality of the ASIC. This reduction is the consequence of the column driver being dimensioned too small.

The simultaneous injection and readout of several pixels was tested to reduce the time needed to calibrate the ToPix 3. It showed that an interference between the measurements occurs, which led to data loss. This interference could also be an effect of the column driver being too small.

## 7. Conclusion

For the first time a high rate test of the ToPix has been performed in a proton beam with a beam momentum of 2.95 GeV/c at the COSY accelerator at the Forschungszentrum Jülich. At high particles rates the ASIC showed a drop in hit detection efficiency.

The drop in the hit detection efficiency has several reasons. With the reduced ASIC frequency the ToPix 3 is three times slower than designed. Also, the external steered column changer is slower compared to the final end-of-column logic that will be available in the next prototype. In addition to the known points which reduce the hit detection efficiency in the ToPix 3, two additional points were found during this test beam.

A significant hit loss is observed at certain trailing edge time stamps that correlate to a time in the readout sequence. The second effect is a strange asymmetry between the odd and the even sides of a double column, which gets more pronounced with higher rates. The results of these measurements are the basis for a detailed design review at INFN Turin to solve these problems for the next prototype of the ToPix ASIC.

**Analysis of the  $\bar{\Lambda}\Lambda$  Final State** The reaction channel  $\bar{p}p \rightarrow \bar{\Lambda}\Lambda \rightarrow \bar{p}\pi^+p\pi^-$  has been used as a test channel for the reconstruction ability of the  $\bar{\text{PANDA}}$  detector concerning long living particles like ground state hyperons. The question has been investigated if additional semiconductor sensors, so-called  $\Lambda$ -disks, in the empty space between MVD and GEM stations could improve the resolutions and the count rates. Four different positions of the semiconductor disks have been investigated.

The reaction has been simulated with the PandaRoot simulation and analysis framework on the PandaGRID at three different beam momenta. The PandaRoot framework is still under development, so different parts of the simulation and the analysis needed to be supported by MC information to enable a complete workflow.

The reconstructed invariant mass distribution for  $\Lambda \rightarrow p\pi^-$  and  $\bar{\Lambda} \rightarrow \bar{p}\pi^+$  with  $\bar{\text{PANDA}}$  was simulated to have a resolution between 2-3 MeV/c. The  $\Lambda$ -disks have no effect on the invariant mass resolution. For the lower two beam momenta the FWHM of the obtained vertex resolutions are on the order of (550-700)  $\mu\text{m}$  for  $x$ - and  $y$ -direction (perpendicular to the beam axis) and around 1.35-1.5 mm ( $\Lambda$ ) and 2.15-2.25 mm ( $\bar{\Lambda}$ ) for  $z$ -direction (parallel to the beam axis). The effect on the count rate of  $\bar{\Lambda}\Lambda$  candidates before analysis is less than 3.5 percentage points and thus comparably small. The effect on the reconstruction efficiency is less than 0.7 percentage points and due to the analysis even smaller. Despite the small quantitative improvements, the  $\Lambda$ -disk lead to no qualitative improvements of the measurements. From this point of view the  $\Lambda$ -disks do not seem to be necessary.

Further simulations with other decay channels and a more developed analysis framework are necessary for a final evaluation whether the  $\Lambda$ -disks should be included into the  $\bar{\text{PANDA}}$  detector.

## A. Appendix to $\bar{\Lambda}\Lambda$ Final State

### A.1. Armenteros-Podolanski-Plot Analysis of the $\bar{\Lambda}\Lambda$ System

The Armenteros-Podolanski-Plot is a tool to analyze neutral particles which decay into two oppositely charged particles like  $\Lambda$  or  $K^0$  and to identify them without PID information. This tool was invented in 1953 by J. Podolanski and R. Armenteros [80].

This method takes the measured three-momenta of the daughter particles to calculate with respect to the flight direction of the initial neutral particle the transverse momentum  $p_t$  and the longitudinal momentum asymmetry  $\alpha$ :

$$\alpha = \frac{p_{\parallel}^+ - p_{\parallel}^-}{p_{\parallel}^+ + p_{\parallel}^-} = \frac{p_{\parallel}^p - p_{\parallel}^{\pi^-}}{p_{\parallel}^p + p_{\parallel}^{\pi^-}} = \frac{p_{\parallel}^{\pi^+} - p_{\parallel}^{\bar{p}}}{p_{\parallel}^{\pi^+} + p_{\parallel}^{\bar{p}}} \quad (\text{A.1})$$

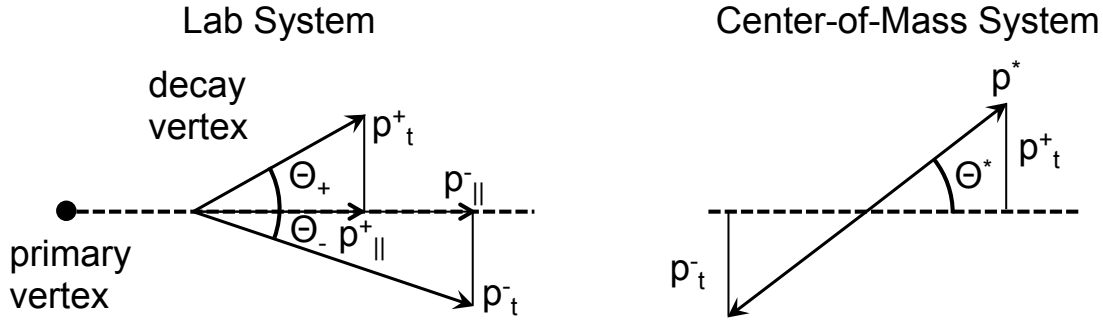


Figure A.1.: Decay kinematics in the reference frame and the CMS for the Armenteros-Podolanski-Plot. Picture based on [81].

In a histogram of  $\alpha$  versus  $p_t$  different neutral particles populate clearly distinguishable arcs (see Figure A.2). This behavior can be used to remove background from the considered particles. If the two daughter particles have the same mass the arc is symmetric about  $\alpha=0$ . If the daughter particles do have not the same mass, like for the  $\Lambda$ , the arcs are symmetric about  $\alpha^*$  which depends on the masses of the particles.

$$\alpha^* = \frac{(m^+)^2 - (m^-)^2}{m_{\Lambda}^2} = \pm 0.69 \quad (\text{A.2})$$

The Armenteros-Podolanski-Plot for the simulated  $\bar{\Lambda}\Lambda$  events is shown in Figure A.3. The arcs for the  $\Lambda$  particles (right) and  $\bar{\Lambda}$  particles (left) are clearly visible.

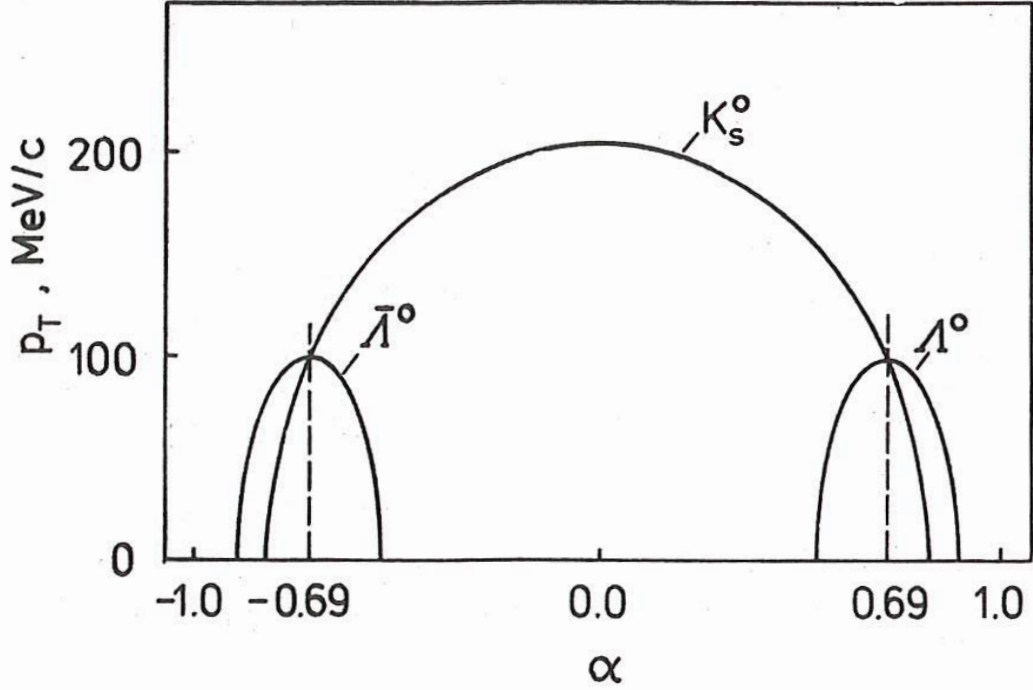


Figure A.2.: Schematic drawing of  $\Lambda$  and  $K_S^0$  arcs in the Armenteros-Podolanski-Plot. Figure taken from Ref. [81].

The higher the momentum of a particle, the sharper and narrower the arc in the Armenteros-Podolanski-Plot becomes. This can be nicely seen at the  $\bar{\Lambda}$ , which has a rising forward boost for rising beam momenta.

The Armenteros-Podolanski-Plot for the reconstructed particles after the cut is shown in Figure A.4. The reconstructed arcs are more diffuse.

As the beam momentum increases, the  $\Lambda$  arc becomes less populated in comparison to the  $\bar{\Lambda}$  arc. This is expected due to the different reconstruction efficiencies of the particles. For the lowest beam momentum the outside branches of the arcs are not reconstructed. Also for the middle beam momentum the branches are missing, but the  $\Lambda$  arc is more strongly effected than the  $\bar{\Lambda}$  arc. For the highest beam momentum the  $\bar{\Lambda}$  arc is nearly complete, while the  $\Lambda$  arc is nearly half missing. Events on the outside branch of the arcs have a high absolute value of  $\alpha$ , meaning a high longitudinal momentum for the  $p$  ( $\bar{p}$ ) and a low longitudinal momentum for the  $\pi^-$  ( $\pi^+$ ). The lower momentum for the pions leads to a worse reconstruction ability for these events. As the beam momentum gets higher, the final state particles of the  $\bar{\Lambda}$  are more strongly boosted and have sufficient momentum to be reconstructed. Due to this the  $\bar{\Lambda}$  arc at 6.00 GeV/c is completely populated. The opposite case is valid for the  $\Lambda$  arc. With higher beam momentum the

### *A.1. Armenteros-Podolanski-Plot Analysis of the $\bar{\Lambda}\Lambda$ System*

final state particles have low momentum, with a worse reconstruction ability.

A comparison between the reconstructed and the MC truth plot show that entries outside of the arcs are mostly combinatorial background. A cut along the borders of the arcs would help to reduce the background for this decay.

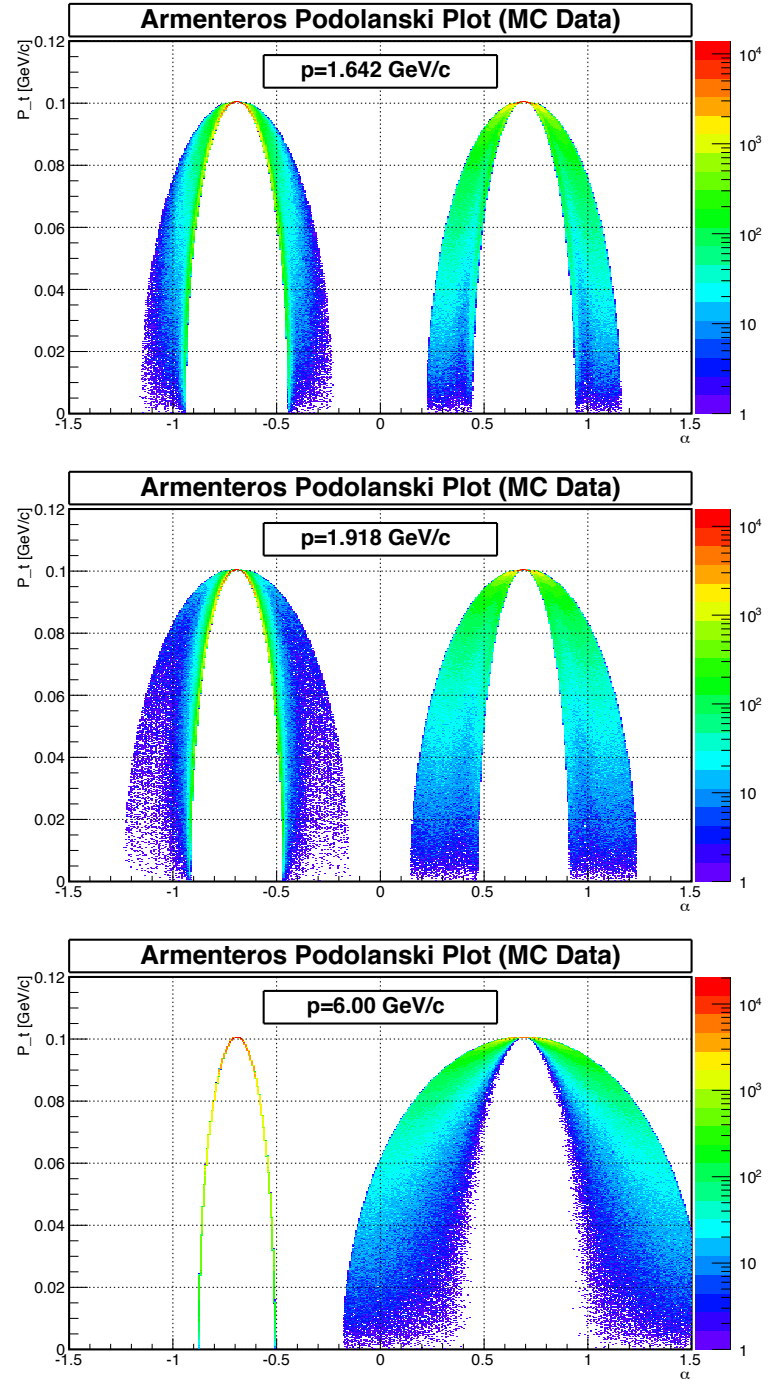


Figure A.3.: Armenteros-Podolanski-Plot for the three different beam momenta using the MC generator data. The right arc belongs to the  $\Lambda$ , the left arc belongs to the  $\bar{\Lambda}$ .



### A.1. Armenteros-Podolanski-Plot Analysis of the $\bar{\Lambda}\Lambda$ System

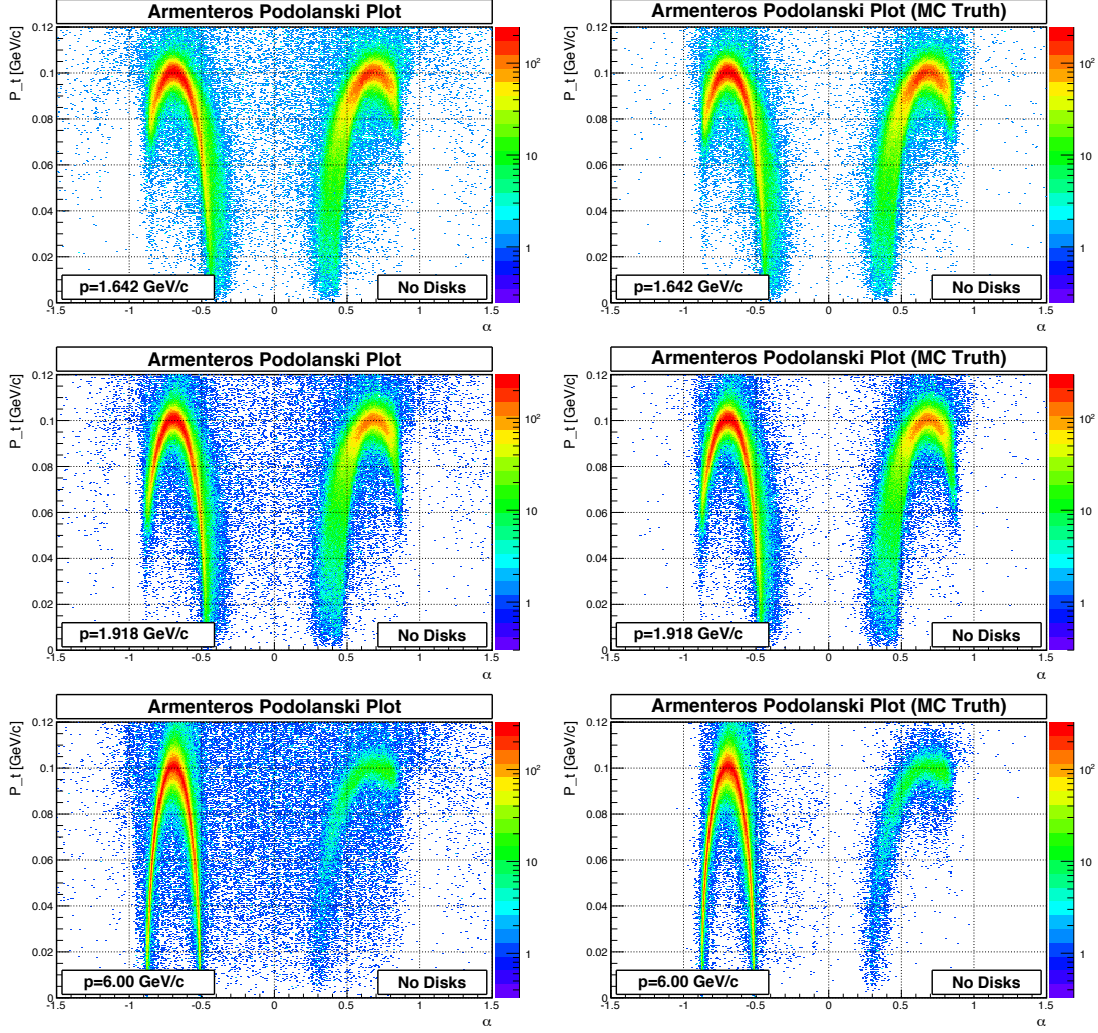


Figure A.4.: Armenteros-Podolanski-Plot for the three different beam momenta for Pos-1. Left: Reconstructed Plot including background. Right: Plot for MC truth particles. Upper: 1.642 GeV/c. Center: 1.918 GeV/c. Lower: 6.000 GeV/c. The right arc within a picture belongs to  $\Lambda$ , the left arc belongs to the  $\bar{\Lambda}$ .

## A.2. Counting Statistics

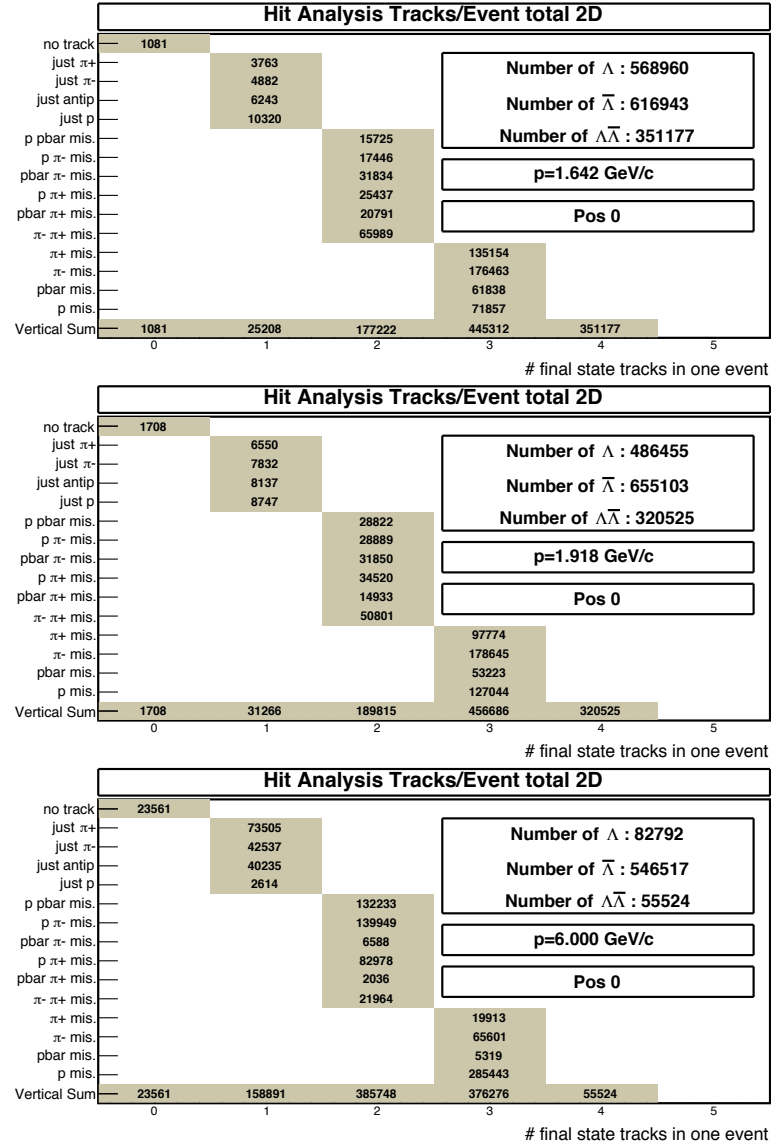


Figure A.5.: Analysis of simulated final state tracks per event which fulfill the selection criteria for Pos0.

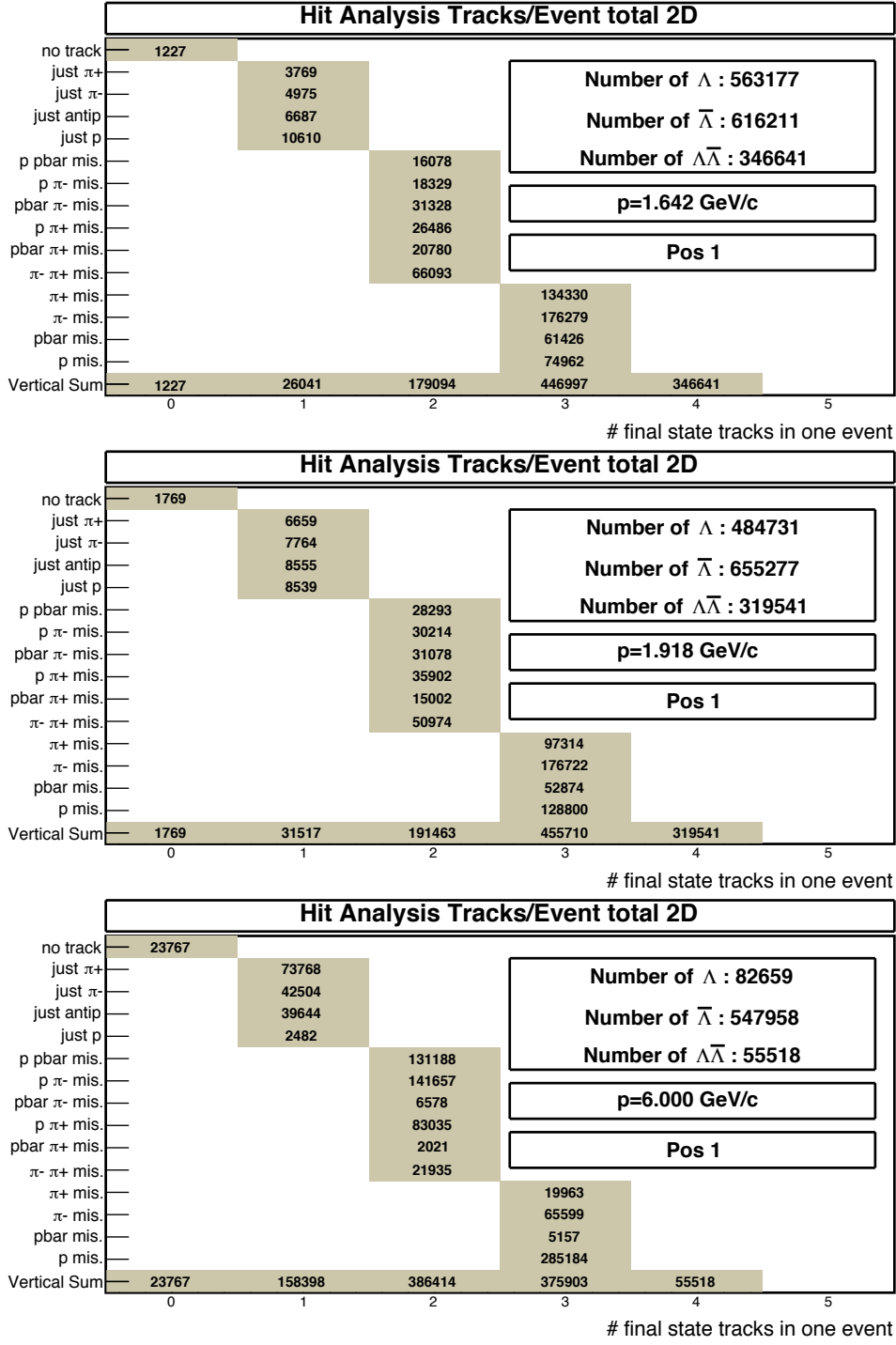


Figure A.6.: Analysis of simulated final state tracks per event which fulfill the selection criteria for Pos1.

A. Appendix to  $\bar{\Lambda}\Lambda$  Final State

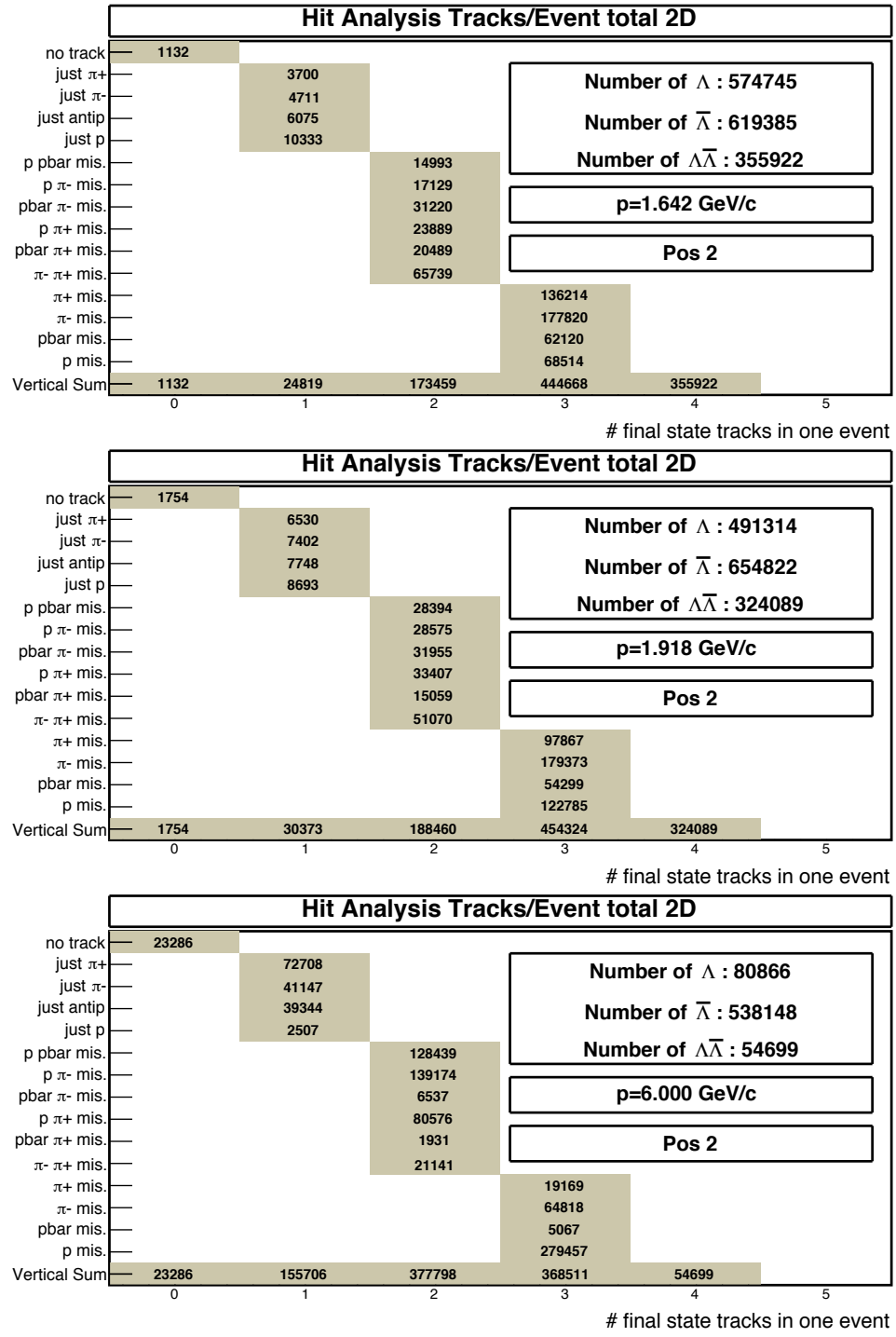


Figure A.7.: Analysis of simulated final state tracks per event which fulfill the selection criteria for Pos2.

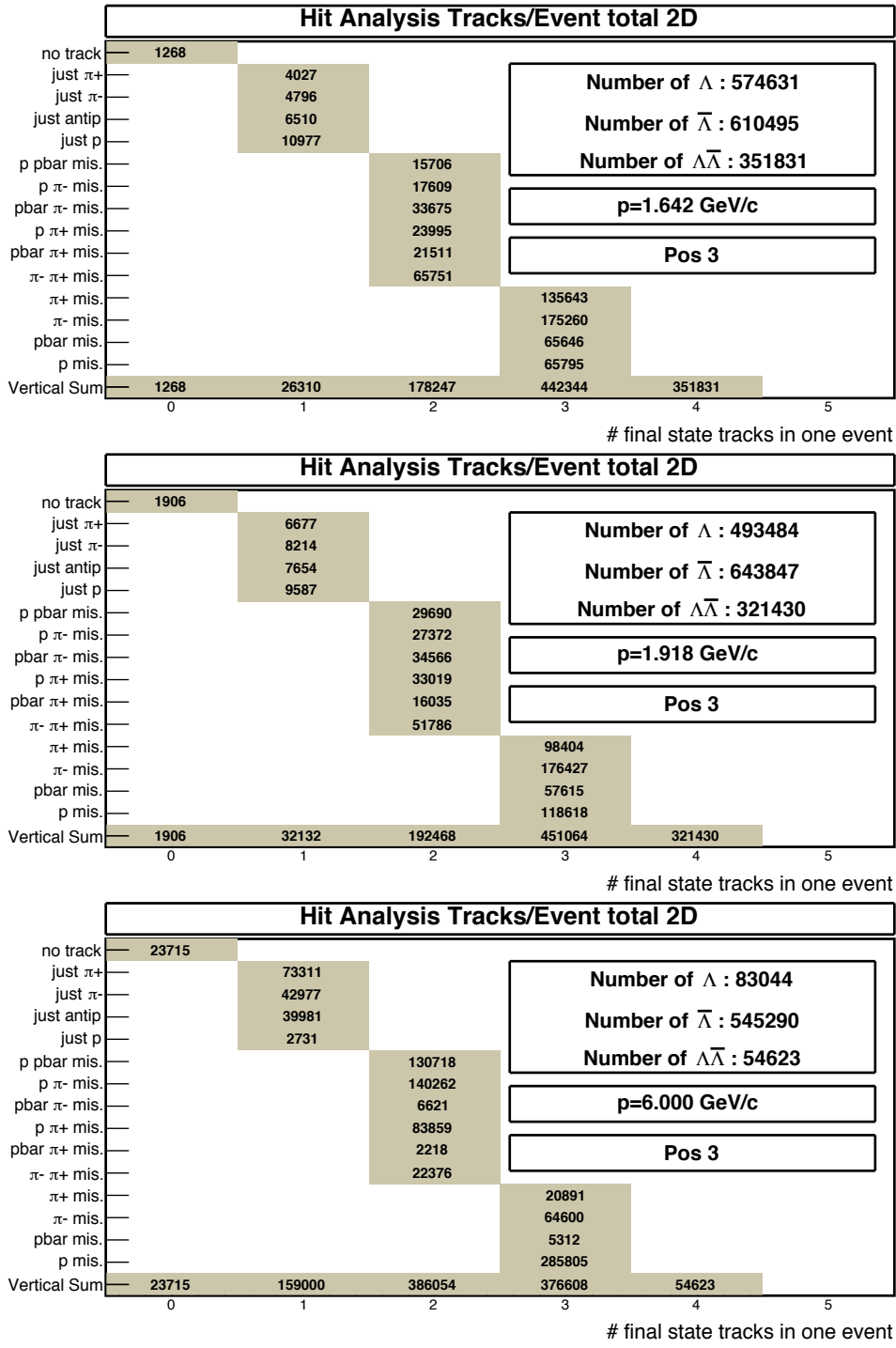


Figure A.8.: Analysis of simulated final state tracks per event which fulfill the selection criteria for Pos3.

# A. Appendix to $\bar{\Lambda}\Lambda$ Final State

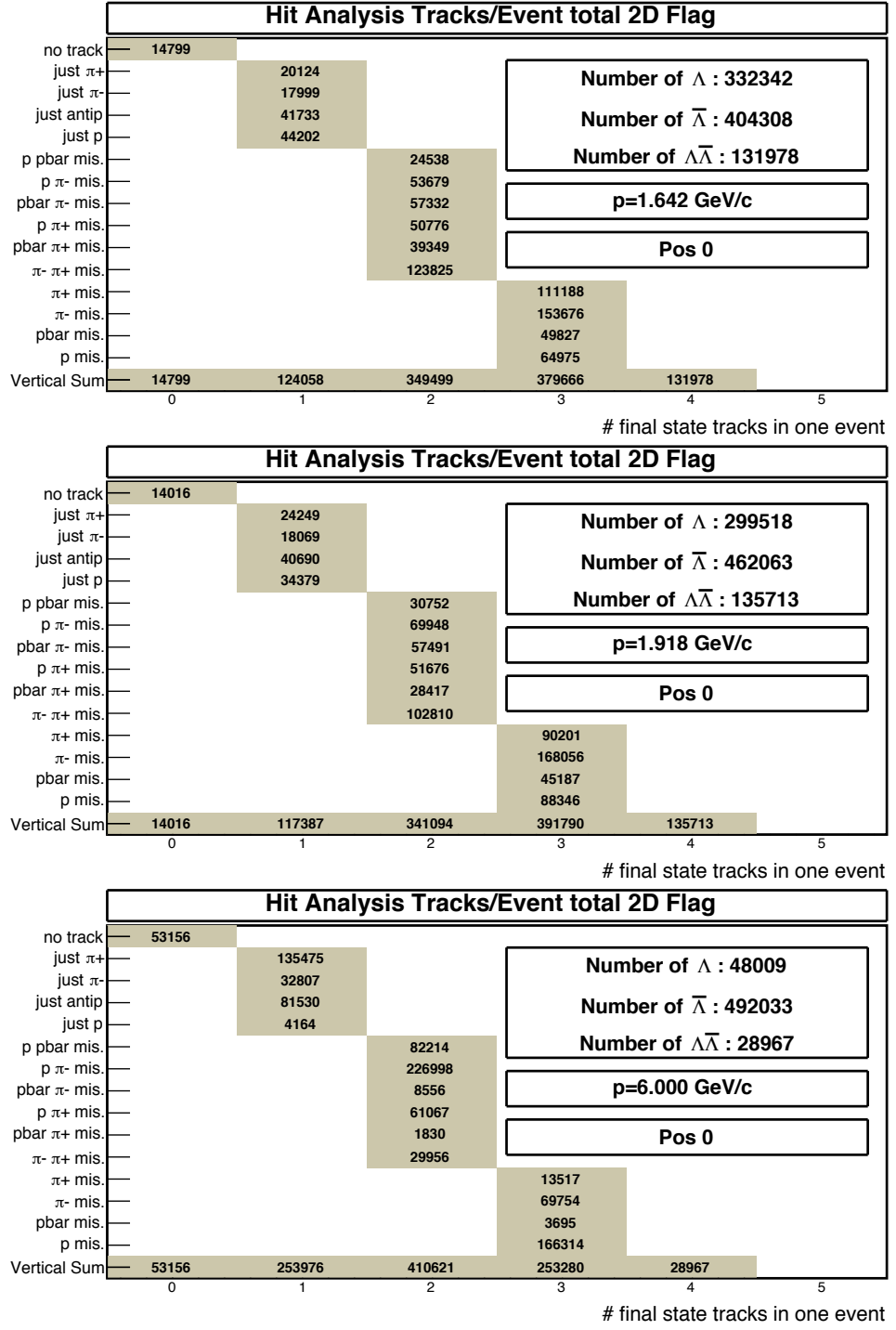


Figure A.9.: Analysis of simulated final state tracks per event which fulfill the selection criteria after track fitting for Pos0.

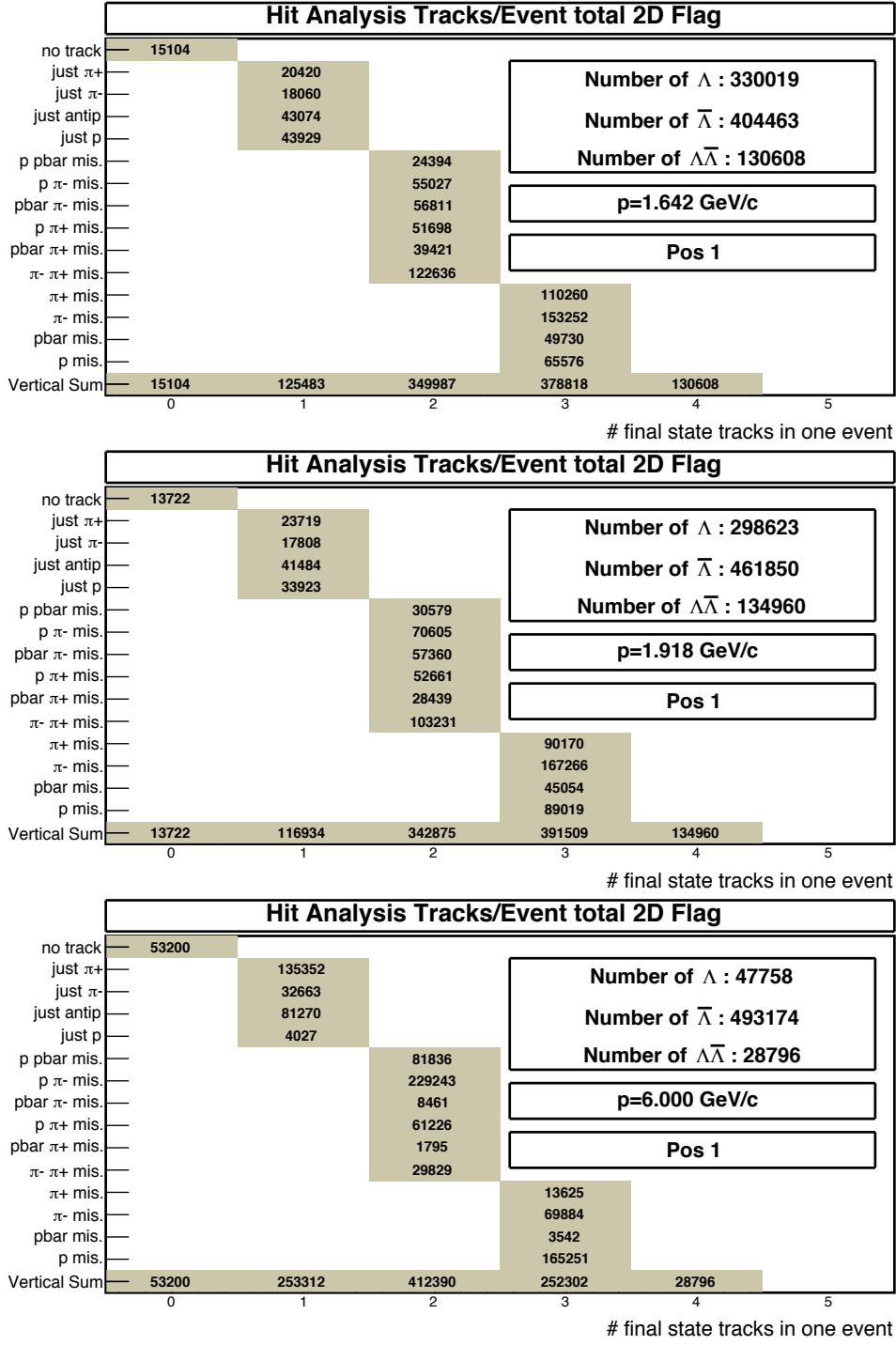


Figure A.10.: Analysis of simulated final state tracks per event which fulfill the selection criteria after track fitting for Pos1.

# A. Appendix to $\bar{\Lambda}\Lambda$ Final State

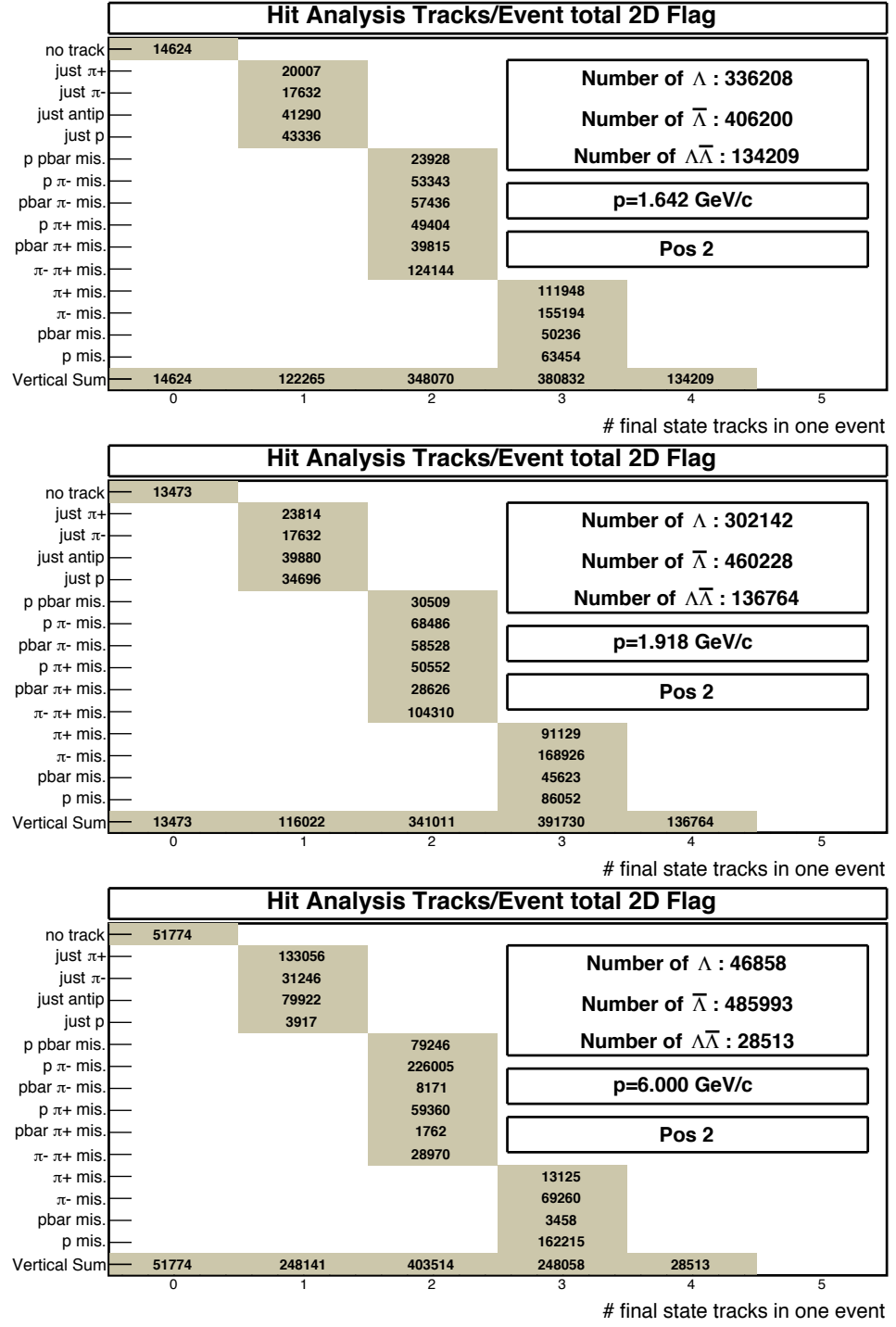


Figure A.11.: Analysis of simulated final state tracks per event which fulfill the selection criteria after track fitting for Pos2.



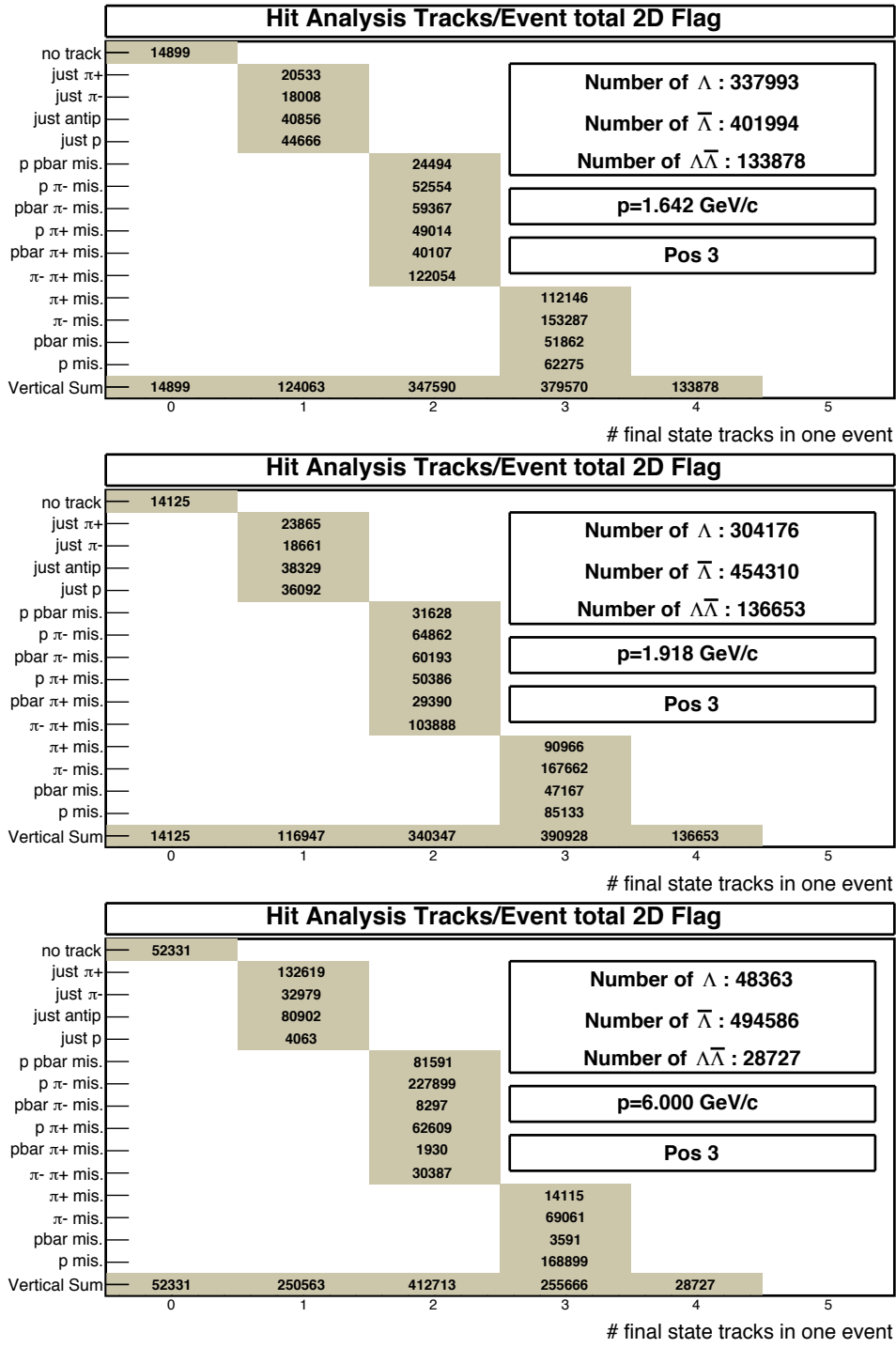


Figure A.12.: Analysis of simulated final state tracks per event which fulfill the selection criteria after track fitting for Pos3.



# Bibliography

- [1] *Wikimedia Commons - The free media repository*. 2013. URL: <http://commons.wikimedia.org/wiki/File:Bosons-Hadrons-Fermions-RGB-png2.png> (visited on 01/15/2014).
- [2] G. Aad et al. “Observation of a new particle in the search for the Standard Model Higgs boson with the ATLAS detector at the LHC”. In: *Physics Letters B* 716.1 (2012), pp. 1–29. ISSN: 0370-2693. DOI: [10.1016/j.physletb.2012.08.020](https://doi.org/10.1016/j.physletb.2012.08.020).
- [3] S. Chatrchyan et al. “Observation of a new boson at a mass of 125 GeV with the CMS experiment at the LHC”. In: *Physics Letters B* 716.1 (2012), pp. 30–61. ISSN: 0370-2693. DOI: [10.1016/j.physletb.2012.08.021](https://doi.org/10.1016/j.physletb.2012.08.021).
- [4] *Wikimedia Commons - The free media repository*. 2013. URL: [http://commons.wikimedia.org/wiki/File:Standard\\_Model\\_of\\_Elementary\\_Particles.svg](http://commons.wikimedia.org/wiki/File:Standard_Model_of_Elementary_Particles.svg) (visited on 01/15/2014).
- [5] *Wikimedia Commons - The free media repository*. 2013. URL: [http://commons.wikimedia.org/wiki/File:Baryon\\_octet.svg](http://commons.wikimedia.org/wiki/File:Baryon_octet.svg) (visited on 01/15/2014).
- [6] *Wikimedia Commons - The free media repository*. 2013. URL: [http://commons.wikimedia.org/wiki/File:Baryon\\_decuplet.svg](http://commons.wikimedia.org/wiki/File:Baryon_decuplet.svg) (visited on 01/15/2014).
- [7] *Wikimedia Commons - The free media repository*. 2013. URL: [http://commons.wikimedia.org/wiki/File:Meson\\_nonet\\_spin\\_0.svg](http://commons.wikimedia.org/wiki/File:Meson_nonet_spin_0.svg) (visited on 01/15/2014).
- [8] *Wikimedia Commons - The free media repository*. 2013. URL: [http://commons.wikimedia.org/wiki/File:Meson\\_nonet\\_spin\\_1.svg](http://commons.wikimedia.org/wiki/File:Meson_nonet_spin_1.svg) (visited on 01/15/2014).
- [9] B. Povh, K. Rith, C. Scholz and F. Zetsche. *Teilchen und Kerne*. Springer Verlag, 1999. ISBN: 9783540659280.
- [10] J. Beringer et al. “Review of Particle Physics”. In: *Phys. Rev. D* 86 (1 2012), p. 010001. DOI: [10.1103/PhysRevD.86.010001](https://doi.org/10.1103/PhysRevD.86.010001).
- [11] W. Erni et al. “Physics Performance Report for PANDA: Strong Interaction Studies with Antiprotons”. In: *ArXiv e-prints* (2009). arXiv:[0903.3905](https://arxiv.org/abs/0903.3905) [hep-ex].
- [12] *Public Technical Progress Report*. Tech. rep. 2005. URL: [http://www-panda.gsi.de/archive/public/panda\\_tpr.pdf](http://www-panda.gsi.de/archive/public/panda_tpr.pdf).
- [13] S. Godfrey and N. Isgur. “Mesons in a relativized quark model with chromodynamics”. In: *Phys. Rev. D* 32 (1 1985), pp. 189–231. DOI: [10.1103/PhysRevD.32.189](https://doi.org/10.1103/PhysRevD.32.189).
- [14] M. Di Pierro and E. Eichten. “Excited heavy-light systems and hadronic transitions”. In: *Phys. Rev. D* 64 (11 2001), p. 114004. DOI: [10.1103/PhysRevD.64.114004](https://doi.org/10.1103/PhysRevD.64.114004).

## Bibliography

- [15] Paola Gianotti. “Results and perspectives in hadron spectroscopy”. In: *Physica Scripta* 2012.T150 (2012), p. 014014. DOI: [10.1088/0031-8949/2012/T150/014014](https://doi.org/10.1088/0031-8949/2012/T150/014014).
- [16] N. Brambilla et al. “Heavy quarkonium: progress, puzzles, and opportunities”. In: *The European Physical Journal C* 71.2 (2011), pp. 1–178. ISSN: 1434-6044. DOI: [10.1140/epjc/s10052-010-1534-9](https://doi.org/10.1140/epjc/s10052-010-1534-9).
- [17] K.K. Seth. “A Personal Journey Through Hadronic Exotica”. In: *Few-Body Systems* 45.2-4 (2009), pp. 85–90. DOI: [10.1007/s00601-009-0034-7](https://doi.org/10.1007/s00601-009-0034-7).
- [18] Eric Thomé. “Multi-Strange and Charmed Antihyperon-Hyperon Physics for PANDA”. PhD thesis. Uppsala University, 2012. URL: [http://www-panda.gsi.de/db/theses/DB/ET10-121123\\_Erik\\_Thesis.pdf](http://www-panda.gsi.de/db/theses/DB/ET10-121123_Erik_Thesis.pdf).
- [19] P. Achenbach et al. “Hypernuclear Physics at PANDA”. In: *Hyperfine Interact.* 209 (2012), pp. 99–104. DOI: [10.1007/s10751-012-0571-1](https://doi.org/10.1007/s10751-012-0571-1).
- [20] E. Klempt and A. Zaitsev. “Glueballs, hybrids, multiquarks: Experimental facts versus QCD inspired concepts”. In: *Physics Reports* 454.1–4 (2007), pp. 1–202. ISSN: 0370-1573. DOI: [10.1016/j.physrep.2007.07.006](https://doi.org/10.1016/j.physrep.2007.07.006).
- [21] FAIR GmbH and GSI. *Green Paper, The Modularized Start Version : FAIR - Facility for Antiproton and Ion Research*. Darmstadt: FAIR, 2009, 19p. URL: <http://repository.gsi.de/record/54094>.
- [22] FAIR. “Baseline Technical Report, Volume 2, Accelerator and Scientific Infrastructure”. In: (2006). URL: [http://www.fair-center.de/fileadmin/fair/publications\\_FAIR/FAIR\\_BTR\\_2.pdf](http://www.fair-center.de/fileadmin/fair/publications_FAIR/FAIR_BTR_2.pdf).
- [23] *Facility for Antiproton and Ion Research*. URL: <http://www.fair-center.de/>.
- [24] W. Erni et al. “Technical design report for the PANDA Straw Tube Tracker”. In: *The European Physical Journal A* 49 (2013). DOI: [10.1140/epja/i2013-13025-8](https://doi.org/10.1140/epja/i2013-13025-8).
- [25] A. Lehrach et al. “Beam performance and luminosity limitations in the high-energy storage ring (HESR)”. In: *Nuclear Instruments and Methods in Physics Research Section A: Accelerators, Spectrometers, Detectors and Associated Equipment* 561.2 (2006), pp. 289–296. ISSN: 0168-9002. DOI: [10.1016/j.nima.2006.01.017](https://doi.org/10.1016/j.nima.2006.01.017).
- [26] Panda Collaboration. “Technical Design Report for the PANDA Target”. In: (2012). URL: <http://www-panda.gsi.de/html/reports.php>.
- [27] W. Erni et al. “Technical Design Report for the PANDA Micro Vertex Detector”. In: *ArXiv e-prints* (2012). arXiv:[1207.6581](https://arxiv.org/abs/1207.6581) [physics.ins-det].
- [28] *PANDA Collaboration Website*. <http://www-panda.gsi.de/>. URL: <http://www-panda.gsi.de/>.
- [29] M. Galuska et al. “Hough Transform Based Pattern Recognition for the PANDA Forward Tracking System”. In: *51st International Winter Meeting on Nuclear Physics, Bormio* (2013). URL: <http://inspirehep.net/record/1265424/>.

- [30] N. Akopov et al. “The HERMES dual-radiator ring imaging Cherenkov detector”. In: *Nuclear Instruments and Methods in Physics Research Section A: Accelerators, Spectrometers, Detectors and Associated Equipment* 479.2–3 (Mar. 2002), pp. 511–530. DOI: [10.1016/S0168-9002\(01\)00932-9](https://doi.org/10.1016/S0168-9002(01)00932-9).
- [31] W. Erni et al. “Technical Design Report for the PANDA Electromagnetic Calorimeter (EMC)”. In: *ArXiv e-prints* (Oct. 2008). arXiv:[0810.1216](https://arxiv.org/abs/0810.1216) [[physics.ins-det](#)].
- [32] H. Moeini et al. “Design studies of the PWO Forward End-cap calorimeter for PANDA”. In: *The European Physical Journal A* 49.11 (2013), pp. 1–22. ISSN: 1434-6001. DOI: [10.1140/epja/i2013-13138-0](https://doi.org/10.1140/epja/i2013-13138-0).
- [33] R W Novotny and the PANDA Collaboration. “The Electromagnetic Calorimetry of the PANDA Detector at FAIR”. In: *Journal of Physics: Conference Series* 404.1 (2012), p. 012063. DOI: [10.1088/1742-6596/404/1/012063](https://doi.org/10.1088/1742-6596/404/1/012063).
- [34] Fabian Hügging. “Development of a Micro Vertex Detector for the PANDA-Experiment at the FAIR Facility”. In: *Nuclear Science Symposium Conference Record, 2006. IEEE*. Vol. 2. 2006, pp. 1239–1243. DOI: [10.1109/NSSMIC.2006.356068](https://doi.org/10.1109/NSSMIC.2006.356068).
- [35] M. D. Rolo et al. “TOFPET ASIC for PET applications”. In: *Journal of Instrumentation* 8.02 (2013), p. C02050. DOI: [10.1088/1748-0221/8/02/C02050](https://doi.org/10.1088/1748-0221/8/02/C02050).
- [36] Marius C. Mertens. “Der Panda Mikro Vertex Detektor: Endwicklung eines Labormesssystems, Simulation der MVD-Betriebsparameter sowie Untersuchung zur Auflösung der Breite des  $D_{s0}^*$ (2317)”. PhD thesis. Ruhr-Universität Bochum, 2010. URL: <http://www-brs.ub.ruhr-uni-bochum.de/netathtml/HSS/Diss/MertensMariusC/>.
- [37] M. Drochner et al. “A VME controller for data aquisition with flexible gigabit data link to PCI”. In: *Proceedings of the 12th IEEE Real Time congress on Nuclear and Plasma Science* (2001). URL: <http://juser.fz-juelich.de/record/43395>.
- [38] *Qt 4 Framework*. 2010. URL: <http://www.trolltech.com>.
- [39] H. Kleines et al. “Developments for the readout of the PANDA micro vertex detector”. In: *Real Time Conference (RT), 2010 17th IEEE-NPSS*. 2010, pp. 1–3. DOI: [10.1109/RTC.2010.5750459](https://doi.org/10.1109/RTC.2010.5750459).
- [40] Ivan Perić et al. “The FEI3 readout chip for the ATLAS pixel detector”. In: *Nuclear Instruments and Methods in Physics Research Section A: Accelerators, Spectrometers, Detectors and Associated Equipment* 565.1 (2006), pp. 178 –187. ISSN: 0168-9002. DOI: [10.1016/j.nima.2006.05.032](https://doi.org/10.1016/j.nima.2006.05.032).
- [41] Gianni Mazza. *Private communication*.
- [42] P. Moreira et al. “The GBT Project”. In: *Topical Workshop on Electronics for Particle Physics* (2009). URL: <http://cds.cern.ch/record/1235836>.
- [43] L. Amaral and S. Dris et al. “The versatile link, a common project for super-LHC”. In: *Journal of Instrumentation* 4 (2009), P12003. DOI: [10.1088/1748-0221/4/12/P12003](https://doi.org/10.1088/1748-0221/4/12/P12003).

- [44] S. Baron et al. “Implementing the GBT data transmission protocol in FPGAs”. In: *Topical Workshop on Electronics for Particle Physics* (2009). URL: <http://cds.cern.ch/record/1236361>.
- [45] Thanushan Kugathasan. “Low-Power High Dynamic Range Front-End Electronics for the Hybrid Pixel Detectors of the PANDA MVD”. PhD thesis. Universiti Turino, 2011. URL: <http://dottorato.ph.unito.it/Studenti/Tesi/XXIII/kugathasan.pdf>.
- [46] G. Mazza et al. “A CMOS 0.13  $\mu\text{m}$  Silicon Pixel Detector Readout ASIC for the PANDA experiment”. In: *Journal of Instrumentation* 7.02 (2012), p. C02015. DOI: [10.1088/1748-0221/7/02/C02015](https://doi.org/10.1088/1748-0221/7/02/C02015).
- [47] L. Gonella et al. “Total ionizing dose effects in 130-nm commercial CMOS technologies for HEP experiments”. In: *Nuclear Instruments and Methods in Physics Research Section A: Accelerators, Spectrometers, Detectors and Associated Equipment* A582 (2007), pp. 750–754. DOI: [10.1016/j.nima.2007.07.068](https://doi.org/10.1016/j.nima.2007.07.068).
- [48] *LT Linear Technology*. URL: <http://www.linear.com/product/LTC2604> (visited on 10/01/2013).
- [49] David-Leon Pohl. “Charakterisierung eines Silizium-Pixel-Auslesechips für den PANDA Mikro-Vertex-Detector”. MA thesis. Universität Bochum, 2011. URL: <http://www.ep1.rub.de/lehre/abschlussarbeiten/thesis/MscDavidPohl.pdf>.
- [50] *IKP Annual Report 2013*. 2013. URL: [http://www.fz-juelich.de/ikp/EN/Service/Download/Downloads/jahresbericht\\_2013.html](http://www.fz-juelich.de/ikp/EN/Service/Download/Downloads/jahresbericht_2013.html).
- [51] Ralf Kliemt. “Simulations with the Panda Micro-Vertex-Detector”. PhD thesis. Universität Bonn, 2012. URL: <http://hss.ulb.uni-bonn.de/2013/3303/3303.htm>.
- [52] S. Spataro and the PANDA Collaboration. “The PandaRoot framework for simulation, reconstruction and analysis”. In: *Journal of Physics: Conference Series* 331.3 (2011), p. 032031. DOI: [10.1088/1742-6596/331/3/032031](https://doi.org/10.1088/1742-6596/331/3/032031).
- [53] I Fröhlich et al. “Design of the pluto event generator”. In: *Journal of Physics: Conference Series* 219.3 (2010), p. 032039. DOI: [10.1088/1742-6596/219/3/032039](https://doi.org/10.1088/1742-6596/219/3/032039).
- [54] Torbjorn Sjostrand, Stephen Mrenna, and Peter Z. Skands. “A Brief Introduction to PYTHIA 8.1”. In: *Comput.Phys.Commun.* 178 (2008), pp. 852–867. DOI: [10.1016/j.cpc.2008.01.036](https://doi.org/10.1016/j.cpc.2008.01.036). arXiv:[0710.3820](https://arxiv.org/abs/0710.3820) [[hep-ph](#)].
- [55] A. Capella et al. “Dual parton model”. In: *Physics Reports* 236 (1994), pp. 225–329. DOI: [10.1016/0370-1573\(94\)90064-7](https://doi.org/10.1016/0370-1573(94)90064-7).
- [56] A. Galoyan et al. “Parametrization of the anti-P P Elastic Scattering Differential Cross Section Between 2-GeV/c  $\leq$  P(lab)  $\leq$  16-GeV/c”. In: *ArXiv e-prints* (2008). arXiv:[0809.3804](https://arxiv.org/abs/0809.3804) [[hep-ex](#)].

- [57] S.A. Bass et al. “Microscopic models for ultrarelativistic heavy ion collisions”. In: *Progress in Particle and Nuclear Physics* 41.0 (1998), pp. 255–369. ISSN: 0146-6410. DOI: [10.1016/S0146-6410\(98\)00058-1](#).
- [58] A. Galoyan, J. Ritman, and V. Uzhinsky. “Patches to UrQMD Model Code”. In: (2006). arXiv:[nucl-th/0605021](#) [[nucl-th](#)].
- [59] A.S. Galoyan and A. Polanski. “Simulation of anti-proton nucleus interactions in the framework of the UrQMD model”. In: (2003). arXiv:[hep-ph/0304196](#) [[hep-ph](#)].
- [60] EvtGen Collaboration. *The EvtGen package home page*. URL: <http://www.slac.stanford.edu/~lange/EvtGen/> (visited on 10/01/2013).
- [61] *Geant - detector description and simulation tool*. URL: <http://wwwasd.web.cern.ch/wwwasd/geant/>.
- [62] J. Allison et al. “Geant4 developments and applications”. In: *IEEE Transactions on Nuclear Science* 53.1 (2006), pp. 270–278. ISSN: 0018-9499. DOI: [10.1109/TNS.2006.869826](#).
- [63] Rene Brun and Fons Rademakers. “Root - an object oriented data analysis framework”. In: *Nuclear Instruments and Methods in Physics Research Section A: Accelerators, Spectrometers, Detectors and Associated Equipment* A.389 (1996), pp. 81–86. DOI: [10.1016/S0168-9002\(97\)00048-X](#).
- [64] I. et al. Hrivnacova. “The Virtual Monte Carlo”. In: *Computing in High Energy and Nuclear Physics (CHEP)* C0303241 (2003), THJT006. arXiv:[cs/0306005](#) [[cs-se](#)].
- [65] R. Frühwirth, A. Strandlie, and W. Waltenberger. “Helix fitting by an extended Riemann fit”. In: *Nuclear Instruments and Methods in Physics Research Section A: Accelerators, Spectrometers, Detectors and Associated Equipment* 490.1–2 (2002), pp. 366–378. ISSN: 0168-9002. DOI: [10.1016/S0168-9002\(02\)00911-7](#).
- [66] Pablo Yepes. “A fast track pattern recognition”. In: *Nuclear Instruments and Methods in Physics Research Section A: Accelerators, Spectrometers, Detectors and Associated Equipment* 380.3 (1996), pp. 582–585. ISSN: 0168-9002. DOI: [10.1016/0168-9002\(96\)00726-7](#). URL: <http://www.sciencedirect.com/science/article/pii/0168900296007267>.
- [67] P. Hough. “Machine Analysis of Bubble Chamber Pictures”. In: *Proc. Int. Conf. High Energy Accelerators and Instrumentation* (1959). URL: <http://inspirehep.net/record/919922>.
- [68] R. O. Duda and P. E. Hart. “Use of the Hough Transformation to Detect Lines and Curves in Pictures”. In: *Comm. ACM, Vol. 15, pp. 11* (1972). DOI: [10.1145/361237.361242](#).
- [69] C. Höppner et al. “A novel generic framework for track fitting in complex detector systems”. In: *Nuclear Instruments and Methods in Physics Research Section A: Accelerators, Spectrometers, Detectors and Associated Equipment* 620.2–3 (2010), pp. 518–525. ISSN: 0168-9002. DOI: [10.1016/j.nima.2010.03.136](#).

## Bibliography

- [70] Rudolph Emil Kalman. “A New Approach to Linear Filtering and Prediction Problems”. In: *Transactions of the ASME—Journal of Basic Engineering* 82.Series D (1960), pp. 35–45. URL: <http://www.cs.unc.edu/~welch/kalman/kalmanPaper.html>.
- [71] R. Frühwirth. “Application of Kalman filtering to track and vertex fitting”. In: *Nuclear Instruments and Methods in Physics Research Section A: Accelerators, Spectrometers, Detectors and Associated Equipment* 262.2–3 (1987), pp. 444–450. ISSN: 0168-9002. DOI: [10.1016/0168-9002\(87\)90887-4](https://doi.org/10.1016/0168-9002(87)90887-4).
- [72] *Rho Framework*. <https://code.google.com/p/rhoframework/>.
- [73] BaBar Collaboration. *Workbook for BaBar Offline Users - Beta: the Analysis*. [http://www.slac.stanford.edu/BFR00T/www/doc/workbook\\_kiwi/beta1/beta1.html](http://www.slac.stanford.edu/BFR00T/www/doc/workbook_kiwi/beta1/beta1.html). (Visited on 01/31/2014).
- [74] P. Buncic et al. “The architecture of the AliEn system”. In: *Computing in High Energy and Nuclear Physics (CHEP)* (2005). URL: <http://cds.cern.ch/record/865533>.
- [75] *MonALISA portal*. <http://monalisa.cern.ch>.
- [76] Sophie Grape. “PWO Crystal Measurements and Simulation Studies of  $\bar{\Lambda}$  Hyperon Polarisation for PANDA”. PhD thesis. Uppsala University, 2008. URL: <http://www-panda.gsi.de/framework/docsearch.php?subject=thesis&papers=on>.
- [77] T. Johansson. “Antibaryon-baryon production in antiproton-proton collisions”. In: *Proceedings of the international school of physics "Enrico Fermi"* (2004), pp. 423–450.
- [78] P. D. Barnes et al. “Observables in high-statistics measurements of the reaction  $p\bar{p} \rightarrow \Lambda\bar{\Lambda}$ ”. In: *Phys. Rev. C* 54 (4 1996), pp. 1877–1886. DOI: [10.1103/PhysRevC.54.1877](https://doi.org/10.1103/PhysRevC.54.1877).
- [79] H. Becker et al. “Measurement of the reactions  $\bar{p}p \rightarrow \bar{\Lambda}\Lambda$ ,  $\bar{p}p \rightarrow \Lambda\Sigma^0$  and  $\bar{p}p \rightarrow \Lambda(\text{missing mass})$  at 6 GeV”. In: *Nuclear Physics B* 141.1–2 (1978), pp. 48–64. ISSN: 0550-3213. DOI: [10.1016/0550-3213\(78\)90333-4](https://doi.org/10.1016/0550-3213(78)90333-4).
- [80] J. Podolanski and R. Armenteros. “III. Analysis of V-Events”. In: *Philosophical Magazine* 7 (1954), pp. 13–30. DOI: [10.1080/14786440108520416](https://doi.org/10.1080/14786440108520416).
- [81] J. Bartke. *Introduction to Relativistic Heavy Ion Physics*. World Scientific Publishing, 2009. ISBN: 9810212313.



# Acronyms

ALICE	A Large Ion Collider Experiment
AliEn	Alice Environment
ASIC	Application Specific Integrated Circuit
ATLAS	A Torodial LHC Apparatus
CAL	Chip Access Layer
CBM	Compressed Baryonic Matter
CCR	Chip Configuration Register
CELSIUS	Cooling with Electrons and Storing of Ions from the Uppsala Synchrocyclotron
CERN	Conseil Européen pour la Recherche Nucléaire
CMC	Common Mezzanine Card
CMOS	Complementary Metal Oxide Semiconductor
CMS	Center-of-Mass System
CMS	Compact Muon Solenoid
COSY	Cooler Synchrotron
CR	Collector Ring
CRCU	Column Readout Control Unit
CSA	Charge Sensitive Amplifier
CSR	Configuration Shift Register
DAC	Digital to Analog Converter
DAQ	Data Acquisition
DIRC	Detection of Internally Reflected Cherenkov Light
DMA	Direct Memory Access
DSSD	Double-sided Silicon Strip Detectors
DUT	Device under Test
EMC	Electromagnetic Calorimeter
ENC	Equivalent Noise Charge
EndoTOFPED-US	Endoscopic TOFPET & Ultrasound
ESR	Experimental Storage Ring
FAIR	Facility for Antiproton and Ion Research
FIFO	First In First Out
FMC	FPGA Mezzanine Card

## Acronyms

FPGA	Field Programmable Gate Array
FS	Forward Spectrometer
FTS	Forward Tracking System
FWHM	Full-Width at Half Maximum
GAL	Generic Access Layer
GBT	GigaBit Transceiver
GEM	Gas Electron Multiplier
GSi	Gesellschaft für Schwerionenforschung
GUI	Graphical User Interface
HESR	High Energy Storage Ring
HL	high luminosity mode
HPGe	High purity germanium
HR	high resolution mode
INFN	Istituto Nazionale di Fisica Nucleare
IP	Interaction Point
JDL	Job Description Language
JDRS	Jülich Digital Readout System
JULIC	Jülich Light Ion Cyclotron
LAAPD	Large Area Avalanche Photo-Diode
LHC	Large Hadron Collider
LPC-FMC	Low Pin Count FPGA Mezzanine Card
LVDS	Low Voltage Differential Signal
MC	Monte Carlo
MCT-PMT	Micro-Channel Plate Photomultiplier
MDT	Mini Drift Tubes
MIP	Minimum Ionizing Particle
MonALISA	Monitoring Agents using a Large Integrated Services Architecture
MP	Micropulse
MRF	MVD Readout Framework
MSB	Most Significant Bit
MVD	Micro Vertex Detector
OSI	Open Systems Interconnection
$\bar{\text{P}}\text{ANDA}$	Anti <b>P</b> roton <b>A</b> nnihilation at <b>D</b> armstadt
PASTA	$\bar{\text{P}}\text{ANDA}$ Strip ASIC

PCB	Printed Circuit Board
PCI	Peripheral Component Interconnect
PCLR	Pixel Configuration Local Register
PDAC	Pixel DAC
PDF	Probability Density Function
PDG	Particle Data Group
PID	Particle Identification
Pixel	<b>P</b> icture <b>E</b> lement
PMT	Photomultiplier Tubes
QCD	Quantum Chromodynamics
RESR	Recycled Experimental Storage Ring
RICH	Ring Imaging Cherenkov Detector
SciTil	Scintillator Tiles
SFP	Small Form Factor Pluggable
SFP+	Enhanced Small Form Factor Pluggable
SIS18	Schwerionen Synchrotron
SLVS	Scalable Low Voltage Signal
SM	Standard Model
STL	Standard Template Library
STT	Straw Tube Tracker
SU(3)	special unitary group of degree 3
TAL	Transport Access Layer
TID	Total Ionizing Dose
TOF	Time-of-Flight
TOFPET	Time-of-Flight Positron Emission Tomography
ToPix	Torino Pixel
ToT	Time-over-Threshold
TS	Target Spectrometer
UNILAC	Universal Linear Accelerator
UrQMD	UltraRelativistic Quantum Molecular Dynamics
VHDL	<b>V</b> ery <b>H</b> igh <b>S</b> peed <b>I</b> ntegrated <b>C</b> ircuit <b>H</b> ardware <b>D</b> escription <b>L</b> anguage
VMC	Virtual Monte Carlo
VPTT	Vacuum Photo-Tetrodes
WASA	Wide Angle Shower Apparatus



# List of Figures

2.1.	Particle classification in the SM. Picture taken from Ref. [1]. . . . .	4
2.2.	Elementary particles of the SM. The first three columns show the leptons and quarks arranged in three generations. The fourth column shows the gauge bosons and the fifth column displays the Higgs boson. Picture taken from Ref. [4]. . . . .	5
2.3.	Classification of baryons (upper, left: $J^P = \frac{1}{2}^+$ , right: $J^P = \frac{3}{2}^+$ ) and mesons (lower, left: $J^P = 0^-$ , right: $J^P = 1^-$ ) built from the lightest quarks up, down and strange. The particles are sorted according to their strangeness (S) and electrical charge (Q). The strangeness is defined by the number of strange antiquarks in the hadron. Pictures taken from Ref. [5, 6, 7, 8]. . . . .	6
2.4.	Summary of measurements of the strong coupling constant $\alpha_s$ as a function of the respective energy scale Q. Picture taken from [10]. . . . .	7
2.5.	Mass range corresponding systems accessible with the HESR. Picture taken from Ref. [12]. . . . .	8
2.6.	$D_s$ spectrum predictions (solid/dotted lines) and experimental values (black dots: older, red dots: newer). Picture taken from Ref. [15]. . . . .	9
2.7.	Comparison between the positronium ( $e^+e^-$ ) and charmonium ( $c\bar{c}$ ) spectra with the ratio of energy scales. Picture taken from Ref. [17]. . . . .	10
2.8.	The charmonium spectrum. Solid lines indicate predictions, shaded lines indicate conventional charmonium states. Red dots indicate newly discovered charmonium-like states. Picture taken from Ref. [15]. . . . .	11
2.9.	Spectra of different strange hyperons. The colored boxes indicate states for which little is known about their quantum numbers. These states comprise significant potential for measurements with $\bar{P}$ ANDA (status Nov. 2011). Figure based on Ref. [10]. . . . .	12
2.10.	Spectrum of glueball masses predicted by Lattice-QCD calculations. Picture taken from Ref. [20]. . . . .	13
3.1.	Overview of the full FAIR facility. The existing accelerators of the GSI are displayed in blue, displayed in red are the new systems which belong to the FAIR facility. Picture taken from Ref. [23]. . . . .	16
3.2.	Schematic drawing of the HESR. The $\bar{P}$ ANDA experiment will be located in the lower straight part. The electron cooling will be located in the upper straight section. Picture taken from Ref. [24]. . . . .	17

## List of Figures

3.3.	Side view of the $\overline{\text{P}}$ ANDA target spectrometer with all sub-detectors. The antiproton beam approaches from the left. Picture taken from Ref. [27].	20
3.4.	Side view of the $\overline{\text{P}}$ ANDA forward spectrometer with its sub-detectors. The antiproton beam approaches from the left. Picture taken from Ref. [27].	21
3.5.	Technical drawings of the STT: Left: Front view along the beam axis. Green indicate straw tubes oriented parallel to the beam axis, blue and red indicate straw tubes skewed by an angle of $\pm 3^\circ$ with respect to the beam axis [24]. Right: STT with beam and target pipe [28]. The antiproton beam enters from the left.	22
3.6.	Schematic drawing of the barrel and forward end-cap EMC with support and cooling structures. Picture taken from Ref. [31].	24
3.7.	Technical drawing of the MVD with support structure, cooling, and beam pipe. The antiproton beam enters from the left. Picture taken from Ref. [27].	28
3.8.	Schematic overview of the MVD detector. Red structures indicate pixel detectors, green structures indicate strip detectors. Yellow is the outer boundary of the MVD. Picture taken from Ref. [27].	29
3.9.	Schematic overview of the sensor module sizes of the MVD. Left: Pixel modules. Center and right: Strip modules [27].	30
3.10.	Schematic profile of a hybrid pixel sensor with readout, support structure and cooling. Picture taken from Ref. [27].	31
4.1.	Schematic drawing of the JDRS.	34
4.2.	Schematic overview of the JDRS. Every hardware component of the system corresponds to one of the four defined communication layers and has a representation in software or firmware. Figure adapted from Ref. [36].	35
4.3.	The digital readout board A of the readout system: 1) SIS1100 CMC 2) Xilinx Virtex-4 FPGA 3) power connectors 4) 68-pin connector to adapter board. Picture taken from Ref. [36].	36
4.4.	The digital readout board B ML605 from Xilinx: 1) Virtex-6 2) SFP port 3) FMC connectors to adapter board 4) Compact flash slot 5) DDR3 RAM.	38
4.5.	Schematic firmware setup. Data delivered via SIS1100 will be distributed to the modules indicated by the address. The red arrows indicate the path the data packet will take for the example given.	39
4.6.	Schematic overview of the GBT and Versatile Link project [42].	43
4.7.	Schematic usage of the GBT-FPGA core within the GBT project [44].	44
5.1.	ToPix 3 analog part of a pixel cell. Figure from Ref. [45].	47
5.2.	Pixel Control Logic for a single pixel. Figure taken from Ref. [45].	48
5.3.	Double column readout logic of the final production version of the ToPix ASIC. Picture taken from Ref. [45].	49
5.4.	Layout scheme of the ToPix 3. In the lower part are the pixels in double columns located. Figure taken from Ref. [45].	50

5.5. Numbering scheme of the pixel cells on the ToPix 3. Four double columns with an even and an odd side. The two short columns (0b00 and 0b11) are at the top and the bottom of the matrix, the two folded long double columns (0b01 and 0b10) are located in the middle. Arrows indicate the direction of rising pixel addresses. . . . .	52
5.6. Photograph of the ToPix 3 test setup. . . . .	53
5.7. ToPix Readout Board: 1) LVDS↔SLVS level converter 2) Potentiometer 3) ToPix 3 4) DAC 5) Measurement jumper 6) Power connectors. . . . .	54
5.8. Time difference between the switching of TESTP versus the detected charge of the pixel. The TESTP has to keep the polarity for at least 8 $\mu$ s to ensure the complete processing of the testpulse for all injectable charges. . . . .	56
5.9. Calibration measurement of the DAC channel for the internal injection circuit for Module 4. Upper frame: Calibration curve with quadratic fit function. Lower frame: Deviation of the data points from the quadratic fit. . . . .	57
5.10. Test of ToT linearity for the full charge range. Upper frame: ToT as a function of the injected charge. Lower frame: Deviation of the ToT data from the linear fit. . . . .	58
5.11. Test of ToT linearity for low injected charges. Upper frame: ToT as a function of the injected charge. Lower frame: Deviation of the ToT data from the linear fit. . . . .	59
5.12. Measurement of the signal shape for the ToPix 3. Displayed are the leading edge (left side of the peak) and trailing edge (right side of the peak) times stamps for hits with different injected charges. . . . .	60
5.13. Pixel check measurement at 50 MHz without address filtering. 10 injections/Pixel. . . . .	61
5.14. Frequency variation measurement of a ToPix 3 prototype at 50 MHz clock frequency. Left frame: number of detected hits for 10 injections. Middle frame: Average leading edge. Right frame: Average trailing edge. . . . .	61
5.15. Frequency variation measurement of a ToPix 3 prototype. Left frames: number of detected hits. Middle frames: Average leading edge. Right frames: Average trailing edge. From top to bottom at 60 MHz, 70 MHz, 80 MHz, 90 MHz and 100 MHz clock frequency. . . . .	62
5.16. Frequency variation measurement of a ToPix 3 prototype. Left frames: number of detected hits. Middle frames: Average leading edge. Right frames: Average trailing edge. From top to bottom at 110 MHz, 120 MHz, 130 MHz, 140 MHz and 155 MHz clock frequency. . . . .	63
5.17. S-curve measurement of a pixel cell. The number of detected hits for a constant number of injections is displayed as a function of the injected charge. The black line indicates the fitted error-function. . . . .	65
5.18. Threshold distribution for untuned pixel cells. . . . .	66
5.19. 2D threshold distribution for untuned pixel cells. The black line indicates a gaussian fit. . . . .	66

5.20. Pixel cells threshold distributions. Green: Untuned threshold distribution. Violet: Tuned threshold distribution. The black lines indicates gaussian fits. . . . .	67
5.21. 2D threshold distribution for tuned pixel cells. . . . .	67
5.22. Noise distribution of all pixel cells. The black line indicates a gaussian fit. . . . .	69
5.23. 2D noise distribution of all pixel cells. . . . .	69
5.24. S-curve determination of two pixel cells (1 and 17) of the same side of a double column (col 0, side 0). Each measurement was done with a different PDAC setting. If the pixel threshold are close to each other, the s-curve measurements show a drop of efficiency. . . . .	70
5.25. Overview of the COSY accelerator complex at the Forschungszentrum Jülich. At the bottom of the picture is the JULIC cyclotron with the proton and deuteron ion source. The pre-accelerated particles from the cyclotron are injected into to COSY ring at the top of the picture. After the acceleration and cooling to the desired beam momentum the particles are delivered to the different experiments and experimental places marked in yellow in the middle of the picture. Picture taken from Ref. [50]. . . . .	72
5.26. Number of protons in the COSY accelerator versus the number of detected hits per spill for the complete ToPix 3 ASIC. . . . .	73
5.27. Number of protons in the COSY accelerator versus the number of detected hits in double column 0. Comparison of the settings with and without the column loop. . . . .	74
5.28. Trailing edge distribution for five different beam intensities with column loop. Upper frame: Both sides. Lower left: even side. Lower right: odd side. . . . .	76
5.29. Trailing edge distribution for five different beam intensities with column loop. Upper frame: Both sides. Lower left: even side. Lower right: odd side. . . . .	77
5.30. Trailing edge distribution for double column 0 for five different beam intensities without column loop. Upper frame: Both sides. Lower left: even side. Lower right: odd side. . . . .	79
5.31. Leading edge distribution for five different beam intensities for double column 0 (short) with column loop. Upper frame: Both sides. Lower left: even side. Lower right: odd side. . . . .	80
5.32. Leading edge distributions for five different beam intensities for double column 1 (long) with column loop. Upper frame: Both sides. Lower left: even side. Lower right: odd side. . . . .	81
5.33. Leading edge vs. trailing edge distribution for different beam intensity of the long double column 1. Upper: MP 0.1. Middle: MP 0.5. Lower: MP 0.9. . . . .	83
5.34. Leading edge vs. trailing edge distribution for different beam intensity of the short double column 0. Upper: MP 0.1. Middle: MP 0.5. Lower: MP 0.9. . . . .	84



6.1.	Schematic workflow of data processing with the PandaRoot framework. The reconstruction and analysis part can use either simulated or real data as input. Figure taken from Ref. [51]. . . . .	88
6.2.	The center-of-mass frame for the $\bar{p}p \rightarrow \bar{\Lambda}\Lambda$ system. Drawn in this sketch is the coordinate system for the CMS frame of the $\Lambda$ or $\bar{\Lambda}$ . Figure taken from Ref. [76]. . . . .	92
6.3.	Sketch of the MVD and the different $\Lambda$ -disk positions. Solid lines indicate the MVD, dashed lines the $\Lambda$ -disks. The point of origin is identical with the interaction point. The upper sketch displays the proposed disk position at 40 cm and 60 cm, the lower picture displays three disk positions with the proposed double disk at around 40 cm, 60 cm and 80 cm. . . . .	93
6.4.	PANDA geometry of the beampipe (red), MVD sensors (blue, left) and $\Lambda$ double disk (blue and yellow). Blue indicates active sensor material, yellow indicated front-end electronics and support. Just the front-end electronics and support for the $\Lambda$ double-disk (Pos2) are displayed. . . . .	94
6.5.	Geometry of a single $\Lambda$ -disk. Green indicates semiconductor material. Blue/grey blocks represent the readout, cooling and support structure. . . . .	95
6.6.	Simulated angular distribution of the $\bar{\Lambda}$ for three different event generator models. Green/Triangle down: 1.642 GeV/c. Violet/Circle: 1.918 GeV/c. Blue/Triangle up: 6.000 GeV/c. Upper: <i>LambdaLambdaBar</i> , Center: <i>LambdaLambdaBarPol</i> , Lower: <i>LambdaLambdaBarHE</i> . . . . .	96
6.7.	Angular distribution of the $\bar{\Lambda}$ . Left: Simulated angular distributions. Right: Measured differential cross section from the PS185 experiment, Figure taken from Ref. [78]. . . . .	97
6.8.	Simulated radial vs. longitudinal decay position of the $\Lambda$ (first and third frame) and $\bar{\Lambda}$ (second and fourth frame) hyperon in the lab reference frame for beam momenta of 1.642 GeV/c (first and second frame) and 6.00 GeV/c (third and fourth frame). . . . .	99
6.9.	Simulated proper time distribution of the $\Lambda$ (left) and $\bar{\Lambda}$ (right). . . . .	100
6.10.	Analysis of simulated final state tracks per event which fulfill the selection criterion. Upper: 1.642 GeV/c. Center: 1.918 GeV/c. Lower: 6.000 GeV/c. . . . .	101
6.11.	Analysis of simulated final state tracks per event which fulfill the selection criterion after track fitter filtering. Upper: 1.642 GeV/c. Center: 1.918 GeV/c. Lower: 6.000 GeV/c. . . . .	102
6.12.	Track fitter bad-flag reduction per final state particle type for three beam momenta. Upper: 1.642 GeV/c. Center: 1.918 GeV/c. Lower: 6.000 GeV/c. . . . .	103
6.13.	$\chi^2$ -probability distribution of <b>PndVtxPRGFitter</b> vertex fitter. All events with a $\chi^2$ -probability $< 0.01$ have been removed. . . . .	105
6.14.	The detection efficiency as a function of the CMS production angle of the $\bar{\Lambda}$ for all three beam momentum and all disk positions. Upper: 1.642 GeV/c. Center: 1.918 GeV/c Lower: 6.00 GeV/c. . . . .	109
6.15.	Detection efficiency of the antiproton as a function of the angle $\Theta_p$ between the antiproton and the normal vector $\hat{y}$ in the $\bar{\Lambda}$ reference frame. Upper: 1.642 GeV/c. Center: 1.918 GeV/c Lower: 6.00 GeV/c. . . . .	110

## List of Figures

6.16.	$\bar{p}\pi^+$ invariant mass distribution for beam momenta of 1.642 GeV/c (upper), 1.918 GeV/c (middle) and 6.00 GeV/c (lower) beam momentum for Pos-1 (no disks).	113
6.17.	$\bar{p}\pi^+$ invariant mass distributions for the 1.642 GeV/c at the different $\Lambda$ -disk positions.	114
6.18.	Vertex Resolution when using <b>PndVtxPRGFitter</b> for $p_{\text{beam}}=1.642$ GeV/c for Pos-1. Upper: x-coordinate. Center: y-coordinate. Lower: z-coordinate.	116
6.19.	Vertex Resolution when using <b>PndVtxPRGFitter</b> for $p_{\text{beam}}=1.942$ GeV/c for Pos-1. Upper: x-coordinate. Center: y-coordinate. Lower: z-coordinate.	117
6.20.	Vertex Resolution when using <b>PndVtxPRGFitter</b> for $p_{\text{beam}}=6.00$ GeV/c for Pos-1. Upper: x-coordinate. Center: y-coordinate. Lower: z-coordinate.	118
A.1.	Decay kinematics in the reference frame and the CMS for the Armenteros-Podolanski-Plot. Picture based on [81].	123
A.2.	Schematic drawing of $\Lambda$ and $K_S^0$ arcs in the Armenteros-Podolanski-Plot. Figure taken from Ref. [81].	124
A.3.	Armenteros-Podolanski-Plot for the three different beam momenta using the MC generator data. The right arc belongs to the $\Lambda$ , the left arc belongs to the $\bar{\Lambda}$ .	126
A.4.	Armenteros-Podolanski-Plot for the three different beam momenta for Pos-1. Left: Reconstructed Plot including background. Right: Plot for MC truth particles. Upper: 1.642 GeV/c. Center: 1.918 GeV/c. Lower: 6.000 GeV/c. The right arc within a picture belongs to $\Lambda$ , the left arc belongs to the $\bar{\Lambda}$ .	127
A.5.	Analysis of simulated final state tracks per event which fulfill the selection criteria for Pos0.	128
A.6.	Analysis of simulated final state tracks per event which fulfill the selection criteria for Pos1.	129
A.7.	Analysis of simulated final state tracks per event which fulfill the selection criteria for Pos2.	130
A.8.	Analysis of simulated final state tracks per event which fulfill the selection criteria for Pos3.	131
A.9.	Analysis of simulated final state tracks per event which fulfill the selection criteria after track fitting for Pos0.	132
A.10.	Analysis of simulated final state tracks per event which fulfill the selection criteria after track fitting for Pos1.	133
A.11.	Analysis of simulated final state tracks per event which fulfill the selection criteria after track fitting for Pos2.	134
A.12.	Analysis of simulated final state tracks per event which fulfill the selection criteria after track fitting for Pos3.	135

# Danksagung

Am Ende dieser Arbeit möchte ich vielen Personen danken, die mich in den letzten Jahren unterstützt haben.

Professor James Ritman für die Ermöglichung und die Unterstützung bei der Erstellung dieser Arbeit.

Tobias Stockmanns für viele Diskussionen, Hilfe und besonders dass er *immer* eine offene Tür und ein offenes Ohr hatte, wenn ich es brauchte.

René Dosdall und Günter Sterzenbach für die schnelle und unkomplizierte Hilfe bei allen möglichen Computer und Grid Problemen, auch ausserhalb der „Öffnungszeiten“.

Marius Mertens, David-Leon Pohl, Huagen Xu, Andreas Herten, Andre Goerres, Dariusch Deermann, Lu Cao und Elisabetta Prencipe für ein wundervolles Arbeitsklima und die nötige Zerstreung wenn es allzu schwierig wurde.

Willi Erven, Michael Ramm und Peter Wüstner für die geduldvollen Fragestunden zu VHDL und SIS1100.

Steffen Muschter für die Hilfe bei der GBT Implementierung.

Gianni Mazza, Angelo Rivetti, Daniel Calvo, Paolo De Remigis, Laura Zotti and Richard Wheadon for their support around the ToPix 3 and the test beam.

Thomas Sefzick, Heinrich Schiffer, Dieter Prasuhn, dem Team der Elektronikwerkstatt und den Mitarbeitern der COSY-Warte für die Hilfe zum Testbeam.

Wilfried Schubert und Günter Schmitt für die seelische Unterstützung zu allen Tages- und Nachtzeiten.

Meiner Familie für all die Hilfe, die sie mir gaben.

Meinem Mann Tobit für all seine Kraft, Unterstützung und dass er mich liebt wie ich bin.

All diesen und natürlich auch den Menschen die mir geholfen, ich aber hier vergessen habe:

Danke, Thank you, Grazie, Xièxie





# Lebenslauf

## Persönliche Daten

Name: Simone Ulrike Esch  
Geburtsdatum: 16.09.1984  
Geburtsort: Troisdorf-Sieglar  
Familienstand: verheiratet  
Anschrift: Siegfried-Leopold-Strasse 69  
53225 Bonn-Beuel

## Schulbildung

07/1991 - 06/1995 Gemeinschaftsgrundschule Troisdorf-Spich  
07/1995 - 06/2004 Gesamtschule Troisdorf-Oberlar „Europaschule“  
Allgemeine Hochschulreife

## Studium

10/2004 - 04/2010 Studium der Physik an der Universität Bonn  
Diplomarbeit: „Auslese neuer DEPFET-Sensoren mit  
verbesserter Ansteuerung und charakterisierenden Messungen  
zum Antwortverhalten und zur Homogenität“

## Promotion

8/2010 - 02/2014 Promotion im Fach Physik an der Universität Bochum in  
Kooperation mit dem Institut für Kernphysik am  
Forschungszentrum Jülich  
Doktorarbeit: „Evaluation of the  $\bar{P}$ ANDA Silicon Pixel  
Front-End Electronics and Investigation of the  $\Lambda\Lambda$  Final State “